Doctoral theses at NTNU, 2022:187

Emir Ahmet Oguz

Rainfall-Induced Landslides in a Changing Climate

Doctoral thesis

NTNU
Norwegian University of Science and Technology
Thesis for the Degree of
Philosophiae Doctor
Faculty of Engineering
Department of Civil and Environmental
Engineering

NTNU
Norwegian University of
Science and Technology

Emir Ahmet Oguz

Rainfall-Induced Landslides in a Changing Climate

Thesis for the Degree of Philosophiae Doctor

Trondheim, June 2022

Norwegian University of Science and Technology
Faculty of Engineering
Department of Civil and Environmental Engineering

NTNU
Norwegian University of
Science and Technology

NTNU
Norwegian University of Science and Technology

Thesis for the Degree of Philosophiae Doctor

Faculty of Engineering
Department of Civil and Environmental Engineering

ISBN 978-82-326-6230-2 (printed ver.)
ISBN 978-82-326-6459-7 (electronic ver.)
ISSN 1503-8181 (printed ver.)
ISSN 2703-8084 (online ver.)

Doctoral theses at NTNU, 2022:187

Printed by NTNU Grafisk senter

Preface

This PhD study was conducted at the Department of Civil and Environmental Engineering at Norwegian University of Science and Technology, NTNU. It was made possible through the financial support from the Research Council of Norway to the research and development project KlimaDigital (2018-2022, grant number: 281059) and by the Department of Civil and Environmental Engineering at NTNU, and the generous involvement of the partners in the KlimaDigital project: SINTEF, the Norwegian Meteorological Institute (MET), Geonor, Nordic Semiconductor, Telia, the Norwegian Public Roads Administration, and the Norwegian Water Resources and Energy Directorate (NVE). The study was conducted under the supervision of Professor Vikas Thakur and Associate Professor Ivan Depina.

The PhD dissertation is organized as an article-based thesis and divided into two parts. Part I provides an introduction to the research topics covered in this PhD work, and Part II is comprised of a selection of publications that the author prepared in collaboration with several researchers during the PhD study.

The committee for the appraisal of this PhD dissertation comprises the following members:

Associate Professor Michele Calvello (first opponent)
University of Salerno, Italy

Dr. Anteneh Biru Tsegaye (second opponent)
Norwegian Geotechnical Institute, Norway

Professor Rao Martand Singh (administrator)
Norwegian University of Science and Technology, Norway

Supervisors of this PhD study are:

Professor Vikas Thakur (main supervisor)
Norwegian University of Science and Technology, Norway

Associate Professor Ivan Depina (co-supervisor)
Norwegian University of Science and Technology, Norway

Abstract

Rainfall-induced landslides pose a great risk to society and cause catastrophic consequences including environmental damages, economic losses, deaths, and injuries all around the world. Such landslides are typically relatively shallow and occur frequently on hillsides with the capacity to evolve into destructive debris flows. The frequency of rainfall-induced landslides is expected to increase due to the ongoing climate change and the corresponding changes in the rainfall patterns. Moreover, the expansion of human settlement towards landslide-prone areas will increase the risks due to negative effects of human activities on slope stability and more severe consequences. The expected higher risks in the future necessitate better landslide risk assessment and management strategies. Therefore, this PhD thesis examines several topics that contribute to mitigating societal risks resulting from rainfall-induced landslides.

Development and implementation of efficient landslide risk mitigation measures rely on accurate and reliable spatiotemporal prediction of rainfall-induced landslides. Providing such predictions is often a challenging task due to the uncertainties in landslide prediction model parameters. Spatial variability of the model parameters contributes significantly to the uncertainties and limits the capacity of models to provide accurate spatial and temporal predictions. The model parameters might greatly vary over space and affect the landslide predictions. This PhD thesis examines the effects of spatial variability on the prediction of rainfall-induced landslides. This study proposes a new probabilistic three-dimensional landslide susceptibility model that accounts for spatial variability. Spatial variability of landslide model parameters is modeled by random field approach. In addition, Monte Carlo method is utilized in the developed model to quantify the effects of the uncertainties in model parameters on landslide predictions. The developed landslide model is validated using benchmark problems from literature and extensive simulations using a finite element-based program. Results of this study reveal the importance of spatial variability on the predictions of spatially distributed rainfall-induced landslides.

In addition to developing more accurate landslide prediction models, there is a need to quantify the effects of climate change on rainfall-induced landslides. Climate change is becoming more visible as climate abnormalities and corresponding catastrophic events are happening more frequently. There exist climate projections to understand how climate will change based on different socioeconomic narratives. For many countries worldwide, these climate projections display more intense and frequent rainfall events. The changes in rainfall patterns will have effects on the occurrence of rainfall-induced landslides but are not explicitly quantified. Through the quantification of the climate change impact on rainfall-induced landslides, mitigation strategies can be applied to strengthen the resilience and adaptive capacity of society to climate change and corresponding changes in landslide risk. This PhD study addresses this issue with a framework coupling climate and landslide modeling chains. A novel probabilistic framework is proposed for the integration of the modeling chains. In this framework, impacts of extreme intense rainfall events are scaled with their occurrence probability to obtain an ‘overall’ climate change impact. This approach provides a more realistic basis for the quantification of the climate change impact on rainfall-induced landslides without bias due to extreme rainfall events. Using the proposed approach, a comprehensive study is conducted on a landslide-prone study area in Trøndelag, central Norway. The study reveals the overall climate change impact on rainfall-induced landslides with increased probabilities of landslide initiations in the future.

Improved assessment of landslide risk contributes to better landslide risk management strategies. Among the different strategies relying on structural and nonstructural solutions, a landslide early warning system (LEWS) is recognized as an efficient strategy due to its lower costs and higher flexibility in comparison to alternative solutions. Landslide risk can be mitigated by these systems, which issue early warning to take necessary actions, such as evacuating people, moving mobile infrastructure, or closing road or railway sections. Landslide monitoring can support LEWSs and improve their reliability by providing consistent and reliable hazard assessments based on collected data. This PhD study examines a landslide-prone study area in Trøndelag, central Norway for the deployment of a hydrological monitoring system. The hydrological monitoring system is supported by state-of-the-art IoT-based technologies that provide efficient data acquisition and transmission. The system was deployed at two locations in the study area. The response of the slopes to seasonally cold climate conditions is monitored by volumetric water content sensors, suction sensors, and piezometers. The deployed system collected valuable information on the effects of ground freezing and thawing, rainfall, and snowmelt on the monitored parameters. A pilot study was implemented to develop an automated landslide prediction model, which integrates collected data with a physical-based landslide prediction model. This pilot study showed the potential of the collected data to be used in combination with a landslide prediction model, which can be a basis for a landslide warning model.

Acknowledgements

I would like to express my sincere gratitude to my supervisors, Professor Vikas Thakur and Associate Professor Ivan Depina. Their assistance and dedicated involvement in every step in the process helped me to accomplish my PhD. I am thankful to Associate Professor Ivan Depina for sharing his inspiring insights to clarify and formulate research questions through my PhD, and always being available to have a discussion with me. I feel privileged to have their trust in me to find my own way as an independent researcher.

I have enjoyed being a member of the Geotechnical Engineering group at NTNU. I would like to thank all members of the group for guiding me through insightful discussions, exchanging ideas and knowledge. All professors were always welcoming when I needed a technical discussion. As the group is quite international, I had the opportunity to know wonderful people from all around the world. I would like to thank all my colleagues for their direct and indirect support through my PhD study. They gave me a lot of good memories and companionship over the years in my PhD. I feel lucky to know them and would like to thank each and every one of them. I must also thank the technical staff and the administration at the Department of Civil and Environmental Engineering for helping me throughout my PhD.

I wish to express my gratitude to the researchers involved in the KlimaDigital project. I had the chance to collaborate with many of them during my PhD study. I would like to thank Bård Myhre from SINTEF for helping me to understand the advanced Internet of Things-based technologies and related concepts. I must acknowledge the great help from Rasmus E. Benestad and Kajsa M. Parding from the Norwegian Meteorological Institute (MET) on climate modeling. Besides, I would like to thank Graziella Devoli from the Norwegian Water Resources and Energy Directorate (NVE) for helping me with the interpretation of geology and landslide inventory. I greatly appreciate all of their contribution to my PhD study. Through these collaborations on interdisciplinary research topics, I could find the possibility to improve myself.

I would like to thank my parents and my sisters for their continuous encouragement, and their default expectancy of my success throughout my life. They always supported me with the warmness of family and reminded me about other important aspects of life than PhD. Besides, I wish to express my gratitude to my friends for supporting me in this process and making my life more enjoyable with their accompany. Lastly, I would like to express my deepest

appreciation to my wife, Nihan. None of this could have happened without her support and her trust in me. I must also appreciate her accompany in my life as a partner. We have had wonderful memories since the beginning of my PhD in Norway.

Support from my supervisors, colleagues, friends, and family, and their encouragement are evident in this dissertation. I wish you a pleasant reading experience.

Thanks!

Contents

Table of figures

Table of tables

List of Symbols and Acronyms

Latin symbols

$a_e - b_e - c_e$	principal semi-axes of the ellipsoidal sliding surface
c'	effective soil cohesion
$\boldsymbol{C}$	covariance matrix
$C_{mn}(l_m, l_n)$	covariance between the values of the model parameters at the locations l_m and l_n
d_u	initial groundwater depth
f_w	wet-day frequency
f_X	probability density function of parameter X
F_S	factor of safety
F_S^g	global factor of safety
g	function representing model output
g_{cr}	critical value of model output
H	depth to bedrock
H_w	initial groundwater depth
I	rainfall intensity
I_{ZLT}	long-term vertical infiltration rate
K_S	saturated hydraulic conductivity
$l = [l_1, l_2, \dots, l_k]$	a vector of spatial coordinated at k locations
l_x	correlation lengths in the direction of x
l_y	correlation lengths in the direction of y
L	rainfall duration
$\boldsymbol{L}$	lower triangle matrices
$\boldsymbol{L_x}$	lower triangle matrices in x direction
$\boldsymbol{L_y}$	lower triangle matrices in y direction
N	number of realizations/simulations
P_f	probability of failure

$P_{f,limit}$	threshold limit of probability of failure
t	time
$\boldsymbol{U}$	a vector of standard normal random variables
x_L	return level
$\boldsymbol{X} = [X(l_1), X(l_2), \dots, X(l_k)]$	a vector of normally distributed model parameter
$\boldsymbol{X_{LN}}$	a vector of lognormally distributed model parameter
z_e	perpendicular offset of the center of the ellipsoidal sliding surface above the ground
Z	vertical depth from the ground surface

Greek symbols

α	slope angle
α_e	aspect of the ellipsoidal sliding
α_{rain}	parameter related to the divergence of daily rainfall statistics from exponential distribution
α_{fit}	fit parameter
β	a constant assuming slope parallel flow of water
β_e	inclination of the ellipsoidal sliding surface in the direction of the motion
β_G	scale parameter of Gumbel distribution
γ_s	unit weight of soil
γ_w	unit weight of water
ζ	parameter related to connection between different time scales
θ	volumetric water content
θ_r	residual volumetric water content
θ_s	saturated volumetric water content
Θ	saturation coefficient
κ_G	location parameter of Gumbel distribution
λ	indicator function
μ	wet-day mean precipitation

$\boldsymbol{\mu} = [\mu(l_1), \mu(l_2), \dots, \mu(l_k)]^T$	a vector of mean values at k locations
μ_g	mean global factor of safety
μ_{F_S}	mean factor of safety
ρ	correlation coefficient
σ	standard deviation
$\sigma_{\Delta\mu}$	standard deviation of change in wet-day mean precipitation
$\sigma_{\Delta f_w}$	standard deviation of change in wet-day frequency
τ	return interval
τ_x	separation distances in the directions of x
τ_y	separation distances in the directions of y
ϕ'	effective friction angle
χ	Bishop's effective stress parameter
ψ	pore pressure head
ψ_0	steady-state long-term pore pressure head
ψ_1	transient short-term pore pressure head
ψ_0^{cap}	capillary fringe above ground water table

Acronyms

cdf	cumulative distribution function
CORDEX	Coordinated Regional Climate Downscaling Experiment
ESD	empirical-statistical downscaling
FEM	finite element method
GCM	global climate model
IDF	Intensity-Duration-Frequency
IoT	Internet of Things
IPCC	Intergovernmental Panel on Climate Change
LEWS	landslide early warning system
pdf	probability distribution function
RCM	regional climate model
RCP	Representative Concentration Pathways
SSP	Shared Socioeconomic Pathways

SWCC	soil water characteristics curve
TRIGRS	Transient Rainfall Infiltration and Grid-Based Regional Slope Stability
VWC	volumetric water content
3DPLS	3-Dimensional Probabilistic Landslide Susceptibility model

Part I

Primer

1. Introduction

1.1. Background and motivation

Landslides are defined as downslope movement of a mass of soil, rock, debris, or organic material under the effect of gravity. Landslides are ubiquitous events causing catastrophic consequences such as fatalities and injuries to people, economic losses, and environmental damages (e.g., Nadim et al. 2006; Petley 2012; Haque et al. 2016, 2019; Froude and Petley 2018; Görüm and Fidan 2021). Based on the Global Fatal Landslide Database, 4862 fatal landslides[1] occurred between 2004 and 2016 (Froude and Petley 2018). The research by Haque et al. (2019) revealed that 3876 fatal landslide events led to 163,658 deaths and 11,689 injuries globally from 1995 to 2014. In this 20-year period, 476 fatal landslides caused 1370 deaths and 784 injuries in Europe (Haque et al. 2016). Figure 1.1 shows the casualties in the period from 2010 to 2014 worldwide. The annual average economic loss in Europe associated with landslides was reported to be ca. € 4.7 billion (Haque et al. 2016). Another database, the Emergency Database by the Centre for Research on the Epidemiology of Disasters shows that 19 thousand people have been killed by natural hazards associated with landslides[1] in the period from 2000 to 2022, with the corresponding economic loss being US$ 5.0 billion.

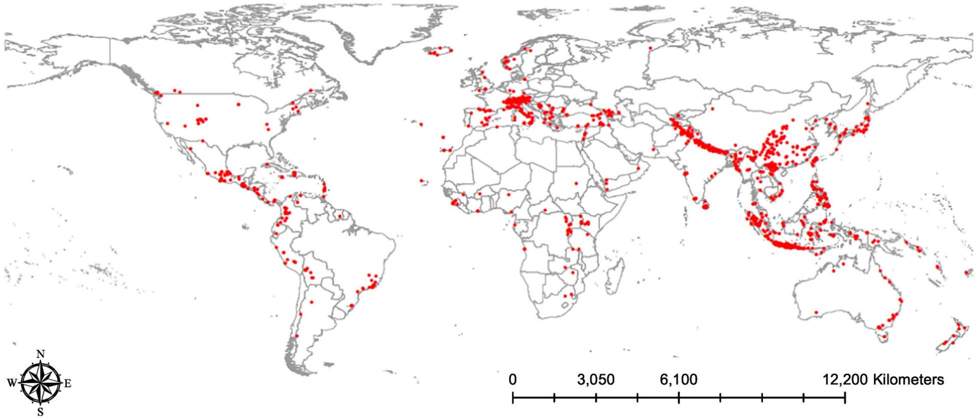

Figure 1.1: Worldwide distribution of casualties from fatal landslide events in the period of 2010-2014 (Haque et al. 2019).

---

[1] The events triggered by earthquakes are excluded.

In the report of the World Bank (Dilley et al. 2005), 3.7 million square kilometers of the land area was reported to be prone to landslides with 300 million people, ca. 5 percent of the world population. The research by Stanley and Kirschbaum (2017) showed that a great portion of the world has high to very high landslide susceptibility, as shown in Figure 1.2. Similarly, Emberson et al. (2020) provided exposure of population, road, and infrastructure to rainfall-induced landslides on a global scale and showed the widespread threat due to rainfall-induced landslides.

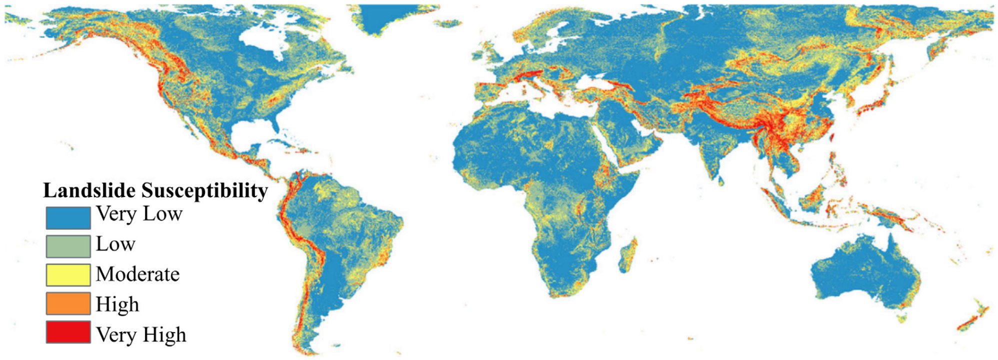

Figure 1.2: Landslide susceptibility map on a global scale (Stanley and Kirschbaum 2017).

Rainfall-induced landslides are generally shallow and pose a great risk to society due to their high frequency on hillsides and capacity to evolve in destructive debris flows. Shallow landslides can be triggered by a wide range of phenomena, such as rainfall, snowmelt, erosion, seismicity, human activities, or a combination of different phenomena. Among the triggering factors, water is mainly involved in slope destabilizations (Lacasse et al. 2010; Michoud et al. 2013; Pecoraro et al. 2019) by increasing the soil water content and soil unit weight, decreasing matric suction, causing erosion or artesian pressure.

The Intergovernmental Panel on Climate Change (IPCC) stated that there will be more intense and frequent extreme precipitation events over the 21st century in most parts of the world (IPCC 2014, 2021). This increase in the frequency and intensity of rainfall events is expected to result in higher risk associated with the rainfall-induced landslides in most of the countries and regions (e.g., Ho et al. 2017). In addition to climate change and its impacts on the rainfall-induced landslide risk, the population growth towards landslide-prone areas and corresponding human activities will also contribute to the increase in the landslide risk to society (Froude and Petley 2018).

Dealing with the increasing landslide risk requires developing and implementing corresponding landslide risk assessment and management strategies. Spatial and temporal predictions of landslide occurrence are of high importance in accurate identification of landslide risk. One of the main challenges in accurate spatiotemporal predictions of landslides are uncertainties associated with geotechnical, hydrological, and meteorological parameters controlling the stability of the slopes. There is a need to account for these uncertainties in landslide prediction models to improve the predictions in terms of location and timing. Additionally, accounting for uncertainty in landslide prediction allows one to implement approaches to reduce these uncertainties as new information becomes available (e.g., soil sampling, monitoring) and develop improved risk-reduction measures.

Landslide risk management is a complex process involving scientific, legal, and socio-political issues with the decision being mostly taken by the politicians or project owners (Fell 1994). Dai et al. (2002) grouped the strategies to deal with the landslide risk into four; planning control, engineering solutions, acceptance, and monitoring and early warning. The proper strategy is generally selected by risk comparison and cost-benefit analysis. Among these mitigation strategies, the landslide early warning system (LEWS) is commonly regarded as a cost-efficient strategy (Glade and Nadim 2014; Pecoraro et al. 2019). In an LEWS, landslide monitoring is one of the vital elements in establishing reliable landslide models and functional landslide early warning systems based on actual data. Through monitoring, a more consistent and reliable hazard assessment can be achieved based on collected data on the triggering variables and reduction of consequences with timely warnings to protect the elements under risk.

The increase in the risk associated with rainfall-induced landslides requires, among other, more robust landslide prediction models with better approaches to deal with uncertainties in landslide risk assessment, quantification of climate change impact to detect upcoming higher risk, and more consistent, and reliable LEWS through integrated monitoring systems to tackle the risk. These identified knowledge needs should be addressed for society to manage the expected higher landslide risks. Improving landslide risk assessment and management strategies to mitigate the upcoming landslide risk will strengthen the resilience and adaptive capacity of the society in the face of climate change. These knowledge needs motivate this PhD research.

1.2. Scope and objectives

This PhD work was conducted in collaboration with the KlimaDigital project (see Research Council of Norway: Project Bank) to contribute to the development of a novel geohazard assessment framework. KlimaDigital project aims to reduce the societal risks imposed by geohazards, such as shallow landslides, in the changing climate with a novel geohazard assessment framework supported by digital technology. The KlimaDigital project combines geohazard assessment, climate modelling, and digital technologies for data acquisition, storage, and processing into one framework. Figure 1.3 demonstrates the framework of the KlimaDigital project. The framework illustrates data flow and the interactions between the four work packages of the project. Starting from the physical domain on the left side of Figure 1.3, a landslide-prone case study area is monitored continuously by sensors. Rainfall, snow melt, or a combination of them trigger landslides, which pose a high risk to infrastructure, buildings, and lives. The collected data are transmitted to a cloud-based server for data storage. Then, the data are sent to the geohazard assessment model. On the right side of Figure 1.3, the weather predictions and climate projections for the future conditions are provided, respectively, by the weather and climate models to the geohazard assessment model. The geohazard assessment model is responsible to integrate the collected data on the landslide triggering variables with the weather predictions and climate projections to provide an accurate and reliable landslide hazard assessment.

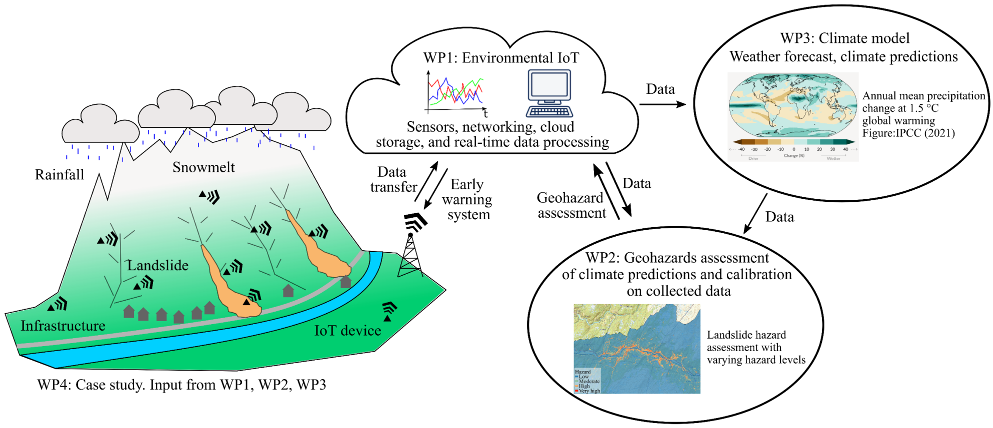

Figure 1.3: KlimaDigital framework (WP: work package).

In parallel to the overall framework of the KlimaDigital project, this PhD aims to contribute to mitigating the risk imposed by rainfall-induced landslides in a changing climate. To achieve this aim, several research topics were covered within the PhD study. These topics are better prediction of spatially distributed landslides by accounting for the uncertainties in prediction models, quantification of the increased threat imposed by rainfall-induced landslides in a changing climate, and better landslide risk assessment based on monitoring strategies supported by digital technologies.

Prediction of spatially-distributed rainfall-induced landslides is a difficult task due to the uncertainties originating often due to lack of knowledge, inherent natural variability, and model uncertainties (Phoon and Kulhawy 1999a). Avoiding these uncertainties in the landslide prediction models can result in either unrealistic or too conservative estimates (Fenton and Griffiths 2008). Several studies investigated the effects of variability of landslide model parameters with a single random variable approach where variable parameters are uncertain but still homogeneous within a single geological unit (e.g., Raia et al. 2014; Arnone et al. 2016). The single random variable approach does not account for the heterogeneous nature of the soil through space. Soil properties, such as cohesion and friction angle, might vary significantly from point to point within the same soil type. This spatially variable nature of soil might lead to local zones, which can be more prone to landslide occurrence. Only a few attempts have been made to investigate the effect of spatially variable model parameters in the prediction of landslides over larger extents, e.g., spatial variability of hydraulic conductivity in the study of Lizárraga and Buscarnera (2020). *In this PhD, one of the main objectives is to account for the spatial variability of the geotechnical model parameters in the landslide susceptibility assessment (see Paper I).* To address this objective, a robust landslide susceptibility model, which can account for the spatial variable model parameters, was developed. Spatially variable model parameters were modelled with random fields (Fenton and Griffiths 2008; Li et al. 2019) and integrated into landslide susceptibility analyses.

Climate change is an unequivocal process affecting landslide occurrence (IPCC 2021). A large number of countries have performed country-specific or region-specific climate predictions (Ho et al. 2017). Except for a few regions, increasing trends in air temperature, annual cumulative rainfall, and frequency of intense rainfall events were reported. These long-term climate changes are expected to have a significant impact on both nature and society. The upcoming climate conditions are available at varying spatial and temporal scales for most parts of the world. However, the impact of climate change on landslide susceptibility is mainly estimated indirectly from the expected changes in rainfall patterns, but rarely explicitly quantified. Explicit quantification of the change in landslide occurrence due to changing climate patterns will enable corresponding risk mitigation strategies to be developed. Several studies investigated the expected changes in landslide occurrence under climate change (e.g., Melchiorre and Frattini 2012; Shou and Yang 2015; Salciarini et al. 2019; Scheidl et al. 2020). However, these studies mainly employed extreme precipitation events with a low probability of occurrence. The strategy of utilizing only extreme rainfall events in climate change impact studies may overestimate the impact and provide a misleading impression of climate change. *In this PhD thesis, one of the main objectives is to quantify the climate change impact on landslide susceptibility (see Paper II).* For this purpose, climate and landslide susceptibility models were coupled into a probabilistic framework. The climate projections in terms of Intensity-Duration-Frequency (IDF) curves were integrated into a physical-based landslide susceptibility model to obtain landslide susceptibility projections. The probabilistic framework was developed to integrate the climate and landslide susceptibility modelling to account for the occurrence frequency of the extreme rainfall events and uncertainties in the landslide model parameters (see Paper II).

In addition to addressing the increasing threat of rainfall-induced landslides due to climate change, efficient strategies are needed to mitigate landslide risk to society. One efficient and widely employed strategy is landslide monitoring. The data collected through the monitoring system can be utilized in combination with physical-based or data-driven models to estimate landslide hazard levels. Then, the risk can be mitigated by issuing early warnings to evacuate people and mobile infrastructure under threat or close road or railway sections (Guzzetti et al. 2020). For landslides triggered by rainfall or snow melting, it is essential to understand the hydrological conditions leading to landslide occurrence. Hydrological monitoring can reveal the response of the ground to the weather conditions and provide significant insights into the hydrological processes occurring in similar hillsides (e.g., Bordoni et al. 2015; Comegna et al. 2016; Kim et al. 2021). *One of the objectives of this PhD study is to help to implement and deploy a hydrological monitoring system as a risk mitigation measure in a landslide-prone study area in Trøndelag, central Norway (see Paper III).* The deployed hydrological monitoring system is supported by state-of-the-art technologies within the domain of the Internet of Things (IoT) that provide flexible, cost- and power-efficient solutions with lower maintenance requirements. *In addition to the implementation of the hydrological monitoring system, another objective was to integrate the collected data into a physical-based landslide prediction model to obtain a more reliable hazard assessment.*

In summary, the PhD study aims to address the following objectives:

i. Account for the spatial variability of the geotechnical model parameters in the landslide susceptibility assessment.
ii. Quantify the climate change impact on landslide susceptibility.
iii. Implement and deploy a hydrological monitoring system as a risk mitigation measure in a landslide-prone study area in Trøndelag, central Norway.
iv. Integrate landslide monitoring data into a physical-based landslide prediction model to obtain a more reliable hazard assessment.

1.3. Outline of the PhD thesis

This thesis is organized as a paper-based thesis with two main parts: Part I – the overview of the research work and Part II – a selection of publications. Part I provides an introduction to the research topics covered during this PhD. This is followed by Part II, which is comprised of a selection of publications that the author prepared in collaboration with several researchers. Part I is divided into the following seven chapters:

- Chapter 1: Introduction

This chapter provides background information and motivation for this PhD study. The chapter presents the scope, objectives, and outline of the PhD thesis. Finally, a list of publications with a description of the authors' contributions is provided.

- Chapter 2: Spatial variability impact on rainfall-induced landslide susceptibility

This chapter briefly presents uncertainties in landslide susceptibility model parameters and random field method to explicitly model spatial variable parameters. An overview of the physical-based modelling strategy for shallow landslides is presented. The chapter introduces the 3-Dimensional Probabilistic Landslide Susceptibility model, which was developed to investigate the spatial variability impact on rainfall-induced landslide susceptibility. The chapter provides background information to the research work in Paper I and Paper II and presents the impact of spatial variability on landslide susceptibility (Paper II).

- Chapter 3: Climate change and its impact on landslide susceptibility

This chapter introduces climate modelling, changes in rainfall patterns, and elaborates the research work in Paper II. This chapter presents coupled climate and landslide modelling with a novel probabilistic framework, which combines the climate and landslide modellings. The projected climate change and associated landslide susceptibility maps will be provided for a case study area in Trøndelag, central Norway. The chapter relates to the findings in Paper II.

- Chapter 4: IoT-based hydrological monitoring and early warning model strategies

This chapter provides a brief background to the landslide monitoring and early warning systems. In this PhD study, a hydrological monitoring system was deployed at two locations in a landslide-prone case study area in central Norway. The locations and the technical details of the deployed monitoring system are explained in this chapter. This chapter briefly discusses technological developments within the domain of IoT, which were utilized in the deployed hydrological monitoring system to improve data acquisition and transmission. Landslide early warning model strategies relying on collected data are provided with a pilot study for an automated landslide prediction model. This chapter relates to the findings in Paper III.

- Chapter 5: Summary

This chapter presents the summary of the PhD work.

- Chapter 6: Conclusion

This chapter gives a brief conclusion of the PhD work by addressing the findings and conclusions of each one of the research works conducted during the PhD.

- Chapter 7: Recommendations for future work

This chapter points out the topics which need further research.

1.4. List of publications and declaration of authorship

The second part of the thesis consists of a selection of publications that the author prepared in collaboration with several researchers. The publications comprise three journal papers, with the author as the corresponding author in all papers. Paper I and Paper III are published, and the other journal paper are submitted to a journal for publication. The list of publications with the contribution of each author is provided below.

- Paper I: Emir Ahmet Oguz, Ivan Depina, and Vikas Thakur. *Effects of soil heterogeneity on susceptibility of shallow landslides*. Landslides 19, 67–83 (2022). https://doi.org/10.1007/s10346-021-01738-x

The main idea of the paper was proposed by Emir Ahmet Oguz. The development and implementation of the proposed physical-based model with its validation by finite element model were performed by Emir Ahmet Oguz. Ivan Depina contributed to the implementation of statistical methods, technical discussions, and guidance. The paper writing was performed by Emir Ahmet Oguz. The comments and suggestions from Ivan Depina and Vikas Thakur were beneficial during the paper writing.

- Paper II: Emir Ahmet Oguz, Rasmus E. Benestad, Kajsa M. Parding, Ivan Depina, and Vikas Thakur. *Quantification of climate change impact on rainfall-induced shallow landslide susceptibility*. Submitted.

The main idea of the paper was proposed by Emir Ahmet Oguz and Ivan Depina. The development and implementation of landslide susceptibility modelling were performed by Emir Ahmet Oguz. Rasmus E. Benestad and Kajsa M. Parding contributed to the paper with the climate modelling study and helped writing the corresponding sections of the paper. The integration of climate modelling and landslide susceptibility modelling was performed by Emir Ahmet Oguz with the technical discussions on the methodology with Ivan Depina. The paper writing was performed by Emir Ahmet Oguz. The comments and suggestions from Rasmus E. Benestad, Kajsa M. Parding, Ivan Depina, and Vikas Thakur were beneficial during the paper writing.

- Paper III: Emir Ahmet Oguz, Ivan Depina, Bård Myhre, Graziella Devoli, Helge Rustad, and Vikas Thakur. *IoT-based hydrological monitoring of water-induced landslides: a case study in central Norway*. Bull Eng Geol Environ 81, 217 (2022). https://doi.org/10.1007/s10064-022-02721-z

The main idea of the paper was proposed by Emir Ahmet Oguz. The technological aspects of the IoT system were handled by Bård Myhre and Helge Rustad. Deployment of the landslide monitoring system in the landslide-prone case study area was performed by Emir Ahmet Oguz and Ivan Depina. The geological study over the study area and the study on landslide inventory were performed by Emir Ahmet Oguz and Graziella Devoli. The paper writing was mainly performed by Emir Ahmet Oguz. Bård Myhre contributed to writing with the parts related to the IoT concept. The comments and suggestions from Ivan Depina, Graziella Devoli, Helge Rustad, and Vikas Thakur were beneficial during the paper writing.

2. Spatial variability impact on rainfall-induced landslide susceptibility

2.1. Introduction

This PhD thesis examined the effects of spatially variable geotechnical parameters on the predictions of rainfall-induced landslides by implementing physical-based landslide susceptibility models. Variability of the model parameters was accounted for in the analyses and the model predictions were utilized to assess the likelihood of landslide occurrence as an index of landslide susceptibility. To examine the impact of spatially variable geotechnical model parameters, a new Three-Dimensional Probabilistic Landslide Susceptibility (3DPLS) model was developed. In the 3DPLS model, random field approach is utilized to explicitly model the spatially variable model parameters. Besides, the Monte Carlo method is coupled with the model to propagate the uncertainties from the input model parameters to the model predictions in terms of probability of failure.

This chapter provides a basis to evaluate the impact of spatial variability of geotechnical and hydrological model parameters on the susceptibility of rainfall-induced landslides. In Section 2.2, an overview of the uncertainties in landslide susceptibility assessment and the random field approach to model spatially variable parameters are presented. Section 2.3 aims to explain physical-based landslide susceptibility models, the TRIGRS and 3DPLS, which were employed in this PhD thesis. Finally, the impact of spatially variable parameters on landslide susceptibility will be provided in Section 2.4, which relates to the findings in Paper I.

2.2. Uncertainties in landslide susceptibility assessment

Predictions of spatially distributed landslides often include uncertainties emerging from geotechnical, hydrological, and meteorological parameters controlling the stability of slopes, Geographic Information System data sources (e.g., Sandric et al. 2019), model uncertainties, and raster resolution limitations (e.g., Shirzadi et al. 2019). The uncertainties in geotechnical and hydrological parameters emerge from a variety of sources, but primarily from inherent natural variability, measurement error, and transformation uncertainty (Phoon and Kulhawy

1999a). These sources can be further divided into two categories: aleatory and epistemic uncertainties (Baecher and Christian 2003; Lee and Jones 2014). Aleatory uncertainty describes the variability of natural phenomena, and therefore, inherent natural variability is categorized as aleatory uncertainty. Measurement error and transformation uncertainty are denoted as epistemic uncertainty, which originates from a lack of knowledge.

Significant uncertainties in geotechnical and hydrological parameters were reported in the literature (Phoon and Kulhawy 1999a, b). These uncertainties present a great challenge in accurate spatial and temporal predictions of the landslides. This study performed probabilistic landslide susceptibility analyses accounting for the uncertainties of the model parameters. Landslide susceptibility assessments rely on the probability of landslide initiation based on slope stability analyses. In the landslide susceptibility analyses, accounting for these uncertainties has a vital role as it allows a rational calculation of slope stability (Lacasse et al. 2010). Estimates of landslide occurrences might be unrealistic or too conservative without accounting for the effects of uncertainties in the analyses. Therefore, these uncertainties in landslide susceptibility analysis should be accounted for in a probabilistic framework to obtain a more unbiased assessment of slope stability.

Probabilistic landslide susceptibility analysis accounts for the variability of the model parameters and provides the probability of landslide initiation. The uncertainties in the model parameters can be propagated to the model output by using statistical simulation methods by sampling the model parameters randomly from their corresponding probability distributions. In this PhD thesis, the Monte Carlo method was utilized due to its straightforward implementation and robust nature. Probabilistic analyses feature one of the two main approaches for modelling uncertain parameters: single random variable approach and random field approach. The single random variable approach assumes a single random parameter for each simulation, which is sampled from the corresponding probability distribution. The model parameters, such as geotechnical and hydrological parameters, are assumed to be uniform over space. In the random field approach, the spatial variability of the model parameters is explicitly modelled by generating random fields. This approach is found to be more realistic as it allows the parameters to vary spatially (Fenton and Griffiths 2008), and it is utilized in this study.

2.2.1. Random fields

The uncertainties in model parameters can be modeled by random fields that account for variability through space (Baecher and Christian 2003; Fenton and Griffiths 2008). In the modeling of random fields, a probability density function (pdf) is used to statistically describe the uncertainties in the parameters. In addition to the pdf, a covariance function is employed to define the spatial dependence of the parameter. In Paper I, the Gaussian (normal) and lognormal random fields were utilized to explicitly model the spatial variable model parameters.

Gaussian random fields

The Gaussian random field is corresponding to the multivariate Gaussian or normal distribution, which is the most fundamental distribution in statistics due to the central limit theorem (Baecher and Christian 2003). This theorem states that the sum of independent and arbitrarily distributed random variables has a Gaussian distribution as the number of summed variables goes to infinity. In natural sciences, the Gaussian distribution is the widely preferred distribution due to its advantages including simple probabilistic nature and characterization (Fenton and Griffiths 2008).

Given a set of spatial coordinates, $\boldsymbol{l} = [l_1, l_2, \dots, l_k]$, the joint pdf of the multivariate Gaussian distribution of a model parameter, $\boldsymbol{X} = [X(l_1), X(l_2), \dots, X(l_k)]$, $f_X(\boldsymbol{X})$, is defined as follows:

$$f_X(\boldsymbol{X}) = \frac{1}{(2\pi)^{k/2}\,|\boldsymbol{C}|^{1/2}} exp\left\{-\frac{1}{2}(\boldsymbol{X}-\boldsymbol{\mu})^T\boldsymbol{C}^{-1}(\boldsymbol{X}-\boldsymbol{\mu})\right\} \tag{2.1}$$

where $\boldsymbol{\mu}$ is the vector of mean values, $\boldsymbol{\mu} = [\mu(l_1), \mu(l_2), \dots, \mu(l_k)]^T$, $\boldsymbol{C}$ is the covariance matrix between the values of $\boldsymbol{X}$, and k is the number of elements in $\boldsymbol{X}$. $\boldsymbol{C}$ is a $k \times k$ positive definite matrix (Eq. 2.2) and each element of $\boldsymbol{C}$, $C_{mn}(l_m, l_n)$, defines the covariance between the values of the model parameters at the corresponding locations, $X(l_m)$ and $X(l_n)$, as specified in Eq. 2.3.

$$\boldsymbol{C} = \begin{bmatrix} C_{11} & C_{12} & \cdots & C_{1k} \\ C_{21} & C_{22} & \cdots & C_{2k} \\ \vdots & \vdots & \ddots & \vdots \\ C_{k1} & C_{k2} & \cdots & C_{kk} \end{bmatrix} \tag{2.2}$$

$$C_{mn}(l_m, l_n) = \begin{cases} \sigma^2(l_m) & , m = n \\ \sigma(l_m)\sigma(l_n)\rho(l_m, l_n) & , m \neq n \end{cases} \tag{2.3}$$

where $\sigma(l_m)$ and $\sigma(l_n)$ are the standard deviations of the model parameter at coordinates l_m and l_n, respectively, and $\rho(l_m, l_n)$ is the correlation coefficient of the model parameters at coordinates l_m and l_n.

A widely used parameter for generating random fields is correlation length, which describes the variability of a random field, i.e., variability of parameter through space. A simple interpretation of correlation length is that it defines the distance over which the soil parameters are significantly correlated, i.e., by more than 10% (Fenton and Griffiths 2008). Otherwise, the parameters separated by a distance greater than the correlation length are largely uncorrelated.

In Paper I, two-dimensional random fields were generated by using the two-dimensional ellipsoidal autocorrelation function (Eq. 2.4) and two-dimensional separable Markov autocorrelation function (Eq. 2.5), as shown below:

$$\rho(l_m, l_n) = exp\left\{-2\sqrt{\left(\frac{\tau_x}{l_x}\right)^2 + \left(\frac{\tau_y}{l_y}\right)^2}\right\} \qquad 2.4$$

$$\rho(l_m, l_n) = exp\left\{-2\left(\frac{|\tau_x|}{l_x}\right) - 2\left(\frac{|\tau_y|}{l_y}\right)\right\} = exp\left\{-2\left(\frac{|\tau_x|}{l_x}\right)\right\} exp\left\{-2\left(\frac{|\tau_y|}{l_y}\right)\right\} \qquad 2.5$$

where l_x and l_y are correlation lengths in the direction of x and y respectively, and τ_x and τ_y are separation distances in the directions of x and y between the model parameters at coordinates l_m and l_n, respectively. Figure 2.1 shows the autocorrelation functions, Eq. 2.4 and Eq. 2.5, in two-dimensional space assuming $l_x = l_y = 1$.

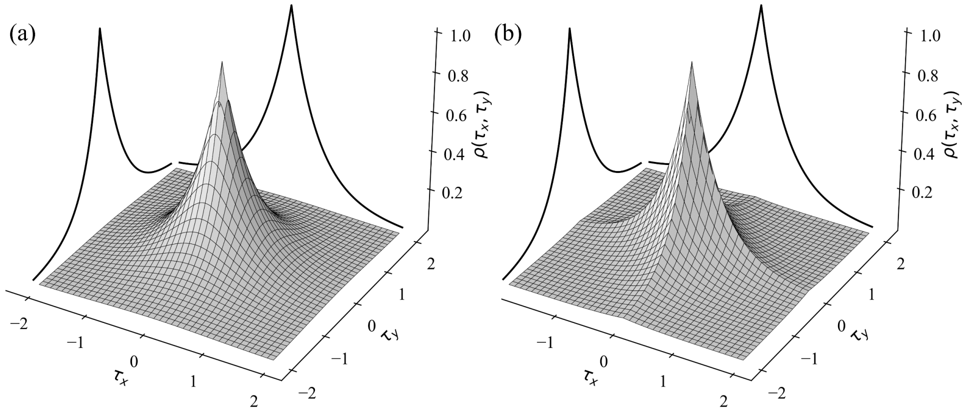

Figure 2.1: Two-dimensional (a) ellipsoidal autocorrelation function and (b) separable Markov autocorrelation function ($l_x = l_y = 1$).

There exist several algorithms to generate random fields, such as the moving average method, the covariance matrix decomposition method, the discrete transform method, and the local average subdivision method (Fenton and Griffiths 2008). In this work, the covariance matrix decomposition method was utilized to generate random fields due to its simplicity (Paper I). The random field of the model parameter, $\boldsymbol{X}$, at k different coordinates, can be defined as:

$$\boldsymbol{X} = \boldsymbol{L}\boldsymbol{U} \qquad 2.6$$

where $\boldsymbol{L}_{\boldsymbol{k}\times\boldsymbol{k}}$ is a lower triangular matrix such that $\boldsymbol{C} = \boldsymbol{L}\boldsymbol{L}^{\boldsymbol{T}}$, and $\boldsymbol{U}_{\boldsymbol{k}\times\boldsymbol{1}}$ is a normalized Gaussian random variable vector. $\boldsymbol{L}$ is typically obtained by performing the Cholesky decomposition (Fenton and Griffiths 2008). However, generating and decomposing $\boldsymbol{C}$ become a challenging task due to computation time and memory requirements when the number of elements in $\boldsymbol{C}$ increases. With the aid of separable autocorrelation functions, such as Eq. 2.5, Li et al. (2019) proposed the stepwise covariance matrix decomposition method to overcome the time and computational demanding nature of decomposing large matrices. Utilizing a separable autocorrelation function allows to disassemble $\boldsymbol{C}$ and $\boldsymbol{L}$ into one-dimensional matrices in the dimensions of the random field as follows:

$$\boldsymbol{C} = \boldsymbol{C}_{\boldsymbol{y}} \otimes \boldsymbol{C}_{\boldsymbol{x}} \qquad 2.7$$

$$\boldsymbol{L} = \boldsymbol{L}_{\boldsymbol{y}} \otimes \boldsymbol{L}_{\boldsymbol{x}} \qquad 2.8$$

where $\boldsymbol{C}_{\boldsymbol{x}}$ and $\boldsymbol{C}_{\boldsymbol{y}}$ are the one-dimensional covariance matrices in the directions of x and y respectively, $\boldsymbol{L}_{\boldsymbol{x}}$ and $\boldsymbol{L}_{\boldsymbol{y}}$ are lower triangle matrices in x and y directions, such that $\boldsymbol{L}_{\boldsymbol{x}}\boldsymbol{L}_{\boldsymbol{x}}^{\boldsymbol{T}} = \boldsymbol{C}_{\boldsymbol{x}}$ and $\boldsymbol{L}_{\boldsymbol{y}}\boldsymbol{L}_{\boldsymbol{y}}^{\boldsymbol{T}} = \boldsymbol{C}_{\boldsymbol{y}}$, and ⊗ is the Kronecker product. Following the disassembling, the random field of the model parameter, $\boldsymbol{X}$, can be redefined using the matrix-array multiplication operations as shown below:

$$\boldsymbol{X} = \boldsymbol{L}_{\boldsymbol{x}}\boldsymbol{U}\boldsymbol{L}_{\boldsymbol{y}}^{\boldsymbol{T}} \qquad 2.9$$

Figure 2.2 illustrates several examples of two-dimensional Gaussian random fields for spatially variable friction angle parameter, ϕ, with a mean of 30° and a standard deviation of 4.5°. The random fields are generated by utilizing the two-dimensional ellipsoidal autocorrelation function (Eq. 2.4) and two-dimensional separable Markov autocorrelation function (Eq. 2.5) for correlation lengths of $l = \{0, 10, 50, 500\}$ m. l is assumed to be equal in both x and y directions such that $l_x = l_y$. The random fields are 100×100 m discretized into

1 m cells. When $l = 0$ m (Figure 2.2a, e), there is no spatial dependence among the parameters, and they are assigned randomly to the field. As the correlation length increases, the parameters become correlated through larger distances and the random field becomes smother through space. Employing a larger l compared to the extent of the random field, such as 500 m in Figure 2.2d, h, lead to a more homogeneous random field. From Figure 2.2, it can be observed that the two-dimensional separable Markov autocorrelation function results in sharper changes through space compared to the two-dimensional ellipsoidal autocorrelation function.

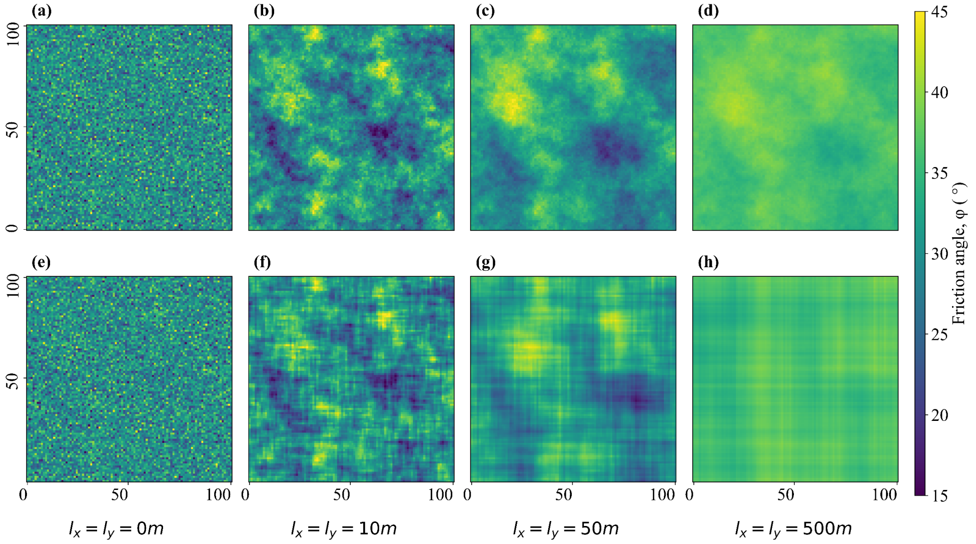

Figure 2.2: Gaussian random fields generated by utilizing (a, b, c, d) the two-dimensional ellipsoidal autocorrelation function and (e, f, g, h) two-dimensional separable Markov autocorrelation functions for $l_x = l_y = \{0, 10, 50, 500\}$ m.

Lognormal random fields

The lognormal random field is corresponding to the lognormal distribution, which is related to the Gaussian random distribution such that:

$$\boldsymbol{X_{LN}} = exp(\boldsymbol{Y}) \tag{2.10}$$

where $\mathbf{X_{LN}}$ is lognormally distributed spatially variable parameter and $\boldsymbol{Y}$ is underlying normally distributed spatially variable parameter with the corresponding parameters of mean, μ_Y, and standard deviation, σ_Y, which can be calculated as shown below:

$$\sigma_Y = \sqrt{ln\left(1 + \frac{\sigma_{X_{LN}}}{\mu_{X_{LN}}}\right)} \tag{2.11}$$

$$\mu_Y = ln(\mu_{X_{LN}}) - \frac{1}{2}\sigma_Y^2 \tag{2.12}$$

The Gaussian random field can be first generated for $\boldsymbol{Y}$. Then, the generated Gaussian random field can be transferred to the lognormal random field of $\boldsymbol{X_{LN}}$ using Eq. 2.10.

Monte Carlo method

Given a set of random parameters, $\boldsymbol{\lambda} = [\lambda_1, \lambda_2, \dots, \lambda_n]$ where n is the number of random parameters, some model output can be represented by a function of $g(\boldsymbol{\lambda})$ such that system fails when $g(\boldsymbol{\lambda})$ is lower than a critical value of $g(\boldsymbol{\lambda})$, g_{cr}. The model output in terms of $g(\boldsymbol{\lambda})$ becomes random as $\boldsymbol{\lambda}$ is random. The Monte Carlo method is a robust stochastic algorithm to simulate random model output by computing a large number of deterministic simulations in which random input parameters are sampled from their corresponding probability distributions. In the Monte Carlo method, N number of independent and identically distributed realizations of $\boldsymbol{\lambda}$ are utilized to evaluate corresponding $g(\boldsymbol{\lambda})$. Then, the probability of failure, P_f, are defined as follows:

$$P_f = \frac{1}{N}\sum_{i=1}^{N} \Lambda_i \tag{2.13}$$

where Λ_i is the indicator function providing 1 in case of failure $g(\boldsymbol{\lambda}) \leq g_{cr}$, otherwise 0.

2.3. Physical-based landslide susceptibility modeling

Physical-based landslide susceptibility models explicitly account for physics, such as infiltration, slope stability, rather than statistical and empirical methods to assess the susceptibility. They account for the effects of geotechnical, hydrological, and meteorological parameters on slope stability. These physical-based landslide susceptibility models commonly combine hydrological and slope stability models to predict the spatiotemporal occurrence of landslides. These models became widely utilized tools for predicting landslide-prone zones over large areas. Some of these physical-based models are provided in Table 2.1. Among these models, the Transient Rainfall Infiltration and Grid-Based Regional Slope Stability (TRIGRS) model (Baum et al. 2008) was utilized in this PhD study to obtain landslide susceptibility (Paper II and Paper III). Additionally, a new 3-Dimensional Probabilistic Landslide Susceptibility (3DPLS) model was developed to investigate the effects of spatially variable model parameters on landslide susceptibility assessment (Paper I).

These models allow users to investigate the response of large areas (from few km^2 to hundreds of km^2) to rainfall events, and to determine the location and timing of landslides. In hydrological models, the effect of rainfall on pore pressure build-up is evaluated by using analytical solutions of the one-dimensional governing partial differential equation of the infiltration process. Slope stability models rely mainly on the infinite slope stability method, which is only applicable to shallow landslides. The infinite slope stability method provides time and computational efficiency in investigating the slope stability over large areas. In these physical-based models, an area of interest is described by a grid of cells each of which has its own model parameters. The number of cells might be a few hundred to thousands depending on the extent of the area and refinement.

Table 2.1: List of a few physical-based landslide susceptibility models.

Model	Reference
distributed Shallow Landslide Analysis Model (dSLAM)	Wu and Sidle (1995)
Shallow Slope Stability Model (SHALSTAB)	Montgomery and Dietrich (1994)
Stability Index Mapping (SINMAP)	Pack et al. (2005)
Shallow Landslides Instability Prediction (SLIP)	Montrasio and Valentino (2008)
GEOtop-FS	Simoni et al. (2008)
Transient Rainfall Infiltration and Grid-Based Regional Slope Stability (TRIGRS)	Baum et al. (2002, 2008)
TRIGRS-P	Raia et al. (2014)
High Resolution Slope Stability Simulator (HIRESS)	Rossi et al. (2013)
r.rotstab	Mergili et al. (2014b, a)
Fast Shallow Landslide Assessment Model (FSLAM)	Medina et al. (2021)
*3-Dimensional Probabilistic Landslide Susceptibility (3DPLS)	Oguz et al. (2021)

*The 3DPLS model was developed as a part of the current PhD work (see Paper I).

2.3.1. TRIGRS model

The TRIGRS model provides the spatial and temporal distribution of rainfall-induced shallow landslides (Baum et al. 2002, 2008). The model comprises a hydrological model, a model for routing of surface runoff, and an infinite slope stability model.

TRIGRS can account for both wet initial (saturated) conditions appropriate for saturated or nearly saturated soils and unsaturated initial conditions where there exists a partially unsaturated soil above the water table. For saturated conditions, Iverson's linearized solution of the Richards equation (Iverson 2000) is utilized with the addition of the Heaviside step function to model the complex time-varying rainfall events (Baum et al. 2010). The solution of the transient pore pressure response, $\psi(Z,t)$, is the summation of steady-state long-term response, $\psi_0(Z)$, and transient short-term response to a rainfall event, $\psi_1(Z,t)$:

$$\psi(t,Z) = \psi_0(Z) + \psi_1(t,Z) \tag{2.14}$$

$$\frac{\psi_0(Z)}{Z} = \left(1 - \frac{H_w}{Z}\right)\beta \tag{2.15}$$

$$\beta = cos^2\,\alpha - \left(\frac{I_{ZLT}}{K_s}\right) \tag{2.16}$$

where t is the time, Z is the vertical depth from the ground surface, H_w is the initial groundwater depth, β is a constant assuming slope parallel flow of water, α is the slope angle in degrees, I_{ZLT} is the long-term vertical infiltration rate, and K_S is the saturated hydraulic conductivity. In the wet initial (saturated) conditions, $\psi_1(Z,t)$ is calculated based on the Richards partial differential equation that is simplified based on the assumption of tension saturation with saturated hydraulic conductivity (Iverson 2000). For short-term pore pressure response, TRIGRS supports solutions for two subsurface conditions: an infinite depth basal boundary and an impermeable basal boundary at finite depth. The solution for an infinite depth basal boundary is suited for the subsurface conditions with relatively uniform hydraulic properties through depth. Conversely, the other solution applies when there is high contrast in hydraulic properties through depth or there exists an impermeable boundary at a finite depth.

In the unsaturated initial conditions, the hydrological model relies on the analytical solution for one-dimensional vertical infiltration into unsaturated soil medium that was implemented by Srivastava and Yeh (1991). This solution treats the soil as a two-layer system with the unsaturated zone located above the saturated zone with a capillary fringe. The unsaturated zone captures some amount of water infiltrating from the ground surface and delays the process of water infiltrating to deeper depths. The rest of the water passes through the unsaturated zone to the water table and results in water table rise. The soil water characteristics curve (SWCC) of unsaturated soil is modeled by an exponential function (Gardner 1958) and the one-dimensional Richards partial differential equation is linearized for modeling infiltration into unsaturated soil medium (Srivastava and Yeh 1991).

The unsaturated model uses four parameters consisting of residual volumetric water content (VWC), θ_r, saturated VWC, θ_s, the fit parameter of the unsaturated model, α_{fit} (Gardner 1958), and saturated hydraulic conductivity in the vertical direction, K_S (Baum et al. 2008). The analytical solution is obtained by solving the one-dimensional form of the Richards equation that describes infiltration at the ground surface and infiltration through the unsaturated zone. By using the coordinate transformation to account for the effects of the sloping ground surface, the following expression for the Richards equation is obtained:

$$\frac{\partial \theta}{\partial t} = \frac{\partial}{\partial Z}\left[K(\psi)\left(\frac{1}{cos^2\alpha}\frac{\partial \psi}{\partial Z} - 1\right)\right] \qquad 2.17$$

where θ is the VWC, ψ is the pressure head, α is the slope angle. Srivastava and Yeh (1991) showed that Gardner's SWCC can be used to linearize Eq. 2.17 and provided an analytic solution for transient infiltration. The mathematical formulation for the computation of flux, hydraulic conductivity, pore pressure build-up in unsaturated soil, and groundwater table rise can be found in the TRIGRS manual (Baum et al. 2008).

The model for routing of surface runoff is implemented in TRIGRS to distribute the surface runoff from areas with excess surface water to adjacent downslope areas that can absorb it or route it further down (Baum et al. 2008). The TRIGRS is a cell-based model where the calculations for the infiltration and slope stability are performed on a cell-by-cell basis, i.e., individually for each cell over the discretized problem domain. For each cell, the stability of a slope is evaluated based on the factor of safety, F_S, as a ratio of resisting forces over driving gravitational forces:

$$F_S(Z,t) = \frac{tan\,\phi'}{tan\,\alpha} + \frac{c' - \psi(Z,t)\gamma_w\,tan\,\phi'}{\gamma_s z\,sin\,\alpha\,cos\,\alpha} \qquad 2.18$$

where c' is effective soil cohesion, ϕ' is the effective friction angle, γ_w is the unit weight of water, γ_s is the soil unit weight. For the unsaturated zone, the $\psi(Z,t)$ is multiplied by Bishop's effective stress parameter, $\chi = (\theta - \theta_r)/(\theta_s - \theta_r)$. Slope stability assessment is conducted by evaluating the minimum F_S along with depth as follows:

$$F_S(t) = \min_{Z \in [0,H]} F_S(Z,t) \qquad 2.19$$

where H is the depth to bedrock.

The TRIGRS model has several limitations arising from the simplifications and assumptions in the implementation of infiltration, routing of runoff, and slope stability model, while there exist several advantages such as accounting for infiltration into unsaturated soil, several methods for routing of excess water, allowing water table rise. The hydrological infiltration model assumes one-dimensional infiltration into a homogeneous and isotropic soil medium. In case of strong anisotropy, heterogeneity, or having dominant lateral flow during prolonged rainfall events, the results might be misleading. The model is highly sensitive to the initial groundwater conditions and simple runoff routing algorithms do not account for evapotranspiration and streamflow. In the slope stability model, employing a simple infinite slope stability model might result in misleading landslide stability assessment, although it is very straightforward to use with being not computationally demanding. Additionally, the model does not account for the effects of vegetation, which was shown to have notable impacts on landslide susceptibility (Scheidl et al. 2020).

2.3.2. 3DPLS model

The 3DPLS model is a probabilistic landslide susceptibility model, which was developed to address the need to investigate the impact of spatially variable model parameters on landslide susceptibility assessment (Paper I). The 3DPLS model couples a hydrological model to calculate transient pore pressure changes due to a rainfall event and a slope stability model to assess the stability of the sliding surface. The hydrological model relies on Iverson's solution of the Richards equation assuming tension saturation (Iverson 2000). The slope stability model employs the extension of Bishop's method of slope stability (Bishop 1955) to three dimensions, proposed in Hungr (1987). The details of the hydrological and slope stability models can be found in Paper I.

The 3DPLS model calculates the stability of ellipsoidal sliding surfaces that are generated over the study area for each cell unit. Figure 2.3 illustrates a three-dimensional illustration of an ellipsoidal sliding surface (Figure 2.3a), a single column with forces acting on it (Figure 2.3b), plane-view, and side-view of the ellipsoidal sliding surface (Figure 2.3c, d). An ellipsoidal sliding surface is defined by the dimensions of the ellipsoid along the three principal semi-axes, $a_e - b_e - c_e$, aspect of the motion, α_e, the inclination of the ellipsoid in the direction of the motion, β_e, perpendicular offset of the center of the ellipsoid, z_e above the ground, and the coordinates of the center of the cell where the ellipsoid is placed. Among the principal semi-axes, a_e is defined in the direction of motion, i.e., steepest slope, and b_e is defined as perpendicular to a_e and parallel to the slope surface. Other principal semi-axis, c_e are defined as perpendicular to a_e and b_e. In the current version of the model, β_e is assigned as the average slope angle over a rectangular zone with the dimensions of $2a_e \times 2b_e$ located at the center of the ellipsoid. Other parameters describing the ellipsoidal surfaces are defined by the user.

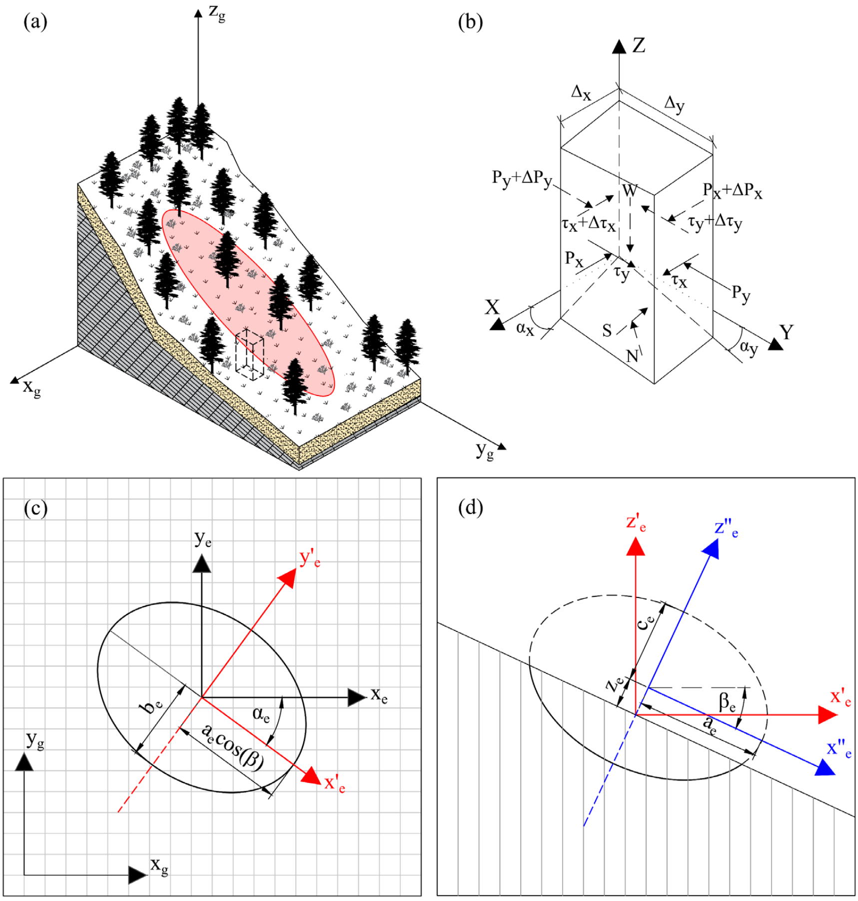

Figure 2.3: 3DPLS model: (a) three-dimensional illustration of the landslide body, (b) a single column with the forces, (c) plane view, and (d) side view of the ellipsoidal sliding surface.

For a given ellipsoid, the depth to the sliding surface is first calculated for each cell inside the sliding surface. The sliding surface is truncated at the cells where the depth to the sliding surface is greater than the thickness of the cell. The pore pressure values at the depth of sliding are calculated for each cell discretization inside the sliding surface at a given time within the rainfall duration. Then, the F_S is calculated for the ellipsoidal sliding surface by employing a three-dimensional extension of Bishop's simplified method of slope stability (see Paper I). The 3DPLS model generates ellipsoidal sliding surfaces centered at each discretized cell unit over the problem domain. Each cell unit mainly intersects with several ellipsoidal sliding surfaces with different F_S values. Among these F_S values, the cell is assigned with the minimum F_S value.

In the 3DPLS model, spatially variable model parameters are modeled by generating two-dimensional random fields, such as Gaussian or lognormal random fields (Section 2.2.1). Additionally, the model is coupled with the Monte Carlo method to propagate the uncertainties in the spatially variable model parameters to the model predictions. Following a series of model simulations in which the geotechnical parameters are randomly generated based on the spatially variable soil properties, the uncertainty in model predictions is calculated. The 3DPLS model provides maps of an empirical distribution of F_S from which the mean, μ_{F_S}, and P_f maps were estimated over the problem domain.

2.4. Impact of spatial variability on shallow landslide susceptibility

In landslide susceptibility studies, the variability of the model parameters was mainly integrated by considering different homogeneous geological units over the study area (e.g., Salciarini et al. 2006; Schilirò et al. 2021). Some of the physical-based models listed in Table 2.1, such as SINMAP, GEOtop-FS, HIRESS, TRIGRS-P, FSLAM, are capable of modelling the variability of model parameters with the single random variable approach. However, the single random variable approach treats parameters as variables but homogeneous within a single geological unit.

In the literature, many researchers addressed the need of accounting for the spatially variable geotechnical and hydrological parameters on the landslide susceptibility assessment (e.g., Burton et al. 1998; Mergili et al. 2014b, a; Arnone et al. 2016). Without accounting for spatial variability, the slope stability analyses may result in non-conservative results (Fenton and Griffiths 2008). Lizárraga and Buscarnera (2019, 2020) investigated the impact of spatially variable hydraulic conductivity, K_S, on the regional modeling of shallow landslides. The results revealed that accounting for the spatially variable K_S affected the shallow landslide susceptibility considerably. However, no attempt was made to study the spatial variability of geotechnical parameters on shallow landslide susceptibility using physical-based models. Paper I addresses this issue by accounting for the spatially variable geotechnical parameters in the rainfall-induced shallow landslide susceptibility by using the 3DPLS model.

In Paper I, a probabilistic parametric study was conducted on a simplified problem to investigate the impact of spatially variable geotechnical parameters on shallow landslide stability. Both drained case (effective stress-based) with effective cohesion, c', and effective friction angle, ϕ', and undrained case (total stress-based) with undrained shear strength, S_u, were studied. For each case, three variability levels and eight correlation lengths ranging from 0 m to 1000 m were examined. The simplified problem is a 2 m thick slope with a 25° inclination over a 100×100 m problem domain. The slope is fully saturated with a groundwater table at the ground surface, and slope-parallel groundwater flow is assumed. The domain was discretized into 20×20 equally sized cells.

The study was performed using three physical-based models: the three-dimensional finite element method (FEM) based PLAXIS program, the 3DPLS model, and a cell-based equivalent model of the 3DPLS model. The FEM model was used to validate the capacity of the 3DPLS model to capture the effects of spatial variability. Additionally, a cell-based equivalent of the 3DPLS model, which will be called the Cell-based model hereafter, was used for the comparison purpose. The Cell-based model uses the same hydrological model and statistical framework including random field generation and Monte Carlo method as the 3DPLS does. The difference emerges from the slope stability model. That is, the Cell-based model employs the infinite slope stability method to calculate the F_S (Eq. 2.18) for each cell individually, while the 3DPLS model calculates the F_S for ellipsoidal sliding surfaces over the study area.

The initiation of a landslide is a complex process that includes the development of the initial weak zone, the propagation of the weak zone, and corresponding load distributions prior to the sliding. In the FEM model, the complex processes are explicitly modeled. Therefore, a single and reliable F_S value representing the safety of the whole problem domain, i.e., the global factor of safety, F_S^g, can be obtained. However, the 3DPLS and Cell-based model output a map of F_S over the problem domain. These model predictions over the problem domain should be related to F_S^g to compare them with the FEM model results.

As the FEM model explicitly accounts for the complex processes, the model prediction was directly used as F_S^g. For the Cell-based model, the model predictions of F_S over the problem domain, $\{F_{Si},\ i = 1, 2, \dots,\ n\}$, was attributed to the F_S^g by harmonic average (Eq. 2.20), which was demonstrated to be well suited to characterize the effects of soil heterogeneity on slope stability (Fenton and Griffiths 2008). For the 3DPLS model, the F_S of the most critical ellipsoidal sliding surface was assigned to be F_S^g, as shown in Eq. 2.21.

$$F_S^g = \left[\frac{\sum_{i=1}^{n} F_{Si,Cell-based}}{n}\right]^{-1} \qquad 2.20$$

$$F_S^g = min\left[F_{Si,3DPLS}\colon i = 1, \dots,\ n\right] \qquad 2.21$$

where n is the number of cells in the discretized problem domain.

1000 Monte Carlo model simulations were conducted for each variability level and each correlation length in the probabilistic simulations for each one of the models. The results of the simulations in terms of F_S^g were averaged over the results of the Monte Carlo analyses to calculate the mean global factor of safety, μ_g, for comparison of the models.

The results of the probabilistic parametric study to see the effects of spatially variable geotechnical parameters on the μ_g are presented in Figure 2.4 for the drained case and in Figure 2.5 for the undrained case. The FEM model results are compared with both the Cell-based model results (Figure 2.4a, Figure 2.5a) and the 3DPLS model results (Figure 2.4b, Figure 2.5b). Considering the FEM model results for both drained and undrained cases, the following observations were made:

- The spatial variability of the geotechnical model parameters significantly affects the model predictions in terms of μ_g. Both the variability level and the degree of spatial dependence have essential effects on μ_g.
- Depending on the degree of spatial dependence, i.e., correlation length, a weak zone might exist with an extent large enough to dominate the μ_g. For this simplified problem with a domain of 100×100 m, μ_g decreases remarkably as the correlation length increases to 50 m.
- Further increase in the correlation length from 50 m up to 1000 m causes an increase in μ_g as the problem domain is less likely to contain a weak zone that can lower μ_g.

- In addition to the degree of spatial dependence, the variability level of the geotechnical model parameters affects μ_g. When the variability level increases, μ_g decreases for each correlation length. In particular, the decrease in μ_g due to the variability level is larger at 50 m correlation length.

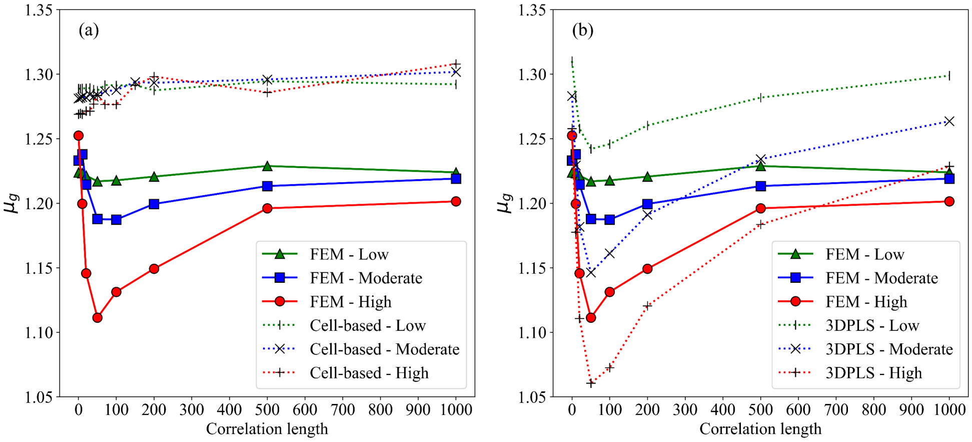

Figure 2.4: Effects of spatial variability on μ_g for the drained case: the FEM model results (a) with the Cell-based model results and (b) with the 3DPLS model results.

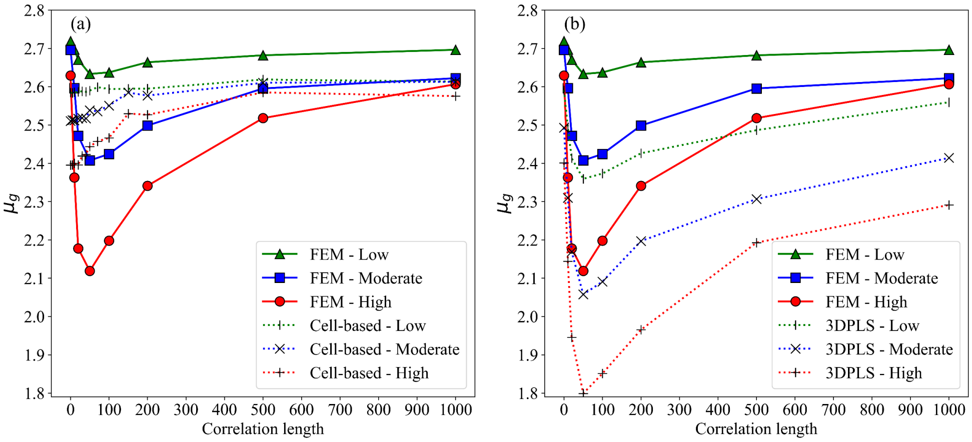

Figure 2.5: Effects of spatial variability on μ_g for the undrained case: the FEM model results (a) with the Cell-based model results and (b) with the 3DPLS model results.

Comparison of the FEM model results with the Cell-based model results (Figure 2.4a, Figure 2.5a) revealed that the Cell-based model is not able to capture the effect of spatial variability on μ_g. The reason is that the Cell-based model performs the calculations for each cell individually and the effect of weak zones on the μ_g is not captured. When it comes to the performance of the 3DPLS model, the 3DPLS model results showed similar trends compared to the FEM model results with respect to the variability levels and the degree of spatial dependence (Figure 2.4b, Figure 2.5b). These results validated the capacity of the 3DPLS model to capture the effects of spatial variability on the landslide susceptibility assessments.

For the simplified problem, the effect of mesh coarseness in the FEM model was investigated. The mesh coarseness was decided considering the trade-off between the mesh size and the computational runtime in the FEM model, and the convergence of the model estimate. Additionally, the number of cells inside an ellipsoidal sliding surface was investigated as it affects the 3DPLS model estimates. In the 3DPLS model, a threshold value was defined to specify the minimum number of cells inside a generated ellipsoidal sliding surface. When the number of cells in the slope stability calculation for a single ellipsoid is less than the given threshold value, the model is capable of sub-discretizing the cells by halving the cell size until the threshold value is reached. It should be noted that the geotechnical and hydrological parameters are not changed in the sub-discretization process. Similar to the coarseness in the FEM model, the threshold in the 3DPLS model was assigned by considering the convergence of the model estimates and the required time for model simulations.

Additionally, the number of Monte Carlo simulations might affect the model estimates in probabilistic analyses. Figure 2.6 shows the effect of the number of Monte Carlo simulations on μ_g for the parametric study. It was observed that μ_g values converge to a stable zone for all probabilistic analyses using the FEM model, the 3DPLS model, and the Cell-based model. For both undrained and drained cases, 1000 Monte Carlo simulation number was found to be sufficient to provide relatively accurate values without the effect of simulation number.

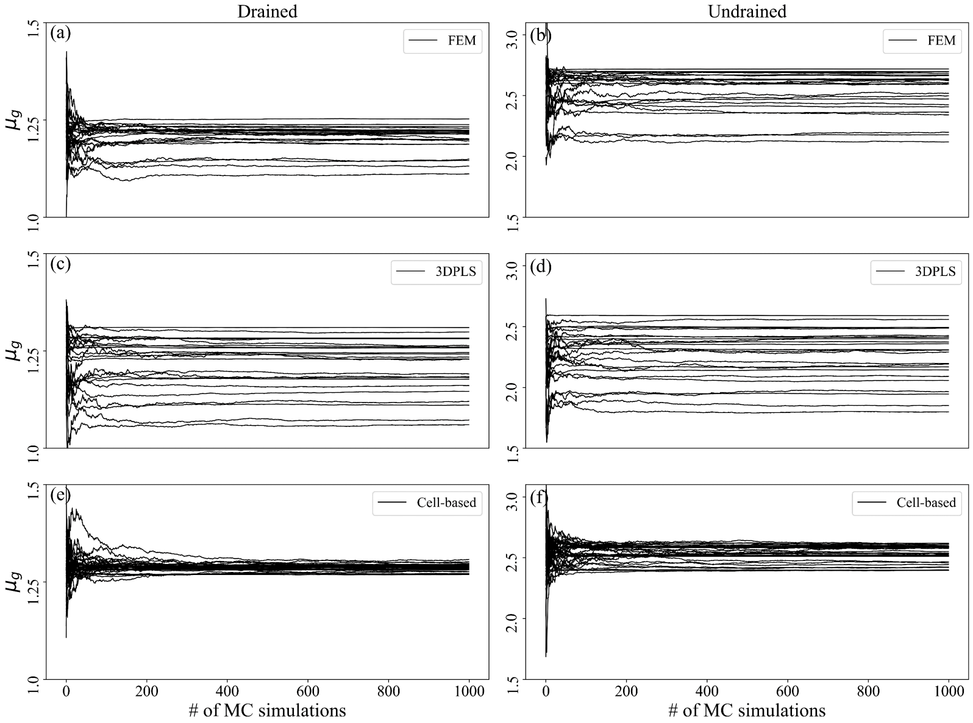

Figure 2.6: The effect of the number of Monte Carlo simulations on the calculated μ_g for (a, c, e) drained and (b, d, f) undrained cases: analysis results with (a, b) the FEM model, (c, d) the 3DPLS model, and (e, f) the Cell-based model.

Following the validation of the capacity of the 3DPLS model to capture the effects of spatial variability on shallow landslide stability, the model was tested on a landslide-prone study area in central Norway. In the study area, several shallow landslides occurred after an intense rainfall event in 2011. The 3DPLS model performance was compared to the Cell-based model performance in terms of capturing the landslide events. Comparison of the models was performed using the receiver operating characteristic (ROC) graph with the common performance metrics (e.g., Fawcett 2006). The results revealed that more accurate and precise results were obtained using the 3DPLS model than the Cell-based model. The details of the case study and the performance of the 3DPLS model can be seen in Paper I.

3. Climate change and its impact on landslide susceptibility

3.1. Introduction

This chapter introduces climate change and its impact on rainfall-induced landslide susceptibility. Section 3.2 defines anthropogenic climate change and the corresponding expected increase in temperature and precipitation. It presents future climate projections based on different greenhouse gas emission scenarios provided in the Fifth Assessment Report (AR5) and the Sixth Assessment Report (AR6) of the Intergovernmental Panel on Climate Change (IPCC) (IPCC 2014, 2021). In Section 3.3, a coupled climate and landslide modelling framework is introduced to be used in the quantification of the climate change impact on landslide susceptibility. Along with the modelling framework, this section presents a novel probabilistic framework providing a realistic basis for the evaluation of climate change impact on landslide susceptibility. Finally, in Section 3.4, the coupled climate and landslide modelling framework was demonstrated on a case study area in central Norway. Climate projections for the case study area and the corresponding changes in the landslide susceptibility are provided. This chapter relates to the findings in Paper II.

3.2. Climate change

Climate change is an ongoing worldwide problem due to emissions of greenhouse gases (GHGs). Increasing concentrations of GHGs result in more heat trapped in the atmosphere, which results in increasing temperatures as well as changes in the hydrological cycle, atmospheric circulation, and many other aspects of the climate system. Among GHGs, carbon dioxide (CO_2) contributes the most to climate change as it remains in the atmosphere much longer than other gases despite its lower heat-trapping capacity (IPCC 2013). Since pre-industrial times (here defined as the 1750s), the concentration of CO_2 in the atmosphere has increased by over 47%, and it continues to increase (IPCC 2014, 2021).

Global climate models (GCM) are useful tools for studying the consequences of increased GHG emissions in the coming decades and centuries. However, because of the inherently chaotic nature of the climate system, a single GCM simulation represents only one of many possible outcomes. To better understand the range of possible and probable climate change outcomes, an ensemble of GCM simulations is required. The World Meteorological Research Programme (WRCP) has since 1995 organized experiments via the Climate Model Intercomparison Project (CMIP), providing a common framework and experimental protocol to many climate modelling groups employing different GCMs (IPCC 2014, 2021). The GCM simulations performed in the fifth CMIP phase, CMIP5 (Taylor et al. 2012) provided a scientific basis to AR5 (IPCC 2014), while the latest assessment report AR6 (IPCC 2021) relied on simulations from the latest state-of-the-art GCMs produced under the sixth CMIP phase, CMIP6 (Eyring et al. 2016). This current PhD study utilized the GCM simulations performed in the CMIP5.

In the CMIP framework, emission scenarios are used to represent how different assumptions about future societal and technological development lead to changes in GHG emissions, land use, and other drivers of climate change. In CMIP5, the emission scenarios are known as Representative Concentration Pathways (RCPs) and are labelled by the corresponding level of radiative forcing in 2100, which is a metric defined by IPCC to define the net change in the energy-balance of the Earth system (Myhre et al. 2014). Four emissions scenarios were featured in AR5: RCP2.6, RCP4.5, RCP6.0, and RCP8.5 (numbers in Wm-2) (IPCC 2014). RCP2.6 is based on extensive mitigation measures leading to relatively low radiative forcing. RCP4.5 and RCP6.0 are intermediate scenarios where emissions peak around 2040 and 2080, respectively, and then decline. RCP8.5 is a worst-case scenario without any climate policy, increased population growth, high energy demand, and the corresponding increase in GHG emission throughout the 21st century. For CMIP6, a new set of emission scenarios were defined, known as Shared Socioeconomic Pathways (SSPs). There are five SSPs that represent different socioeconomic narratives including the population size, economic activities, energy use, climate policy, among others. For each SSP, several RCPs are generated, describing probable outcomes in terms of the radiative forcing. For example, SSP1-1.9 is an optimistic scenario assuming sustainable development (SSP1) that results in radiative forcing of 1.9 Wm-2. Many SSP-RCP scenarios were selected to drive climate models for CMIP6, but only five were featured in AR6 (SSP1-1.9, SSP1-2.6, SSP2-4.5, SSP4-6.0, and SSP5-8.5). The SSP scenarios of AR6 can be related to the closest RCP scenario of AR5 (e.g., RCP8.5 and SSP5-8.5) as they result in a similar radiative forcing by 2100, although the GHG composition, climate sensitivity in different models, and the resulting warming may differ somewhat (IPCC 2021). In this PhD study (Paper II), the high emission RCP scenario, RCP8.5 (IPCC 2014) was studied in the quantification of the climate change impact on landslide susceptibility.

Based on the emission scenarios, the response of the climate system is simulated by GCMs which incorporate the key physical and chemical processes in the atmosphere and provide multifaceted climate projections. However, GCMs have a relatively coarse spatial resolution (on the order of 100 km) and cannot resolve smaller scale physical processes. In order to use the projections obtained by GCMs to study local climate change, the data must be refined to a finer spatial resolution by the process known as downscaling (Takayabu et al. 2016). There are different downscaling methods including dynamic downscaling (e.g., Laprise 2008), empirical-statistical downscaling (ESD) (e.g., Benestad et al. 2008), and hybrid downscaling (e.g., Erlandsen et al. 2020). In dynamic downscaling, Regional Climate Models (RCMs), which are physical-based models accounting for the local atmospheric phenomena, are utilized. RCMs take boundary conditions from the GCMs and provide future projections on a finer resolution. In ESD, the method statistically analyzes the link between large and small scales in the historic data and applies the same link to future projections. Lastly, the hybrid downscaling combines the ESD and RCM data for the climate projections.

The Coordinated Regional Climate Downscaling Experiment (CORDEX) was initiated to provide a coordinated framework to evaluate and improve the dynamic downscaling using RCMs (Giorgi et al. 2009). The CMIP ensembles were downscaled according to the CORDEX framework globally. Among these global CORDEX data, the EURO-CORDEX ensemble (Jacob et al. 2014) was employed in this PhD work.

The increase in global surface temperature will increase evaporation and intensify the Earth's water cycle (IPCC 2021). This will lead to more intense and frequent rainfall events and more climate abnormalities such as typhoons in most parts of the world. On the other hand, some regions will also experience less precipitation, which will increase the risk of drought. On a regional scale, the expected climate change and its consequences rely strongly on location and corresponding regional variations in the atmospheric dynamics and the existence of physical phenomena such as convection, atmospheric rivers, cyclones. Many countries performed country-specific or region-specific climate change predictions and the corresponding change in the rainfall patterns (Ho et al. 2017). The future climate predictions were made until the end of the 21st century. The findings of the majority of the country- and region-specific reports in Ho et al. (2017) revealed an increase in the air temperature, annual cumulative rainfall amount with more intense and frequent rainfall events until the end of the 21st century. This increase in both long-term and short-term rainfall amounts will affect the frequency of rainfall-induced landslides.

In this PhD study, the impact of climate change, in terms of rainfall events, on the landslide susceptibility was investigated on a case study area in Trøndelag, central Norway (see the attached Paper II). In the 20th century, observations over Norway showed an increase of 1°C in air temperature and an 18% increase in annual mean precipitation. The climate projections for Norway show a further increase in the mean air temperature and the corresponding increase in the annual precipitation across Norway. In the report "Climate in Norway 2100" by Hanssen-Bauer et al. (2017), the expected increase in annual mean air temperature and annual precipitation were reported to be 4.5°C and 18% respectively, as calculated by the ensemble median value for RCP8.5 emission scenario (Figure 3.1). The frequency of days with intense rainfall events is expected to double in the RCP8.5 scenario. The projected increase in precipitation with more frequent, short duration, and high-intensity rainfall events is expected to increase the probability of rainfall-induced landslide occurrence. To address this increase, this PhD study utilized a coupled climate and landslide modelling framework, which will be presented in the following section.

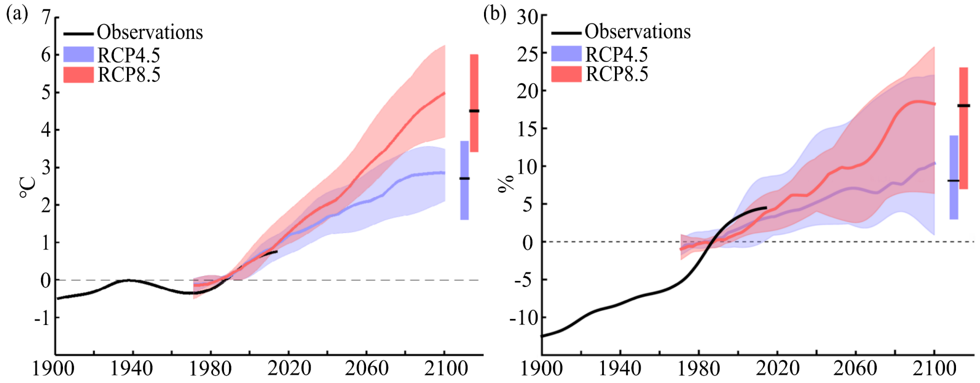

Figure 3.1: Expected change (a) in annual mean air temperature of Norwegian mainland and (b) in annual precipitation over Norway compared to the period 1971-2000: for two emission scenarios RCP4.5 and RCP8.5 with corresponding 5th and 95th percentile zones as shadings (Hanssen-Bauer et al. 2017).

3.3. Coupled climate – landslide susceptibility modelling

Many aspects of climate change, such as altered weather systems, air temperature, rainfall intensity, frequency of intense rainfall events, and cumulative rainfall, have direct and indirect impacts on landslide occurrence (Gariano and Guzzetti 2016). Landslide susceptibility over large areas requires a good linkage between meteorological conditions and landslides occurrence. This linkage can be achieved by several approaches such as simple rainfall – landslide relationship based on a defined threshold (Ciervo et al. 2017; Sangelantoni et al. 2018), empirical methods including several factors associated with the landslides (Dixon and Brook 2007; Shou and Yang 2015), or physical-based model (Chiang and Chang 2011; Melchiorre and Frattini 2012; Alvioli et al. 2018; Salciarini et al. 2019; Scheidl et al. 2020). In Paper II, the physical-based modelling approach was employed to relate the meteorological conditions to landslide susceptibility.

Studying the impact of climate change on landslide susceptibility necessitates incorporating both climate and landslide models (e.g., Gariano and Guzzetti 2016; Alvioli et al. 2018). This PhD study utilized a modelling framework consisting of a climate modelling chain and a landslide modelling chain, as shown in Figure 3.2. The climate modelling chain investigates both the present and future climate conditions, while the landslide modelling chain includes the calibration of the physical-based model based on the information over the study area, and the susceptibility analyses using the output of the climate modelling chain.

In the climate modelling chain, the present and future climate conditions are analyzed in terms of Intensity-Duration-Frequency (IDF) curves. These climate-dependent IDF curves are estimated by using a straightforward semi-empirical formulation that estimates approximate return levels for daily and sub-daily rainfall events for varying return intervals proposed by Benestad et al. (2019, 2021). The formulation in Eq. 3.1 does not assume stationarity in natural variations and therefore is well-suited for projecting IDF curves under climate change impact (Benestad et al. 2021).

$$x_L = \alpha_{rain}\, \mu \left(\frac{L}{24}\right)^{\zeta} ln(f_w \tau) \qquad 3.1$$

where x_L is the return level, in mm, for a given duration L, in hours, μ is the wet-day mean precipitation in mm/day, f_w is the wet-day frequency, τ is the return interval in years, and α_{rain}

and ζ are parameters related to the divergence of daily rainfall statistics from exponential distribution and connection between different time scales, respectively.

For the present climate conditions, historic observations from the weather stations were utilized in the formulation of the IDF curves. For the future climate conditions, the RCP8.5 projections from the EURO-CORDEX ensemble (Jacob et al. 2014) were used in combination with the present climate conditions. The Euro-CORDEX ensemble includes 56 projections by 22 RCMs applied to 8 GCMs from CMIP5 (Taylor et al. 2012). Although the ensemble provides an overall impression of how the climate will change, all possible outcomes might not be represented by such a limited number of projections (Mezghani et al. 2019).

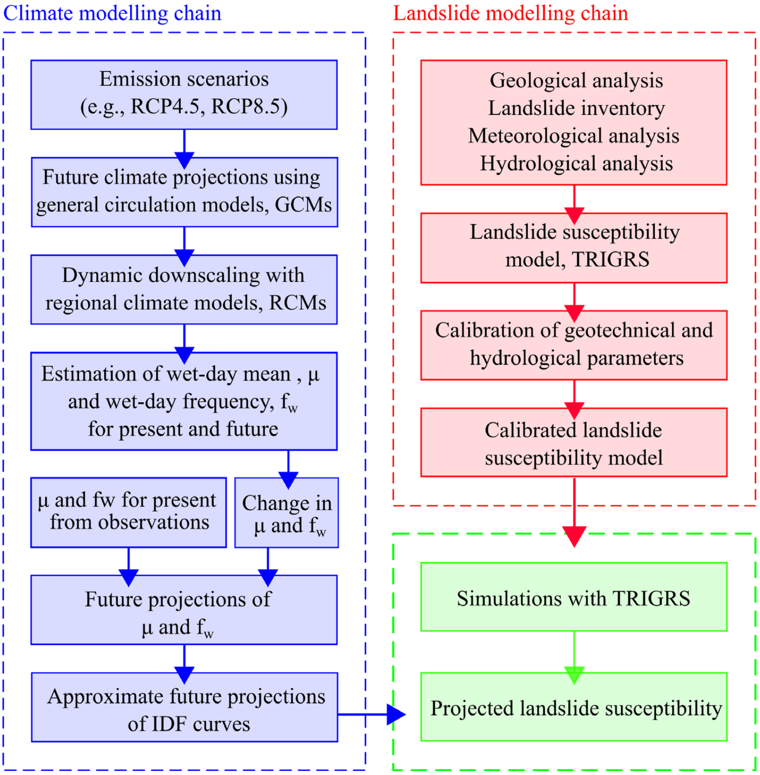

Figure 3.2: Modelling framework with climate and landslide modelling chains. The variables μ and f_w represents the wet-day mean and wet-day frequency respectively (From Paper II).

The coupled climate and landslide modelling framework includes a probabilistic framework combining the two modelling chains and providing a realistic interpretation of the climate change impact on landslide susceptibility. This framework will be presented in the following section.

3.3.1. A probabilistic framework for overall climate change impact

In the literature, the impact of climate change on landslide susceptibility was mainly investigated under extreme conditions (e.g., Melchiorre and Frattini 2012; Shou and Yang 2015; Salciarini et al. 2019; Scheidl et al. 2020). That is, very intense rainfall events of long return intervals, such as 50-, 100-year, were employed on the impact studies despite the fact that the probabilities of occurrence of these rainfall events are very low. Only considering these extreme rainfall events could over- or under-estimate the impact of climate change on landslide susceptibility depending on the utilized geotechnical and hydrological parameters. Therefore, it is necessary to account for the probability of occurrence of rainfall events to fully understand the impact of climate change on landslide susceptibility.

In this PhD study, a novel probabilistic framework was proposed to obtain overall climate change impact on landslide susceptibility by accounting for the probability of occurrence of rainfall events of a given duration. The term 'overall' refers only to the rainfall-induced landslide hazard by considering rainfall events of the varying return periods. It does not cover landslide hazards related to other triggering factors such as snow melt or earthquakes.

The proposed probabilistic framework leads to more reasonable results without bias due to the extreme rainfall events (see Paper II). The framework integrates the results from the landslide susceptibility and the climate modelling chains as follows:

$$P_f(L) = P(F_S \leq 1.0|L) = \int P(F_S \leq 1.0|L, I)\, f(I|\kappa_G, \beta_G, L)\, dI \qquad 3.2$$

where $P(F_S \leq 1.0|L)$, i.e., $P_f(L)$, is the probability of landslide initiation for a given rainfall duration, L, F_S is the factor of safety, $P(F_S \leq 1.0|L, I)$, i.e., $P_f(L, I)$, is the probability of landslide initiation conditioned on L and I obtained from the landslide modelling chain, $f(I|\kappa_G, \beta_G, L)$ is the pdf of rainfall event with an intensity of I conditioned on L, the location, κ_G, and scale, β_G, parameters of the underlying Gumbel distribution, obtained from climate modelling chain.

In this proposed framework, landslide susceptibility analyses are conducted for a given duration of rainfall events of different intensity values. For a given L, the range of the I is discretized into *n* values, $\{I_i,\ i = 1,\ 2, \dots, n\}$, covering IDF curves at both present and future climate conditions. These intensity values are then utilized in probabilistic landslide susceptibility analysis by employing the Monte Carlo method to account for the variability of model parameters. The probabilistic landslide susceptibility analyses provide values of $P(F_S \leq 1.0|L, I_i)$. Then, $P(F_S \leq 1.0|L, I_i)$ values are multiplied with the value of the $f(I_i|\kappa_G, \beta_G, L)$ so that I is integrated out of the expression in Eq. 3.2 and $P_f(L)$ is obtained. In this framework, the impact of climate change is represented by the changes in $f(I|\kappa_G, \beta_G, L)$ in Eq. 3.2. For illustration purposes, Figure 3.3 shows sample IDF curves representing the present and future climate conditions with the corresponding cumulative distribution function, cdf, and pdf. In Figure 3.3a, cdf for 6-, 12- and 24-hour rainfall durations are shown along with the IDF curves for both present and future climate conditions. For 24-hour rainfall duration, the present and future cdf values are provided separately in Figure 3.3b. Similarly, the pdf values for different L values are provided with IDF curves in Figure 3.3c, and for 24-hour rainfall duration separately in Figure 3.3d. From Figure 3.3, it can be observed that climate change causes an increase in the intensity values of the same return intervals. Additionally, intense rainfall events, e.g., 70 mm or greater, become more probable with higher pdf values due to climate change.

3.4. Quantification of climate change impact on a study area in central Norway

In this PhD study, the coupled modelling framework, shown in Figure 3.2, was applied to a case study area in central Norway. The proposed probabilistic framework (Section 3.3.1) was utilized to combine the climate and landslide modelling chains. The study area, in Figure 3.4, was investigated in terms of weather conditions, geology, and landslide inventory to calibrate the TRIGRS model. The details of the model calibration can be seen in the attached Paper II.

The output of the climate modelling chain in terms of climate-dependent IDF curves was utilized to simulate multiple rainfall events with varying duration and intensity values. Then, these rainfall events were utilized in the landslide susceptibility analyses using the TRIGRS model. Uncertainties in the model parameters were propagated to the landslide model predictions by conducting 1000 Monte Carlo simulations and corresponding values of $P_f(L, I)$ in Eq. 3.2 were calculated for daily and sub-daily rainfall events with varying intensities. Following the landslide susceptibility analyses, the probabilistic framework, explained in Section 3.3.1, was utilized to obtain overall climate change impact, i.e., values of $P_f(L)$, by multiplying the $P_f(L, I)$ and corresponding pdf values of $f(I|\kappa_G, \beta_G, L)$.

The overall climate change impact was explicitly quantified in terms of $P_f(L)$ for daily and sub-daily rainfall events at three time periods: present (1981-2010), near-future (2021-2050), and far-future (2071-2100). In the following sections, present, near future, and far future climate conditions will be first presented. Then, corresponding landslide susceptibility maps will be provided.

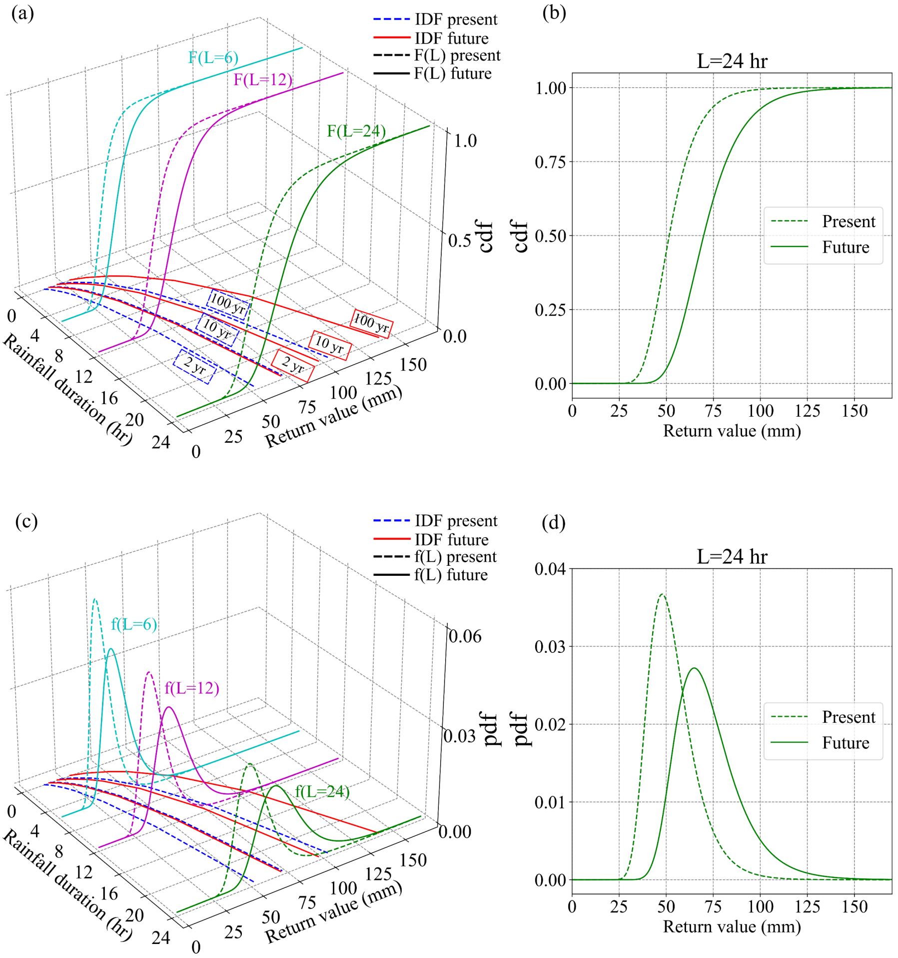

Figure 3.3: Illustration of IDF curves representing present and future climate conditions with the corresponding (a) cdf, F(L) and (c) pdf, f(L), for 6-,12- and 24-hour rainfall durations, and (b) cdf and (d) pdf for 24-hour rainfall duration separately.

3.4.1. Climate projections

Based on the projections from the EURO-CORDEX CMIP5 ensemble for emission scenario RCP8.5, climate projections were obtained for three time periods: present (1981-2010), near future (2021-2050), and far future (2071-2100). The projections were obtained for three weather stations in the proximity of the study area: Østas I Hegra, Hegra II, and Meråker-Krogstad (Figure 3.4). Nine grids of the EURO-CORDEX RCMs, which are shown in Figure 3.4c as colored dots, exist over the study area. For each of the weather stations, the closest grid point was utilized for future projections.

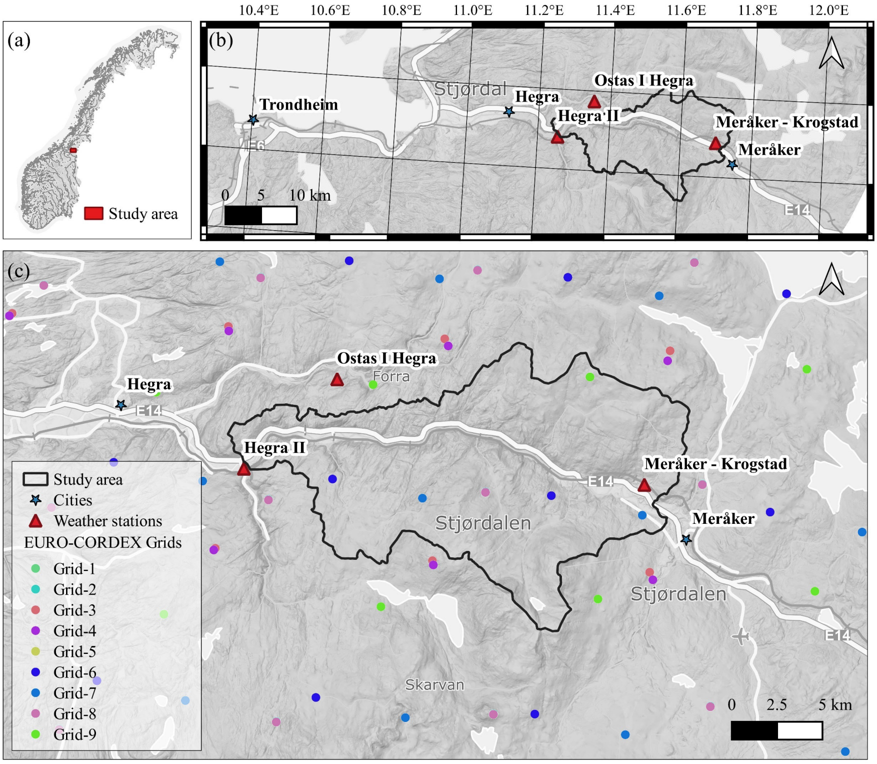

Figure 3.4: Study area (a) on national scale and (b) in the Trøndelag region of Norway with (c) the map showing different grids of the EURO-CORDEX RCMs in the proximity of the study area.

The parameters μ and f_w at the three time periods were calculated for each of the weather stations based on the nearest grid point using the projections from the EURO-CORDEX ensemble. However, the IDF curves were not directly obtained using these parameters because the EURO-CORDEX ensemble data were not bias-corrected. Bias-correction is an important process that removes the biases in simulated values relative to the observations in a control period (Wong et al. 2016). To address the bias-correction, a delta change approach (e.g., Hay et al. 2000) was employed. That is, the IDF curves for present climate condition were calculated based on the μ and f_w obtained from the observations at the weather stations for the present time period. Then, the IDF curves for the future time periods were obtained by adding the change in the μ and f_w from the EURO-CORDEX ensemble to the corresponding parameters for present climate condition from the observations.

Figure 3.5 shows the projected change in μ, $\Delta\mu$, and f_w, Δf_w, from the present time period of 1981-2010 to the near future, 2021-2050, and to the far future, 2071-2100 for the three weather stations. In Table 3.1, ensemble statistics including the average values of the changes with the corresponding standard deviations are provided. From both Figure 3.5 and Table 3.1, it was observed that the majority of the EURO-CORDEX RCM simulations resulted in an increase in both μ and f_w for all weather stations.

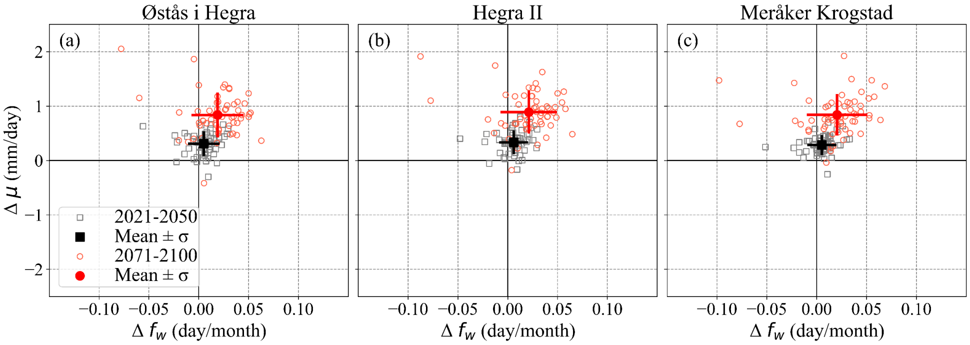

Figure 3.5: Projected change in μ, $\Delta\mu$, and f_w, Δf_w, from the reference period of 1981-2010 representing the present climate condition to the near future, 2021-2050, and far future, 2071-2100: (a) Østas I Hegra, (b) Hegra II, and (c) Meråker Krogstad. The projections and the ensemble mean with variability ($\pm\sigma$ as solid lines) are based on EURO-CORDEX ensembles of RCM simulations assuming RCP8.5.

Table 3.1: Average projected change in μ ($\overline{\Delta\mu}$) and in f_w ($\overline{\Delta f_w}$) with the corresponding standard deviation of the ensemble values, $\sigma_{\Delta\mu}$ and $\sigma_{\Delta f_w}$.

Weather station	Period	$\overline{\Delta\mu}$	$\sigma_{\Delta\mu}$	$\overline{\Delta f_w}$	$\sigma_{\Delta f_w}$
Østas I Hegra	Near future	0.310	0.204	0.0051	0.0145
	Far future	0.836	0.387	0.0190	0.0249
Hegra II	Near future	0.333	0.195	0.0060	0.0133
	Far future	0.889	0.369	0.0212	0.0271
Meråker Krogstad	Near future	0.283	0.158	0.0053	0.0134
	Far future	0.839	0.357	0.0205	0.0292

In Figure 3.6, 10-, 50- and 100-year IDF curves at three time periods are provided for the weather stations. The IDF curves for the near and far future climate conditions have variability arising from the EURO-CORDEX ensemble. Therefore, corresponding IDF curves are provided as the ensemble mean, 5th, and 95th percentiles as dashed lines. Upon closer inspection of the 5th percentile curves in Figure 3.6, it can be observed that they intersect with the mean return values of an earlier time period. This implies that the great majority of the results predict an increase in the return values.

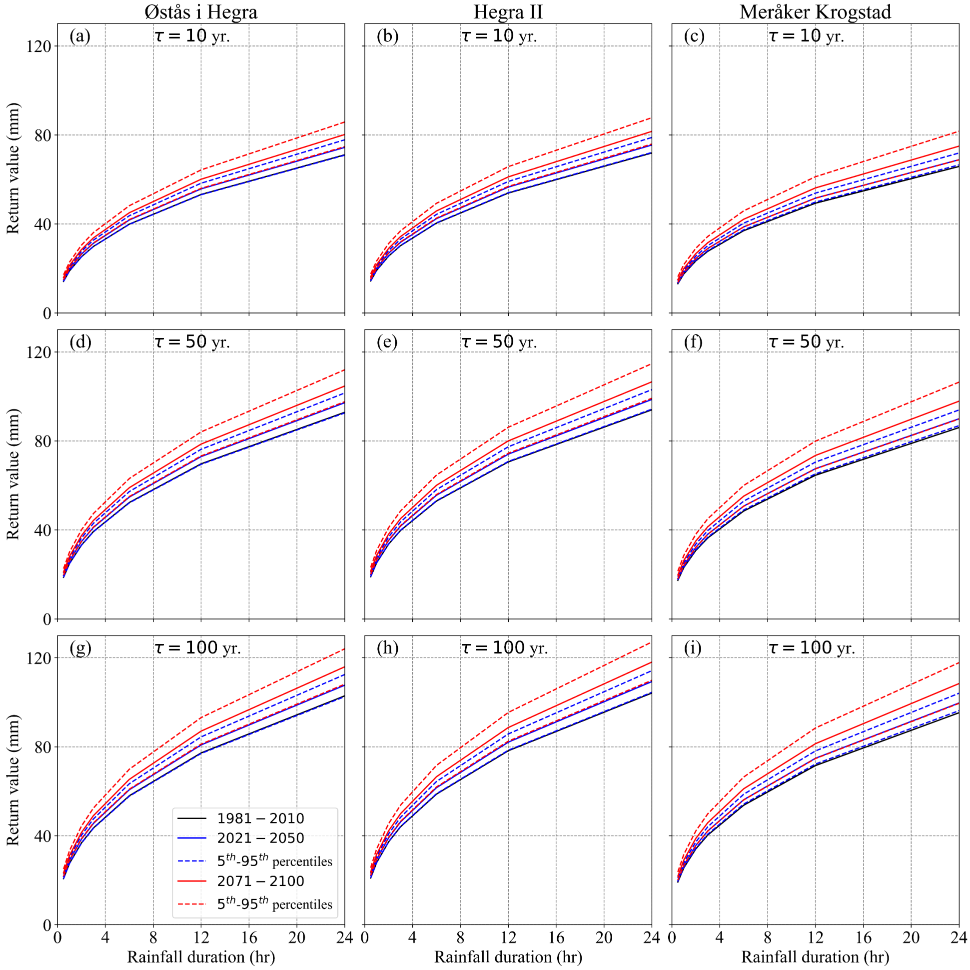

Figure 3.6: Estimated return values with 5th and 95th percentiles for (a, b, c) 10-year, (d, e, f) 50-year, and (g, h, i) 100-year return intervals based on EURO-CORDEX RCM simulations assuming RCP8.5: (a, d, g) Østas I Hegra, (b, e, h) Hegra II, and (c, f, i) Meråker Krogstad.

This study utilized the mean values of the changes in μ and f_w to calculate the IDF curves at three time periods, which will be used to evaluate the climate change impact on landslide susceptibility. Figure 3.7 provides the IDF curves for return intervals from 2 years to 200 years at three time periods. It can be seen that the return values at Østås I Hegra and Hegra II weather stations are similar as they are closely located. Additionally, these stations have similar observations at the present time period and share many EURO-CORDEX grids, shown in Figure 3.4c. From the present to the far future climate conditions, the projections showed that the return values of different return intervals increase by a mean factor of 1.128 for Østås I Hegra, 1.135 for Hegra II, and 1.139 for Meråker Krogstad.

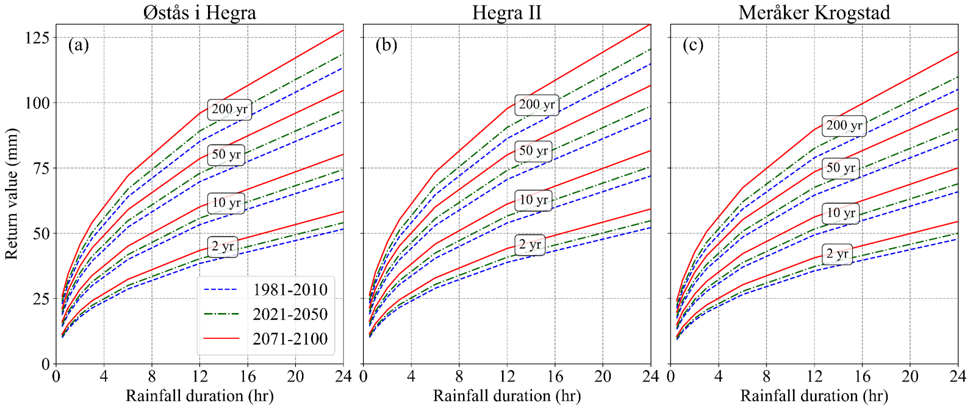

Figure 3.7: Estimated return values based on ensemble mean of EURO-CORDEX RCM simulations assuming RCP8.5 at present (1981-2010), near future (2021−2050) and far future (2071-2100) climate conditions for the weather stations: (a) Østas I Hegra, (b) Hegra II, and (c) Meråker Krogstad.

3.4.2. Projected landslide susceptibility

Among the three weather stations, Østas i Hegra was selected to be used in the landslide susceptibility analysis due to being more reliable with long-term observations that started in 1895. A small extent representative zone, as shown in Figure 3.8, was selected to show the climate change impact because of the large extent of the study area. The selected zone has two soil types, moraine and fluvial deposits (Figure 3.8c) that are prone to landsliding. Additionally, the zone features steep slopes on the hillside with both soil types of interest. Statistics of the change in landslide susceptibility due to climate change will be tabulated for the entire study area. The details on the geology and the landslide modelling can be seen in the attached Paper II.

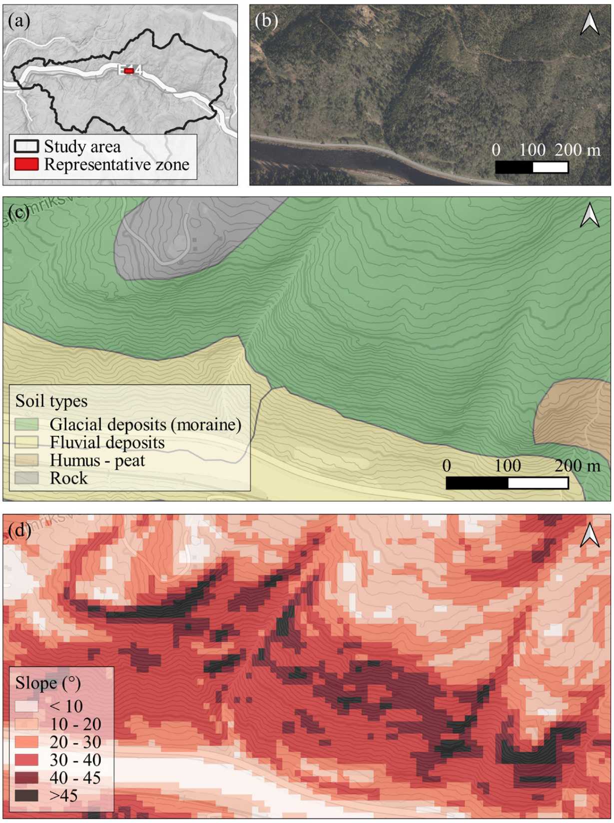

Figure 3.8: (a) Representative zone for climate change impact on landslide susceptibility: (b) aerial photo, (c) geology, and (d) slope maps.

Overall climate change impact

In Figure 3.9, the overall climate change impact on landslide susceptibility is provided for 6-, 12-, and 24-hour rainfall events by providing the $P_f(L)$ maps at present, near future, and far future climate conditions. The projections of landslide susceptibility maps at three time periods show a considerable increase in $P_f(L)$ for all durations of rainfall events. The results revealed that $P_f(L)$ at certain parts of the study area may increase by up to 9.9%, 8.4%, and 3.7% for 6-, 12-, and 24-hour rainfall events respectively until the end of the 21st century.

Compared to investigating only extreme rainfall events, the proposed probabilistic framework provided somewhat smaller changes in the values of probability of landslide initiation. This was attributed to the nature of the proposed probabilistic framework. That is, high values $P_f(L, I)$ due to intense rainfall events, such as rainfall events of 50-, 100-year return intervals, were weighted by their relatively low occurrence probability.

In the landslide susceptibility simulations, this study utilized infinite depth basal boundary assumption in the TRIGRS model (see Section 2.3.1). This assumption resulted in similar transient pore pressure responses at the end of varying duration rainfall events of the same return intervals and corresponding similar values of $P_f(L, I)$. In Figure 3.9, the values of $P_f(L)$ are higher for 6-hour rainfall compared to the 12- and 24-hour rainfall at all time periods. This was attributed to the higher values of $f(I|\kappa_G, \beta_G, L)$ at shorter return intervals for 6-hour rainfall compared to the 12- and 24-hour rainfall.

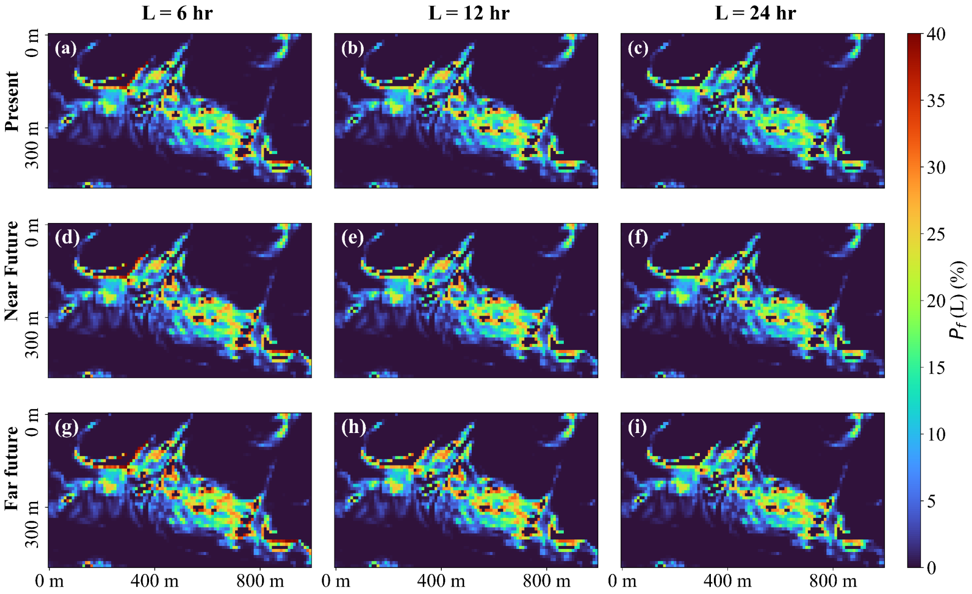

Figure 3.9: $P_f(L)$ maps for (a, d, g) 6-hour, (b, e, h) 12-hour and (c, f, i) 24-hour rainfall events at (a, b, c) present, (d, e, f) near future, and (g, h, i) far future climate conditions.

In Figure 3.9, $P_f(L)$ maps at present, near future, and far future show an increase due to climate change. Although the maps look similar, larger values $P_f(L)$ were obtained for 6-hour rainfall event. In Table 3.2, the mean values of the $P_f(L)$ for the entire study area at the three time periods are tabulated for different ranges of slopes. It can be seen that 6-hour rainfall led to higher values of mean $P_f(L)$ compared to the 12- and 24-hour rainfall at all time periods. The changes in the mean $P_f(L)$ from present to future climate conditions were observed to be similar for different duration rainfall events with a slightly higher increase for short-duration rainfall events.

Table 3.2: Mean values of $P_f(L)$ for the entire study area for 6-, 12-, and 24-hour rainfall duration at present, near future, and far future climate conditions.

Slope range (°)	L = 6 hr.			L = 12 hr.			L = 24 hr.		
	Present	Near future	Far future	Present	Near future	Far future	Present	Near future	Far future
25 - 30	0.29	0.33	0.40	0.06	0.07	0.10	0.03	0.03	0.03
30 - 35	1.65	1.79	2.03	1.06	1.14	1.29	0.83	0.89	0.98
35 - 40	7.47	8.01	8.95	6.50	6.94	7.79	5.35	5.71	6.42
40 - 45	22.18	23.49	25.53	20.69	21.78	23.68	18.23	19.31	21.19

In probabilistic studies, there is no general agreement on the landslide susceptibility assessment criteria in terms of P_f. Therefore, this study utilized several threshold values of P_f, $P_{f,limit}$ to determine landslide susceptible zones, which have $P_f > P_{f,limit}$. In Table 3.3, extents of landslide susceptible zones are provided based on varying values of $P_{f,limit}$ for the entire study area at three time periods. The results showed that there is a substantial increase in the extent of landslide susceptible zones due to climate change for all rainfall durations. Additionally, shorter duration rainfall events led to larger increase in the landslide susceptible extents at each value of $P_{f,limit}$.

Table 3.3: Extent of landslide susceptible zones, specified as $P_f(L) > P_{f,limit}$ for the entire study area for 6-, 12-, and 24-hour rainfall duration at present, near future, and far future climate conditions.

$P_{f,limit}$ (%)	L = 6 hr.			L = 12 hr.			L = 24 hr.		
	Present	Near future	Far future	Present	Near future	Far future	Present	Near future	Far future
10	112.9	120.6	130.7	94.7	103.3	114.9	82.0	89.0	96.7
20	47.7	55.3	65.4	36.6	41.5	49.6	24.2	27.5	37.4
30	11.6	15.2	24.0	0.8	4.9	12.5	0.0	0.0	3.1
40	2.6	3.1	4.2	0.0	0.0	0.0	0.0	0.0	0.0

Unit: 10^{-2} km^2

Climate change impact for a given rainfall event

In this work, climate change impact on landslide susceptibility was also investigated for particular rainfall events with a given duration and return interval. This might be useful for specific projects designed based on a rainfall event of a given return interval. In Figure 3.10, landslide susceptibility maps for 12-hour rainfall events of 10- and 50-year return intervals are provided in terms of $P_f(L, I)$ at three time periods. The results revealed that climate change leads to higher values of $P_f(L, I)$ in the near and far future climate conditions. Compared to the present time period, $P_f(L, I)$ at certain parts of the study area increases by up to 26.6% and 18.7% for 12-hour rainfall events of 10-, and 50-year return intervals respectively until the end of the 21st century.

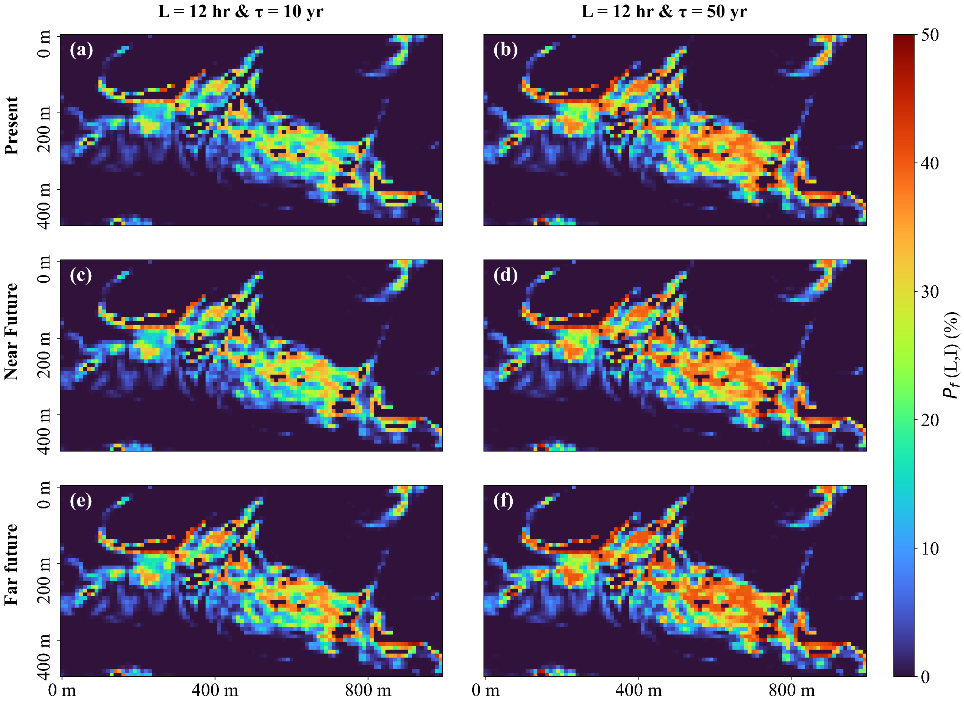

Figure 3.10: $P_f(L, I)$ maps for 12-hour rainfall events of (a, c, e) 10-year and (b, d, f) 50-year return intervals at (a, b) present, (c, d) near future, and (e, f) far future climate conditions.

In Table 3.4, the mean values of the $P_f(L, I)$ for the entire study area at the three time periods are tabulated for different ranges of slopes. Rainfall event of the 50-year return interval led to higher values of mean $P_f(L, I)$ compared to the event of the 10-year return interval at all time periods. From Table 3.4, it can be observed that climate change cause a significant increase in the mean values of $P_f(L, I)$. The results reveal that the increase in mean $P_f(L, I)$ is higher for 10-year return interval compared to the increase for 50-year return interval.

Table 3.4: Mean values of $P_f(L, I)$ for the entire study area for 12-hour rainfall events of 10- and 50-year return intervals at present, near future, and far future climate conditions.

Slope range (°)	τ = 10 yr.			τ = 50 yr.		
	Present	Near future	Far future	Present	Near future	Far future
25 - 30	0.16	0.21	0.31	0.52	0.57	0.64
30 - 35	1.44	1.67	2.08	3.39	3.57	3.83
35 - 40	9.77	10.90	12.85	16.86	17.60	18.78
40 - 45	28.74	30.63	33.84	36.87	37.66	38.97

In Table 3.5, extents of landslide susceptible zones, specified by the criterion $P_f(L, I) \geq P_{f,limit}$, are provided for the entire study area at three time periods. The extents of landslide susceptible zones show a substantial increase due to climate change for both 12-hour rainfall events of 10- and 50-year return intervals.

Table 3.5: Extent of landslide susceptible zones, specified with $P_f(L, I) \geq P_{f,limit}$, for the entire study area for 12- hour rainfall events of the 10- and 50-year return intervals at present, near future, and far future climate conditions.

$P_{f,limit}$ (%)	τ = 10 yr.			τ = 50 yr.		
	Present	Near future	Far future	Present	Near future	Far future
10	137.0	146.2	162.3	195.9	202.4	213.3
20	73.6	83.3	97.4	132.3	135.2	141.8
30	35.3	43.9	60.8	86.5	91.4	99.5
40	5.2	7.6	16.5	24.4	25.7	43.6

Unit: 10^{-2} km^2

This study revealed that investigating only extreme rainfall events of long return intervals would result in a misleading impression of climate change impact on rainfall-induced landslide susceptibility with higher values of P_f. For example, for 12-hour rainfall events of 10-year return interval, climate change leads to an increase in $P_f(L, I)$ by up to 26.6% at certain parts of the study area until the end of the century. When varying intensity rainfall events of 12-hour duration were investigated using the proposed probabilistic framework, the increase in $P_f(L)$ becomes only up to 8.4%. The proposed probabilistic framework was found to be more comprehensive than investigating only extreme events as the method investigates varying intensity of rainfall events of the same duration with their corresponding probability of occurrences.

4. IoT-based hydrological monitoring and early warning model strategies

4.1. Introduction

In this PhD thesis, substantial work was performed on a case study for hydrological monitoring in order to understand the response of slopes to seasonally cold climate conditions in Norway. A hydrological monitoring system was deployed in central Norway. Internet of Things (IoT)-based technologies providing efficient data acquisition and transmission were utilized in the deployed system. Additionally, a pilot work was conducted to develop a landslide warning model providing landslide predictions based on the weather forecast and collected data through the hydrological monitoring system.

In this chapter, Section 4.2 briefly introduces components of a landslide early warning system (LEWS) among which monitoring is a vital component providing reliable landslide models and functional LEWSs. Section 4.3 provides an overview of the technological developments within the domain of IoT, which can improve the monitoring component of an LEWS. Then, in Section 4.4, the landslide-prone study area is presented with two locations where an IoT-based hydrological monitoring system was deployed. The details of the study area, deployment of the system, and collected data on volumetric water content (VWC) and matric suction can be found in Paper III. Collected data have strong potential to be utilized in a landslide early warning model. Section 4.5 briefly explains landslide early warning model strategies examined in the KlimaDigital project. Finally, a pilot work on an automated physical-based landslide prediction model is presented in Section 4.6. This chapter relates to the findings in Paper III.

4.2. Landslide monitoring and early warning systems

The risk associated with landslides is increasing as the population expands towards the landslide-prone regions and due to the increasing frequency of intense rainfall events in many regions of the world due to climate change (Ho et al. 2017). There is a need to select a proper mitigation strategy among different alternatives including planning control, engineering solutions, and landslide early warning to mitigate and control the existing and increasing landslide risk (e.g., Dai et al. 2002; Calvello 2017). Among these mitigation strategies, LEWS is commonly regarded as a cost-efficient strategy (Glade and Nadim 2014). LEWS is a system that generates and disseminates timely warnings to take necessary actions to reduce the landslide risk such as warning authorities, evacuating people, or closing road sections. (UNISDR 2009; Guzzetti et al. 2020). The United Nations Office for Disaster Risk Reduction (UNISDR) states that a complete and effective early warning system shall consist of the following components: knowledge of risk including hazards and vulnerabilities; information from monitoring, field observation and warning service; dissemination of warning to the population exposed to landslide risk, and communication; response capability including public awareness and preparedness. In a slightly more technical approach, Calvello (2017) divided early warning systems for landslides into three components: landslide model, warning model, and warning system (Figure 4.1). A landslide model represents the core of an LEWS as it includes weather, monitoring, geological characterization, and landslide events. The warning model includes, in addition to the landslide model, warning criteria, i.e., decision-making procedures, to associate the landslide model with the different levels of warnings. Finally, the last and complementary component is a warning system embedding landslide and warning models with additional elements: dissemination of warning, communication and education, community involvement, and emergency planning. These components should work in conjunction with each other. Otherwise, the whole system might not work due to a failure in any of the components of an LEWS.

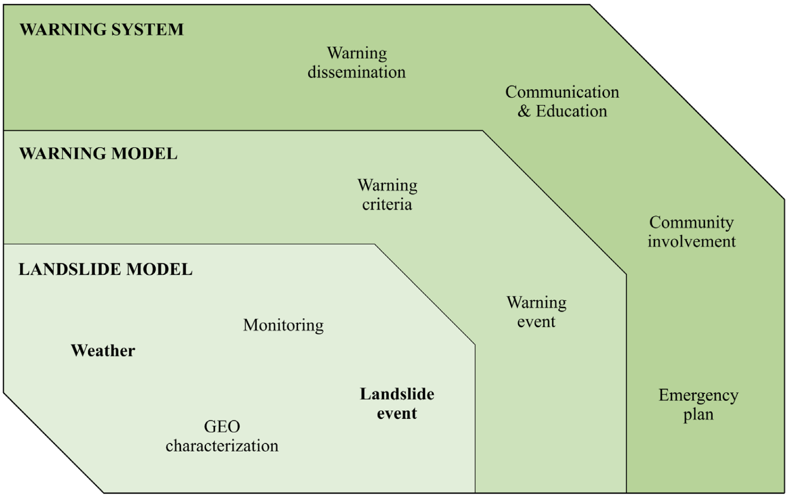

Figure 4.1: Early warning system for water-induced landslides (Calvello 2017).

There exist a wide range of landslide triggering factors such as rainfall, snowmelt, earthquake, human activity, erosion, or a combination of different phenomena. Water is involved in the majority of slope destabilizations due to the various triggering factors (Lacasse et al. 2010; Michoud et al. 2013; Pecoraro et al. 2019). Having up-to-date knowledge on triggering factors and corresponding changes in slopes within the area of interest is a prerequisite for any LEWS. Therefore, monitoring is one of the vital elements in establishing reliable landslide models and functional LEWSs as early warnings should be issued and disseminated based on actual data. Monitoring supports LEWSs with a more consistent and reliable hazard assessment based on collected data on the triggering variables and reduction of consequences with timely warnings to protect the elements under risk.

Monitoring methods can be either remote sensing (e.g., laser scanning, satellite radar interferometry, laser technology) or ground-based techniques (e.g., electrical resistivity, instrumental techniques). In the former techniques, there is no physical contact with the slope, while the latter utilizes sensors instrumented in the landslide-prone zone. Ground-based monitoring methods can provide greater details regarding the local underlying mechanism of landslide phenomena (Pecoraro et al. 2019). Many research studies implemented sensor-based monitoring in LEWSs (e.g., Chaturvedi et al. 2018; Abraham et al. 2020; Song et al. 2021) and developed landslide risk mitigation strategies based on monitoring and early warning.

Monitoring can further be classified based on monitored activities/parameters and methods (SafeLand 2012; Calvello 2017). The monitored activities are classified into four main categories: (i) monitoring deformation activity, i.e., any parameter related to deformation characteristics (kinematic behavior) of a landslide; (ii) monitoring groundwater activity such as groundwater table, suction, pore water pressure, VWC; (iii) monitoring triggering activities such as weather (e.g., precipitation, temperature, wind), seismic activities; and (iv) monitoring other driving factors. The monitoring methods are classified into geotechnical, hydrological, geophysical, geodetic, remote sensing, and meteorological methods (Calvello 2017). Based on the method to be used and the activities to be monitored, different instruments are available in the market. Monitoring methods, monitored parameters, and the instruments should be selected based on the landslide type and triggering mechanism, yet redundancy in the instrument types to monitor different parameters might provide useful information that might be crucial in decision making (Pecoraro et al. 2019).

4.3. IoT-based monitoring strategies

Monitoring systems in geotechnical engineering are continuously evolving towards being more efficient to address the requirements of being scalable, flexible, easy to maintain, and inexpensive. The advancements brought forth by wireless communication through Wi-Fi, Bluetooth, and 2G/GSM-based cellular communication solutions improved the monitoring systems and widened the deployments of these systems. However, Wi-Fi and Bluetooth are not suited for long-distance data transmission and the old-fashioned cellular communication solutions are costly, high energy demanding, and require expensive hardware and services (Mekki et al. 2019).

Recent developments in the domain of IoT applications have generated a spectrum of new opportunities for developing solutions for the mitigation of landslide risks with advanced LEWSs. IoT can be defined as a concept of a network of devices transmitting and receiving data, processing collected information, or exchanging information among themselves, without human intervention. IoT-based systems can significantly support the automatization of LEWSs through the efficient integration of data with advanced landslide prediction models and early warning systems.

To address the needs of IoT applications, a new networking concept, Low Power Wide Area Networks (LPWANs), has emerged. LPWANs advance wireless communication by solving the weaknesses of prior wireless solutions (e.g., 2G/GSM, Wi-Fi, Bluetooth) and offer cost- and power-efficient wireless data transmission over long distances. Such state-of-the-art networking solutions are especially well suited for the implementations of landslide monitoring and early warning systems as these systems often require data transmission over long distances (e.g., tens of kilometers), low data transmission rates (e.g., tens of bytes per second or lower), low maintenance, and long battery life (e.g., five to ten years). During the last decade, several technologies enabling LPWAN deployments have been developed (Mekki et al. 2019). Among them, SigFox, LoRa, LTE-M, and NB-IoT can be listed as leading technologies.

The developments within the domain of IoT are expected to overcome many of the challenges related to landslide monitoring by reducing costs, simplifying installation, and enabling more efficient data acquisition from anywhere through suitable communication technologies without the need for human intervention during operation. Landslide monitoring supported by IoT technology will thus ease the deployment of the warning system by providing more efficient management of limited resources. In this PhD study, an automated hydrological monitoring system was deployed in central Norway. The system is supported by state-of-the-art IoT technologies, NB-IoT and LTE-M employing 4G public mobile networks (Myhre and Rustad 2021). The IoT-based system proved to be efficient in the deployment of the systems and operation without a major problem in data acquisition and transfer. The architecture of the IoT-based hydrological monitoring system including layers common in IoT-based applications (ITU 2012) can be found in Paper III. Besides, the technical details of the KlimaDigital Environmental IoT System can be found in the KlimaDigital project memo (Myhre and Rustad 2021).

4.4. Case study of IoT-based hydrological monitoring

4.4.1. Study area

The landslide-prone case study area in Trøndelag, central Norway (Figure 4.2a) was investigated in terms of geology, landslide inventory, and landslide triggering parameters (see Paper II and Paper III). Water infiltration due to rainfall or snow melt was considered as the main landslide triggering condition. Therefore, a landslide monitoring system was deployed to monitor hydrological conditions, which can help to understand the response of similar slopes to seasonally cold climate conditions in Norway.

Substantial work was performed to understand the geological settings over the study area and landslide history with the corresponding hydro-meteorological conditions (Depina et al. 2021). The soil-related landslide events were mainly associated with two types of Quaternary deposits: moraine and fluvial deposits. Following field observations and local geological interpretations, two locations, Location 1 and Location 2 (Figure 4.2b), were selected for detailed investigation and deployment of the IoT-based hydrological monitoring systems. In Location 1, the bedrock is covered mainly by thick fluvial deposits on the hillside, and by moraine deposits towards the higher parts of the hill (Figure 4.2b). In Location 2, there exist moraine deposit, which is locally thin, i.e., less than 0.5 m thick.

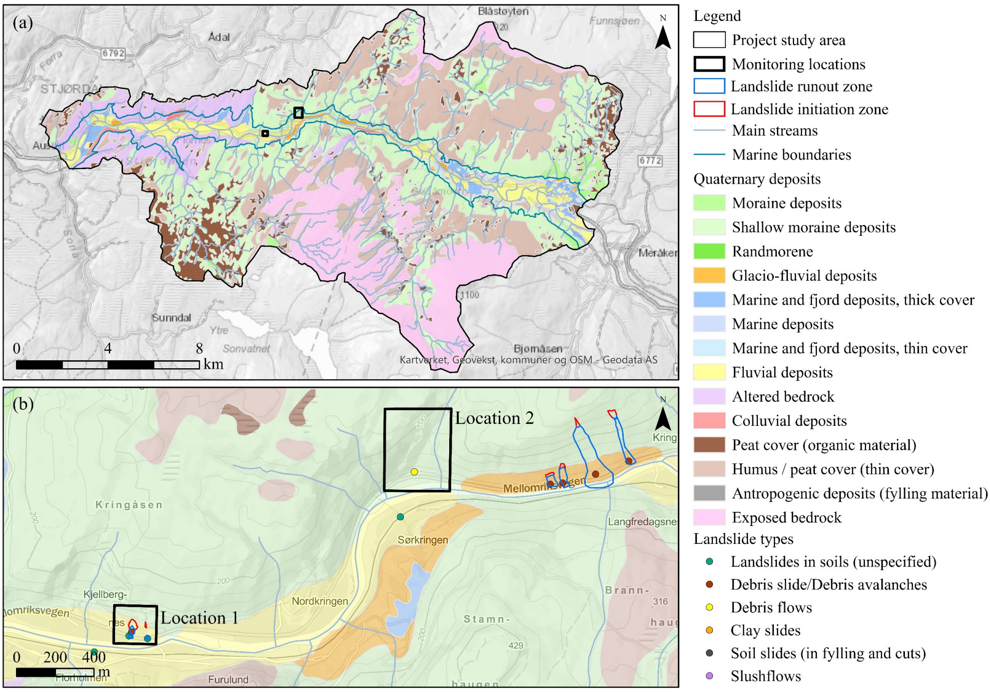

Figure 4.2: (a) Quaternary geology over the study area with (b) two selected monitoring locations, Location 1 and Location 2, at detailed scale.

4.4.2. Deployed hydrological monitoring systems

At each location, the hydrological monitoring systems were installed at two monitoring points: D1.1 and D1.2 in Location 1, and D2.1 and D2.2 in Location 2 (Figure 4.3). The monitoring points were selected to be at different elevations on both sides of channels present at both locations.

The full setup of the hydrological monitoring system consists of two piezometers, three suction sensors, and three VWC sensors. In location 1, the full setup was deployed at monitoring points D1.1 and D1.2. The monitoring systems deployed in Location 2 are reduced setups without piezometers as the thickness of the moraine is shallow, even locally less than 0.5 m. In general, one VWC sensor and one suction sensor were placed at three depths in the top 1 m soil crust, approximately at 0.3 m, 0.5 m, 0.9 m depths, at all monitoring points. The piezometers in Location 1 were placed at 1.25 m and 2.0 m depths at D1.1, and 1.4 m and 2.2 m depths at D1.2.

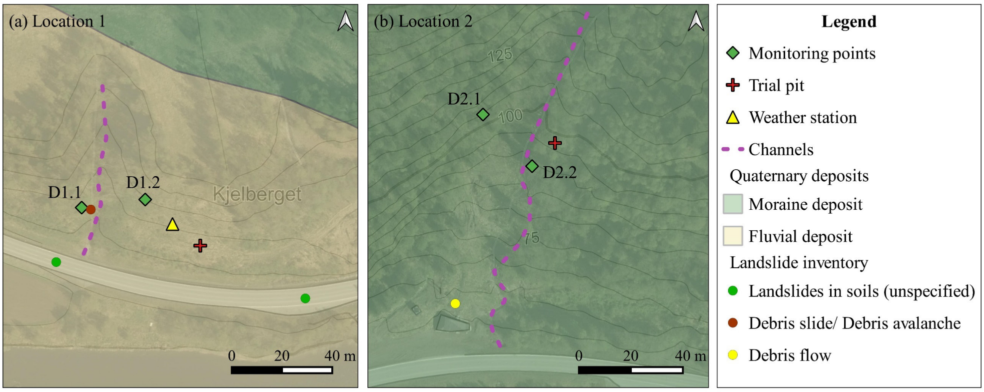

Figure 4.3: IoT-based hydrological monitoring systems deployed at (a) two points, D1.1 and D1.2 in Location 1, and at (b) two points, D2.1 and D2.2, in Location 2.

Figure 4.4 shows the completed IoT-based hydrological monitoring system at monitoring point D1.2 in Location 1. In Figure 4.4b, it can be observed that sand was used as a filtering soil medium around the piezometers and thin bentonite layers were placed on top of the sand layers to prevent vertical water passage. The excavated soil was used as backfill material and compacted to maintain the in-situ density of the original soil. IoT device was placed on a pole at approximately 1 m height and the sensor cables were connected to the device using a cable trench and a PVC pipe along the pole (Figure 4.4a).

In addition to the sensors utilized in the IoT-based hydrological monitoring system, weather conditions have been monitored by a weather station, ATMOS 41 (METER Group 2022a) with a data logger, ZL6 (METER Group 2022b), as shown in Figure 4.5. The weather station is a compact all-in-one weather station being able to monitor several weather variables including air temperature, relative humidity, vapor pressure, atmospheric pressure, wind speed, and precipitation among others. The data are transmitted over a single wire to the data logger, which has a built-in solar panel providing long-term power efficiency. The data logger transfers the data to the cloud-based user platform, called the Zentra Cloud, that enables near real-time data viewing and data retrieval. The frequency or time interval of data recording can be adjusted over the internet.

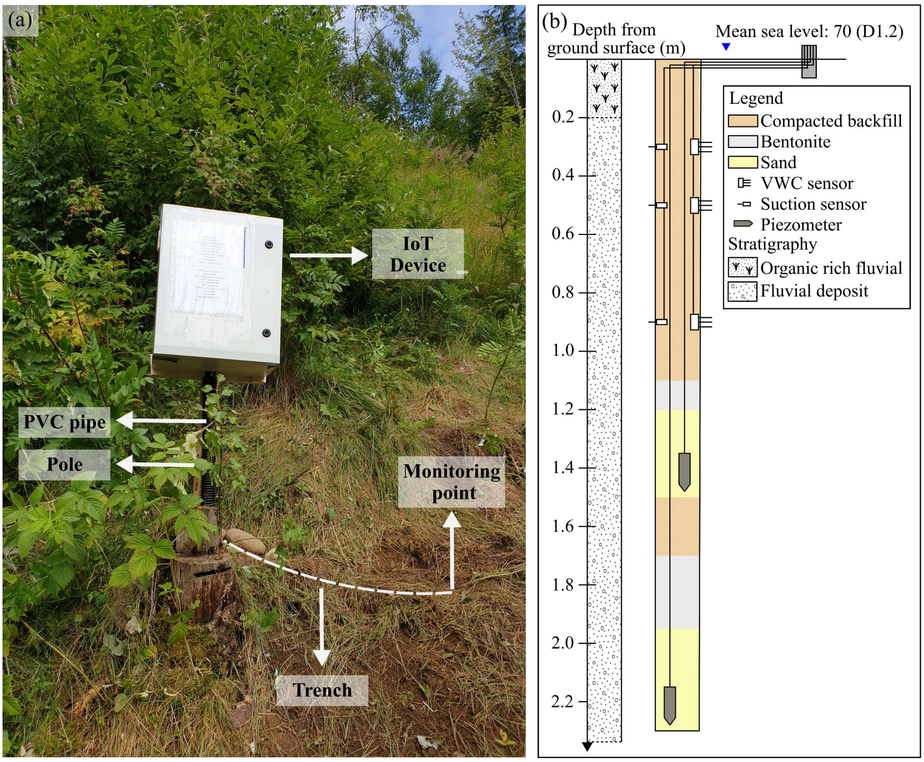

Figure 4.4: Completed IoT-based hydrological monitoring system at monitoring point D1.2: (a) IoT device placed on a pole and (b) sensor column with soil stratigraphy.

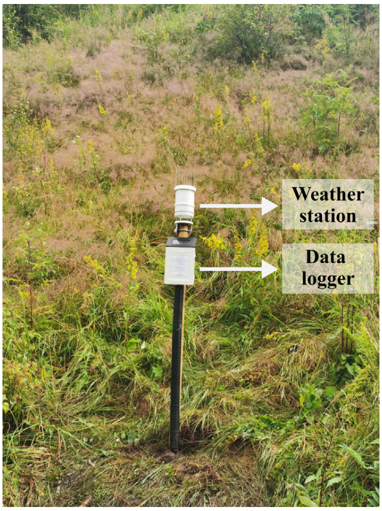

Figure 4.5: Weather station deployed at Location 1.

4.4.3. Operation of the monitoring system

The deployed IoT-based hydrological monitoring system has been in operation since August 2020 and is collecting data on VWC and suction at four monitoring points, and pore water pressure at two monitoring points in Location 1. The IoT device collects data from the sensors every fifteen minutes and transmits the data to an online cloud-based server once every hour using the public mobile network. The data can be accessed by an external user for the interpretation of data and implementation of a landslide early warning model.

In general, the deployed system has two main limitations. The first limitation is that the piezometers were placed at depths where there was no groundwater in the monitored period. Therefore, sensory data are affected by atmospheric pressures. The other limitation is that suction sensors have a measurement range from 9 kPa to air-dry state with matric suction values being more accurate in the range from 9 kPa to 100 kPa with an accuracy of ±10%. The sensors do not capture the suction range below 9 kPa, which might be important for soil water characteristics at highly saturated conditions.

During the monitoring period, two landslide events were reported on the 23rd of November 2021: one in the east part of the study area (Figure 4.6) and one in the proximity of Location 1 (Figure 4.7). The landslide events happened after a heavy rainfall with an approximate intensity of 50 mm in the 24-hour period before sliding. Both landslide events initiated on hillsides with slope angles in the range of 30° - 40°. The landslide event on the east side of the study area, as shown in Figure 4.6, was classified as a debris avalanche with a volume greater than 10000 m^3 (Varsom Xgeo). The landslide initiated in landslide deposits, which are sediments formed by landslides, rockfall, or snow. The debris moved 300 m away from the approximate initiation zone (Figure 4.6b).

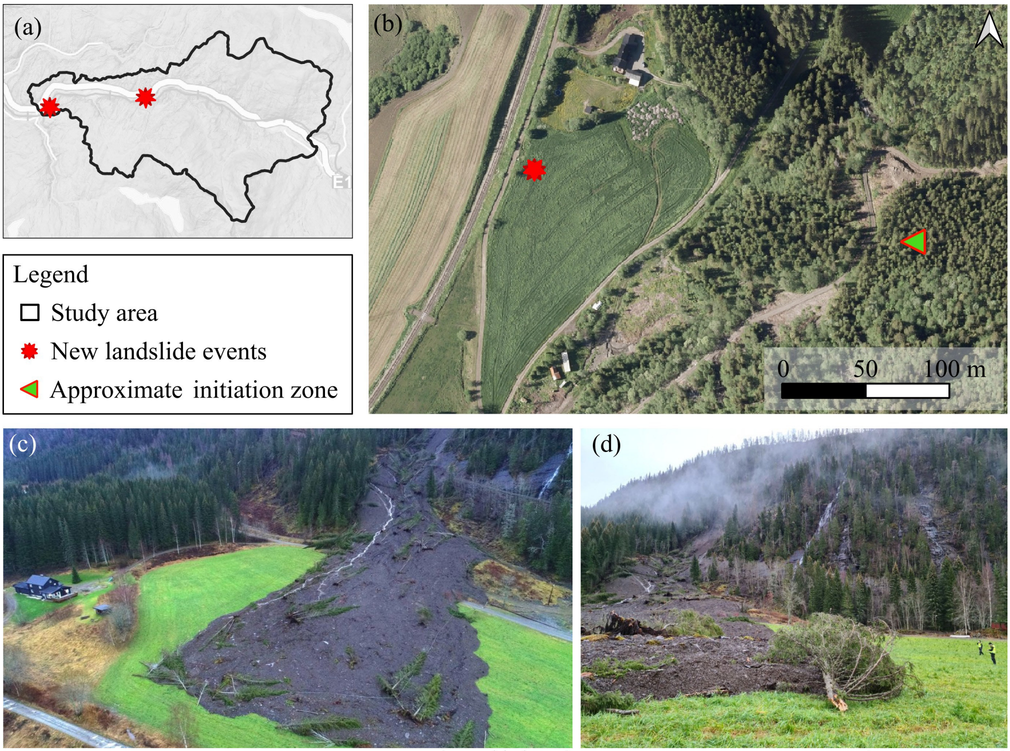

(www.bladet.no)

(www.adressa.no)

Figure 4.6: (a) Landslide events occurred on the 23rd of November 2021, (b) landslide event on the east part of the study area with photos from (c) www.bladet.no (2021) and (d) www.adressa.no (2021).

The landslide event in Location 1, shown in Figure 4.7, was classified as debris flow initiated by erosion. The initiated debris flowed towards the road (Figure 4.7b) and caused further erosion near the road as shown in Figure 4.7c. There is another landslide event in the landslide inventory that was initiated at almost the same zone over the hillside, but the runout reached another point on the road. The collected data on VWC and suction at the monitoring points D1.1 and D1.2 revealed very high VWC values and low matric suction values. At D1.1, VWC values at the instant of sliding were the highest values in the monitored period for the sensors at 0.5 m and 0.9 m depths, and very high at the sensor at 0.3 m depth. Similarly, the VWC values at D1.2 were very high. Suction values at both D1.1 and D1.2 were at the sensor's lower limit, ca. 9 kPa.

(a) Location 1

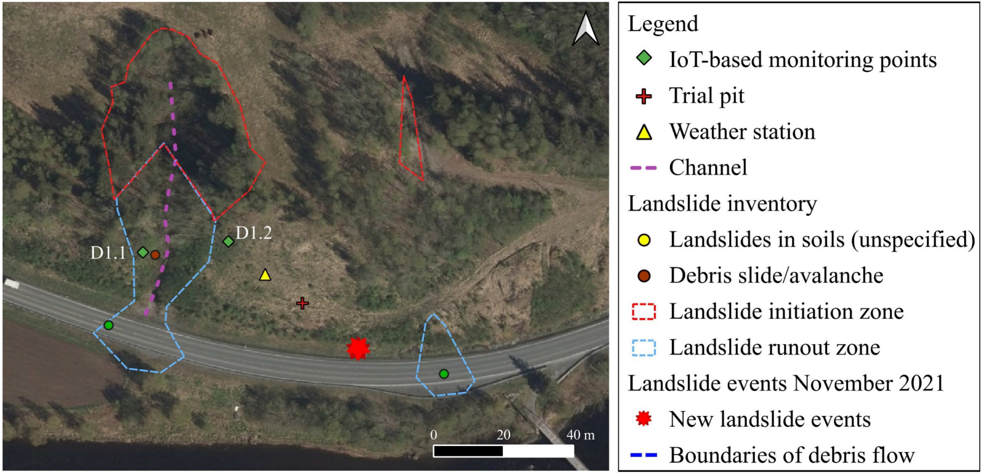

(b) Landslide runout zone

(c) Erosion near road due to debris flow

Figure 4.7: (a) Landslide event occurred in the proximity of Location 1 on the 23rd of November 2021 with (b) runout zone on the hillside and (c) further erosion near the road due to debris flow.

Additionally, two landslide events occurred on the 13th of January 2022 after an intense rainfall event combined with excessive snow melt. These landslide events were registered in the proximity of Location 1 as debris avalanches (Varsom Xgeo). There is currently limited information on the initiation zones and the volume of the landslides. The collected data showed very high VWC values at all monitoring points, with suction values being at the sensor's lower limit. Another shallow slide was registered on the 14th of January 2022 at the side of the main road close to Location 2. The volume of this road slippage was estimated to be less than 10 m^3 (Varsom Xgeo).

With the IoT-based hydrological monitoring system, valuable insights into the hydrological response of the slopes to the seasonally cold climate in Norway were obtained. The hydrological responses to rainfall, snow melting, ground freezing, and thawing have been captured in terms of VWC and matric suction. Details of the collected data on VWC, matric suction, and weather conditions can be found in Paper III. Such information can be of high value to efforts in reducing weather-induced landslide risk by employing landslide early warning model strategies based on collected data. That is, collected data can be utilized in combination with physical-based or data-driven warning models to estimate accurate landslide hazard levels. Then, the risk can be mitigated by issuing early warnings, evacuating people under threat, or closing road sections (Guzzetti et al. 2020). Section 4.5 will present landslide early warning model strategies examined in the KlimaDigital project.

4.5. Landslide early warning model strategies

A landslide early warning model, shown in Figure 4.1, includes decision-making procedures to associate monitored parameters with different levels of warning (Calvello 2017). Data collected through landslide monitoring systems, such as the IoT-based hydrological monitoring system deployed in this study, can be used as a basis for defining warning levels for issuing early warnings in LEWSs. Different approaches can be considered for a landslide warning model based on collected data. These approaches can be classified into data-driven or physical-based approaches both of which were examined in the KlimaDigital project (Depina and Oguz 2021). Each approach has certain advantages and disadvantages when it comes to the operation of early warning models based on collected data. In the following sections, data-driven and physical-based early warning model approaches will be explained.

4.5.1. Data-driven early warning model strategy

A warning model can be associated with the sensory data collected on monitored parameters, such as deformations (e.g., deformation, velocity, acceleration), groundwater variations (e.g., groundwater table, suction, pore water pressure, VWC), or triggering parameters (e.g., precipitation, snow melt, earthquake). In several LEWSs worldwide, early warning levels are generated by employing data-driven early warning models. In Pecoraro et al. (2018), 29 worldwide local LEWSs have been examined with respect to the different components of early warning systems for weather-induced landslides and the monitoring strategies presented in Calvello (2017). Among the 29 local LEWSs, 26 systems address weather-induced landslides. These LEWSs have different monitored parameters based on which the warning levels are associated. A great majority of these LEWSs, 27 out of 29, employ a data-driven early warning model. While 8 LEWSs are based on the relationship between the historic monitored parameters and landslide observations, the remaining 19 systems rely on sensor-based thresholds without any mathematical or statistical criterion.

Sensory readings from a single sensor or a set of sensors can be directly used to obtain associated warning levels. The warning levels are decided based on threshold values applied to monitored data. These threshold values might be determined by considering long-term observation on sensory data and landslide observations. Additionally, physical-based landslide prediction models can be also utilized to determine threshold values by relating the sensory readings to the slope stability assessments. Such warning models have certain drawbacks including no predictive capability as warnings are issued based on already observed sensor values, lack of redundancy in defining the warning levels based on a limited number of parameters.

In a different approach, sensory readings from a single sensor or a set of sensors are utilized in combination with landslide observations to derive a functional relationship between the sensory data and warning levels. In these functional relationships, geotechnical, meteorological, or other parameters related to landslide occurrence can be also integrated to increase the complexity and reliability of the models. Such functional relationships can support LEWSs by providing redundancy to the model with several data sources, and the possibility to account for hydrological and geotechnical parameters in the model. However, complex high-dimensional models might be difficult to interpret and require large datasets.

4.5.2. Physical-based early warning model strategy

Physical-based models can be utilized to associate the sensory data to landslide warning levels by explicitly accounting for the physics involved in associated phenomena. For water-induced landslide prediction, physical-based models mainly incorporate analytical or numerical solutions of differential equations governing the infiltration of water into the soil medium and the slope stability. Such physical-based models can support an LEWS with increased reliability, redundancy in data resources, and the ability to forecast landslide warnings. However, some of the main drawbacks of these models include being computational-demanding, requirements for knowledge of several hydrological and geotechnical properties. The following section will demonstrate a pilot work on an automated physical-based early warning model developed for the study area explained in Section 4.4.

4.6. An automated physical-based landslide prediction model

In the KlimaDigital project, a pilot study on an automated physical-based landslide prediction model was conducted (Depina and Oguz 2021). The automated model utilizes the TRIGRS model to obtain landslide predictions over the study area in terms of F_S. These predictions can be used a basis for determining warning levels and issuing early warnings. In TRIGRS model, the unsaturated initial condition is assumed (see Section 2.3.1). In the analyses, conventional deterministic approach is utilized with the parameters assumed to be constant for each geological unit.

In the TRIGRS model, the initial groundwater conditions for the two geological units, namely moraine and fluvial deposits are being updated based on the collected data at four monitoring points (Figure 4.3). Weather predictions are extracted from the Nowcast service by the Meteorological Service through the Weather application programming interface, "https://api.met.no/". The physical-based landslide prediction model is set to run every hour to provide landslide predictions at $t = \{0, 24, 48\}$-hours through an online dashboard with the sensory data from two locations (Figure 4.8).

The research on the automated physical-based landslide prediction model is limited to the pilot model development and model prediction. Further improvements are required to improve the predictive capacity of the landslide prediction model. In the following section, the proposed approach for updating the initial groundwater condition in the TRIGRS model will be explained.

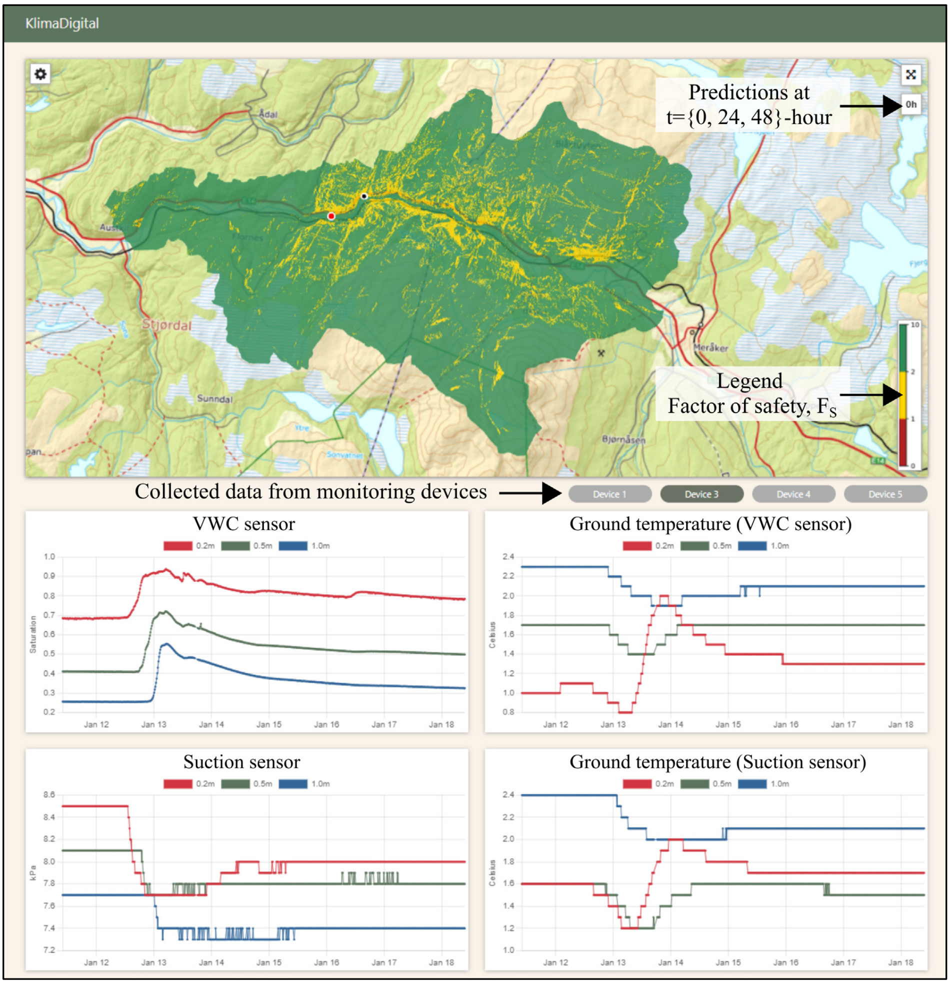
Predictions at t={0, 24, 48}-hour

Legend Factor of safety, F_S

Collected data from monitoring devices

VWC sensor

Ground temperature (VWC sensor)

Suction sensor

Ground temperature (Suction sensor)

Figure 4.8: Online dashboard for the automated physical-based landslide prediction model.

4.6.1. Updating initial groundwater condition

In the automated model, the initial groundwater depth, d_u, in the TRIGRS model is adjusted based on the sensory readings on VWC (Depina and Oguz 2021) as the VWC sensors provide VWC values with a greater degree of resolution in highly saturated conditions. On the contract, the suction sensors have a lower limit of 9 kPa and do not provide suction values close to high saturation, i.e., lower than 9 kPa. The updating of the initial groundwater level is explained in the following paragraphs.

The TRIGRS model utilizes the exponential hydraulic parameter model provided by Gardner (1958). The dependence of the hydraulic conductivity, K, and the VWC, θ, on the pressure head, ψ is defined as:

$$K(\psi) = K_S\, exp\left(\alpha_{fit}\left(\psi - \psi_0^{cap}\right)\right) \tag{4.1}$$

$$\theta = \theta_r + (\theta_s - \theta_r)\, exp\left(\alpha_{fit}\left(\psi - \psi_0^{cap}\right)\right) \tag{4.2}$$

where θ_r and θ_s are the residual and saturated VWC values, ψ_0^{cap} is a constant representing the capillary fringe above the ground water table, and α_{fit} is the fit parameter. ψ_0^{cap} can be calculated as $1/\alpha_{fit}$. However, this study assumes ψ_0 to be zero to simplify the expression for the relationship between d_u and VWC observations.

In the TRIGRS model, initial conditions for hydraulic conductivity, K, are defined (Baum et al. 2008) as follows:

$$K(Z,0) = I_{ZLT} - \left[I_{ZLT} - K_S\, exp\left(\alpha_1 \psi_0^{cap}\right)\right] exp[-\alpha_1(d_u - Z)] \tag{4.3}$$

where $K(Z,0)$ is the hydraulic conductivity at depth Z measured vertically from the ground surface, I_{ZLT} is the long-term vertical infiltration rate, K_S is the saturated hydraulic conductivity in the vertical direction, α_1 is the parameter estimated by a coordinate transformation of α_{fit} due to the inclination of the ground surface, δ, and calculated as $\alpha_1 = \alpha_{fit}\cos^2\delta$. As the ψ_0^{cap} is assumed to be zero, Eq. 4.3 becomes:

$$K(Z,0) = I_{ZLT} - [I_{ZLT} - K_S]\, exp[-\alpha_1(d_u - Z)] \tag{4.4}$$

Dividing Eq. 4.4 with $\mathrm{K_S}$ and inserting Eq. 4.1 result in the following expression:

$$exp\,(\alpha_{fit}\psi) = \frac{I_{ZLT}}{K_S} - \left[\frac{I_{ZLT}}{K_S} - 1\right] exp[-\alpha_1(d_u - Z)] \tag{4.5}$$

From Eq. 4.2, the saturation coefficient, Θ can be calculated as follows:

$$\Theta = \frac{\theta - \theta_r}{\theta_s - \theta_r} = exp\left(\alpha_{fit}\psi\right) \tag{4.6}$$

Using the Eq. 4.6, Eq. 4.5 can be rewritten as follows:

$$\Theta = R - [R - 1]\,exp[-\alpha_1(d_u - Z)] \tag{4.7}$$

where $R = I_{ZLT}/K_S$. Then, the expression for d_u can be formulated as shown below:

$$d_u = Z - \frac{1}{\alpha_1} ln\left(\frac{\Theta - R}{1 - R}\right) \tag{4.8}$$

Assuming that there exist N measurements of Θ, $\{\Theta_i; i = 1, 2, \dots, N\}$ at the corresponding depths of $\{Z_i; i = 1, 2, \dots, N\}$, d_u is calculated as

$$d_u = \bar{Z} - \frac{1}{\alpha_1} ln\left(\frac{\bar{\Theta} - R}{1 - R}\right) \tag{4.9}$$

in which

$$\bar{\Theta} = \frac{1}{N}\sum_{i=1}^{N} \Theta_i \tag{4.10}$$

$$\bar{Z} = \frac{1}{N}\sum_{i=1}^{N} Z_i \tag{4.11}$$

where $\overline{\Theta}$ is the average saturation coefficient and $\bar{Z}$ is the average depth. It should be noted that $\overline{\Theta}$ should be greater than R for Eq. 4.9 to be valid.

To demonstrate the performance of the proposed approach, an example is provided in Figure 4.9 for a given set of parameters: $R = 0.009$, $\bar{Z} = 0.5$ m, $\delta = 30^{\circ}$, $\alpha_{fit} = 0.5$ 1/m, and $\overline{\Theta} = \{0.01, 0.1, 0.2, 0.3, 0.4, 0.5, 0.6,\ 0.7, 0.8, 0.9, 1.0\}$. The relationship between d_u and $\overline{\Theta}$ is shown in Figure 4.9a. It can be seen that d_u becomes equal to $\bar{Z}$ when fully saturation condition is reached at $\bar{Z}$, i.e., $\overline{\Theta} = 1.0$,. As the $\overline{\Theta}$ decreases to R, d_u approaches infinity. Additionally, Figure 4.9b shows the values of Θ with depth, $Z \in [0, 3]$, for the values of $\overline{\Theta}$. It can be observed that the values of Θ increases with depth until Θ reaches 1.0 representing fully saturated condition. This behavior also highlights the limitations of the implemented updating approach. The proposed approach cannot represent the initial groundwater conditions with higher saturation levels at shallower depths.

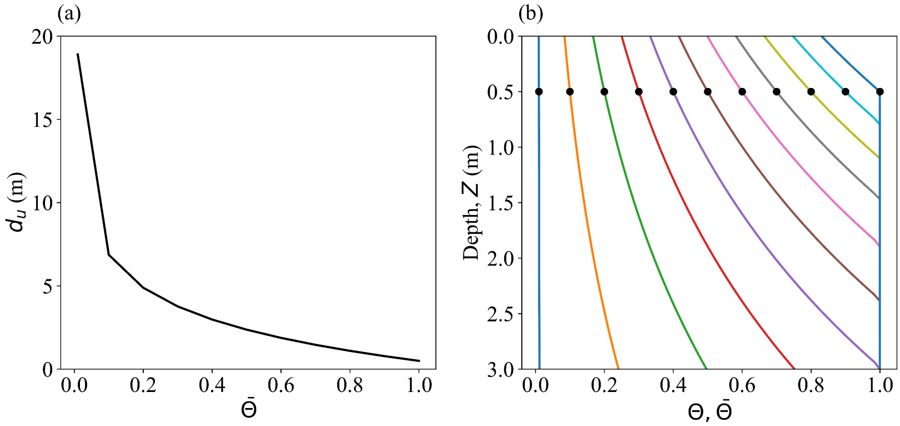

Figure 4.9: (a) Relationship between d_u and $\bar{\Theta}$, and (b) saturation values, Θ, with depth, $Z \in [0,3]$, for a range of $\bar{\Theta}$ at 0.5 m depth (black dots for each line).

5. Summary

Climate change is an ongoing and unequivocal process. The adverse effects of climate change on society are becoming more evident in every aspect of life. The frequency of rainfall-induced landslides is likely to increase in the near future in regions associated with increased intensity and frequency of rainfall as a result of climate change. Additionally, the expansion of the population towards landslide-prone areas further increases the risk to society. This risk obligates the geotechnical community, among others, to develop more efficient landslide risk assessment and management strategies to tackle and mitigate the risk. To meet the requirements of this obligation, this PhD study addressed the following research objectives: (i) investigation of the effects of soil heterogeneity on landslide susceptibility assessment, (ii) quantification of the climate change impact on rainfall-induced landslide susceptibility, and (iii) implementation of hydrological monitoring system supported by the state-of-the-art IoT technologies, and integration of collected data into a physical-based landslide prediction model.

The uncertainties in landslide predictions arise from a lack of knowledge, the inherent variability of model parameters, and assumptions and limitations associated with prediction models. Among these sources, substantial contribution to the uncertainties in landslide predictions originates from spatially variable geotechnical and hydrological parameters. These uncertainties hinder accurate spatial and temporal predictions of landslides and pose a great challenge. Therefore, the effects of spatial variability of model parameters on predictions of rainfall-induced landslides were investigated in a probabilistic framework. A robust and efficient physical-based landslide susceptibility model was developed to account for the variability of model parameters. In the developed 3DPLS model, the hydrological and slope stability models were coupled to assess the landslide susceptibility following a rainfall event. The rainfall infiltration and the corresponding change in the transient pore pressure changes were modelled by one-dimensional Iverson's linearized solution of the Richards equation for tension saturated soils. The slope stability condition was evaluated by utilizing the extension of Bishop's simplified method of slope stability analysis to three dimensions. The capacity of the model to correctly assess the slope stability was validated by three example problems from the literature. The spatial variability was explicitly modelled by two-dimensional Gaussian or lognormal random fields by employing the covariance matrix decomposition method or the stepwise covariance matrix decomposition method depending on the problem size. The uncertainties in the model parameters were propagated to the model predictions by the Monte Carlo method and the probability of landslide initiation was estimated. The capacity of the 3DPLS model to capture the effects of the spatial variability of the model parameters, i.e., the soil heterogeneity, on landslide predictions was validated by a comprehensive study with an FEM-based software. The findings on the effects of spatial variability on landslide susceptibility were reported. Following the validation, the 3DPLS model was implemented on a landslide-prone area in Norway. The predictive capacity of the 3DPLS model was compared to an equivalent cell-based model, which employs the same hydrological model but the infinite slope stability method in the slope stability model.

The changes in the rainfall patterns due to climate change are commonly known to a certain degree for different spatial and temporal scales. However, the effect of this change on landslide susceptibility was rarely quantified explicitly. Quantification of the effects of climate change on landslide susceptibility will provide a basis for the development of landslide risk mitigation strategies. A landslide-prone region in the county of Trøndelag, central Norway was examined for this research, and corresponding novel climate-dependent IDF curves were derived by a straightforward statistical formulation. Three time periods, present (1981-2010), near-future (2021-2050), and far-future (2071-2100), were investigated using the EURO-CORDEX CMIP5 ensemble for the emission scenario RCP8.5. The IDF curves for the present climate condition were obtained by using the precipitation data from observations. For the future climate conditions, the IDF curves were obtained by using the climate estimates from the EURO-CORDEX ensemble for both present and future conditions that were combined with the precipitation data from observations. Rainfall events with varying durations and intensities were simulated based on the IDF curves. Climate change impact on landslide susceptibility was investigated by performing simulations with the physical-based TRIGRS model. A novel probabilistic framework was proposed and implemented to obtain the overall climate change impact accounting for the likelihood of rainfall events. The proposed probabilistic framework integrates the landslide susceptibility estimated for a set of daily or sub-daily rainfall events with varying intensities. Through this integration, the impacts of the extreme events were scaled proportionally to their likelihood. In addition to the overall climate change impact, individual rainfall events of different return intervals were also utilized separately in the climate change impact study.

Efficient landslide risk management strategies are required to mitigate the landslide risk to the society. Among structural and non-structural mitigation strategies, LEWSs are often deployed due to their flexibility and cost-efficiency. In an LEWS, landslide monitoring is the vital component as the warning is issued and disseminated based on the monitored parameters. In this PhD study, a landslide-prone case study area was investigated in terms of geology and landslide inventory. Following the investigations, most of the landslide events were associated with the two Quaternary deposits: moraine and fluvial deposits. Additionally, rainfall and snow melt were identified as the main triggering events for most of the landslide events in the landslide inventory. Therefore, hydrological monitoring systems were deployed in the study area to collect information on the response of the slopes to seasonally cold climate conditions in central Norway. The deployed system is supported by state-of-the-art IoT technologies that provide efficient data acquisition and transmission. The designed IoT-based hydrological monitoring system was deployed at two locations that were selected within two geological units of interest. The VWC sensors, suction sensors, and piezometers were used in the monitoring system. The VWC sensors were calibrated for the two geological units in a controlled lab environment. The collected data were evaluated to obtain insights into the hydrological response of the slopes to the weather characteristic of seasonally cold climates. Additionally, a pilot study was conducted to integrate the collected data in an automated physical-based landslide prediction model that utilizes the TRIGRS model. In the automated model, the collected data were utilized to update the initial groundwater conditions. This PhD thesis does not cover long-term calibration and fine-tuning of the model, which are beyond the scope of this thesis.

6. Conclusions

The following research topics were implemented to address the objectives of the PhD study: probabilistic simulations of rainfall-induced shallow landslides through the implementations of physical-based models, investigation of the impact of spatially variable model parameters on shallow landslide susceptibility assessment, quantification of the climate change impact on landslide susceptibility, and implementation of an IoT-based hydrological landslide monitoring with an early warning model.

This PhD study investigated the impact of spatial variability of the geotechnical strength parameters on the shallow landslide susceptibility assessments. This study was made possible by the development of a new 3-Dimensional Probabilistic Landslide Susceptibility, 3DPLS model. The results revealed the importance of accounting for the spatial variability of the geotechnical model parameters in the landslide susceptibility assessment. Depending on the degree of spatial dependence, significantly lower factor of safety values were obtained in comparison to considering homogeneous conditions. Modelling the variability of the parameters without spatial dependence could result in landslide susceptibility assessment with overestimated factor of safety values. The effect of spatial variability becomes higher as the variability level increases. A higher variability level might result in an increased reduction in factor of safety due to spatial variability depending on the degree of spatial dependence. The developed model was tested in a landslide-prone area, Kvam, in central Norway. The performance of the developed model in capturing the landslide events was compared with an equivalent cell-based model utilizing the infinite slope stability method on a cell-by-cell basis. The results showed that the 3DPLS model provided more accurate and precise predictions regardless of having a lower true positive ratio. More critical zones with a lower factor of safety were obtained by the 3DPLS model. Additionally, the 3DPLS model results had less variability as the model utilizes ellipsoidal sliding surfaces, which smooths the transition of the factor of safety predictions over the study area.

Quantification of the climate change impact on landslide susceptibility will provide a basis to mitigate the upcoming risk and to strengthen the resilience and adaptive capacity of society to landslides. Therefore, this PhD focused on quantifying the impact through a framework including both climate and landslide susceptibility modelling. Climate projections using the EURO-CORDEX ensembles of RCM simulations assuming RCP8.5 and observations from three weather stations showed that the study area will experience more frequent and intense rainfall events. A novel probabilistic framework was proposed to obtain the overall climate change impact on landslide susceptibility without the bias due to the extreme rainfall events of long return intervals. This method provided a more realistic basis to interpret climate change impact on landslide susceptibility. The results showed the overall climate change impact on rainfall-induced landslide susceptibility with increased values of probability of landslide initiation. Until the end of the 21st century, the probability of landslide initiation might increase by up to 10% at certain zones in the studied area depending on rainfall duration. In addition to the overall climate change impact, the climate change impact was also investigated by using only extreme rainfall events of long return intervals. When the extreme events were considered without accounting for their occurrence probability, the increase in the probability of landslide initiation due to climate change was found to be much greater. This reveals that investigating only extreme rainfall events might result in overestimated climate change impact while the proposed probabilistic method provides a more realistic impression of climate change impact by accounting for the probability of occurrences of rainfall events.

One efficient way to mitigate the risk associated with landslides is landslide monitoring and early warning systems. In this PhD study, a hydrological monitoring system was installed in a landslide-prone area to monitor hydrological activities in the slopes. The hydrological monitoring system is supported by IoT-based technologies that provide more efficient data acquisition and transmission. The performance of deployed IoT-based hydrological monitoring system was overall quite satisfactory and proved IoT-solution providing simplified installation, reliable data acquisition and transmission. During the operation of the landslide monitoring system, one network outage was experienced but the quality of data acquisition was not affected. The data collected through the IoT-based hydrological monitoring system provided significant insights into the hydrological response of the slopes to meteorological conditions. The important phenomenon including ground freezing and thawing, and effects of rainfall and snow melting on matric suction and VWC were observed. During the cold period with air temperature being below 0°C, VWC values dropped due to the ground freezing. Meanwhile, values of matric suction increased sharply, especially at 0.3 m top crust. Following the cold period, very high VWC values were observed due to a combination of ground thawing, snow melting, and rainfall. Matric suction values were at the sensor's lower limit for the majority of the monitored period. High values of matric suction were observed in the cold period due to ground freezing and in the dry period due to increased evapotranspiration and less rainfall. The collected data showed strong potential to be used in combination with physical-based or data-driven landslide prediction models to estimate the hazard levels in the study area. Such integration of collected data might be particularly important to extrapolate collected information from several monitoring locations to a larger extent at a catchment scale. A pilot study was conducted to integrate the collected data into an automated landslide prediction model. The collected data were used to calibrate the unsaturated characteristics of soil types and to update the initial groundwater conditions. The automated model has been set to run every hour. For each run, the model uses the collected data to update the initial groundwater conditions and extracts the weather forecasts as an input to the model. The model shows the potential of the collected data to be used in collaboration with a landslide prediction model.

7. Recommendations for future work

In this research, probabilistic modelling approach was utilized in the simulations of rainfall-induced landslides to account for the uncertainties in the model parameters (Paper I and Paper II). Despite the capacity of the probabilistic approaches to handle the uncertainties explicitly, the time- and computational-demanding nature of the probabilistic approaches were regarded as a limitation. This aspect is especially important for real-time LEWSs relying on probabilistic predictions of landslide prediction models. Therefore, further research should be conducted to increase the computational efficiency by investigating efficient probabilistic methods.

In this PhD study, the transient pore pressure change due to the rainfall infiltration was simulated by Iverson’s one-dimensional linearized solution of the Richards equation. However, complex physical processes such as snow melting, ground freezing/thawing were not accounted for. Further research is needed to incorporate these complex physical processes in the simulations of the infiltration process and in the landslide susceptibility models. Such integration will provide more reliable pore pressure values and more accurate landslide susceptibility predictions.

Quantification of climate change impact on landslide susceptibility is an international problem of high importance due to the high risks that landslides impose on society. Therefore, this was one of the topics covered in this PhD research (Paper II). Climate modelling and landslide susceptibility modelling chains were integrated into a conceptual framework to obtain future hazards due to landslides. Both modelling chains have room for further improvements to obtain better climate projections and the corresponding landslide susceptibility assessments. In landslide susceptibility modelling, more robust stochastic calibration methods can be utilized to obtain more accurate estimates of the geotechnical and hydrological model parameters. Additionally, different strategies can be investigated to incorporate climate change into the landslide susceptibility modelling. In climate modelling, more robust and inclusive climate projections can be achieved by investigating a larger number of simulations by GCMs and RCMs. Additionally, better downscaling of the GCMs can be performed by hybrid models involving both dynamic downscaling by RCMs and ESD.

A considerable potential was detected in the automatization of the physical-based landslide prediction models based on the monitored parameters through IoT-based landslide monitoring systems. Such automatization of the physical-based models can support the landslide forecasting and early warning systems by more accurate real-time predictions. Eventually, better performance can be achieved in the operation of LEWSs. Further research is needed for efficient integration of the monitored parameters into physical-based landslide prediction models.

References

Abraham MT, Satyam N, Pradhan B, Alamri AM (2020) IoT-based geotechnical monitoring of unstable slopes for landslide early warning in the Darjeeling Himalayas. Sensors (Switzerland) 20:. https://doi.org/10.3390/s20092611

Alvioli M, Melillo M, Guzzetti F, et al (2018) Implications of climate change on landslide hazard in Central Italy. Sci Total Environ 630:1528–1543. https://doi.org/10.1016/j.scitotenv.2018.02.315

Arnone E, Dialynas YG, Noto L V., Bras RL (2016) Accounting for soil parameter uncertainty in a physically based and distributed approach for rainfall-triggered landslides. Hydrol Process 30:927–944. https://doi.org/10.1002/hyp.10609

Baecher GB, Christian JT (2003) Reliability and statistics in geotechnical engineering. John Wiley \& Sons

Baum BRL, Savage WZ, Godt JW (2002) TRIGRS — a fortran program for transient rainfall infiltration and grid-based regional slope-stability analysis: open-file report 02-424

Baum RL, Godt JW, Savage WZ (2010) Estimating the timing and location of shallow rainfall-induced landslides using a model for transient, unsaturated infiltration. J Geophys Res Earth Surf 115:. https://doi.org/10.1029/2009JF001321

Baum RL, Savage WZ, Godt JW (2008) TRIGRS — a Fortran program for transient rainfall infiltration and grid-based regional slope-stability analysis, version 2.0: U.S. Geological Survey open-file report, 2008-1159

Benestad RE, Hanssen-Bauer I, Chen D (2008) Empirical-statistical downscaling. World Scientific

Benestad RE, Lutz J, Dyrrdal AV, et al (2021) Testing a simple formula for calculating approximate intensity-duration-frequency curves. Environ Res Lett 16:. https://doi.org/10.1088/1748-9326/abd4ab

Benestad RE, Parding KM, Erlandsen HB, Mezghani A (2019) A simple equation to study changes in rainfall statistics. Environ Res Lett 14:. https://doi.org/10.1088/1748-9326/ab2bb2

Bishop AW (1955) The use of the slip circle in the stability analysis of slopes. Geotechnique 5:7–17. https://doi.org/10.1680/geot.1955.5.1.7

Bordoni M, Meisina C, Valentino R, et al (2015) Hydrological factors affecting rainfall-induced shallow landslides: From the field monitoring to a simplified slope stability analysis. Eng Geol 193:19–37. https://doi.org/10.1016/j.enggeo.2015.04.006

Burton A, Arkell TJ, Bathurst JC (1998) Field variability of landslide model parameters. Environ Geol 35:100–114. https://doi.org/10.1007/s002540050297

Calvello M (2017) Early warning strategies to cope with landslide risk. Riv Ital di Geotec 51:63–91. https://doi.org/10.19199/2017.2.0557-1405.063

Chaturvedi P, Thakur KK, Mali N, et al (2018) A Low-Cost IoT Framework for Landslide

Prediction and Risk Communication. In: Internet of Things A to Z. pp 593–610

Chiang SH, Chang KT (2011) The potential impact of climate change on typhoon-triggered landslides in Taiwan, 2010-2099. Geomorphology 133:143–151. https://doi.org/10.1016/j.geomorph.2010.12.028

Ciervo F, Rianna G, Mercogliano P, Papa MN (2017) Effects of climate change on shallow landslides in a small coastal catchment in southern Italy. Landslides 14:1043–1055. https://doi.org/10.1007/s10346-016-0743-1

Comegna L, Damiano E, Greco R, et al (2016) Field hydrological monitoring of a sloping shallow pyroclastic deposit. Can Geotech J 53:1125–1137. https://doi.org/10.1139/cgj-2015-0344

Dai FC, Lee CF, Ngai YY (2002) Landslide risk assessment and management: An overview. Eng Geol 64:65–87. https://doi.org/10.1016/S0013-7952(01)00093-X

Depina I, Devoli G, Oguz EA (2021) KlimaDigital Work Package 4: KlimaDigital Case Study

Depina I, Oguz EA (2021) KlimaDigital Work Package 2: Dissemination of sensor data and landslide predictions through an early warning system

Dilley M, Chen RS, Deichmann U, et al (2005) Natural disaster hotspots: A global risk analysis. World Bank Publications

Dixon N, Brook E (2007) Impact of predicted climate change on landslide reactivation: Case study of Mam Tor, UK. Landslides 4:137–147. https://doi.org/10.1007/s10346-006-0071-y

Emberson R, Kirschbaum D, Stanley T (2020) New global characterisation of landslide exposure. Nat Hazards Earth Syst Sci 20:3413–3424. https://doi.org/10.5194/nhess-20-3413-2020

Erlandsen HB, Parding KM, Benestad R, et al (2020) A hybrid downscaling approach for future temperature and precipitation change. J Appl Meteorol Climatol 59:1793–1807. https://doi.org/10.1175/JAMC-D-20-0013.1

Eyring V, Bony S, Meehl GA, et al (2016) Overview of the Coupled Model Intercomparison Project Phase 6 (CMIP6) experimental design and organization. Geosci Model Dev 9:1937–1958. https://doi.org/10.5194/gmd-9-1937-2016

Fawcett T (2006) An introduction to ROC analysis. Pattern Recognit Lett 27:861–874. https://doi.org/10.1016/j.patrec.2005.10.010

Fell R (1994) Landslide risk assessment and acceptable risk. Can Geotech J 31:261–272. https://doi.org/10.1139/t94-031

Fenton GA, Griffiths DV (2008) Risk assessment in geotechnical engineering. John Wiley \& Sons New York

Froude MJ, Petley DN (2018) Global fatal landslide occurrence from 2004 to 2016. Nat Hazards Earth Syst Sci 18:2161–2181. https://doi.org/10.5194/nhess-18-2161-2018

Gardner WR (1958) Some steady-state solutions of the unsaturated moisture flow equation with application to evaporation from a water table. Soil Sci 85:228–232

Gariano SL, Guzzetti F (2016) Landslides in a changing climate. Earth-Science Rev 162:227–252. https://doi.org/10.1016/j.earscirev.2016.08.011

Giorgi F, Jones C, Asrar GR, others (2009) Addressing climate information needs at the regional level: the CORDEX framework. World Meteorol Organ Bull 58:175

Glade T, Nadim F (2014) Early warning systems for natural hazards and risks. Nat Hazards 70:1669–1671. https://doi.org/10.1007/s11069-013-1000-8

Görüm T, Fidan S (2021) Spatiotemporal variations of fatal landslides in Turkey. Landslides 18:1691–1705. https://doi.org/10.1007/s10346-020-01580-7

Guzzetti F, Gariano SL, Peruccacci S, et al (2020) Geographical landslide early warning systems. Earth-Science Rev 200:102973. https://doi.org/10.1016/j.earscirev.2019.102973

Hanssen-Bauer I, Førland EJ, Haddeland I, et al (2017) Climate in Norway 2100 – a knowledge base for climate adaptation

Haque U, Blum P, da Silva PF, et al (2016) Fatal landslides in Europe. Landslides 13:1545–1554. https://doi.org/10.1007/s10346-016-0689-3

Haque U, da Silva PF, Devoli G, et al (2019) The human cost of global warming: Deadly landslides and their triggers (1995–2014). Sci Total Environ 682:673–684. https://doi.org/10.1016/j.scitotenv.2019.03.415

Hay LE, Wilby RL, Leavesley GH (2000) A comparison of delta change and downscaled GCM scenarios for three mountain basins in the United States. J Am Water Resour Assoc 36:387–397. https://doi.org/10.1111/j.1752-1688.2000.tb04276.x

Ho K, Lacasse S, Picarelli L (2017) Slope safety preparedness for impact of climate change, 1st edn.

Hungr O (1987) An extension of Bishop's simplified method of slope stability analysis to three dimensions. Geotechnique 37:113–117. https://doi.org/10.1680/geot.1987.37.1.113

IPCC (2021) Climate Change 2021: The Physical Science Basis. Contribution of Working Group I to the Sixth Assessment Report of the Intergovernmental Panel on Climate Change

IPCC (2014) Climate Change 2014: Synthesis Report. Geneva, Switzerland

IPCC (2013) Climate Change 2013: The Physical Science Basis. Contribution of Working Group I to the Fifth Assessment Report of the Intergovernmental Panel on Climate Change. Cambridge University Press

ITU (2012) Overview of the Internet of things (recommendation ITU-T Y.2060)

Iverson MR (2000) Landslide triggering by rain infiltration. Water Resour Res 36:1897–1910

Jacob D, Petersen J, Eggert B, et al (2014) EURO-CORDEX: New high-resolution climate change projections for European impact research. Reg Environ Chang 14:563–578. https://doi.org/10.1007/s10113-013-0499-2

Kim K, Jeong S, Song Y, et al (2021) Four-Year Monitoring Study of Shallow Landslide Hazards Based on Hydrological Measurements in a Weathered Granite Soil Slope in South Korea

Lacasse S, Nadim F, Kalsnes B (2010) Living with landslide risk. Geotech Eng J SEAGS AGSSEA 41:

Laprise R (2008) Regional climate modelling. J Comput Phys 227:3641–3666. https://doi.org/10.1016/j.jcp.2006.10.024

Lee EM, Jones DKC (2014) Landslide Risk Assessment, Second edi. ICE Publishing

Li DQ, Xiao T, Zhang LM, Cao ZJ (2019) Stepwise covariance matrix decomposition for efficient simulation of multivariate large-scale three-dimensional random fields. Appl Math Model 68:169–181. https://doi.org/10.1016/j.apm.2018.11.011

Lizárraga JJ, Buscarnera G (2020) Probabilistic modeling of shallow landslide initiation using regional scale random fields. Landslides 17:1979–1988. https://doi.org/10.1007/s10346-020-01438-y

Lizárraga JJ, Buscarnera G (2019) Spatially distributed modeling of rainfall-induced landslides in shallow layered slopes. Landslides 16:253–263. https://doi.org/10.1007/s10346-018-1088-8

Medina V, Hürlimann M, Guo Z, et al (2021) Fast physically-based model for rainfall-induced landslide susceptibility assessment at regional scale. Catena 201:105213. https://doi.org/10.1016/j.catena.2021.105213

Mekki K, Bajic E, Chaxel F, Meyer F (2019) A comparative study of LPWAN technologies for large-scale IoT deployment. ICT Express 5:1–7. https://doi.org/10.1016/j.icte.2017.12.005

Melchiorre C, Frattini P (2012) Modelling probability of rainfall-induced shallow landslides in a changing climate, Otta, Central Norway. Clim Change 113:413–436. https://doi.org/10.1007/s10584-011-0325-0

Mergili M, Marchesini I, Alvioli M, et al (2014a) A strategy for GIS-based 3-D slope stability modelling over large areas. Geosci Model Dev 7:2969–2982. https://doi.org/10.5194/gmd-7-2969-2014

Mergili M, Marchesini I, Rossi M, et al (2014b) Spatially distributed three-dimensional slope stability modelling in a raster GIS. Geomorphology 206:178–195. https://doi.org/10.1016/j.geomorph.2013.10.008

METER Group (2022a) Atmos 41 Manual. https://www.metergroup.com/environment/products/atmos-41-weather-station/

METER Group (2022b) ZL6 Manual. https://www.metergroup.com/environment/products/zl6-data-logger/

Mezghani A, Dobler A, Benestad R, et al (2019) Subsampling impact on the climate change signal over poland based on simulations from statistical and dynamical downscaling. J Appl Meteorol Climatol 58:1061–1078. https://doi.org/10.1175/JAMC-D-18-0179.1

Michoud C, Bazin S, Blikra LH, et al (2013) Experiences from site-specific landslide early warning systems. Nat Hazards Earth Syst Sci 13:2659–2673. https://doi.org/10.5194/nhess-13-2659-2013

Montgomery DR, Dietrich WE (1994) A physically based model for the topographic control on shallow landsliding. Water Resour Res 30:1153–1171.

https://doi.org/10.1029/93WR02979

Montrasio L, Valentino R (2008) A model for triggering mechanisms of shallow landslides. Nat Hazards Earth Syst Sci 8:1149–1159. https://doi.org/10.5194/nhess-8-1149-2008

Myhre B, Rustad H (2021) KlimaDigital Work Package 1: The KlimaDigital Environmental IoT System

Myhre G, Shindell D, Bréon F-M, et al (2014) Anthropogenic and Natural Radiative Forcing. In: Climate Change 2014: The Physical Science Basis. Contribution of Working Group I to the Fifth Assessment Report of the Intergovernmental Panel on Climate Change. Cambridge University Press, Cambridge

Nadim F, Kjekstad O, Peduzzi P, et al (2006) Global landslide and avalanche hotspots. Landslides 3:159–173. https://doi.org/10.1007/s10346-006-0036-1

Oguz EA, Depina I, Thakur V (2021) Effects of soil heterogeneity on susceptibility of shallow landslides. Landslides. https://doi.org/10.1007/s10346-021-01738-x

Pack RT, Tarboton DG, Goodwin CN, Prasad A (2005) SINMAP 2.0: a stability index approach to terrain stability hazard mapping

Pecoraro G, Calvello M, Piciullo L (2019) Monitoring strategies for local landslide early warning systems. Landslides. https://doi.org/10.1007/s10346-018-1068-z

Petley D (2012) Global patterns of loss of life from landslides. Geology 40:927–930. https://doi.org/10.1130/G33217.1

Phoon K-K, Kulhawy FH (1999a) Characterization of geotechnical variability. Can Geotech J 36:612–624. https://doi.org/10.1139/t99-038

Phoon K-K, Kulhawy FH (1999b) Evaluation of geotechnical property variability. Can Geotech J 36:625–639. https://doi.org/10.1139/t99-039

Raia S, Alvioli M, Rossi M, et al (2014) Improving predictive power of physically based rainfall-induced shallow landslide models: A probabilistic approach. Geosci Model Dev 7:495–514. https://doi.org/10.5194/gmd-7-495-2014

Research Council of Norway: Project Bank KlimaDigital, Project number: 281059. https://prosjektbanken.forskningsradet.no/en/project/FORISS/281059. Accessed 17 Jan 2022

Rossi G, Catani F, Leoni L, et al (2013) HIRESSS: a physically based slope stability simulator for HPC applications. Nat Hazards Earth Syst Sci 13:151–166. https://doi.org/10.5194/nhess-13-151-2013

SafeLand (2012) Living with landslide risk in Europe: Assessment, effects of global change, and risk management strategies. Deliverable 4.6: Report on evaluation of mass movement indicators

Salciarini D, Brocca L, Camici S, et al (2019) Physically based approach for rainfall-induced landslide projections in a changing climate. Proc Inst Civ Eng Geotech Eng 172:481–495. https://doi.org/10.1680/jgeen.18.00216

Salciarini D, Godt JW, Savage WZ, et al (2006) Modeling regional initiation of rainfall-induced shallow landslides in the eastern Umbria Region of central Italy. Landslides

3:181–194. https://doi.org/10.1007/s10346-006-0037-0

Sandric I, Ionita C, Chitu Z, et al (2019) Using CUDA to accelerate uncertainty propagation modelling for landslide susceptibility assessment. Environ Model Softw 115:176–186. https://doi.org/10.1016/j.envsoft.2019.02.016

Sangelantoni L, Gioia E, Marincioni F (2018) Impact of climate change on landslides frequency: the Esino river basin case study (Central Italy). Springer Netherlands

Scheidl C, Heiser M, Kamper S, et al (2020) The influence of climate change and canopy disturbances on landslide susceptibility in headwater catchments. Sci Total Environ 742:140588. https://doi.org/10.1016/j.scitotenv.2020.140588

Schilirò L, Cepeda J, Devoli G, Piciullo L (2021) Regional analyses of rainfall-induced landslide initiation in upper gudbrandsdalen (South-eastern Norway) using TRIGRS model. Geosci 11:1–15. https://doi.org/10.3390/geosciences11010035

Shirzadi A, Solaimani K, Roshan MH, et al (2019) Uncertainties of prediction accuracy in shallow landslide modeling: Sample size and raster resolution. Catena 178:172–188. https://doi.org/10.1016/j.catena.2019.03.017

Shou KJ, Yang CM (2015) Predictive analysis of landslide susceptibility under climate change conditions - A study on the Chingshui River Watershed of Taiwan. Eng Geol 192:46–62. https://doi.org/10.1016/j.enggeo.2015.03.012

Simoni S, Zanotti F, Bertoldi G, Rigon R (2008) Modelling the probability of occurrence of shallow landslides and channelized debris flows using GEOtop-FS. Hydrol Process 22:532–545. https://doi.org/10.1002/hyp.6886 Modelling

Song YS, Chae BG, Kim KS, et al (2021) A landslide monitoring system for natural terrain in korea: Development and application in hazard evaluations. Sensors 21:1–22. https://doi.org/10.3390/s21093040

Srivastava R, Yeh T-. J (1991) Analytical solutions for one-dimensional, transient infiltration toward the water table in homogeneous and layered soils. Water Resour Res 27:753–762. https://doi.org/10.1029/90WR02772

Stanley T, Kirschbaum DB (2017) A heuristic approach to global landslide susceptibility mapping. Nat Hazards 87:145–164. https://doi.org/10.1007/s11069-017-2757-y

Takayabu I, Kanamaru H, Dairaku K, et al (2016) Reconsidering the quality and utility of downscaling. J Meteorol Soc Japan 94A:31–45. https://doi.org/10.2151/jmsj.2015-042

Taylor KE, Stouffer RJ, Meehl GA (2012) An overview of CMIP5 and the experiment design. Bull Am Meteorol Soc 93:485–498. https://doi.org/10.1175/BAMS-D-11-00094.1

UNISDR (2009) Terminology on Disaster Risk Reduction

Varsom Xgeo Varsom Xgeo. https://www.regobs.no/Registration/278548. Accessed 3 Jan 2022

Wong WK, Haddeland I, Lawrence D, Beldring S (2016) Gridded 1 x 1 km climate and hydrological projections for Norway

Wu W, Sidle RC (1995) A distributed slope stability model for steep forested basins. Water Resour 31:2097–2110 www.adressa.no (2021) Skred skal ha tatt med seg telefonstolper: – Det er cirka hundre meter bredt. https://www.adressa.no/pluss/nyheter/2021/11/24/Skred-skal-ha-tatt-med-seg-telefonstolper-—-Det-er-cirka-hundre-meter-bredt-24857604.ece. Accessed 3 Jan 2022

www.bladet.no (2021) Odd Magne var i skogen med hodelykt natten skredet gikk: – Var heftig å se det i dagslys. https://www.bladet.no/nyheter/i/y4V8Ae/odd-magne-var-i-skogen-med-hodelykt-natten-skredet-gikk-var-heftig-aa-se-det-i-dagslys. Accessed 3 Jan 2022

Part II

Publications

Paper I: Effects of soil heterogeneity on susceptibility of shallow landslides

Original Paper

Landslides (2022)19:67–83
DOI 10.1007/s10346-021-01738-x
Received: 17 December 2020
Accepted: 6 July 2021

Emir Ahmet Oguz · Ivan Depina · Vikas Thakur

Effects of soil heterogeneity on susceptibility of shallow landslides

Abstract Uncertainties in parameters of landslide susceptibility models often hinder them from providing accurate spatial and temporal predictions of landslide occurrences. Substantial contribution to the uncertainties in landslide assessment originates from spatially variable geotechnical and hydrological parameters. These input parameters may often vary significantly through space, even within the same geological deposit, and there is a need to quantify the effects of the uncertainties in these parameters. This study addresses this issue with a new three-dimensional probabilistic landslide susceptibility model. The spatial variability of the model parameters is modeled with the random field approach and coupled with the Monte Carlo method to propagate uncertainties from the model parameters to landslide predictions (i.e., factor of safety). The resulting uncertainties in landslide predictions allow the effects of spatial variability in the input parameters to be quantified. The performance of the proposed model in capturing the effect of spatial variability and predicting landslide occurrence has been compared with a conventional physical-based landslide susceptibility model that does not account for three-dimensional effects on slope stability. The results indicate that the proposed model has better performance in landslide prediction with higher accuracy and precision than the conventional model. The novelty of this study is illustrating the effects of the soil heterogeneity on the susceptibility of shallow landslides, which was made possible by the development of a three-dimensional slope stability model that was coupled with random field model and the Monte Carlo method.

Keywords Landslide · Susceptibility · 3D slope stability · Rainfall · Variability · Probability

Introduction

Landslides are one of the major hazards in the world causing adverse consequences to society, such as fatalities (e.g., Haque et al. 2016; Petley 2012), injuries to people, economical losses (e.g., Nadim et al. 2006), and environmental damages. Among the different types of landslides, shallow landslides are one of the most detrimental types due to their high frequency on hillsides, and the capacity to evolve in destructive debris flows. Shallow landslides can be initiated by extreme events of rainfall, snowmelt, or a combination of rainfall and snowmelt.

In the landslide hazard and susceptibility mapping, physical-based models are being increasingly employed as the hydrological and geotechnical aspects of the landslide can be explicitly considered. A wide range of physical-based landslide susceptibility models have been developed ranging from local (i.e., single slope to 10 km^2) to national scales (i.e., hundreds to thousands of km^2). Some of the most commonly used models include the distributed Shallow Landslide Analysis Model (dSLAM) (Wu and Sidle 1995), the Shallow Slope Stability Model (SHALSTAB) (Montgomery and Dietrich 1994), the Stability Index Mapping (SINMAP) (Pack et al. 2005), the Shallow Landslides Instability Prediction (SLIP) (Montrasio and Valentino 2008), GEOtop-FS (Simoni et al. 2008), the Transient Rainfall Infiltration and Grid-Based Regional Slope Stability (TRIGRS) (Baum et al. 2002, 2008) model, TRIGRS-P (Raia et al. 2014), the High Resolution Slope Stability Simulator (HIRESS) (Rossi et al. 2013), and the r.rotstab (Mergili et al. 2014b, a).

Significant uncertainty in the geotechnical and hydrological parameters of these models has been reported in the literature (e.g., Burton et al. 1998; Mergili et al. 2014b; Arnone et al. 2016). The uncertainties represent one of the major challenges in the accurate spatial and temporal prediction of rainfall-induced shallow landslides. The uncertainties originate often due to the lack of field and laboratory investigations and the inherent natural variability linked to the parameters (e.g., Melchiorre and Frattini 2012). Avoiding quantification of uncertainty by employing a set of deterministic values for the model parameters might result in unrealistic or too conservative estimates (e.g., Raia et al. 2014). In addition to the uncertainties in the geotechnical and hydrological parameters, uncertainties can arise from different sources including initial hydrological conditions (e.g., Grelle et al. 2014). Bossi et al. (2019) investigated the uncertainties in the slope stability modeling due to soil stratigraphy heterogeneity. The results show that soil stratigraphy heterogeneity has a significant effect on the safety of slopes. The uncertainties originating from GIS data sources (Sandric et al. 2019), raster resolution, and sample size (Shirzadi et al. 2019) have been also reported to be significant in landslide susceptibility assessment.

The uncertainties in the spatially variable model parameters can be statistically modeled with random fields (Fenton and Griffiths 2008). Random fields model spatially variable parameter by assigning a probability density function (pdf) to statistically describe the uncertainties in the parameter and using a covariance function to account for spatial dependence of the parameter. Variability of landslide model parameters (e.g., geotechnical and hydrological parameters) has been mainly incorporated by considering different homogeneous geological units over the terrain (Salciarini et al. 2006; Baum et al. 2010; Melchiorre and Frattini 2012; Schilirò et al. 2021) without explicitly modeling spatial variability within a single geological unit. Additionally, some of the abovementioned physical-based models, such as SINMAP, GEOtop-FS, HIRESSS, and TRIGRS-P, have the capacity to model the variability of the model parameters with the single random variable approach, where the parameters are uncertain but homogeneous within a single geological unit, thus not accounting for spatial variability (Hammond et al. 1992; Haneberg 2004; Raia et al. 2014; Arnone et al. 2016).

Spatial variability of physical-based model parameters such as cohesion as a geotechnical parameter has been investigated by extensive field measurements in Burton et al. (1998). The results of the study reveal the significance of the spatial variability on the landslide modeling. Additionally, Fenton and Griffiths (2008) investigated the effects of spatial variability and showed that non-conservative results are obtained without accounting for the spatial variability.

The need of accounting for the spatial variability of the geotechnical and hydrological parameters on the susceptibility of landslides has been addressed by many researchers (e.g., Burton et al. 1998; Mergili et al. 2014a, b; Arnone et al. 2016). In the study of Lizárraga and Buscarnera (2020), spatial variability of hydraulic conductivity, K_S, has been accounted in regional modeling of shallow landslide. The physical-based model described in Lizárraga and Buscarnera (2019) has been combined with random field approach and Monte Carlo realizations to account for the spatial variability of K_S. The results indicate that accounting for spatially varying K_S affects the shallow landslide susceptibility assessment significantly. However, there is yet to make an attempt to study the spatial variability of geotechnical parameters on shallow landslide susceptibility using physical-based models. Accounting the variability of model parameters without spatial dependence (e.g., Rossi et al. 2013; Raia et al. 2014), as homogeneous through space, would result in an overestimated factor of safety, F_S, as the failure might occur through weak zones resulting in lower F_S in case of heterogeneity. This work aims to evaluate the effects of spatial variable model parameters on the estimates of susceptibility of shallow landslides with the development of a three-dimensional landslide susceptibility model accounting for the variability of model parameters over spatial extent.

The study is presented in such a way that the proposed 3D soil column-based limit equilibrium model, capable of modeling the spatial variability over the problem domain, is introduced first. Details on the hydrological model, the slope stability model, and the statistical methods integrated into the model are provided. This is followed by the validation of the slope stability model. Additionally, the effects of the spatial variability of the model parameters on the susceptibility of shallow landslides will be introduced, and the capacity of the proposed model to capture these effects will be validated on a simplified problem by performing an extensive study in a finite element method software. Finally, the model will be tested on a case study in an area prone to shallow landslides, and the results will be provided.

The 3-Dimensional Probabilistic Landslide Susceptibility (3DPLS) model

The **3**-**D**imensional **P**robabilistic **L**andslide **S**usceptibility (3DPLS) model is a Python code developed for landslide susceptibility assessment. The 3DPLS model evaluates the landslide susceptibility on a local to a regional scale (i.e., single slope to 10 km²) and allows for the effects of variability of the model parameters on slope stability to be accounted for.

The 3DPLS model couples the hydrological and slope stability models. The hydrological model calculates the transient pore pressure changes due to rainfall infiltration using Iverson's linearized solution of the Richards equation (Iverson 2000) assuming tension saturation. The slope stability model calculates the F_S by utilizing the extension of Bishop's simplified method of slope stability analysis (Bishop 1955) to three dimensions, proposed in the study of Hungr (1987). The 3DPLS model requires topographic data (e.g., DEM, slope, groundwater depth, depth to bedrock, geological zones), hydrological parameters (e.g., steady background infiltration rate, permeability coefficient, diffusivity), geotechnical parameters (e.g., soil unit weight, cohesion, friction angle), and rainfall data.

The model can have a grid containing hundreds or thousands of cells depending on the problem size and refinement. The smallest unit of the grid is called a grid cell having its own model parameters. The developed model calculates the F_S of an ellipsoidal sliding surface consisting of grid cells over a discretized problem domain, while equivalent cell-based models, as the name states, perform the calculations per each cell individually. The model generates a large number of ellipsoidal sliding surfaces centered at each grid cell over the terrain and calculates the F_S of all sliding surfaces. After the calculation, each cell is involved in several ellipsoidal sliding surfaces with different F_S values. Among all F_S values, the minimum F_S representing the critical ellipsoidal sliding surface is assigned to each cell. Each simulation results in a F_S map over the terrain. After a number simulation, the 3DPLS model provides the F_S map of each simulation, the mean F_S, μ_{F_S}, and the probability of failure, P_f, of each cell.

The 3D slope stability model

The model assumes an ellipsoidal sliding surface, as shown in Fig. 1, and calculates the corresponding F_S. The ellipsoidal sliding surface is characterized by the lengths of three principal semi-axes, a_e, b_e, and c_e and the inclination of the ellipsoid in the direction of motion, β, aspect of the motion, α, and the geographical coordinates of the center with a perpendicular offset of the ellipsoid center, z_e, above the ground, as presented in Fig. 2. The a_e is the principal semi-axis

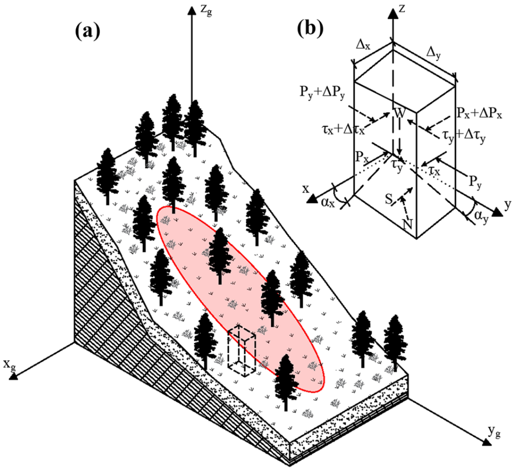

Fig. 1 (**a**) 3D illustration of the landslide body and (**b**) a single grid column with the forces inside the ellipsoidal sliding surface

in the direction of steepest slope, i.e., in the sliding direction, and b_e is the other principal semi-axis perpendicular to the direction of the steepest slope. c_e is the third principal semi-axis perpendicular to the other two principal semi-axes.

After an ellipsoidal sliding surface is specified, the depth to the sliding surface is calculated for each cell inside the ellipsoidal sliding zone. Then, the 3DPLS model truncates the ellipsoidal sliding surface at the cells where depth to the sliding surface is greater than depth to bedrock, i.e., thickness of the cell.

The lengths of three principal semi-axes, a_e, b_e, and c_e, are defined by the user considering the characteristics of the shallow landslides that occurred over the study area. The direction of the motion, α, can be obtained by using the aspect of the cells inside the sliding zone or using reference points inside the ellipsoidal zone (e.g., Mergili et al. 2014b), but it is assigned by the user in the current version of the 3DPLS model. The inclination of the ellipsoid in the direction of motion, β, is calculated by taking the average slope over a rectangular zone with the dimensions of $2a_e \times 2b_e$ located at the center of the ellipsoid. In the 3DPLS model, when the number of cells in the slope stability calculation for a single ellipsoid is less than a given threshold value, the model can sub-discretize the cells by halving the cell size until the threshold value is reached. To have a reasonable ellipsoidal sliding surface in the analysis, the number of cells inside the ellipsoidal zone should be sufficiently high. Otherwise, the generated sliding surface represents a combination of discrete planes. There is a trade-off between the threshold cell number and runtime. Therefore, a reasonable threshold should be selected by investigating the effect of cell number on the F_S.

The slope stability model of the 3DPLS model employs the 3D extension of Bishop's simplified method of slope stability analysis (Bishop 1955), proposed by Hungr (1987). This extended method, Bishop 3D, is a three-dimensional soil column-based limit equilibrium method. The Bishop 3D relies on the same assumptions of Bishop's simplified model. These assumptions are (i) that vertical shear forces acting on the vertical faces of the soil column (both longitudinal and lateral) can be ignored and (ii) that the vertical equilibrium of forces for individual soil columns and the moment equilibrium of the entire system of soil columns are sufficient conditions for the identification of unknowns such as the normal force and shear force at the base of soil columns and F_S.

After placing the ellipsoidal sliding surface, the depth of the ellipsoidal sliding surface, d_e, is calculated using the coordinate and elevation data of each cell. The thickness of the sliding for a given cell, d, is equal to the d_e if the maximum depth to bedrock, Z_{max}, is greater than d_e. Otherwise, the sliding surface is truncated at Z_{max} and $d = Z_{max}$. Then, the total weight of the soil column is calculated as $W = d(\Delta_x \Delta_y)$, where Δ_x and Δ_y are the lateral soil column dimensions. In the case of truncation, the same aspect of the ellipsoidal sliding surface, i.e., α, and the slope angle of the truncated cell are assigned to the sliding base of the truncated cell for simplicity.

Considering a single soil column shown in Fig. 1b, the vertical force equilibrium equation can be derived as follows:

$$W = N_z + S_z = N\ cos(\gamma_z) + \left[\frac{(N - u\ A)tan(\phi)}{F_S} + \frac{cA}{F_S}\right]sin(\theta) \tag{1}$$

where N_z and S_z are the vertical components of the total normal force and shear force at the base, A is the area of the base slip surface, c is the cohesion, ϕ is the friction angle, u is the pore pressure at the base center, γ_z is the angle between normal force and vertical axis, and θ is the inclination of soil column base in direction of motion. Then, normal force, N, can be derived as follows:

$$N = \frac{W - c\ A\ sin(\alpha_y)/F_S + u\ A\ tan(\phi)sin(\alpha_y)/F_S}{m_\theta} \tag{2}$$

where

$$m_\theta = cos(\gamma_z)\left[1 + \frac{sin(\alpha_y)tan(\phi)}{F_S cos(\gamma_z)}\right] \tag{3}$$

The area of the soil column base can be calculated using Δ_x and Δ_y, and apparent dip angles, α_x and α_y, as follows:

$$A = \Delta_x \Delta_y \frac{\left(1 - sin^2(\alpha_x)sin^2(\alpha_y)\right)^{1/2}}{cos(\alpha_x)cos(\alpha_y)} \tag{4}$$

The angle between normal force, N, and vertical axis can be calculated by the following equation:

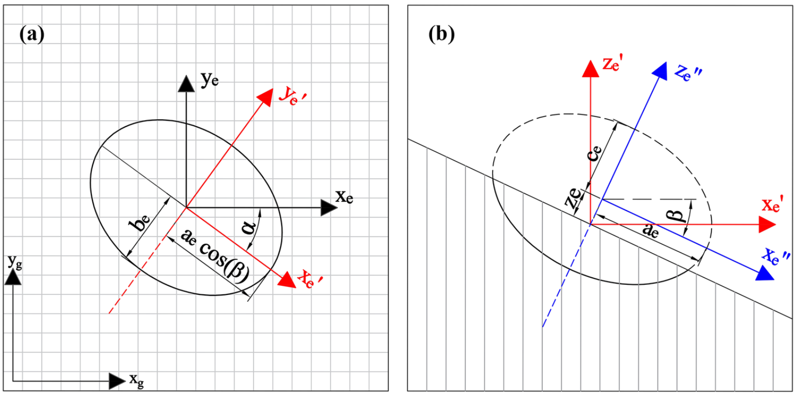

Fig. 2 (**a**) Plane view and (**b**) side view of the 3D ellipsoidal sliding surface

$$cos\left(\gamma_z\right) = \left[\frac{1}{tan^2\left(\alpha_y\right) + tan^2\left(\alpha_x\right) + 1}\right]^{1/2} \tag{5}$$

For the entire sliding volume divided into j number of soil columns, the moment equilibrium equation can be expressed as follows:

$$\sum_{i=1}^{j}\left(N_i - u_iA_i\right)\frac{tan\left(\phi_i\right)}{F_S} + \frac{c_iA_i}{F_S} = \sum_{i=1}^{j} W_isin(\alpha_{y,i}) \tag{6}$$

Then, the F_S can be derived by using the equilibrium equation (Eq. 1) and normal force equation (Eq. 2):

$$F_S = \sum_{i=1}^{j}\frac{\left[\left(W_i - u_iA_icos\left(\gamma_{z,i}\right)\right)tan\left(\phi_i\right) + c_iA_icos\left(\gamma_{z,i}\right)\right]}{m_{\theta,i}} \bullet \left(\sum_{i=1}^{j} W_isin\left(\alpha_{y,i}\right)\right)^{-1} \tag{7}$$

The above equation is implicit in F_S, and this requires one to solve the equation iteratively for F_S. The details can be seen in Hungr (1987).

The hydrological model

In the 3DPLS model, Iverson's linearized solution of the Richard equation for tension-saturated soils (Iverson 2000) is employed in the hydrological model to calculate pore pressure changes. The time-dependent pressure head, $\psi(t, y)$, at a given depth, y, and time, t, composed of a long-term head response (steady component), $\psi_0(y)$, and a short-term head response (transient component), $\psi_1\left(t, y\right)$, is as follows:

$$\psi(t, y) = \psi_0(y) + \psi_1\left(t, y\right) \tag{8}$$

The steady component, $\psi_0(y)$, is defined as a linear function of y with respect to the initial groundwater depth, H_W, assuming slope-parallel flow with a background infiltration rate, I_Z:

$$\frac{\psi_0\left(y\right)}{y} = \left(1 - \frac{H_w}{y}\right)\beta \tag{9}$$

where β is a constant calculated as follows:

$$\beta = cos^2\alpha - \left(\frac{I_Z}{K_s}\right)_{steady} \tag{10}$$

where α is the slope angle in degrees, K_s is the saturated permeability. The transient component is based on the reduced form of the Richard equation assuming tension saturation with a saturated coefficient of permeability:

$$\frac{\partial\psi_1}{\partial t} = D_0cos^2\theta\frac{\partial\psi_1^2}{\partial y^2} \tag{11}$$

where D_0 is the maximum diffusivity observed when the soil becomes saturated. Solving the above equation with the boundary conditions defined in Iverson (2000) results in:

$$\frac{\psi_1(t^*)}{y} = \begin{cases} \frac{I_y}{K_s}R(t^*) & ,0 \le t^* \le T^* \\ \frac{I_y}{K_s}[R(t^*) - R(t^* - T^*)] \;, & t^* > T^* \end{cases} \tag{12}$$

where I_y is the precipitation (surface flux), t^* is normalized time, T^* is the normalized duration of the precipitation, and R is the response function. These parameters are determined as follows:

$$t^* = \frac{t}{y^2/D} \tag{13}$$

$$T^* = \frac{T}{y^2/D} \tag{14}$$

$$R(t^*) = \sqrt{t^*/_\pi}exp\left(-\frac{1}{t^*}\right) - erfc\left(\frac{1}{\sqrt{t}}\right) \tag{15}$$

where $D = 4D_0cos^2\alpha$ is an effective hydraulic diffusivity and erfc is the complementary error function. As the abovementioned model may result in unrealistic pressure heads at shallow depths, calculated pressure heads are restricted by specifying that it cannot exceed the β-line calculated by $\psi = y\beta$ as stated in Iverson (2000). The details and the limitations of Iverson's linearized solution of the Richard equation can be seen in Iverson (2000).

The statistical framework

Soils exhibit heterogeneity and anisotropy in space due to varying deposition and formation processes in geological history. Composition, strength parameters, and physical and chemical properties can vary for the same soil type at the same site because of the inherent variability resulting from the randomness of geological processes. The soil properties display variability through space, and a continuous random field model is often used to model it. The spatial variability of the model parameter is defined by a covariance function to account for spatial dependence of the parameter and a pdf to describe the uncertainties in the parameter.

In the 3DPLS model, the variability of the model parameters is modeled in the horizontal directions with two-dimensional Gaussian and lognormal random fields. The variability in the vertical direction is not modeled for simplicity. As it is relatively straightforward to transform a lognormal random field to a Gaussian random field, the Gaussian random field is only explained here. A Gaussian random field of a model parameter, $\boldsymbol{X} = \left[X(l_1), \ldots, X(l_k)\right]^T$, where the set of values, $l = \left[l_1, \ldots, l_k\right]^T$, represent the spatial coordinates, defines the joint pdf of $\boldsymbol{X}$ as a multivariate normal pdf, $f_X(\boldsymbol{X})$:

$$f_X(\boldsymbol{X}) = \frac{1}{(2\pi)^{k/2}|\mathbf{C}|^{1/2}}exp\left\{-\frac{1}{2}(\boldsymbol{X} - \boldsymbol{\mu})^T\boldsymbol{C}^{-1}(\boldsymbol{X} - \boldsymbol{\mu})\right\} \tag{16}$$

where μ is the mean values of the random field, $\boldsymbol{\mu} = \left[\boldsymbol{\mu}(\boldsymbol{l}_1), \ldots, \boldsymbol{\mu}(\boldsymbol{l}_k)\right]^T$, $\boldsymbol{C}$ is the covariance matrix, and k is the number of elements in $\mathbf{X}$. The elements of the covariance matrix, $\boldsymbol{C}$, are expresses as:

$$C_{mn}\left(l_m, l_n\right) = \begin{cases} \sigma^2\left(l_m\right) & ,m = n \\ \sigma\left(l_m\right)\sigma\left(l_n\right)\rho\left(l_m, l_n\right) & ,m \ne n \end{cases} \tag{17}$$

where $\sigma(l_m)$ is the standard deviation of the parameter at coordinate l_m and $\rho\left(l_m, l_n\right)$ is the correlation coefficient between parameters at coordinates l_m and l_n. Depending on the problem size, either the two-dimensional ellipsoidal autocorrelation function (Eq. 18) or the two-dimensional separable Markov autocorrelation functions (Eq. 19) has been employed:

$$\rho(l_m, l_n) = exp\left\{-2\sqrt{\left(\frac{\tau_x}{l_x}\right)^2 + \left(\frac{\tau_y}{l_y}\right)^2}\right\} \tag{18}$$

$$\rho(l_m, l_n) = exp\left\{-2\left(\frac{\tau_x}{l_x}\right) - 2\left(\frac{\tau_y}{l_y}\right)\right\} = exp\left\{-2\left(\frac{\tau_x}{l_x}\right)\right\}exp\left\{-2\left(\frac{\tau_y}{l_y}\right)\right\} \tag{19}$$

where τ_x and τ_y are separation distances between coordinates l_m and l_n and l_x and l_y are spatial correlation lengths in the direction of x and y, respectively.

To generate random fields, the covariance matrix decomposition method (Fenton and Griffiths 2008) with the ellipsoidal autocorrelation function is utilized for problems with a low number of elements. The soil property, $\boldsymbol{X}$, at k locations can be obtained as:

$$\boldsymbol{C} = \boldsymbol{L}\boldsymbol{L}^T \tag{20}$$

$$\boldsymbol{X} = \boldsymbol{L}\boldsymbol{U} \tag{21}$$

where $\boldsymbol{L}_{k\times k}$ is the lower triangle matrix obtained by the Cholesky decomposition method and $\boldsymbol{U}_{k\times 1}$ is a vector of Gaussian random variables with zero mean and unit variance.

The computational time and required memory space to generate correlation matrices and Cholesky decomposition can be demanding as the number of elements in the problem increases (e.g., 50×50). To overcome this issue, the stepwise covariance matrix decomposition method proposed by Li et al. (2019) is implemented in two-dimensional random field generation. The stepwise matrix decomposition method uses a separable autocorrelation function (Eq. 19) which allows the method to disassemble the correlation matrix, $\boldsymbol{R}$, into the number of dimensions used in the problem:

$$\boldsymbol{R} = \boldsymbol{R}_y \otimes \boldsymbol{R}_x \tag{22}$$

where $\boldsymbol{R}_x$ and $\boldsymbol{R}_y$ are the one-dimensional correlation matrices in x and y directions and ⊗ is the Kronecker product. Similarly, the lower triangle matrix, $\boldsymbol{L}$, can be written as:

$$\boldsymbol{L} = \boldsymbol{L}_y \otimes \boldsymbol{L}_x \tag{23}$$

where $\boldsymbol{L}_x$ and $\boldsymbol{L}_y$ are the lower triangle matrices in x and y directions satisfying $\boldsymbol{L}_x\boldsymbol{L}_x^T = \boldsymbol{R}_x$ and $\boldsymbol{L}_y\boldsymbol{L}_y^T = \boldsymbol{R}_y$. Then, using the matrix-array multiplication operations, Eq. 21 can be rewritten as:

$$\boldsymbol{X} = \boldsymbol{L}_x\boldsymbol{U}\boldsymbol{L}_y^T \tag{24}$$

The method reduces the computational time and required memory space significantly. The details of the stepwise covariance decomposition method can be seen in Li et al. (2019). In the present study, the stepwise covariance matrix decomposition method was implemented when the number of the elements of the problem exceeds a limit causing unfeasible run time (e.g., more than 500 elements).

The 3DPLS model propagates uncertainties from the spatially variable model parameters to the model output in terms of F_S. The 3DPLS model is relatively flexible and can be coupled with a wide range of methods for uncertainty quantification (e.g., Monte Carlo, Importance Sampling). For simplicity, the 3DPLS model was coupled with the Monte Carlo method in this study due to its robustness and straightforward implementation. The 3DPLS model conducts a series of slope stability analyses, in which the values of model parameters are randomly selected based on realizations from statistical models of spatially variable properties (e.g., random fields). The result of the Monte Carlo analysis is a set of F_S values that are statistically analyzed to evaluate the resulting uncertainty in model predictions by calculating modes (e.g., mean, standard deviation) or estimating failure probability. The probability of failure, P_f, for each cell individually is calculated as follows:

$$P_f = P(F_S \leq 1.0) = \frac{1}{N_S}\sum_{i=1}^{N_S} I(F_{S,i} - 1.0) \tag{25}$$

where N_S is the number of simulations, $F_{S,i}$ is the factor of safety of ith simulation, and I is the indicator function providing 1 in case of failure, when $F_{S,i} \leq 1$, otherwise 0.

Validation of the 3DPLS model

Validation of the slope stability model

The performance of the slope stability model on evaluating the F_S of slopes has been tested using three validation problems, all of which feature homogeneous model parameters in space. The first validation problem (Fig. 3a, d) involves a spherical sliding surface in a purely cohesive slope with a 2:1 inclination. In Fig. 3a, R is the radius of the sphere centered 0.5 R above the ground surface. The 3D F_S was calculated as 1.402 by using the closed-form solution proposed by Baligh and Azzouz (1975) and Gens et al. (1988). Using the developed 3DPLS model, the computed 3D F_S ranged from 1.386 to 1.471 depending on the refinement of the sliding volume. In Table 1, the F_S values reported for the validation problem by various researchers are provided for comparison.

The second validation study was conducted on a spherical sliding surface in a $c' - \phi'$slope (Fig. 3b, e) reported in the study of Hungr et al. (1989). In the 3DPLS model, the center of the ellipsoidal sliding surface is introduced with an offset perpendicular to the ground surface. Therefore, it is not possible to introduce the center of the sliding surface shown in Fig. 3b. With a small modification to the proposed model, the center could be defined, and the 3D F_S was calculated as 1.207 using a cell size of 0.01 m. In Table 1, the corresponding 3D F_S values reported in the literature are given.

The third validation problem is the example from Fredlund and Krahn (1977), shown in Fig. 3c and f. The problem has been used by many researchers (Xing 1988; Hungr et al. 1989; Lam and Fredlund 1993; Huang et al. 2002; Xie et al. 2006; Griffiths and Marquez 2007; Mergili et al. 2014b) to verify their proposed 3D models. This validation problem has been investigated for two sliding surfaces shown in Fig. 3f, spherical sliding surface in pure homogeneous drained material (Slip-1) and composite sliding surface due to the existence of a weak layer (Slip-2). Slip-1 without water table and Slip-2 with/without water table were analyzed by using the 3DPLS model. The pore pressures were calculated assuming hydrostatic conditions for the soil columns with a sliding surface below the water table. Negative pore pressure, i.e., suction, was ignored. The composite sliding surface, Slip-2, was obtained by assigning the maximum depth at the level of

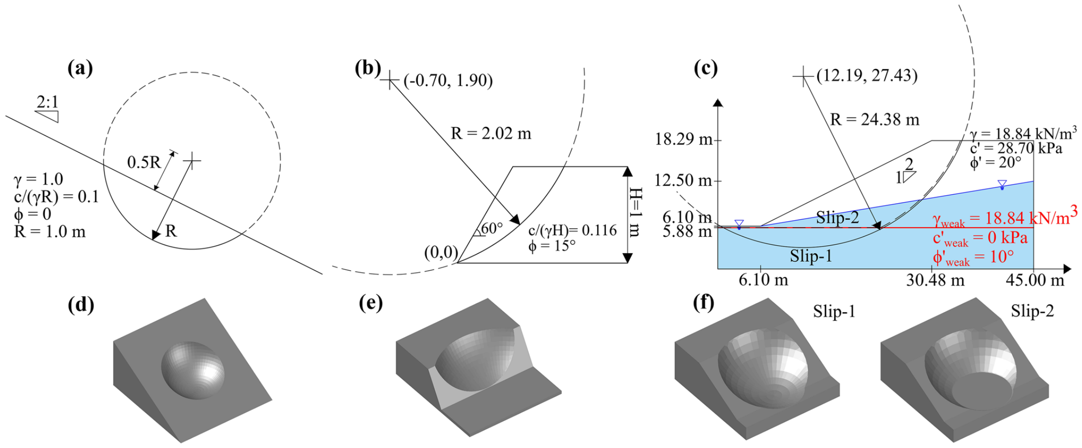

Fig. 3 (**a**) Validation problem – 1: spherical sliding surface in purely cohesive slope; (**b**) validation problem – 2: spherical sliding surface in $c' - \phi'$ slope; and (**c**) validation problem – 3: the problem from Fredlund and Krahn (1977); (**a**, **b**, **c**) 2D center section and (**d**, **e**, **f**) 3D view

the weak layer. Then, the soil columns were truncated when the sliding spherical surface is below the weak layer, and the slope is assigned as zero to those truncated cells instead of surface slopes as originally implemented in the 3DPLS model. In the current study, the 3D F_S yielded 2.276 for Slip-1 without water table, 1.769 for Slip-2 without water table, and 1.692 for Slip-2 with the water table. Table 1 provides the results of the present study and the 3D F_S values obtained by other researchers.

From Table 1, it can be seen that the 3DPLS model results are within the range reported in the literature for the abovementioned three relatively simple validation problems with slight differences. These differences are attributed to the assumption in the models and the level of discretization.

Validation of the model capacity to capture the effects of spatial variability

In this study, the capacity of the 3DPLS model to capture the effect of spatial variability on slope stability has been validated with an extensive study in the finite element method (FEM) based program, PLAXIS. Throughout this paper, the 3DPLS model will be compared with its equivalent cell-based model utilizing the same hydrological model and the statistical framework as the proposed model does, but employing widely used infinite slope stability method on a cell-by-cell basis (e.g., Griffiths et al. 2011). In the infinite slope stability method, the F_S is calculated at maximum depth for each cell using the pore pressure values obtained from the hydrological model. Additionally, for the cells with low slope angle, i.e., flat zones, the

Table 1 Comparison of the 3D F_S values reported by various researchers for the validation problems

Reference	Validation problem – 1	Validation problem – 2	Validation problem – 3[a]		
			Slip-1 (dry)	Slip-2 (dry)	Slip-2 (wet)
Baligh and Azzouz (1975) Gens et al. (1988)	1.402	-	-	-	-
Xing (1988)	-	-	2.122	1.548	1.441
Hungr et al. (1989)	-	1.23	-	1.62	1.54
Lam and Fredlund (1993)	1.386–1.472	-	-	1.534–1.607	1.447–1.511
Huang et al. (2002)	1.379–1.412	1.204–1.243	2.072–2.215	1.645–1.757	
Xie et al. (2006)	1.251–1.455	1.180–1.222	2.043–2.302	1.609–1.711	1.485–1.620
Griffiths and Marques (2007)[b]	1.39	-	-	-	-
Mergili et al. (2014a)	1.35–1.43	1.19	2.03	1.58	1.53
Present study (3DPLS)	**1.386–1.471**	**1.207**	**2.276**	**1.769**	**1.692**

[a] Dry: without groundwater table, wet: with groundwater table.

[b] Finite element method.

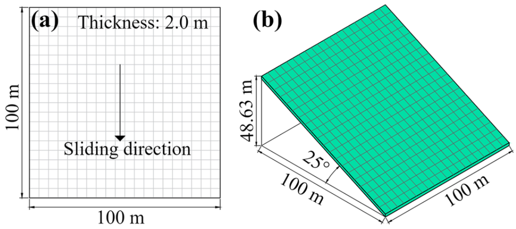

Fig. 4 Simplified validation problem geometry, (**a**) plane view and (**b**) side view

F_S values are limited at 10.0 to prevent possible confusion of the results. The analyses with the infinite slope stability method will be called the "Cell-based model" hereafter.

A simplified case, with a domain of $100 \times 100m$ with 25° inclination, was examined. The thickness of the soil is 2 m with a groundwater table at the ground surface. The domain is discretized into a grid of 20×20 equally sized cells (cell size of 5 m) as shown in Fig. 4. The parametric study has been conducted for both drained (effective stress-based) and undrained (total stress-based) cases with three variability levels: low, moderate, and high. Table 0 shows the parameters used for the validation problem in both drained and undrained cases. In the analyses, the saturated unit weight of soil and the unit weight of water were employed as 20 kPa and 10 kPa, respectively. In the drained case, a slope parallel groundwater flow was modeled, while total stress analysis was performed for the undrained case. The saturated permeability was assigned as $1 \bullet 10^{-6}$ m/s.

The two-dimensional Gaussian random field model was employed to generate random fields for soil strength parameters, c' and ϕ' in the drained case and S_u in the undrained case. Spatial dependence was modeled using the two-dimensional ellipsoidal autocorrelation function (Eq. 18) with a spatial correlation length, l, ranged between 0 and 1000 m. The spatial correlation length of 0 m means no spatial dependence across the study domain. As the spatial correlation length increases, the spatial dependence among the parameters increases. The spatial correlation length of 1000 m is used as an upper limit where the soil approaches homogeneous conditions over the 100 m × 100 m study domain. The spatial correlation length was assumed to be equal in both directions, i.e., $l_x = l_y$. Analyses were conducted for a range of coefficient of variation, CoV, values with 1000 random field realizations for each combination of correlation lengths and CoV values.

There exists a trade-off between the mesh size and the run time for each simulation in the FEM model. Due to a large number of simulations (1000 Monte Carlo simulations for each correlation length for each variability level for both drained and undrained cases; 48,000 simulations in total), the mesh size was optimized considering the convergence of the F_S values and the run time.

In the 3DPLS model, the lengths of three principal semi-axes that define the ellipsoid were assumed to be $20 \times 20 \times 2m$ without any offset from the ground surface, i.e., $z_e = 0$. The aspect of the motion, α, was assigned to be 90° as the sliding was through the downslope direction. The inclination of the ellipsoid in the direction of motion, β, was assigned as 25° as the slope is constant over the problem domain. In the 3DPLS model analyses, the problem domain was extended so that the ellipsoidal sliding surfaces placed close to the boundaries would not be truncated at the sides. Then, the F_S values within the original problem domain were employed in the performance assessment. In the Cell-based model, the calculations are carried out per each cell individually, and therefore, no extension was needed.

The landslide initiation process is a complex process including the formation of the initial weak zone and its propagation prior to landsliding. A thin zone of intense shearing, i.e., shear band, starts to propagate as the initial weak zone is not able to resist the driving load. Then, the driving load exceeding the capacity of the initial weak zone is distributed to the surrounding neighboring initially stable zones. If the neighboring zones cannot withstand this additional load transferred from the initial weak zone, the shear band propagates. Then, the propagation of the shear band might stop if the excess driving load is compensated by the surrounding neighboring zones; otherwise, it leads to the landslide initiation with the movement of upper soil on the shear band. In addition to the complex processes of load distribution and shear band propagation, the presence of soil heterogeneity adds another complexity to the shear band propagation. That is, the shear band tends to propagate along the weakest path with low capacity to withstand the additional loading.

Without the consideration of these complex processes involved in the landslide initiation, relating the predictions of the cell-based physical-based models to a single F_S representing the whole simplified validation problem, that is called the global factor of safety, F_S^g, is quite challenging. In the FEM analyses, the load distributions and the propagation processes are explicitly satisfied, and therefore, reliable and consistent F_S^g can be obtained directly from analyses, i.e., $F_{S,FEM}^g = F_{S,FEM}$. However, the physical-based limit equilibrium models do not consider these complex processes included in the landslide initiation. Thus, approximate approaches are required here to relate the F_S values over the problem domain, $\{F_{Si}, i = 1, \ldots, n\}$, to the F_S^g where n is the number of cells in the discretized problem domain. In Fenton and Griffiths (2008), the harmonic average was empirically demonstrated to be best suited to characterize the

Table 2 Simplified validation problem parameters for both drained and undrained cases

			CoV levels				
Case	Parameter	Mean	Low	Moderate	High	Distribution	Correlation length (m)
Drained	Cohesion, c′ (kPa)	6	0.10	0.20	0.30	Lognormal	0, 10, 20, 50, 100, 200, 500, 1000
	Friction angle, φ′ (°)	40	0.05	0.10	0.15	Normal	
Undrained	Shear strength, S_u (kPa)	40	0.10	0.20	0.30	Lognormal	

effects of heterogeneity. This was explained by the harmonic average being dominated by the low values similar to the tendency of shear band propagation being along the weak zones.

In the Cell-based model, the F_S values are calculated for each cell individually. Therefore, the F_S^g is assumed to be related to the harmonic average of the F_S values of the cells $\{F_{Si}, i = 1, \ldots, n\}$ over the problem domain based on the empirical observations (Fenton and Griffiths 2008):

$$F^g_{S,Cell-based} = H\left[F_{Si} : i = 1, \ldots, n\right] = \left[\frac{\sum_{i=1}^{n} F_{Si}}{n}\right]^{-1} \tag{26}$$

In the 3DPLS model, the F_S is calculated over an ellipsoidal sliding surface including spatially varying strength parameters inside. The F_S of a cell represents the most critical ellipsoidal sliding surface intersecting that cell. Therefore, the F_S^g is related to the minimum F_S, $F_{S,min}$ over the problem domain that represents the most critical ellipsoidal sliding surface with the lowest safety for the entire model:

$$F^g_{S,3DPLS} = min\left[F_{Si} : i = 1, \ldots, n\right] \tag{27}$$

Then, the mean global factor of safety, μ_g, is calculated by averaging the F_S^g values of 1000 Monte Carlo simulations for comparison of the models.

Both deterministic and probabilistic analyses were conducted for the simplified validation problem to validate the capacity of the 3DPLS model to capture the effect of spatial variability on slope stability. In the deterministic analyses, the soil is assumed homogeneous over the problem domain, and the mean values are employed only. In the probabilistic analyses, the shear strength parameters shown in Table 0 are treated as random variables.

Table 3 presents the deterministic results of the simplified validation problem for the FEM, Cell-based, and 3DPLS models. The deterministic model results show that the 3DPLS model results in higher F_S for both drained and undrained cases compared to the Cell-based model.

Table 3 Deterministic model results for the simplified validation problem for both drained and undrained cases

Model	Drained case	Undrained case
FEM	1.22	2.73
Cell-based	1.29	2.61
3DPLS	1.34	2.69

Figure 5 presents the results of the probabilistic analyses on the effects of spatial variability on the μ_g for drained case in Fig. 5a and b and undrained case in Fig. 5c and d. The FEM model results are compared with the Cell-based model results in Fig. 5a and c and with the 3DPLS model results in Fig. 5b and d. The FEM results indicate that the μ_g are higher where there exists no spatial dependence over the problem domain, i.e., 0 m correlation length. It is less likely that there will be large weak zones due to a lack of spatial dependence. As the correlation length increases up to a value of 50 m, the μ_g decreases significantly for both drained and undrained cases. This is due to the weak zones having a larger spatial extent and low capacity to withstand driving loading. That is, there is a higher probability of having a weak zone which can lead to a local failure and a lower F_S. Further increase of correlation length from 50 up to 1000 m causes an increase in the μ_g as the model becomes more homogeneous over space. That is, with high correlation lengths, the F_S is no longer dominated by local weak zones; eventually, this leads to high F_S values.

In addition to the effect of correlation length, the effect of variability level can be also seen in Fig. 5. The FEM model results show that as the variability level increases from low level to high level, the μ_g decreases except for 0 m correlation length. That is, high variability level results in higher μ_g when the correlation length is zero. This is attributed to the weak zones having neighboring zones with higher shear strength values due to the high variability level. Nevertheless, the main trend is that μ_g decreases with increasing variability level. In addition, it can be observed that the effect of variability level decreases as the correlation length increases.

The comparison of the FEM model and the Cell-based model results in Fig. 5a and c shows that the Cell-based model results are not in agreement with the FEM model results. As the undrained case has only one parameter treated as a variable, the effect of variability level on the μ_g and the increase in the μ_g with the increase in correlation length can be observed. For the drained case, the results do not vary significantly. As the calculations are performed for each cell individually, the effect of weak zones leading to local failure is not captured by the Cell-based model. Therefore, the Cell-based model is not able to capture the effect of spatial variability on the μ_g.

When comparing the FEM model and the 3DPLS model results in Fig. 5b and d, it can be detected that the trends in both methods are similar. The μ_g starts with a high value when the correlation length is 0 m. Then, the increase in correlation length up to 50 m causes local failures to dominate the F_S^g and leading to lower μ_g. When the correlation length increases from 50 to 1000 m, the parameters over the problem domain become more homogeneous, and local failures stop dominating the F_S^g. When there is no spatial dependence, i.e., 0 m correlation length, the FEM model results in higher μ_g values for high variability level but not the 3DPLS model. This is attributed to that the 3DPLS model does not explicitly model the landslide initiation process. The effect of variability level, i.e., the decrease in μ_g with the increase of variability level, is the same for both models. Needless to say, there is no perfect fit in the results due to the FEM model involving all processes explicitly, and the 3DPLS model being a simplified soil-column-based limit equilibrium model. Besides, the lengths of three principal semi-axes were assumed to be $20 \times 20 \times 2m$ in the 3DPLS model. A better fit can be obtained by changing the dimensions of the ellipsoid. However, the main aim here is to show the capacity of the 3DPLS model to capture the effect of spatial variability on slope stability not the perfect fit in the results.

Case study: "Kvam landslides"

The performance of the 3DPLS model, capable of accounting for the spatial variability of soil parameters in landslide susceptibility assessment, will be tested on the Kvam landslides that took place in 2011. For the comparison purpose, the analyses were also conducted with the Cell-based model utilizing the same hydrological model to

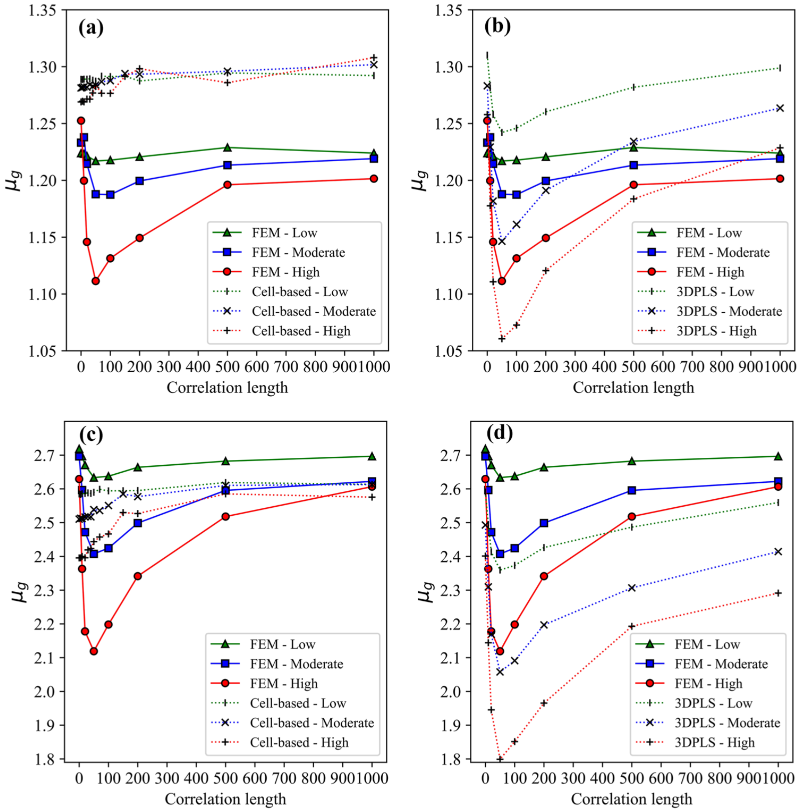

Fig. 5 The effect of spatial variability on the mean global factor of safety, μ_g: the FEM model results for the drained case (**a**) with the Cell-based model results, and (**b**) with the 3DPLS model results, and for the undrained case (**c**) with the Cell-based model results, and (**d**) with the 3DPLS model results

calculate the pore pressure build-up due to rainfall infiltration and employing an infinite slope stability model to calculate F_S value for each cell individually.

In the 3DPLS model, the values of the ellipsoid dimensions were determined by considering the observations of previous landslides. The lengths of three principal semi-axes were selected as $100 \times 20 \times 2.5m$ without any offset from the ground surface. The aspect of the motion, α, was assigned to be zero considering the aspect of the study area being dominantly in the direction of east. The inclination of the ellipsoid in the direction of motion, β, was calculated by taking the average slope over a rectangular zone $(2a_e \times 2b_e)$ located at the center of the ellipsoid.

Study area

Kvam is a village in central southern Norway, situated along the Gudbrandsdalslågen River, within the Gudbrandsdalen Valley. The valley has been re-shaped by glaciers, featuring steep edges covered with glacial deposits, during the Quaternary period. Based on the available geological quaternary map (NGU 2020), the materials present at the terrain surrounding Kvam are classified as moraine, glaciofluvial deposits, fluvial deposits, humus/peat cover, and sub-cropping bedrock (Fig. 6). The valley is characterized by fluvial deposits at the base and by moraine cover at the hillsides. Above the zone covered by moraine material, there exists sub-cropping bedrock with a thin layer of humus and peat.

The area surrounding the Kvam has high landslide susceptibility as the landslide scars are visible on the hillsides mainly in the moraine type geological unit as shown in Fig. 6. This study will focus on the shallow landslides that occurred following the rainfall event in 2011 (Fig. 9) causing multiple landslides in the valley and the flooding of the village. For the detailed study, the study area shown in Fig. 6 is selected as the landslides following the rainfall event in 2011 concentrated inside the selected zone (0.57 km^2). The average slope of the study area is 26.20° with a maximum value of 45.71°.

Aerial photos in Fig. 7 show the studied area in Kvam before the rainfall event in 2010 and after the event in 2011. From Fig. 7a, it can be observed that the hillside is covered by dense vegetation with the existence of channels through the slope. After the rainfall event in 2011, several shallow landslides occur in the studied zones as shown in Fig. 7b. The landslide initiation and runout zones were identified considering high-resolution aerial pictures and orthophotos (Schilirò et al. 2021). The runout zones were not included as the 3DPLS model cannot model the post-failure behavior of the sliding mass. Then, the landslide initiation zones are discretized with respect to the DEM discretization as shown in Fig. 8.

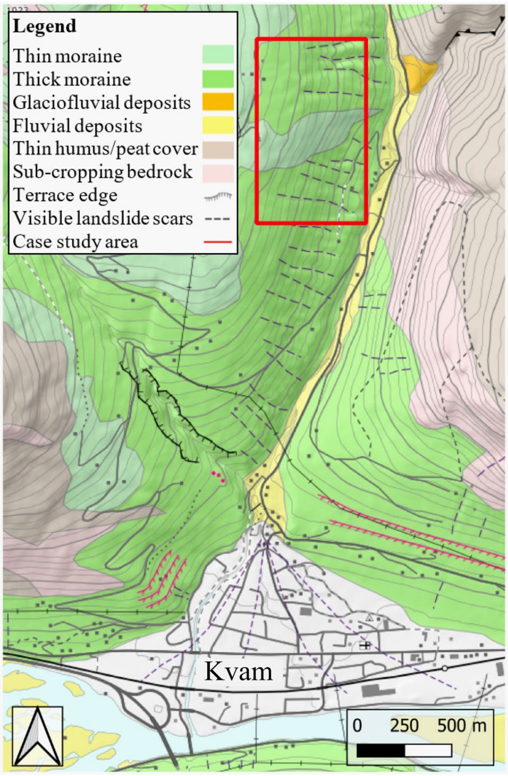

Fig. 6 Study area location and quaternary map of the terrain surrounding Kvam (NGU 2020)

Between June 9 and 10 in 2011, the Kvam area receives total precipitation of 61.72 mm/day as presented in Fig. 9. Hourly precipitation amounts are presented within the period of 24 h starting from the beginning of the rainfall event on 9 of June, with the averaged value of $\overline{I_Z} = 2.572$ mm/h. In the analyses, the average value of precipitation over the 24-h period was used to simplify the implementation of the developed model. The rainfall is assumed to be constant over the study area. The background infiltration rate, $(I_Z)_{steady}$, was obtained from the Norwegian Water Resources and Energy Directorate (NVE) as the average inflow (source: nve.no).

Digital elevation model (DEM) with a resolution of 10 m was obtained from hoydedata.no and utilized for the application of the model. The slope and aspect were derived using the DEM. The thickness of the soil, i.e., depth to bedrock, Z_{max}, was calculated using an empirical relationship between the soil thickness and the tangent of the slope angle in degrees, tan(δ), derived based on the field data from Holm (2012) and Edvardsen (2013). The empirical equation was utilized as follows:

$$Z_{max} = \max\{Z_{min}, \mu_Z\} \quad (28)$$

$$\mu_Z = -2.578 \cdot \tan(\delta) + 2.612 \quad (29)$$

where Z_{min} is the minimum thickness and μ_Z is the mean defined with a linear trend function. Based on the field data, the minimum thickness was assigned as 0.4 m to represent surficial cover at the steep slopes. Considering the estimated thickness of the water table and the degree of saturation according to the gridded water balance model of NVE-Xgeo (source: xgeo.no), the groundwater table was assumed to be at half of the thickness of soil at each cell.

The model parameters are provided in Table 4. Due to the lack of field investigations and laboratory tests, the values in Table 4 are selected from literature sources for the considered moraine type geological unit. Only soil strength parameters, cohesion, and friction angle were treated as random variables, and the others were kept constant at their mean value (i.e., treated as deterministic). The normal and lognormal random field models were employed for the friction angle and cohesion, respectively. In the analyses, the saturated soil unit weight of 20 kPa was employed with a 10 kPa unit weight of water. The random fields were created according to the DEM discretization of the studied area in the Kvam area by using the two-dimensional separable Markov autocorrelation function shown in (Eq. 19). Correlation length was assumed to be equal in both horizontal directions with a value of 50.0 m for both cohesion and friction angle considering the values reported in Phoon and Kulhawy (1999).

Results and discussion

The studied area in the Kvam area was analyzed by the 3DPLS model and the Cell-based model. Both models performed 1000 Monte Carlo simulations while accounting for the spatial variability of soil strength parameters. The results include the mean factor of safety, μ_{F_S}, and probability of failure, P_f, maps of the study area before and after the rainfall event shown in Fig. 9, for both models separately. The comparison of the models is done by using the metrics in the confusion matrix shown in Fig. 12 and the receiver operating characteristic (ROC) graph (e.g., Baum et al. 2010; Mergili et al. 2014b; Raia et al. 2014).

Figure 10 presents the μ_{F_S} map of the studied area for the 3DPLS model in Fig. 10a and b and for the Cell-based model in Fig. 10c and d. The results are presented for the study area before (Fig. 10a, c) and after (Fig. 10b, d) the rainfall event. From Fig. 10a and b, it can be observed that the 3DPLS model smooths the transition of the F_S values that are calculated for an ellipsoidal sliding surface. In the Cell-based model, however, the calculations are performed on a cell-by-cell basis, and therefore, there are rapid transitions between F_S values over the study area (Fig. 10c, d). For both models, the μ_{F_S} values are higher than unity. Comparison of Fig. 10b and Fig. 10d shows that more critical value of the μ_{F_S}, between 1.0 and 1.1, was obtained using the 3DPLS model for the study area after the rainfall event although 3D models are thought to provide higher F_S values. Similarly, Zhang et al. (2013) reported that 3D F_S might be less than the 2D F_S for specific conditions. One can also observe that the 3DPLS model results in a greater number of cells with F_S values closer to unity.

The results of the 1000 Monte Carlo simulations enable one to calculate the standard deviation of the F_S value, σ_{F_S}, for each cell. For flat zones, the σ_{F_S} values are almost zero for the 3DPLS model (~ 0.09) or even zero for the Cell-based model in which the F_S is restricted by 10.0 as an upper limit. Besides, the average σ_{F_S} values over the study area were calculated as 0.128 and 0.123 for the

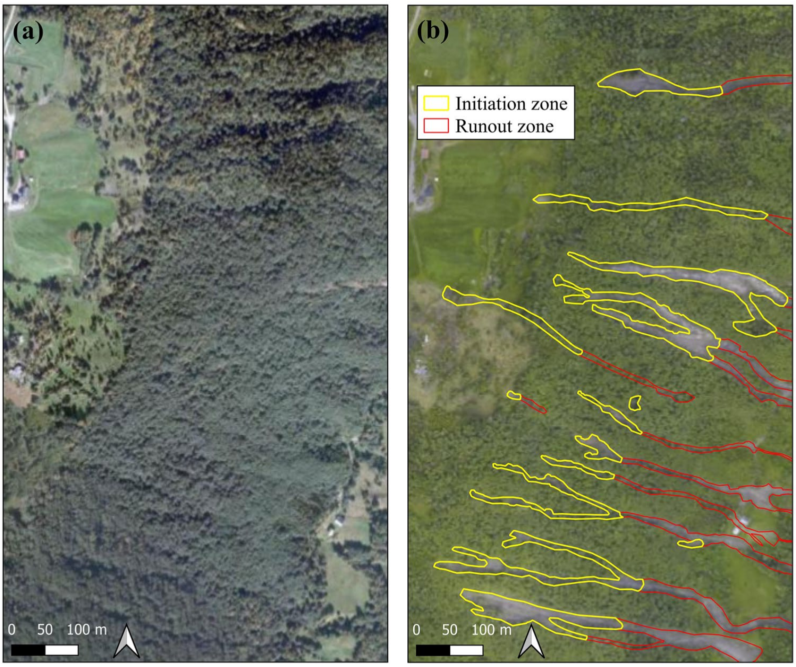

Fig. 7 Aerial photos of the study area in Kvam, (**a**) in 2010 and (**b**) in 2011 (source: norgeibilder.no)

3DPLS model before and after the rainfall event, respectively, while they were calculated as 0.312 and 0.306 for the Cell-based model. It is observed that the 3DPLD model results in less variability of F_S values, meaning more stable results. This is mainly due to the smoothing effect of the 3DPLS model, i.e., spatial averaging that occurs over the ellipsoidal failure surface.

Figure 11 shows the probability of failure, P_f (%) maps of the studied area before (Fig. 11a, c) and after (Fig. 11b, d) the rainfall event using the 3DPLS and Cell-based models. For the 3DPLS model, the values of P_f range from 0.0 to 8.8% before the rainfall event (Fig. 11a) and from 0.0 to 22.5% after the rainfall event (Fig. 11b). The ranges of P_f for the Cell-based model are 0.0–22.8% before the rainfall event (Fig. 11c) and 0.0–31.9% after the rainfall event (Fig. 11d). It has been detected that the Cell-based model

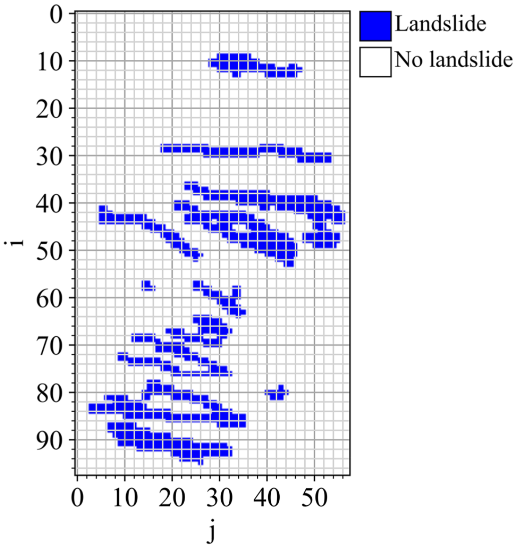

Fig. 8 DEM discretization of the study area in Kvam with the landslide initiation zones

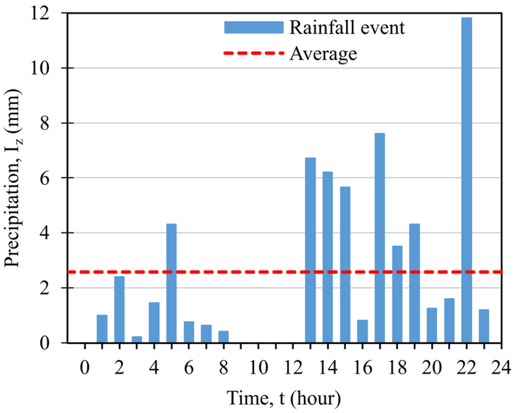

Fig. 9 Rainfall event between June 9 and 10, 2011

Table 4 Model parameters used in the case study analyses

Parameter	Distribution	Distribution parameters	
		μ	CoV
Depth to bedrock, Z_{max} (m)	-	$-2.578 \cdot \tan(\delta) + 2.612$	-
Cohesion, c (kPa)	Lognormal	4[a]	0.3[b]
Friction angle, φ (°)	Normal	32[a]	0.2[a]
Saturated permeability, K_S (m/s)	-	$1.0 \cdot 10^{-6}$[c]	-
Diffusivity, D_0 (m²/s)	-	$5.0 \cdot 10^{-6}$	-

Sources: [a]Melchiorre and Frattini (2012), [b]Lacasse and Nadim (1996), [c]Janbu (1989)

results in quite high P_f values, up to 22.8%, even before the rainfall event when the study area is stable. Figure 11a shows that the values of P_f before the rainfall are fairly low using the 3DPLS model. From Fig. 11c and Fig. 11d, one can observe that there exist sharp changes in the P_f values over the study area as the Cell-based model analyzes each cell individually without consideration of the neighboring zones. However, the F_S value is calculated for an ellipsoidal sliding surface in the 3DPLS model; i.e., a zone is analyzed instead of a single cell. Therefore, the transition of the P_f values in Fig. 11a and Fig. 11b is smoother.

If the results of a landslide susceptibility model can be converted to binary results, i.e., stable or unstable, the receiver operating characteristic (ROC) graph can be utilized to evaluate the performance of the model in predicting stable and unstable zones over the study area (Fawcett 2006). The model performance is measured, in this study, using the parameters in the confusion matrix (Fig. 12) calculated by comparing the model predictions and discretized landslide initiation map shown in Fig. 8. If a cell is predicted to be unstable by the model, and the field observation is consistent with the model prediction, it is considered as "true positive, TP". However, it is considered as "false positive, FP", if the cell is outside of the discretized landslide initiation zone. Similarly, if a cell is predicted as stable and the cell is outside of the discretized landslide initiation zone, it is a "true negative, TN". Otherwise, it is a "false negative, FN". Out of these four possible outcomes assigned to each cell, an additional set of parameters, namely "true positive rate, TPR", "false positive rate, FPR", "accuracy, AC", and "precision, PR", can be also calculated to assess the performance. The TPR is the proportion of the correctly predicted unstable cells inside the discretized landslide initiation zone to the total number of cells in the initiation zone (P) and calculated as $TPR = TP/P$ where $P = TP + FN$. The FPR is the ratio of cells predicted as unstable outside of the discretized landslide zone to the number of cells without landslide observation (N) and calculated as $FPR = FP/N$ where $N = FP + TN$. The ROC curve is plotted by using TPR and FPR as shown in Fig. 13. The upper left corner of the plot ($TPR = 1$ and $\text{FPR} = 0$) represents the perfect performance, and the diagonal line, or the reference line, represents the random classification or "no skill". As the prediction skill plotted on the ROC graph is closer to the upper left, the prediction capacity of the model is better. Another metric to assess the performance of the model is the AC that is the proportion of correctly predicted cells to the total number of cells and calculated as $AC = (TP + TN)/(P + N)$. In addition to AC, the metric PR represents how precise the model predicts the unstable cells and is calculated as $PR = TP/(TP + FP)$. Both AC and PR vary in the range of [0, 1] where a higher value means a better model performance of accuracy and precision.

In the literature, there exist both deterministic (e.g., TRIGRS, SHALSTAB) and probabilistic (e.g., SINMAP, GEOtop-FS, HIRESSS, TRIGRS-P) landslide susceptibility models providing the results mainly in terms of either F_S or P_f to assess the stable and unstable zones. In deterministic models, the stability of each cell is evaluated based on the value of F_S. That is, a cell is considered to be stable if $F_S > 1.0$ and unstable if $F_S < 1.0$. Unlike deterministic models, the probabilistic models might employ different assessment criteria to determine the stable and unstable zones. In the study of Rossi et al. (2013), a zone was considered to be unstable if a sub-zone has more than 1% area with a P_f higher than 80.0%. Different classification systems were also employed to assess the stability, such as the reliability index (Haneberg 2004) and the stability index (Michel et al. 2014). However, there are no widely recognized assessment criteria for the probabilistic models. In this study, the performance of the 3DPLS model has been evaluated by employing different levels of probability limits, $P_{f,limit}$, to estimate landslide stability such that a cell is considered as stable if the $P_f < P_{f,limit}$ and unstable if $P_f > P_{f,limit}$.

As the values of P_f obtained by the 3DPLS model and the Cell-based model are relatively low due to utilizing the model parameters from literature (Table 4) and the bias in the model itself, lower values of $P_{f,limit}$ were employed for the comparison. For different $P_{f,limit}$ values from 2.5 to 15.0%, the P_f results were converted to binary values, i.e., stable or unstable, and the metrics in Fig. 12 were calculated. Figure 13 shows the ROC curves of the 3DPLS and the Cell-based models using different $P_{f,limit}$ values. The metrics such as TPR, FPR, AC, and PR are tabulated in Table 5 for each $P_{f,limit}$ value for both models. In the ROC graph, a point has better performance than the other if the TPR value is higher and FPR is lower. From both Table 5 and Fig. 13, it can be detected that the TPR values of the Cell-based model are higher than that of 3DPLS for each $P_{f,limit}$, but the FPR values are also very high. This means that the Cell-based model overpredicts the spatial extend of the unstable zones, and therefore, the Cell-based model can predict nearly all cells of the landslide but with a high FPR. The performance of the models can be compared by the ratio of TPR/FPR. The larger the ratio, the better the model performance is (e.g., Baum et al. 2010). The 3DPLS model has a higher ratio of TPR/FPR than the Cell-based model for all values of $P_{f,limit}$. This indicates that the performance of the 3DPLS model is better although it has lower TPR. From Table 5, it

Fig. 10 Mean factor of safety, μ_{F_S}, map of the study area: (**a**) before and (**b**) after the rainfall event using the 3DPLS model; (**c**) before and (**d**) after the rainfall event using the Cell-based model

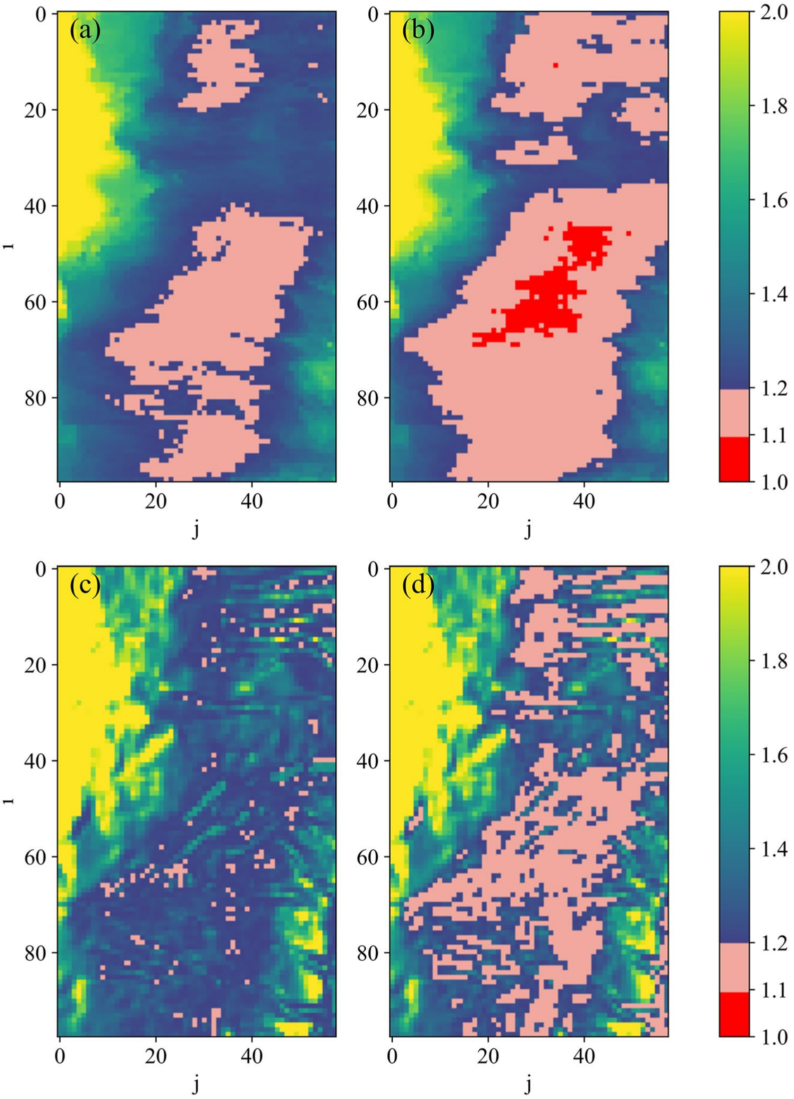

can be seen that the 3DPLS model has higher AC and PR values than the Cell-based models for all $P_{f,limit}$ values. Therefore, the 3DPLS model is more accurate and more precise in predicting despite its low TPR values.

Overall discussion

Investigating the effect of spatial variability on the safety of slopes necessitated the implementation of a 3D model as the parameters vary over the space. Therefore, the 3DPLS model was developed to capture the effects of spatial variability in landslide susceptibility. The 3DPLS model couples the hydrological model calculating the transient pore pressure changes due to rainfall infiltration and the slope stability model utilizing a 3D extension of Bishop's simplified method of slope stability.

In the 3DPLS model, the failure surface is assumed to be at a depth that is not necessarily the critical path in the soil volume. Therefore, the assumption of the ellipsoidal sliding surface with given dimensions may result in an overestimated F_S or underestimated P_f (Griffiths et al. 2011). In the present study, the analyses were performed by placing the ellipsoidal sliding surface at the center of each cell over the discretized problem domain for each simulation. As the number of analyzed ellipsoidal sliding surfaces increases over the study area, there is a higher chance of a cell intersecting a more critical ellipsoidal sliding surface.

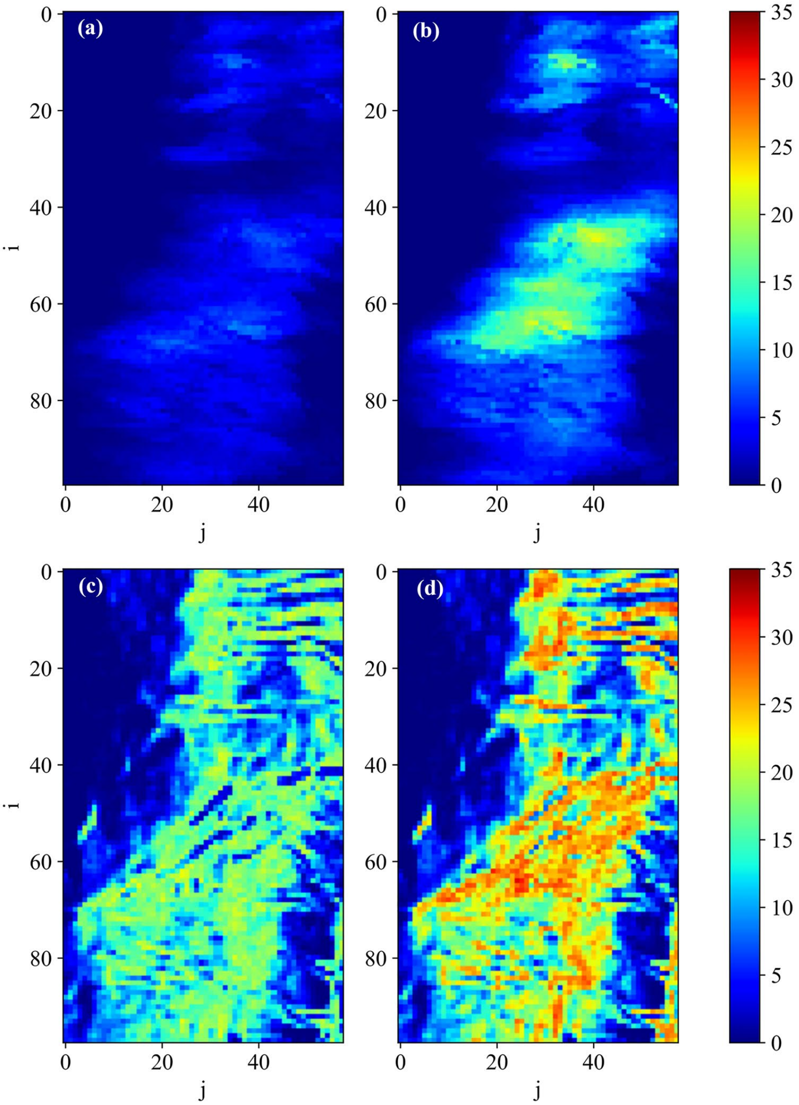

Fig. 11 The probability of failure, P_f, map of the study area: (**a**) before and (**b**) after the rainfall event using the 3DPLS model; (**c**) before and (**d**) after the rainfall event using the Cell-based model

Further investigation of the number of ellipsoids sufficient to cover a region can be done to improve the efficiency of the model. Another limitation is that the 3DPLS model currently does not support cross-correlation among model parameters which may be important in certain situations as shown in Javankhoshdel and Bathurst (2016).

In this study, the uncertainties associated with meteorological, environmental, and geomorphological factors have not been considered. These uncertainties originating from other sources than the model parameters might affect the results significantly (e.g., Bossi et al. 2019; Sandric et al. 2019). The 3DPLS model is very flexible, and with minor modifications, it allows for modeling of uncertainties in a wide range of parameters including meteorological (e.g., rainfall), hydrological (e.g., permeability), and geomorphological (e.g., depth to bedrock) parameters.

The slope stability models in the 3DPLS model were first validated using the example problems in the literature. Then, the capacity of the 3DPLS model to capture the effects of spatial variability of the soil strength parameters was validated by an extensive study in the FEM-based software. The results given in Fig. 5 reveal that the 3DPLS model is able to capture the effects of spatial variability on the μ_g contrary to the Cell-based model. From Fig. 5, one can also detect that the effect of the spatial variability on the μ_g lowers when the correlation length increases up to 1000 m where

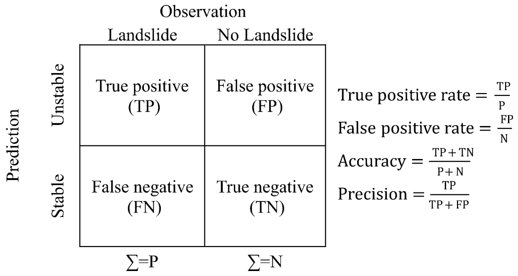

Fig. 12 Confusion matrix with performance parameters (Fawcett 2006)

the soil approaches homogeneous conditions. This shows that the models in the literature attempting to include the variability of the model parameters without spatial dependence of the parameters might overestimate the μ_g depending on the degree of spatial dependence.

The performance of the 3DPLS model was tested on the Kvam landslides that took place in 2011. The rainfall was assumed to be constant over the study area which is a reasonable assumption considering the spatial extent of the study area. However, it should be noted that the effect of spatial variation of rainfall can be significant for problems with a larger extent.

From the results of the case study, it is seen that more critical zones with lower μ_{F_S} can be obtained using the 3DPLS model when the spatial variability is included in the analyses. Despite the lower values of μ_{F_S} with the 3DPLS model, the P_f values are lower due to the results having less variability. The Cell-based model, however, has a much higher P_f values over the study area although it has higher μ_{F_S}. From Fig. 13 and Table 5, one can detect that the 3DPLS model has better performance, accuracy, and precision than the Cell-based model. While the Cell-based model classified nearly all positives correctly regardless of $P_{f,limit}$, it has a higher false-positive rate. This indicates that the Cell-based model overpredicts the extent of the unstable zones. On the contrary, the 3DPLS model predictions are more accurate and precise regardless of having low TPR. In addition, the 3DPLS model has a higher ratio of TPR/FPR than the Cell-based model, meaning better performance in prediction.

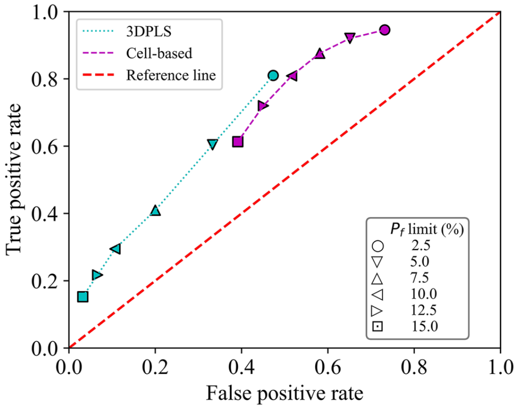

Fig. 13 Performance comparison of the 3DPLS model and the Cell-based model using different $P_{f,limit}$ on the receiver operator characteristic (ROC) graph

Table 5 Performance parameters for different $P_{f,limit}$

Model	$P_{f,limit}$(%)	*TPR*	*FPR*	*AC*	*PR*
3DPLS	2.5	0.810	0.473	0.571	0.238
	5	0.604	0.333	0.657	0.249
	7.5	0.410	0.200	0.740	0.273
	10	0.295	0.107	0.801	0.336
	12.5	0.217	0.066	0.823	0.375
	15	0.152	0.032	0.842	0.465
Cell-based	2.5	0.945	0.732	0.373	0.191
	5	0.920	0.651	0.437	0.205
	7.5	0.876	0.581	0.490	0.216
	10	0.809	0.516	0.534	0.223
	12.5	0.720	0.451	0.576	0.226
	15	0.613	0.391	0.609	0.223

Despite its capacity to improve the landslide prediction, and its better performance than the cell-based approach, one of the main limitations of the 3DPLS model is the computational efficiency. The 3DPLS model performs a high number of Monte Carlo simulations, and this process is time-consuming and computationally demanding. Likewise, the excessive time and memory requirement of probabilistic analysis with Monte Carlo simulations were also addressed in the literature (Rossi et al. 2013; Raia et al. 2014).

Another possible improvement of the 3DPLS model is to utilize parallel computing using the message passing interface (MPI) libraries (e.g., Alvioli and Baum 2016). In this study, the 3DPLS model was implemented on a detailed scale case study to show its power and capacity in prediction. Nevertheless, it is possible, in the future, to implement the model on large-scale problems by optimizing the computational time using parallel computing (e.g., Rossi et al. 2013; Sandric et al. 2019).

Conclusions

This study presented the 3-Dimensional Probabilistic Landslide Susceptibility (3DPLS) model which is a Python-based three-dimensional soil-column-based limit equilibrium model being able to model the spatial variability of the model parameters on the susceptibility of shallow landslides. The study presented the importance of the spatial variability on the safety of the shallow landslides, and the capacity of the 3DPLS in capturing these effects was validated. The study demonstrated that the spatial variability of the model parameters might lower the overall safety of the slopes and affect the landslide susceptibility analyses significantly.

Additionally, it was shown that the conventional cell-based approach is not capable of capturing the spatial variability effect as the analyses are performed on a cell-by-cell basis.

The 3DPLS model was tested on the Kvam landslides that occurred in 2011, and the results indicated that the proposed 3DPLS model leads to more realistic results with a better prediction performance than its cell-based equivalent model. The study showed that the 3DPLS model contributed to the landslide susceptibility analyses by considering the spatial variability as higher TPR/FPR ratio, AC, and PR were calculated for the model.

Acknowledgements

The authors acknowledge the R&D project *KlimaDigital* (2018–2022, grant number: 281059) partly funded by Research Council of Norway, and by SINTEF, Norwegian University of Science and Technology (NTNU), Norwegian Meteorological Institute (MET), Geonor, Nordic Semiconductor, Telia, Norwegian Public Roads Administration, and Norwegian Water Resources and Energy Directorate (NVE). The authors also acknowledge the support through INFRA project KK.01.1.1.02.0027 which is financed by the Croatian Government and the European Union through the Regional Development Fund–the Competitiveness and Cohesion Operational Programme.

Author contributions

Emir Ahmet Oguz: Conceptualization, data curation, formal analysis, funding acquisition, investigation, methodology, project administration, resources, software, supervision, validation, visualization, writing-original draft, writing-review and editing. Ivan Depina: Conceptualization, data curation, formal analysis, funding acquisition, investigation, methodology, project administration, resources, software, supervision, validation, visualization, writing-review and editing. Vikas Thakur: Conceptualization, funding acquisition, methodology, resources, supervision, validation, writing-review and editing.

Funding

Open access funding provided by NTNU Norwegian University of Science and Technology (incl St. Olavs Hospital - Trondheim University Hospital). The research is funded by the R&D project KlimaDigital (2018–2022, grant number: 281059).

Declarations

Conflict of interest/Competing interests. The authors declare no competing interests.

References

Alvioli M, Baum RL (2016) Parallelization of the TRIGRS model for rainfall-induced landslides using the message passing interface. Environ Model Softw 81:122–135. https://doi.org/10.1016/j.envsoft.2016.04.002

Arnone E, Dialynas YG, Noto LV, Bras RL (2016) Accounting for soil parameter uncertainty in a physically based and distributed approach for rainfall-triggered landslides. Hydrol Process 30:927–944. https://doi.org/10.1002/hyp.10609

Baligh MM, Azzouz AS (1975) End effects on stability of cohesive slopes. J Geotech Eng Div 101:1105–1117

Baum BRL, Savage WZ, Godt JW (2002) TRIGRS — a fortran program for transient rainfall infiltration and grid-based regional slope-stability analysis: open-file report 02–424

Baum RL, Godt JW, Savage WZ (2010) Estimating the timing and location of shallow rainfall-induced landslides using a model for transient, unsaturated infiltration. J Geophys Res Earth Surf. https://doi.org/10.1029/2009JF001321

Baum RL, Savage WZ, Godt JW (2008) TRIGRS — a fortran program for transient rainfall infiltration and grid-based regional slope-stability analysis, version 2.0: U.S. Geological Survey open-file report, 2008–1159

Bishop AW (1955) The use of the slip circle in the stability analysis of slopes. Geotechnique 5:7–17. https://doi.org/10.1680/geot.1955.5.1.7

Bossi G, Borgatti L, Gottardi G, Marcato G (2019) Quantification of the uncertainty in the modelling of unstable slopes displaying marked soil heterogeneity. Landslides 16:2409–2420. https://doi.org/10.1007/s10346-019-01256-x

Burton A, Arkell TJ, Bathurst JC (1998) Field variability of landslide model parameters. Environ Geol 35:100–114. https://doi.org/10.1007/s002540050297

Edvardsen DH (2013) Utløsningsårsaker og utløsningsmekansimer til flomskred i

Fawcett T (2006) An introduction to ROC analysis. Pattern Recognit Lett 27:861–874. https://doi.org/10.1016/j.patrec.2005.10.010

Fenton GA, Griffiths D V (2008) Risk assessment in geotechnical engineering

Fredlund DG, Krahn J (1977) Comparison of slope stability methods of analysis. Can Geotech J 14:429–439. https://doi.org/10.1139/t77-045

Gens A, Hutchinson JN, Cavounidis S (1988) Three-dimensional analysis of slides in cohesive soils. Geotechnique 38:1–23

Grelle G, Soriano M, Revellino P et al (2014) Space-time prediction of rainfall-induced shallow landslides through a combined probabilistic/deterministic approach, optimized for initial water table conditions. Bull Eng Geol Environ 73:877–890. https://doi.org/10.1007/s10064-013-0546-8

Griffiths DV, Huang J, Fenton GA (2011) Probabilistic infinite slope analysis. Comput Geotech 38:577–584. https://doi.org/10.1016/j.compgeo.2011.03.006

Griffiths DV, Marquez RM (2007) Three-dimensional slope stability analysis by elasto-plastic finite elements. Geotechnique 57:537–546. https://doi.org/10.1680/geot.2007.57.6.537

Hammond C, Hall D, Miller S, Swetik P (1992) Level I stability analysis (LISA) documentation for version 2.0

Haneberg WC (2004) A rational probabilistic method for spatially distributed landslide hazard assessment. Environ Eng Geosci 10:27–43. https://doi.org/10.2113/10.1.27

Haque U, Blum P, da Silva PF et al (2016) Fatal landslides in Europe. Landslides 13:1545–1554. https://doi.org/10.1007/s10346-016-0689-3

Holm G (2012) Case study of rainfall induced debris flows in Veikledalen, Norway, 10th of June 2011. University of Oslo

Huang C-C, Tsai C-C, Chen Y-H (2002) Generalized method for three-dimensional slope stability analysis. J Geotech Geoenvironmental Eng 128:836–848. https://doi.org/10.1061/(asce)1090-0241(2002)128:10(836)

Hungr O (1987) An extension of Bishop's simplified method of slope stability analysis to three dimensions. Geotechnique 37:113–117. https://doi.org/10.1680/geot.1987.37.1.113

Hungr O, Salgado FM, Byrne PM (1989) Evaluation of a three-dimensional method of slope stability analysis. Can Geotech J 26:679–686. https://doi.org/10.1139/t89-079

Iverson MR (2000) Landslide triggering by rain infiltration. Water Resour Res 36:1897–1910

Janbu N (1989) Grunnlag i geoteknikk. Tapir

Javankhoshdel S, Bathurst RJ (2016) Influence of cross correlation between soil parameters on probability of failure of simple cohesive and c-φ slopes. Can Geotech J 53:839–853. https://doi.org/10.1139/cgj-2015-0109

Lacasse S, Nadim F (1996) Uncertainties in characterising soil properties. In: Uncertainty in the Geologic Environment: from Theory to Practice, ASCE. pp 49–75

Lam L, Fredlund DG (1993) A general limit equilibrium model for three-dimensional slope stability analysis. Can Geotech J 30:905–919. https://doi.org/10.1139/t93-089

Li DQ, Xiao T, Zhang LM, Cao ZJ (2019) Stepwise covariance matrix decomposition for efficient simulation of multivariate large-scale three-dimensional random fields. Appl Math Model 68:169–181. https://doi.org/10.1016/j.apm.2018.11.011

Lizárraga JJ, Buscarnera G (2020) Probabilistic modeling of shallow landslide initiation using regional scale random fields. Landslides 17:1979–1988. https://doi.org/10.1007/s10346-020-01438-y

Lizárraga JJ, Buscarnera G (2019) Spatially distributed modeling of rainfall-induced landslides in shallow layered slopes. Landslides 16:253–263. https://doi.org/10.1007/s10346-018-1088-8

Melchiorre C, Frattini P (2012) Modelling probability of rainfall-induced shallow landslides in a changing climate, Otta, Central Norway. Clim Change 113:413–436. https://doi.org/10.1007/s10584-011-0325-0

Mergili M, Marchesini I, Alvioli M et al (2014a) A strategy for GIS-based 3-D slope stability modelling over large areas. Geosci Model Dev 7:2969–2982. https://doi.org/10.5194/gmd-7-2969-2014

Mergili M, Marchesini I, Rossi M et al (2014b) Spatially distributed three-dimensional slope stability modelling in a raster GIS. Geomorphology 206:178–195. https://doi.org/10.1016/j.geomorph.2013.10.008

Michel GP, Kobiyama M, Goerl RF (2014) Comparative analysis of SHALSTAB and SINMAP for landslide susceptibility mapping in the Cunha River basin, southern Brazil. J Soils Sediments 14:1266–1277. https://doi.org/10.1007/s11368-014-0886-4

Montgomery DR, Dietrich WE (1994) A physically based model for the topographic control on shallow landsliding. Water Resour Res 30:1153–1171. https://doi.org/10.1029/93WR02979

Montrasio L, Valentino R (2008) A model for triggering mechanisms of shallow landslides. Nat Hazards Earth Syst Sci 8:1149–1159. https://doi.org/10.5194/nhess-8-1149-2008

Nadim F, Kjekstad O, Peduzzi P et al (2006) Global landslide and avalanche hotspots. Landslides 3:159–173. https://doi.org/10.1007/s10346-006-0036-1

NGU (2020) NGU, Geological Survey of Norway. https://www.ngu.no/

Pack RT, Tarboton DG, Goodwin CN, Prasad A (2005) SINMAP 2.0: a stability index approach to terrain stability hazard mapping

Petley D (2012) Global patterns of loss of life from landslides. Geology 40:927–930. https://doi.org/10.1130/G33217.1

Phoon K-K, Kulhawy FH (1999) Characterization of geotechnical variability. Can Geotech J 36:612–624. https://doi.org/10.1139/t99-038

Raia S, Alvioli M, Rossi M et al (2014) Improving predictive power of physically based rainfall-induced shallow landslide models: a probabilistic approach. Geosci Model Dev 7:495–514. https://doi.org/10.5194/gmd-7-495-2014

Rossi G, Catani F, Leoni L et al (2013) HIRESSS: a physically based slope stability simulator for HPC applications. Nat Hazards Earth Syst Sci 13:151–166. https://doi.org/10.5194/nhess-13-151-2013

Salciarini D, Godt JW, Savage WZ et al (2006) Modeling regional initiation of rainfall-induced shallow landslides in the eastern Umbria Region of central Italy. Landslides 3:181–194. https://doi.org/10.1007/s10346-006-0037-0

Sandric I, Ionita C, Chitu Z et al (2019) Using CUDA to accelerate uncertainty propagation modelling for landslide susceptibility assessment. Environ Model Softw 115:176–186. https://doi.org/10.1016/j.envsoft.2019.02.016

Schilirò L, Cepeda J, Devoli G, Piciullo L (2021) Regional analyses of rainfall-induced landslide initiation in upper gudbrandsdalen (Southeastern Norway) using TRIGRS model. Geosci 11:1–15. https://doi.org/10.3390/geosciences11010035

Shirzadi A, Solaimani K, Roshan MH et al (2019) Uncertainties of prediction accuracy in shallow landslide modeling: sample size and raster resolution. CATENA 178:172–188. https://doi.org/10.1016/j.catena.2019.03.017

Simoni S, Zanotti F, Bertoldi G, Rigon R (2008) Modelling the probability of occurrence of shallow landslides and channelized debris flows using GEOtop-FS. Hydrol Process 22:532–545. https://doi.org/10.1002/hyp.6886Modelling

Wu W, Sidle RC (1995) A distributed slope stability model for steep forested basins. Water Resour 31:2097–2110

Xie M, Esaki T, Qiu C, Wang C (2006) Geographical information system-based computational implementation and application of spatial three-dimensional slope stability analysis. Comput Geotech 33:260–274. https://doi.org/10.1016/j.compgeo.2006.07.003

Xing Z (1988) Three-dimensional stability analysis os concave slopes in plan view. J Geotech Engine 114:658–671

Zhang Y, Chen G, Wang B, Li L (2013) An analytical method to evaluate the effect of a turning corner on 3D slope stability. Comput Geotech 53:40–45. https://doi.org/10.1016/j.compgeo.2013.05.002

Emir Ahmet Oguz (✉) · **Vikas Thakur**
Department of Civil and Environmental Engineering, Norwegian University of Science and Technology, Trondheim, Norway
Email: emir.a.oguz@ntnu.no

Ivan Depina
Department of Rock and Geotechnical Engineering, SINTEF, Trondheim, Norway

Ivan Depina
Faculty of Civil Engineering, Architecture and Geodesy, University of Split, Split, Croatia

Paper II: Quantification of climate change impact on rainfall-induced shallow landslide susceptibility

Quantification of Climate Change Impact on Rainfall-Induced Shallow Landslide Susceptibility

Emir Ahmet Oguz[a,*], Rasmus E. Benestad[b], Kajsa M. Parding[b], Ivan Depina[c,d], Vikas Thakur[a]

[a]*Norwegian University of Science and Technology, Department of Civil and Environmental Engineering, Trondheim, Norway.*
[b]*The Norwegian Meteorological Institute, Oslo, Norway.*
[c]*SINTEF, Department of Rock and Soil Mechanics, Trondheim, Norway.*
[d]*Faculty of Civil Engineering, Architecture and Geodesy, University of Split, Split, Croatia.*

Abstract

Rainfall-induced landslides are likely to become more frequent in regions associated with increased intensity and frequency of rainfall due to climate change. Estimates of the effects of climate change on rainfall patterns are commonly available for a range of spatial and temporal scales and are continuously being updated. However, the effects of climate change on landslide susceptibility of a certain region are often implied based on the expected changes in rainfall patterns and rarely explicitly quantified. This study aims to address this issue by implementing coupled landslide and climate modelling chains to explicitly assess the effects of climate change on landslide susceptibility. The effects of climate change are integrated in the landslide modelling chain via Intensity-Duration-Frequency (IDF) curves for the present and future climate conditions for a landslide-prone study area located in central Norway. The climate-dependent IDF curves are derived based on a straightforward statistical formulation that estimates approximate values of return levels based on daily precipitation data. The effects of climate on IDF curves were evaluated by the proposed formulation applied to the rainfall data from regional climate model simulations. The effects of climate change on landslide susceptibility of the study area were examined by simulating multiple rainfall events with varying durations and intensities based on the climate-dependent IDF curves. The sim-

---

[*] Corresponding author

Email addresses: `emir.a.oguz@ntnu.no` (Emir Ahmet Oguz), `rasmusb@met.no` (Rasmus E. Benestad), `kajsamp@met.no` (Kajsa M. Parding), `ivan.depina@sintef.no` (Ivan Depina), `vikas.thakur@ntnu.no` (Vikas Thakur)

ulated rainfall events were used as an input to a physical-based landslide prediction model. In addition to accounting for the uncertainties of rainfall events through the probabilistic interpretation of IDF curves, the uncertainties in the landslide model were also examined. For a given rainfall event, the model parameter uncertainties were propagated to the landslide predictions with the Monte Carlo method by estimating the probability of landslide initiation. Finally, the estimates of the probability of landslide initiation were integrated in a probabilistic framework to obtain an overall climate change impact on the landslide susceptibility. The results of the study were examined to evaluate both the overall climate change impact and the climate change impact due to extreme rainfall events of long return intervals. The results of the study reveal that climate change impacts the landslide susceptibility of the study area with increased probabilities of landslide initiation and larger extents of landslide susceptible zones. The novelty of the study stems from the implementation of a probabilistic modelling framework that allows for quantification of uncertainties in both modelling chains and explicit quantification of the effects of climate change on landslide susceptibility.

Keywords: `Landslide, susceptibility, rainfall, climate change, IDF, probabilistic`

1. Introduction

Climate change is an ongoing and unequivocal process (IPCC, 2021). The emission of carbon dioxide (CO_2) and other greenhouse gases over time have caused global warming with increased temperature and more severe rainfall (IPCC, 2012, 2021). In the Sixth Assessment Report (AR6) of the Intergovernmental Panel on Climate Change (IPCC), it is stated that the concentration of CO_2 in the atmosphere has increased by over 47% since 1750 and pre-industrial times (IPCC, 2021). The magnitude of the expected climate change and the local consequences depend on the location and are strongly influenced by natural and stochastic regional variations associated with the atmospheric dynamics and the presence of various physical phenomena, such as cyclones, weather fronts, convection, and atmospheric rivers. In a stable climate, the statistical properties of such natural variations would be stationary, but a climate change implies non-stationary statistical properties such as long-term trends in both temperature and precipitation (Benestad et al., 2016, 2019b).

As extreme precipitation events are one of the most common triggering factors for landslides, changes in climate, such as increasing total precipitation and precipitation intensity, will have a noticeable impact on landslide occurrence, frequency, and severity. A large number of countries have performed country-specific or region-specific climate change predictions and the corresponding impact on landslide occurrence (Ho et al., 2017). Except for a few regions, the majority of the studies have reported an increase in air temperature, annual cumulative rainfall, and frequency of intense rainfall events until the end of the 21^{st} century. These long-term changes in temperature and rainfall are expected to have profound impacts on both nature and society. A predicted increase in the frequency of landslide occurrence and associated risks to society have been reported by most of the countries, although the magnitude of the increase varies from region to region depending on the meteorological, environmental, and geomorphological factors controlling the landslide occurrence.

Global Climate Models (GCMs) are useful tools to simulate the response of the climate system to increased levels of greenhouse gases. The Climate Model Intercomparison Project (CMIP), organized by the World Climate Research Programme (WCRP), has coordinated and provided common experimental protocols to climate modelling groups across the world (Taylor et al., 2012; Eyring et al., 2016). The CMIP ensembles have been an important part of the scientific basis of the Intergovernmental Panel on Climate Change (IPCC) assessment reports (IPCC, 2014, 2021). While GCMs offer a multifaceted view of the large-scale phenomena and processes in the atmosphere, they are unable to provide details on small-scale conditions. Hence, additional information is needed in order to study the local climatic response and consequences of a global climate change. The process of adding such information on smaller scales is known as downscaling (Benestad et al., 2016; Takayabu et al., 2016). One approach is to use empirical-statistical downscaling (ESD), which utilises information about the link between the large and small scales found in historical data. Another approach is dynamical downscaling, in which a regional climate model (RCM) with higher spatial resolution is applied to a limited area, using GCM data as boundary conditions. In addition to these two, there is hybrid downscaling, which involves ESD that is trained on RCM data

(Erlandsen et al., 2020).

The Coordinated Regional Climate Downscaling Experiment (CORDEX) provides a coordinated framework for climate downscaling (Jacob et al., 2014). While RCMs provide a versatile picture of the climate and can resolve many atmospheric processes and interactions, there are drawbacks to dynamical downscaling. RCMs may not be physically consistent with the GCMs from which they take their boundary conditions and RCM output tends to require bias correction before being used in impact studies. Because of the computational costs of dynamical downscaling, RCMs are typically applied to a limited number of GCM simulations and the small RCM ensembles may not provide an adequate sample of regional outlooks (Mezghani et al., 2019). Ideally, it is recommended to combine ESD and RCMs since they have different strengths and weaknesses independent of each other.

The current study will demonstrate the impact of climate change on landslide susceptibility on a case study area located in Norway. In the report of "Climate in Norway 2100" (Hanssen-Bauer et al., 2017), climate projections for Norway were reported for the 21^{st} century. The report is partly based on dynamical downscaling, using an RCM ensemble consisting of 10 bias-corrected simulations (4 RCMs combined with one or several of 5 GCM simulations from CMIP5), assuming two different greenhouse emission scenarios: representative concentration pathways (RCP) 8.5 and 4.5. For the high emission scenario, RCP8.5, the expected increase in annual mean air temperature for Norway, as represented by the ensemble median value, is approximately 4.5°C. The expected change in precipitation is about 18% and the number of days with heavy rainfall is expected to double. For reference, observations from Norway showed an increase in the annual mean precipitation of about 18% and a warming of 1°C during the 20^{st} century. The intensity and frequency of short-duration rainfall have increased during the 20^{st} century and will very likely continue to increase in the 21^{st} century. The expected increase in precipitation with more frequent, short duration, and high-intensity rainfall events is expected to increase the probability of landslide occurrence (Hanssen-Bauer et al., 2017).

Quantifying the impact of climate change on landslide susceptibility is important for mitigating the expected increase in societal risk from climate-driven rainfall-induced landslides (e.g., hazard mapping, emergency management, land use planning). Several researchers have investigated the ongoing climate change and its effects on geohazards, such as shallow landslides (e.g., Ciervo et al., 2017; Salciarini et al., 2019), slow active landslides (e.g., Comegna et al., 2013), reactivation of landslides (e.g., Dixon & Brook, 2007) and deep-seated landslides (e.g., Rianna et al., 2014). Besides, Dehn et al. (2000) examined the displacement rates of the mudslides under climate change by employing hydrological and rheological models. In the study of Barik et al. (2017), the effects of climate change on landslide susceptibility were investigated for sustainable forest management. There exist studies on climate change impact on climatic abnormalities, such as typhoons, and corresponding effects on landslide occurrences (Shou & Yang, 2015; Chiang & Chang, 2011). These studies employed several methods linking climate change with landslide occurrence, such as physical-based models, statistical, and empirical methods. Among them, several studies investigated the effect of climate change on landslide susceptibility by employing a physical-based model with a rainfall event downscaled from GCMs and RCMs (e.g., Chiang & Chang, 2011; Melchiorre & Frattini, 2012; Alvioli et al., 2018). To the extent of our knowledge none of these abovementioned studies attempted to investigate overall climate change impact but mainly investigated only rainfall events of different return intervals, especially extreme rainfall events of long return intervals (e.g., Salciarini et al., 2019; Melchiorre & Frattini, 2012). However, considering only extreme rainfall events with a low probability of occurrence may overemphasize the climate change impact on landslide susceptibility.

This study focuses on quantifying the climate change impact on landslide susceptibility with a modelling framework that includes climate and landslide modelling chains. In the modelling framework, the climate change is represented by Intensity-Duration-Frequency (IDF) curves for the present and future climate conditions in the case study area located in Norway. The climate-dependent IDF curves are derived by a relatively simple formulation, proposed by Benestad et al. (2019b; 2021) to estimate the approximate values of return levels for daily and sub-daily rainfall events. The IDF curves representing present climate condition are obtained by the formulation applied to historical observations of precipitation data. The IDF curves for the future climate conditions are obtained for RCP8.5 by utilizing the future climate projections by the EURO-CORDEX ensemble (Jacob et al., 2014) combined with the present climate condition. For the landslide modelling, a physical-based model, Transient Rainfall Infiltration and Grid-Based Regional Slope Stability (TRIGRS) (Baum et al., 2008), is employed. The effects of climate change on landslide susceptibility are investigated by simulating rainfall events with varying durations and intensities based on the IDF curves from the climate modelling chain. Given the rainfall events, the uncertainties in the TRIGRS model parameters are propagated to the model predictions with the Monte Carlo method. The TRIGRS model predictions are presented in terms of probability of landslide initiation as a measure of landslide susceptibility. This study proposes a novel probabilistic framework to obtain an overall climate change impact on the landslide susceptibility. This is achieved by accounting for the probabilities of rainfall events with varying return intervals. With the proposed probabilistic framework, the climate change impact on landslide susceptibility will be evaluated on a more reasonable basis and not only based on extreme events.

Details of the modelling framework are presented in Section 2. Section 2.3 introduces the novel probabilistic framework. Section 3 provides a description of the study area. In Section 4, the future climate projections and landslide susceptibility maps are provided. Finally, Section 5 addresses several discussion points, and Section 6 summarizes the paper.

2. Methodology

The conceptual framework of the studies on the impact of climate change on landslides mainly involves the climate and landslide modelling chains (Gariano & Guzzetti, 2016; Alvioli et al., 2018), with some studies also incorporating sensitivity analysis (Mtongori et al., 2015) and stress-testing (Benestad et al., 2019a). The climate modelling chain might include different GCMs and RCMs, emission scenarios, and downscaling methods to asses future climate conditions. In the landslide modelling chain, physical-based, statistical, and empirical methods are used depending on, among others, landslide type, spatial and temporal scales.

This section introduces the modelling framework that consists of coupled landslide and climate modeling chains. Implementation of the coupled modelling chains aims at capturing the complex interactions between, among others, climate, weather, and landslide processes.

Figure 1 shows the details of the modelling framework implemented in this study. The climate modelling chain investigates the present climate conditions and provides future climate projections. In this study, the future climate projections are examined in terms of IDF curves by incorporating the simple formulation to estimate the approximate values of return levels for daily and sub-daily rainfall proposed by Benestad et al. (2019b; 2021). The landslide modelling chain employs a physical-based landslide susceptibility model, TRIGRS (Baum et al., 2008), to evaluate slope stability conditions across spatial and temporal scales. Among the main elements of the landslide modelling chain in Figure 1, the crucial part is the calibration of the landslide susceptibility model based on the landslide inventory, geological, and hydrological conditions over the study area. Depending on the implemented calibration strategy, the model may over-predict or under-predict the extent of unstable zones. The outputs of the climate modelling chain, the IDF curves for the present and future climate conditions, were utilized as an input to the calibrated landslide susceptibility model to evaluate the corresponding landslide susceptibility.

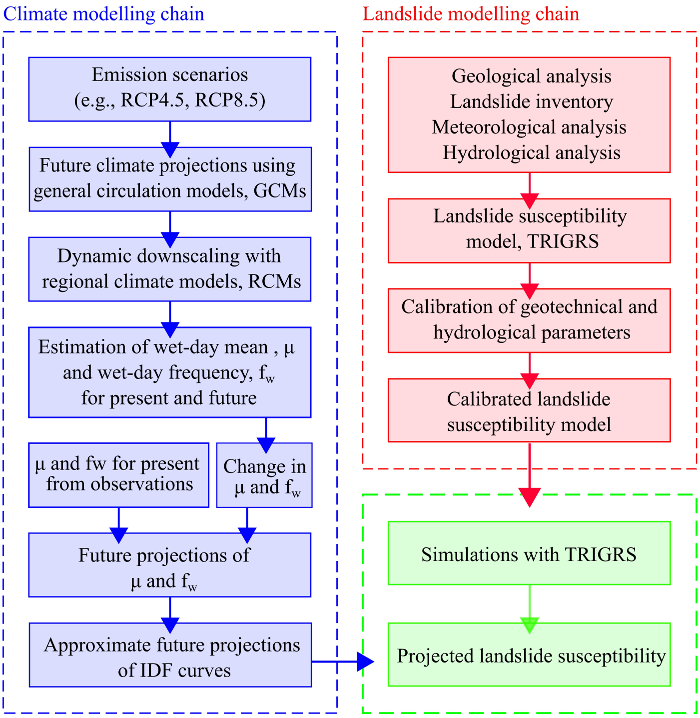

Figure 1: Modelling framework including climate and landslide modelling chains. The variables μ represents the wet-day mean precipitation whereas f_w refers to the wet-day frequency.

2.1. Climate modeling chain

Changes in the climate were calculated based on the dynamically downscaled climate model data and historical observations of precipitation. The present climate condition was examined based on the historical observations of precipitation, while the projections of precipitation from climate model simulations were combined with the historic observations to obtain the future climate conditions. Details of the data sets and methodology are described below.

2.1.1. Precipitation data

Daily precipitation data for the study area in Norway are obtained from dynamically downscaled high-resolution CORDEX simulations for Europe (EUR-11) (Jacob et al., 2014). The data ensemble consists of 56 projections, which combine 22 RCMs with a spatial resolution of 0.11° (≈12.5 km) that are applied to the output from 8 different GCM simulations from

CMIP5 (Taylor et al., 2012). There are inter-dependencies between the different RCM runs, both due to common boundary conditions provided by the same GCM and repeated RCM models with specific biases. The spread nevertheless gives some indication about the level of uncertainty associated with these results, keeping in mind that such a small number of GCM simulations may not represent the whole range of possible outcomes (Mezghani et al., 2019). Additionally, historic precipitation data were obtained from the weather stations and retrieved from the Norwegian Meteorological Institute using the Frost application programming interface (MET).

2.1.2. Intensity-duration-frequency calculations

A simple semi-empirical formula was used to calculate approximate daily and sub-daily rainfall statistics in terms of IDF curves (Benestad et al., 2021):

$$x_L = \alpha\mu\left(\frac{L}{24}\right)^{\zeta}\ln(f_w\tau) \tag{1}$$

where x_L is the return level (in mm) associated with time duration L (in hours), τ is the return interval, μ is the wet-day mean precipitation (in mm/day) and f_w is the wet-day frequency ($f_w \in [0, 1]$). The values for α and ζ reflect how the daily rainfall statistics diverge from an exponential distribution and how the different time scales are connected, respectively. They are approximately constant in Norway, whereas μ and f_w reflect the local rainfall statistics that to a greater extent vary both geographically and temporarily.

Here, μ and f_w were calculated based on daily precipitation data using a threshold of 1 mm/day to define a "wet-day". f_w was calculated as the fraction of days in a month above the threshold and μ as the mean precipitation on those wet days. IDF curves were estimated for two time horizons: 1981–2010 and 2071–2100, using the mean values of μ and f_w applied to Eq. 1. For the present day, the return levels were calculated using all available observational data in the reference period. For the future period, the return levels were calculated using the observed mean values of μ and f_w for the present day, and then adding the projected changes in μ and f_w from the present day to the future period, which were calculated based on RCM simulations.

2.2. Landslide modelling chain

Landslide prediction over large areas often depends on establishing a functional relationship between meteorological conditions and slope stability. The relationship can be developed and implemented with several approaches such as simple rainfall – landslide relationship based on a threshold level (Ciervo et al., 2017; Sangelantoni et al., 2018), empirical methods including several factors associated with landslides (Dixon & Brook, 2007; Shou & Yang, 2015), or physical-based models (Chiang & Chang, 2011; Melchiorre & Frattini, 2012; Alvioli et al., 2018; Salciarini et al., 2019; Scheidl et al., 2020). Among these methods, physical-based models are widely utilized as they generally incorporate hydrological and geotechnical processes explicitly into the landslide modelling. These models can be utilized for spatial and temporal prediction of landslide initiation, or for landslide susceptibility assessment.

There are several physical-based landslide susceptibility models, which have been employed at a local scale for a single slope or multiple slopes (up to 10 km^2), or at a regional scale covering hundreds to thousands of km^2. Some of the commonly used physical-based models can be listed as dSLAM (Wu & Sidle, 1995), SHALSTAB (Montgomery & Dietrich, 1994), SINMAP (Pack et al., 2005), SLIP (Montrasio & Valentino, 2008), GEOtop coupled with geotechnical models, for example, GEOtop-FS by Simoni et al. (Simoni et al., 2008), TRIGRS (Baum et al., 2002, 2008), HIRESS (Rossi et al., 2013), and r.rotstab (Mergili et al., 2014). Among the referenced physical-based models, TRIGRS was applied in this study as one of the most commonly used models (e.g., Park et al., 2013; Weidner et al., 2018; Ciurleo et al., 2019). The calibration of the TRIGRS model was implemented by utilizing the collected information over the study area on geology, landslide inventory, meteorological, and hydrological conditions. The details of the calibration will be provided in Section 3.4.

2.2.1. TRIGRS model

TRIGRS is a Fortran code developed to obtain the spatial and temporal distribution of rainfall-induced shallow landslide occurrence over large areas (Baum et al., 2002, 2008). The model couples a hydrological infiltration model, a model for routing of runoff, and an infinite slope stability model to examine the response of large areas to rainfall events. The TRIGRS is a cell-based model where the calculations for the infiltration and slope stability are performed on cell-by-cell basis, i.e., individually for each cell over the discretized domain.

The hydrological infiltration model is based on analytical solutions to the one–dimensional Richards equation describing the vertical movement of water through the soil medium. In this study, the wet initial condition, appropriate for saturated or nearly saturated soils, was employed in TRIGRS model. For the wet initial condition, the solution for the transient pore pressure head, $\psi(Z,t)$ (Eq. 2) superposes the steady long-term, $\psi_0(Z)$, and transient short-term response, $\psi_1(Z,t)$, to a rainfall event.

$$\psi(Z,t) = \psi_0(Z) + \psi(Z,t) \tag{2}$$

where Z is the vertical depth from the ground surface and t is the time. The steady long-term component is a function of Z, initial ground water depth vertically from ground surface, d, slope angle, δ, long-term vertical infiltration rate, I_{ZLT}, and hydraulic conductivity, K_S (Eq. 3).

$$\psi_0(Z) = (Z-d)[cos^2(\delta) - I_{ZLT}/K_S] \tag{3}$$

For the transient short-term component, TRIGRS provides solutions for two subsurface conditions: an infinite depth basal boundary and an impermeable basal boundary at finite depth. In case of having a relatively uniform hydraulic property through depth, the solution for a subsurface condition with a basal boundary at an infinite depth applies. However, the other solution applies where there is an impermeable basal boundary at a finite depth or a high contrast in hydraulic property through depth. In this study, the solution for infinite depth basal boundary was employed in the model. The formulation for the transient short-term component can be found in TRIGRS manual (Baum et al., 2008). The hydrological infiltration model, based on Iverson's solution, may result in unrealistic pressure heads at shallow depths (Iverson, 2000). Therefore, calculated pressure heads are restricted by $\psi(Z,t) \leq Z[cos^2(\delta) - (I_{ZLT}/K_S)]$ in the model.

The TRIGRS model routes the excess rainfall water due to soil saturation or the exceedance of infiltrability of the soil. The excess rainfall water is routed to downslope to the adjacent cells, proportional to the weighing factors assigned to the adjacent cells.

TRIGRS employs an infinite slope stability model calculating the factor of safety of a slope, F_S, as a ratio of the resisting to driving forces:

$$F_S(Z,t) = tan\phi'/tan\delta + (c' - \psi(Z,t)\gamma_w tan\phi'/(\gamma_s Z sin\delta cos\delta) \tag{4}$$

where c' is the effective cohesion, ϕ' is the effective friction angle, γ_w and γ_s are unit weight of water and soil respectively, and δ is the slope angle. Slope stability assessment is conducted along the depth, and the minimum F_S is provided. A slope is considered to be stable if $F_S > 1.0$ and unstable if $F_S \leq 1.0$.

2.2.2. Uncertainties in model parameters

The uncertainties in the geotechnical and hydrological parameters have been reported in the literature (Phoon & Kulhawy, 1999; Baecher & Christian, 2005; Fenton & Griffiths, 2008). The lack of knowledge on the parameters and the inherent natural variability due to the varying deposition and formation processes in geological history are mainly accepted as sources of the uncertainty. Avoiding this uncertainty and employing deterministic values for the geotechnical and hydrological parameters may result in conservative or unrealistic results.

Several studies have accounted for the variability of the model parameters in physical-based landslide modelling (e.g. Melchiorre & Frattini, 2012; Rossi et al., 2013; Raia et al., 2014; Arnone et al., 2016; Scheidl et al., 2020). Among them, Raia et al. (2014) reported improvement of the predictive capacity of a the TRIGRS model when the variability of the model parameters is accounted in the model simulations. In this study, TRIGRS model has been coupled with Monte Carlo method due to its robustness and straightforward implementation. The uncertainties in the model parameters are propagated to the model output in terms of F_S by performing 1000 Monte Carlo simulations. The TRIGRS model simulation outputs were utilized to evaluate the probability of landslide initiation for a given value of rainfall duration and intensity, $P_f(L,I)$, which is calculated as:

$$P_f(L,I) = P(F_S \leq 1.0|L,I) = \frac{1}{N_S}\sum_{i=1}^{N_S}\lambda(F_{S,i} - 1.0) \tag{5}$$

where L and I are duration and intensity of the rainfall event, N_S is the number of simulations, $F_{S,i}$ is the factor of safety of i^{th} simulation, and λ is the indicator function providing 1 if $F_{S,i} - 1.0 \leq 0$, and 0 otherwise.

2.3. Probabilistic framework

In the literature, the climate change impact on landslide susceptibility has been mainly evaluated under extreme conditions such as very intense rainfall events with long return intervals (e.g., Melchiorre & Frattini, 2012; Shou & Yang, 2015; Salciarini et al., 2019; Scheidl et al., 2020). However, the overall climate change impact cannot be represented by only extreme events, as these events have low probability of occurrences. Therefore, there is a need to account for the probability of occurrence of rainfall events with shorter return intervals to understand the overall climate change impact on landslide susceptibility.

This study proposes a probabilistic framework to account for the probability of occurrence of events and obtain an overall climate change impact on landslide susceptibility. The proposed framework is advantageous as it integrates the results from both the landslide and climate modelling chains in a consistent approach. The resulting estimate is the probability of landslide initiation for a given value of rainfall duration, $P_f(L)$, calculated as follows:

$$P_f(L) = P(F_S \leq 1.0|L) = \int P(F_S \leq 1.0|L, I) f(I|\kappa, \beta, L) dI \tag{6}$$

where $P(F_S \leq 1.0 \mid L, I)$, i.e., $P_f(L, I)$ is the probability of landslide initiation conditioned on L and I values, $f(I \mid \kappa, \beta, L)$ is the probability density function (pdf) of rainfall intensity conditioned on the values of the location κ, scale β, and L. $f(I \mid \kappa, \beta, L)$ was modeled by the Gumbel distribution, with the distribution parameters determined by fitting the distribution to the intensity values provided by the climate model for a given value of L.

To obtain the values of $P(F_S \leq 1.0|L, I)$, the ranges of intensity values in the IDF curves were discretized as $\{I_i, i = 1, 2, ..., n\}$ for different durations. Then, the landslide susceptibility analyses were performed over the range of intensity values for each duration to obtain the corresponding estimates. Finally, the Eq. 6 was utilized to integrate the results and obtain $P_f(L)$ for both present and future climate conditions for a given value of L.

3. Study area

The study area (11.2304–11.7571°E/63.3594–63.5144°N) is located in Trøndelag, central Norway (Figure 2a). It covers around 200 km^2 of the catchment of the Stjørdal river (Figure 2b) that flows from the Swedish border on the east and discharges into the Trondheim Fjord on the west.

3.1. Weather conditions

In the report of "Climate in Norway 2100" (Hanssen-Bauer et al., 2017), the climate observations in Trøndelag, central Norway show that the mean air temperature increased by ca. 0.1 °C per decade since 1900. In the period of 2000-2021, the average mean air temperature is approximately 4.9 °C and may typically vary from -30 °C to +34 °C in a year.

There are two weather stations in operation, one on the east and one on the west of the study area. The weather station on the east is in operation since 2004 and therefore has limited available data. The station on the west, Østås i Hegra (station id: 69550, 11.3536°E/63.4871°N) is in operation since 1895 and has reliable and long observation data. Therefore, for the climate projections, daily precipitation observations from the station Østås i Hegra were utilized.

Based on the historical observations of precipitation from station Østås i Hegra, there has been an increasing trend in annual μ of the order of 0.002 mm/day per year consistent with an increase from 6.8 mm/day in 1900 to 7.1 mm/day in 2020. Similarly, there has been an increase in f_w on the order of 0.0003 per year, from 0.39 in 1900 to 0.43 in 2020. However, these rates of increase are not statistically significant at the 5% level.

3.2. Geology

The study area is underlined by the bedrock composed of Proterozoic and Cambrian metamorphic rocks deformed during the Caledonian orogenesis. There exists a layer of Quaternary deposits of different origin covering the bedrock. Based on the available geological map from the Geological Survey of Norway (NGU), the Quaternary deposits include glacial deposits (moraine), marine deposits below the marine limit in the proximity of the Stjørdal river, river

– stream (fluvial) deposits, fluvial material transported and deposited by glaciers (glaciofluvial deposits), loose masses formed by physical and chemical degradation of the bedrock, thin peat and humus cover over bedrock, and bedrock outcrop. Fluvial and glaciofluvial deposits have the same material composition with different phenomena in transportation and deposition history. Additionally, marine deposits also have similar composition of fluvial deposits and only exist occasionally near the river with small extents. Therefore, the fluvial deposits, glaciofluvial deposits, and marine deposits have been grouped as "fluvial deposits" for simplicity. Similarly, the bedrock outcrop and loose masses formed by the physical and chemical degradation of the bedrock have been grouped as "rock". Figure 2d shows the Quaternary map of the study area including four geology units: moraine deposits, fluvial deposits, humus–peat, and rock.

The moraine deposits were picked up, transported by glaciers, and deposited mainly above the marine limit. The moraine is generally hard-packed, poorly sorted and may contain anything from clay to rock. The thickness varies from very thin, 0.2 m, to a few meters or even more. The fluvial deposits have sorted and rounded sand – gravel dominated composition, and mainly located along the Stjørdal river. Generally, a thick cover of fluvial deposits, from 0.5 m to more than 10 m, does appear in the study area. The humus – peat has high organic content due to roots and plants, and generally exists as a thin cover, less than 0.5 m over the bedrock. Finally, the rock type includes bedrock crops and weathered rocks. NGU reported the infiltration rates as varying from very poor to poor in the deposits that cover the hillslopes (e.g., moraine), while there is a relatively good infiltration capacity in the deposits covering the bottom of the valley (e.g., fluvial deposits).

Due to the TRIGRS model being applicable to soil-related landslides, this study focuses on moraine and fluvial deposits, but not rock and humus–peat. The moraine and fluvial deposits cover 40 % of the study area (Figure 2d), with 32% being moraine and 8% being fluvial deposits. The average slope angle over the moraine area is 14.7° while it is 10.2° for the fluvial deposits as the fluvial deposits are mainly located along the Stjørdal river. Additionally, the extent of the moraine with a slope angle greater than 30° is 4.2 km^2, while it is 0.9 km^2 for the fluvial deposits.

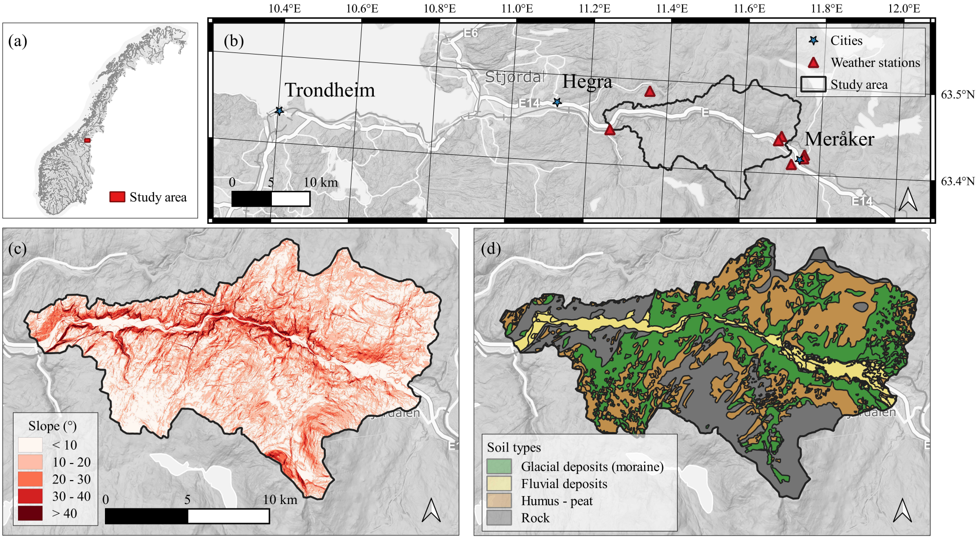

Figure 2: Location of the study area in (a) national scale, (b) Trøndelag, central Norway, with (c) slope and (d) geology maps.

3.3. Landslide inventory

The elevation of the study area was obtained from the map service “hoydedata.no” from the Norwegian Mapping Authority (Kartverket), and ranges from 23.5 m to 1109.6 m with a bumpy topography. Slope angles and direction of runoff were derived from the digital elevation model (DEM) with a resolution of 10 m. Very steep slopes can be found along the Stjørdal river with slope angles greater than 30° (Figure 2c). The study area was reported to have very high landslide susceptibility by the Norwegian Water Resources and Energy Directorate, NVE (Devoli et al., 2019).

The national database of mass movements of Norway, “skredregistrering.no” (NVE) was investigated for the study area. The mass movements in the database include rockfalls, stone slides, snow avalanches, debris flow – avalanches, clay slides, icefalls, and slides on the road fill. In the study area, 93 registered mass movements from 1750 until 2020 were registered, located mainly along the main transportation lines. Among these registered mass movements, 35 events are classified as landslides in soil and were triggered by rainfall, snow-melting, or a combination of these two. These landslide events were reported to be shallow, and the volumes were estimated in the range of 5 − 50 thousand m^3. Among them, 16 landslide events have polygonised source and runout zones that were obtained by evaluating the aerial pictures over time and field surveys. Figure 3 shows the landslide domain over the study area with two zoomed-in locations showing examples of polygonised landslide events. Figure 3a shows also the susceptibility levels at catchment scale (Devoli et al., 2019) by the logistic regression method and the zones susceptible to debris flow (Fischer et al., 2012) by using an index-based approach considering topographic characteristics.

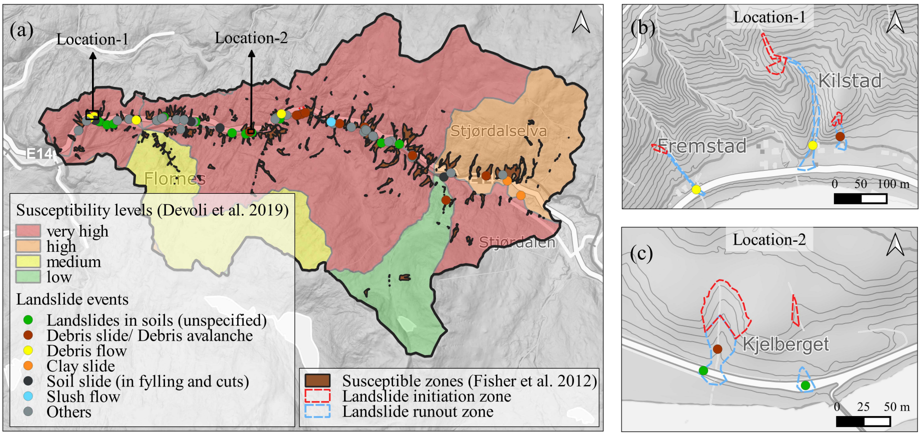

Figure 3: (a) Landslide domain over the study area in Trøndelag, central Norway, with two zoomed-in locations: (b) location-1 and (c) location-2.

Moreover, the landslide events were further filtered considering the quality of registration, date of occurrence (events after 2000), position and time, registration accuracy, and weather conditions on the date of occurrence. Following the filtering of events, 19 events were found to be convenient for the scope of the current study. Among the 19 landslide events, 14 events have polygonised initiation zones. For the remaining 5 events, possible initiation zones were located considering the descriptions in the national database and the topographic characteristics of the study area. A point with a 20 m buffer zone was placed on the possible initiation zone to be used in the TRIGRS model calibration.

Among the 19 events, 13 events are in fluvial deposits, and 3 events are in moraine. The remaining 3 events overlap both soil types. The initiation zones of the 19 landslide events include varying degrees of slopes from soft (0-10°) to very steep (>40°), with 29.2° being the median. Five landslide events do not have cells with a slope greater than 30°. The spatial extent of the 19 landslide landslides events varies from 500 to 3700 m^2, with 1615 m^2 being the average.

The meteorological and hydrological conditions for the landslide events were determined by utilizing the observations at the nearby weather stations and the national web portal, "xgeo.no" (Xgeo) which is a tool for visualizing spatial and temporal data including observations, model simulations, forecasts, and real-time data. The 19 events occurred between 2000 and 2019, mainly in the periods of February – March and August – September. The analysis of hydrometeorological conditions revealed that the selected landslides were triggered by intense rainfall in the period of August – September, or by the combination of precipitation and snow melting in the period of February – May. The average water supply by rainfall and snow melting was 49.8 mm/day in the range of {11.9, 82.0}. The degree of soil saturation data provided by Xgeo shows that the average degree of soil saturation was 79.1 % with a minimum of 49 % and a maximum of 99 %. The reported percentages for degree of soil saturation describe the relationship between the soil water storage compared to the maximum soil water storage simulated by the rainfall-runoff HBV model (Beldring et al., 2003) in the reference period 1981-2010. Additionally, the ground water table levels on the day of landslide events were also reported to be very high compared to the normal levels for most of the events. The pictures of the landslide deposits in the runout zones also revealed the high water content in the sliding mass.

3.4. Calibration

In the calibration process, a conventional deterministic approach was implemented with the parameters assumed to be constant for each geological unit as a compromise between the accuracy and high computational demands of a probabilistic calibration (Depina et al., 2020). Considering the degree of saturation ratio values, and the ground water levels for the 19 landslide events, the soil was assumed to be fully saturated with a ground water table at the ground surface at the time of landslide initiations. The possible ranges of geotechnical strength parameters, i.e., cohesion and friction angle for fluvial deposit and moraine, were determined by considering the literature (Melchiorre & Frattini, 2012; Depina et al., 2020) and the definitions of the soil types by NGU. For the fluvial deposit, low cohesion values, 1 – 5 kPa, with a friction angle in the range of 39 – 43° were examined. Similarly, for the moraine, the cohesion and friction angle parameters were examined in the ranges of 3 – 9 kPa, and 29 – 35°. The parameter ranges were discretized into integer values and all sets of parameters were determined from the combination of the discretized values.

Some of the commonly used metrics to evaluate the performance of the model are provided in Fawcett (2006) and include false/true positive (FP/TP), true/false positive rate (TPR/FPR), accuracy, precision. Similarly, the success rate, the Kappa value, and modified success rate are other metrics used in the literature (Huang & Kao, 2006). For the performance evaluation, this study employed an objective function, which accounts for both the stability of the study area before and after a rainfall event and capturing the landslide initiation zones. The objective function, f_{obj} (Eq. 7) accounts for: (i) the ratio of the number of initiated landslides to the total number of landslide events before the rainfall event; (ii) the ratio of the number of missed landslide events to the total number of landslide events after rainfall event; and (iii) the FPR after the rainfall event. The lower the value of f_{obj}, the better the performance of the model is.

$$\begin{aligned} f_{obj} = & \left[\frac{\sum_{i=1}^{N_l} \lambda(min(F_{Sj} : j = 1, ..., k) - 1.0 - e)}{N_l}\right]_{\substack{before\\rainfall}} \\ & + \left[1 - \frac{\sum_{i=1}^{N_l} \lambda(min(F_{Sj} : j = 1, ..., k) - 1.0 - e)}{N_l}\right]_{\substack{after\\rainfall}} + c(FPR)_{\substack{after\\rainfall}} \end{aligned} \tag{7}$$

where N_l is the number of initiation zones of the landslide events, F_{Sj} is the factor of safety of cell j inside the landslide i, k is the total number of cells inside landslide i, e is the error term, c is the importance weight of predicting the stable zones after the rainfall event, and λ is the indicator function. FPR is the ratio of cells predicted as unstable outside of the discretized landslide zone (FP) to the number of cells without landslide observation (N) and calculated as $FPR = FP/N$.

The criteria in the calibration procedure is that the landslide events should be stable before rainfall and predicted after rainfall, and the zones outside of the discretized landslide initiation zone should be stable after rainfall. An error term, e, was added to account for the uncertainty in the model and model parameters. The landslide initiation zones were accepted as unstable if $F_S \leq 1.0 + e$, and stable otherwise. The coefficient c adjusts the stability of the study area after the rainfall event. As the coefficient c increases, the study area becomes more stable with a lower FP after rainfall. At a certain value of c, the set of parameters providing the best performance gives zero FP after rainfall. At this point, the balance between over- or under-predicting the stable zone and capturing the landslide events is accepted to be achieved. Then, the set of parameters resulting in the lowest F_S over the landslide initiation zones is selected. It should be noted that the parameters, e and c should be selected carefully to achieve the balance between overpredicting the extent of stable zones and capturing the landslide events.

TRIGRS simulations were performed for each set of parameters to determine the optimal geotechnical strength parameters of fluvial deposit and moraine type of soils with the model performance being evaluated by f_{obj}. For the performance evaluation, different values of $e \in \{0.0, 0.05, 0.1\}$ in Eq. 7 were tested. For each value of e, the coefficient c in Eq. 7, increased from zero to a certain value providing zero FP after rainfall for the set of parameters providing the best performance. In case of having several sets of parameters providing the same value of f_{obj} with zero FP, the set of parameters giving the lowest F_S for the landslide initiation zones was selected. Following the performance evaluation of all sets of parameters, cohesion and friction angle were selected as 6 kPa and 35° for moraine, and 5 kPa and 40° for the fluvial deposits.

In this study, the hydrological parameters were not estimated in this calibration process as the infiltration does not change the transient pore pressure response at fully saturation condition. Instead, a parametric hydrological analysis was performed via TRIGRS model to investigate the response of soils with varying hydrological parameters to the present and future IDF curves (Appendix A). The hydrological parameters of two soil types: fluvial deposit and moraine were determined by considering the literature (Melchiorre & Frattini, 2012; Depina et al., 2020), the hydrological characteristics reported by NGU, and the parametric hydrological analysis. The K_S for moraine and fluvial deposit have been selected as $5.0 \cdot 10^{-5}$ and $1.0 \cdot 10^{-4}$ m/s, respectively. Additionally, the ratio of D_0/K_S was decided as 50 to avoid too slow or fast pore pressure build-up.

Table 1 shows the calibrated geotechnical strength parameters and selected hydrological parameters for the geological units, moraine and fluvial deposits. In this study, the humus–peat and rock units were omitted from the analyses. Depth to bedrock, H (m) was calculated by an empirical relationship between the depth and slope inclination in degree, $H = 5.0exp(-0.04\delta)$ (Baum et al., 2010). The variability levels of the model parameters, i.e., CoV, were assigned considering the values in the literature (Melchiorre & Frattini, 2012; Depina et al., 2020; Phoon & Kulhawy, 1999), and used only for moraine and fluvial deposits in the TRIGRS model simulations.

Table 1: Calibrated parameters.

Parameter	Distribution	Moraine	Fluvial deposit	CoV
Depth to bedrock, H (m)	-	$^{(1)}5.0exp(-0.04\delta)$		0.25
Unit weight, γ (kN/m^3)	Normal	20	19	0.02
Cohesion, c (kPa)	Lognormal	6	5	0.3
Friction angle, ϕ $(°)$	Normal	35	40	0.1
Saturated permeability, K_S (m/s)	Lognormal	$5.0 \cdot 10^{-5}$	$1.0 \cdot 10^{-4}$	0.25
Diffusivity, D_0 (m^2/s)	Lognormal	$2.5 \cdot 10^{-3}$	$5.0 \cdot 10^{-3}$	0.25

(1) Slope, δ is in degrees.

4. Results and discussion

4.1. Future climate projections

In this study, the high emission scenario RCP8.5, based on the assumptions of no climate policy, was investigated and the corresponding Euro-CORDEX ensemble was utilized. Figure 4 displays the projected change in wet-day mean precipitation (μ) and frequency (f_w) in

Eq. 1, from the the period of (1981–2010) to the end of the century (2071–2100), based on the Euro-CORDEX ensemble. For each simulation, the grid point of the Euro-CORDEX data closest to the weather station, Østås i Hegra, was selected. From Figure 4, it can be seen that most of the RCMs of the Euro-CORDEX ensemble simulated increases in both μ and f_w with further global warming, both of which are key parameters of Eq. 1. The results revealed the variability in the projections by the RCMs in the ensemble. The projected changes in μ and f_w, by the ensemble mean, are 0.836 mm/day (σ: 0.387) and 0.0189 day/month (σ: 0.0248), respectively.

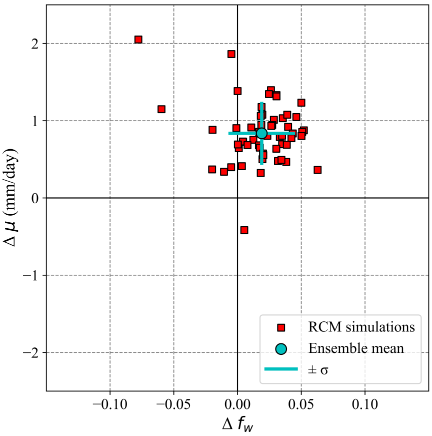

Figure 4: Projected changes in the wet-day mean precipitation (μ) and frequency (f_w) from a reference period (1981-2010) to the future (2071-2100).

Figure 5 shows the 10-, 50- and 100-year IDF curves for the present climate calculated from observations (blue solid line), and ensemble statistics for the end of the century estimated from the Euro-CORDEX ensemble combined with the observations. While red solid lines show the ensemble mean, the dashed lines show 5^{th} and 95^{th} percentiles. The results suggest a considerable increase in the return values for all return intervals. There is some spread within the Euro-CORDEX ensemble, but even the 5^{th} percentile indicates an increase compared to the present day, which makes sense as the majority of models projected an increase in both μ and f_w (Figure 4).

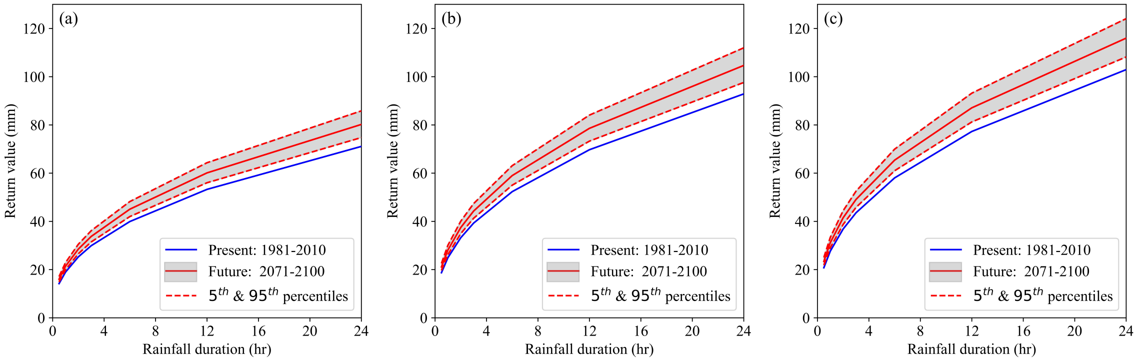

Figure 5: Estimated return values for (a) 10-, (b) 50-, and (c) 100-year return intervals based on regional climate model (RCM) simulations from EURO-CORDEX assuming emission scenario RCP8.5.

Figure 6 shows the IDF curves representing the present climate conditions based on observations, and future projections based on the mean projected change by the Euro-CORDEX ensemble combined with the observations, for a range of return intervals (2, 5, 10, 50, 100 and, 200 years). The climate-dependent IDF curves are presented as return values (in mm) in Figure 6a and as intensity return values (in mm/hr) in Figure 6b by dividing the return values by the corresponding rainfall duration. The results showed that the return values increase by a mean factor of 1.128 ($\in [1.126, 1.130]$) due to climate change.

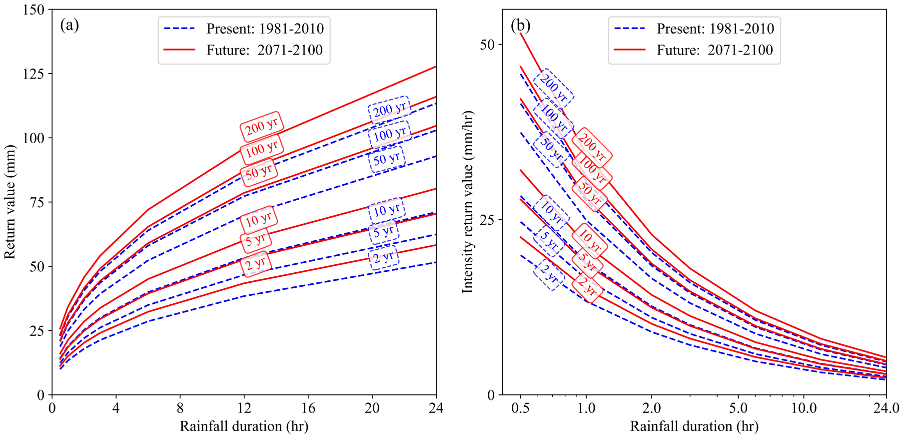

Figure 6: Estimated return values for Østås i Hegra weather station based on regional climate model (RCM) simulations from EURO-CORDEX assuming emission scenario RCP8.5 (a) and intensity return values (b).

4.2. Projected landslide susceptibility

For the landslide susceptibility analyses, the initial ground water table was assumed at the bottom of the soil layer. Additionally, the rainfall was simulated as a uniform spatial event during the rainfall duration.

The impact of climate change on the landslide susceptibility of the study area will be illustrated over a representative zone (Figure 7a), which has both soil types of interest (Figure 7c). On closer inspection in Figure 7d, it can be seen that steep slopes can be found in areas with both soil types of interest.

This section will present, first, the overall climate change impact on the response of the study area to different rainfall durations by providing $P_f(L)$ maps obtained by the proposed probabilistic framework (Section 2.3). Secondly, the climate change impact for the rainfall events of different return intervals will be provided with the corresponding $P_f(L, I)$ maps. The statistics of $P_f(L)$ and $P_f(L, I)$, and all findings will be provided for the whole study area.

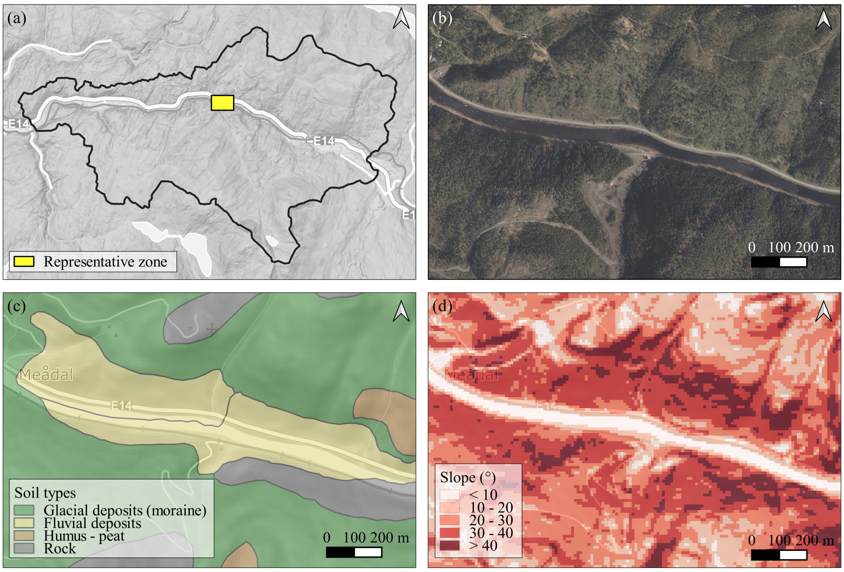

Figure 7: The representative zone for the illustration of climate change impact: (a) regional scale, (b) aerial photo, (c) geology and (d) slope maps.

4.2.1. Overall climate change impact

Figure 8 shows the overall climate change impact for 6-, 12-, and 24-hour rainfall events and provides the $P_f(L)$ maps for both present and future climate conditions. As the proposed probabilistic framework scales the impact of intense rainfall events proportionally to the their likelihood, the events with high return intervals such as 50-, 100-year have less influence on $P_f(L)$ than more frequent rainfall events with a smaller return interval. For this reason, the change in $P_f(L)$ is not large overall for different durations and climate conditions. However, substantial differences can be recognized when the statistics are examined for different ranges of slopes. The analyses showed that the $P_f(L)$ is higher for 6-hour duration at both present and future climate conditions compared to longer duration rainfall events (Figure 8). This is attributed to the fact that the pdf values of the Gumbel distribution for lower return interval events are higher for 6-hour duration than the corresponding values for 12- and 24-hour duration. That is, $P(F_S < 1.0 \mid L, I)$ in Eq. 6 might be similar for different duration rainfalls as the intensity values also vary, but the $f(I \mid \kappa, \beta, L)$ of more frequent rainfall events is higher for shorter durations.

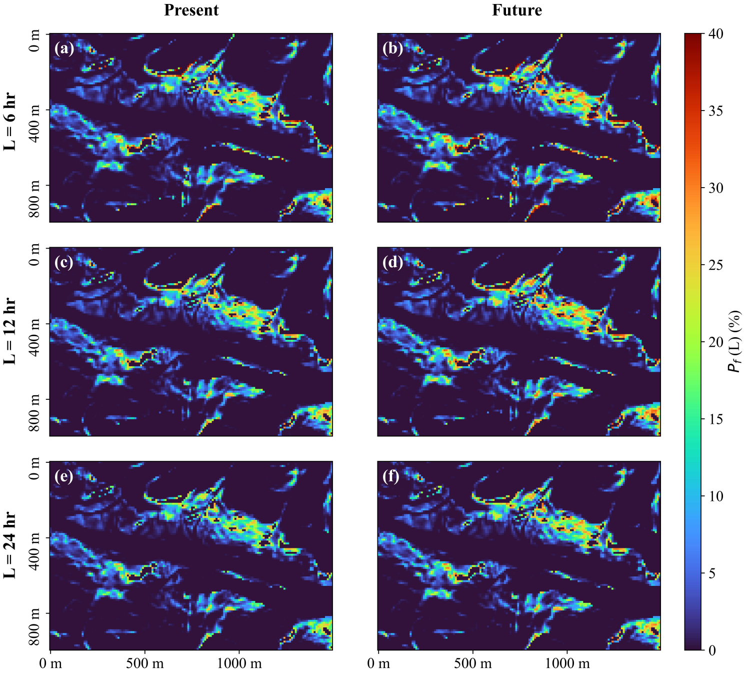

Figure 8: $P_f(L)$, maps for present (a, c, e) and future (b, d, f) climate conditions for 6-hour (a, b), 12-hour (c, d), and 24-hour (e,f) rainfall events.

In the Figure 8, it can be seen that the $P_f(L)$ values for the future climate condition are greater than the present condition. The difference between the $P_f(L)$ values for the present and future climate conditions (Δ) and the relative difference ($\Delta_{rel.}$) are provided in Figure 9. Additionally, mean difference ($\overline{\Delta}$), and mean relative difference ($\overline{\Delta_{rel.}}$) are tabulated in Table 2 for different ranges of slopes. It was observed that that the difference, Δ, may be up to 10%, 9%, and 4% at certain parts of the study area for 6-, 12-, and 24-hour rainfall events, respectively. Figure 9a,b,c and Table 2 show that the $P_f(L)$ increases by approximately $3\% - 4\%$ over very steep slopes. Table 2 shows that the mean difference is higher for 6-hour duration for all ranges of slopes and decreases as the duration increases.

From Figure 9d,e,f, and Table 2, it can be seen that there exists a relative difference of

14-20% in $P_f(L)$ for the slopes in the range 30° to 45°. Table 2 shows that $\overline{\Delta_{rel.}}$ for moderate slopes, from 25° to 30°, are very high as the small change in $P_f(L)$ at low values results in very high $\Delta_{rel.}$. Besides, in this study, the low values of $P_f(L)$ were not estimated with high accuracy due to relatively low number of samples in Monte Carlo analysis, and therefore, these low $P_f(L)$ values have a high degree of uncertainty. Additionally, it is observed that few cells have a negative difference in $P_f(L)$, which is likely due a relatively low number of samples in the Monte Carlo analysis.

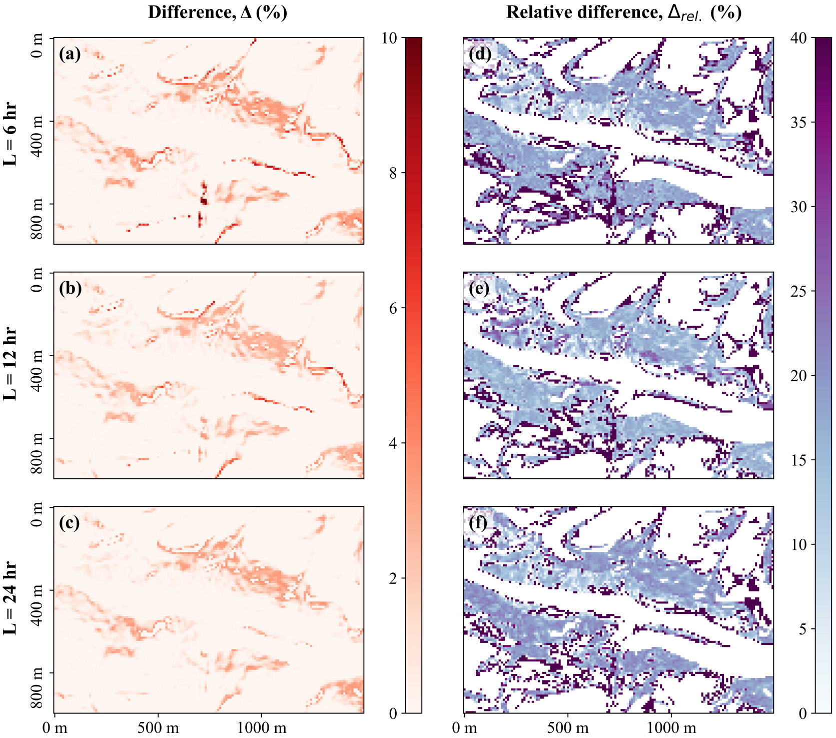

Figure 9: (a, b, c) The difference Δ between the $P_f(L)$ maps for present and future climate conditions and (d, e, f) relative difference $\Delta_{rel.}$: (a, d) 6-hour, (b, e) 12-hour, and (c, f) 24-hour.

Table 2: Mean difference $\overline{\Delta}$ and mean relative difference $\overline{\Delta_{rel.}}$ in the $P_f(L)$ over the entire area due to climate change.

Slope range °	L = 6 hr.		L = 12 hr.		L= 24 hr.	
	$\overline{\Delta}$	$\overline{\Delta_{rel.}}$	$\overline{\Delta}$	$\overline{\Delta_{rel.}}$	$\overline{\Delta}$	$\overline{\Delta_{rel.}}$
25–30	0.11	92.22	0.04	189.93	0.01	112.04
30–35	0.38	16.05	0.23	14.27	0.15	14.00
35–40	1.49	18.34	1.29	18.50	1.08	19.93
40–45	3.35	16.27	2.99	15.67	2.96	16.91

Table 3 provides mean values of $P_f(L)$ for different ranges of slopes. From Table 3, it can be seen that the values of mean $P_f(L)$ are higher for 6-hour duration. As the duration increases, the mean $P_f(L)$ values decrease for each range of slopes. The effect of climate change impact on the mean $P_f(L)$ is absolute for each duration in both Table 2 and Table 3. For example, the mean $P_f(L)$ increases, due to climate change, from 22.18% to 25.53%, by 3.35%, for 6-hour rainfall events over the slopes between 40° and 45°.

Table 3: Mean values of $P_f(L)$ for different slope ranges over the entire area.

Slope range °	L = 6 hr.		L = 12 hr.		L= 24 hr.	
	Present	Future	Present	Future	Present	Future
25–30	0.29	0.4	0.06	0.1	0.03	0.03
30–35	1.65	2.03	1.06	1.29	0.83	0.98
35–40	7.47	8.95	6.5	7.79	5.35	6.42
40–45	22.18	25.53	20.69	23.68	18.23	21.19

In the literature, there exist several methods for the assessment of landslide stability in probabilistic studies, such as the reliability index (Haneberg, 2004), the stability index (Michel et al., 2014), or defining criterion on the extent with the probability of landslide initiation, P_f, greater than a certain value (Rossi et al., 2013). However, there is a lack of consensus on the assessment criteria for the susceptibility condition in the probabilistic studies. That is, there is no widely recognized level of P_f, $P_{f,limit}$ such that a slope is considered as landslide-susceptible if $P_f > P_{f,limit}$ and stable otherwise. Therefore, this study employs several $P_{f,limit}$ values in the range from 10% to 40% and provides the extent of landslide-susceptible zones with a $P_f > P_{f,limit}$.

Table 4 shows the extent of zones with $P_f(L) > P_{f,limit}$ for both present and future climate conditions for 6-, 12-, and 24-hour durations. The values in parentheses are the extents of the moraine and fluvial deposits, respectively. It is observed that 6-hour duration has the larger extent regardless of $P_{f,limit}$, and has highest $P_f(L)$ values exceeding 40%. When the duration increases, the extent of zones with $P_f(L) > P_{f,limit}$ decreases. From Table 4, one can observe that climate change significantly increases the extent of zones for each duration. It can be also seen that the extents of moraine are always greater than the extents of fluvial deposits as the moraine has larger spatial extent with steep slopes compared to the fluvial deposits.

Table 4: Extent of zones with $P_f(L) > P_{f,limit}$ over the entire area for different durations with the proportions of moraine and fluvial deposits in the parentheses.

$P_{f,limit}$ (%)	L = 6 hr.		L = 12 hr.		L= 24 hr.	
	Present	Future	Present	Future	Present	Future
10	112.85 (105.8 - 7)	130.67 (121.9 - 8.8)	94.7 (91.4 - 3.3)	114.85 (109.6 - 5.3)	81.98 (79.6 - 2.4)	96.65 (93.4 - 3.3)
20	47.67 (44.9 - 2.8)	65.42 (61.2 - 4.3)	36.63 (36.5 - 0.1)	49.58 (48.3 - 1.3)	24.21 (24.2 - 0)	37.41 (37 - 0.5)
30	11.62 (10.5 - 1.1)	23.99 (22.1 - 1.9)	0.76 (0.8 - 0)	12.48 (12.5 - 0)	0 (0 - 0)	3.06 (3.1 - 0)
40	2.63 (2.2 - 0.4)	4.24 (3.6 - 0.7)	0 (0 - 0)	0 (0 - 0)	0 (0 - 0)	0 (0 - 0)

Unit: $10^{-2} km^2$

4.2.2. Climate change impact for a given rainfall event

Landslide susceptibility simulations were performed for 6-, 12-, and 24-hour duration rainfall events of varying return intervals. The landslide susceptibility assessments were similar for different duration rainfall events of same return interval. This was attributed to having similar transient pore pressure responses for different duration rainfall events of same return interval (see Appendix A, FigureA.12). In this section, the climate change impact on landslide susceptibility is provided only for 12-hour rainfall events with 10-, 50-, and 100-year return intervals for illustration purposes. The overall conclusions made for 12-hour rainfall events also applies to other durations, 6-hour and 24-hour.

Figure 10 shows the effect of climate change on the $P_f(L, I)$ values for 12-hour rainfall events with 10-, 50-, and 100-year return intervals by providing present and future conditions separately. It can be seen that the $P_f(L, I)$ values appear to be much higher in case of long return intervals, and $P_f(L, I)$ values increase due to the climate change for each return interval. The analyses showed that the increase in $P_f(L, I)$ due to climate change can be up to 27%, 19%, 14% at certain parts of the study area for rainfall events with 10-, 50-, and 100-year return intervals, respectively. In Table 5, the mean difference ($\overline{\Delta}$), and mean relative difference ($\overline{\Delta_{rel.}}$) in the $P_f(L, I)$ values due to climate change are provided for each return interval over different ranges of slopes. It is observed that the $\overline{\Delta}$ and $\overline{\Delta_{rel.}}$ are larger in case of 10-year return interval, and lower for 50- and 100-year return intervals. This is attributed to the fact that the steep slopes are already very close to fully saturated condition at long return intervals at the present condition. Larger precipitation can just make the slope fully saturated, resulting in considerably less change in $P_f(L, I)$ values.

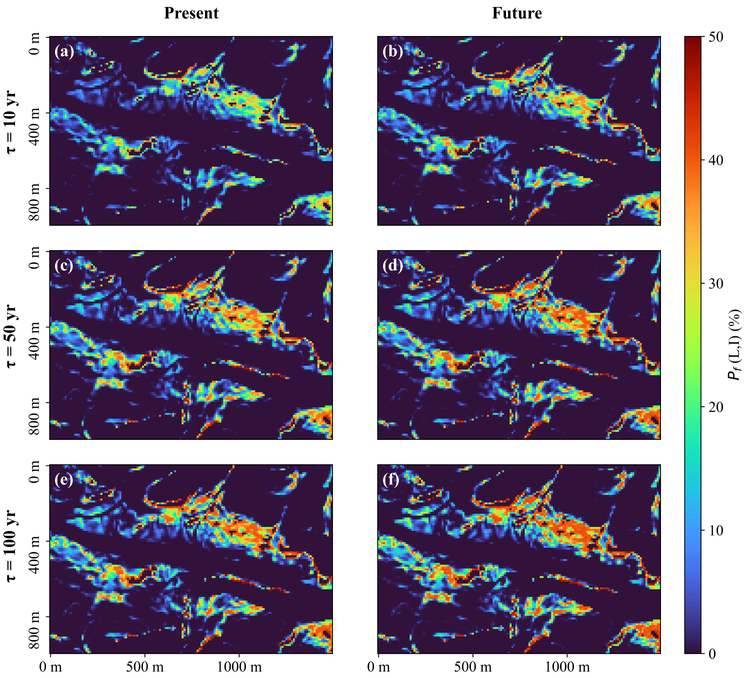

Figure 10: $P_f(L, I)$ for 12-hour rainfall events with 10-year (a, b), 50-year (c, d), and 100-year (e, f) return intervals for present (a, c, e) and future (b, d, f) climate conditions.

Table 5: Mean difference $\overline{\Delta}$ and mean relative difference $\overline{\Delta_{rel.}}$ in $P_f(L, I)$ for 12-hour rainfall events over the entire area due to climate change.

Slope range °	τ = 10 yr.		τ = 50 yr.		τ = 100 yr.	
	$\overline{\Delta}$	$\overline{\Delta_{rel.}}$	$\overline{\Delta}$	$\overline{\Delta_{rel.}}$	$\overline{\Delta}$	$\overline{\Delta_{rel.}}$
25–30	0.15	196.74	0.12	30.56	0.13	28.83
30–35	0.65	38.34	0.43	23.06	0.75	11.94
35–40	3.09	32.59	1.93	17.22	2.96	19.03
40–45	5.10	19.60	2.10	6.37	1.35	4.06

The mean values of $P_f(L, I)$ over different ranges of slopes are provided in Table 6 for each return interval. It can be seen that the mean $P_f(L, I)$ increases as the return interval increases, for each slope range. Table 6 reveals that the climate change increases the mean $P_f(L, I)$ and results in more susceptible slopes for all slope ranges. From both Table 5 and Table 6, it can be seen that the change in mean $P_f(L, I)$ is higher for 10-year return interval events. However, the mean $P_f(L, I)$ values reach the highest value for 100-year return interval events. Additionally, it is observed the $P_f(L, I)$ values over a slope range may have a very large range. That is, two identical slopes might have different $P_f(L, I)$ values. This is attributed, among others, to the observation that the excess rainfall due to fully saturation is redistributed to the surrounding neighboring regions. Therefore, a slope might receive more water than an another slope with the same inclination.

Table 6: Mean values of $P_f(L, I)$ for 12-hour rainfall events for different slope ranges over the entire area.

Slope range °	$\tau = 10$ yr.		$\tau = 50$ yr.		$\tau = 100$ yr.	
	Present	Future	Present	Future	Present	Future
25–30	0.16	0.31	0.52	0.64	0.62	0.75
30–35	1.44	2.08	3.39	3.83	3.77	4.52
35–40	9.77	12.85	16.86	18.78	18.51	21.47
40–45	28.74	33.84	36.87	38.97	38.67	40.01

Table 7 shows the extent of zones with $P_f(L, I) > P_{f,limit}$ for both present and future climate conditions for 12-hour rainfall events of 10-, 50-, and 100-year return intervals. The extents of moraine and fluvial deposits are provided in the parentheses. From Table 7, it is observed that the extent of susceptible zones increases as the return interval increases and 100-year return interval has the largest extent regardless of $P_{f,limit}$. The impact of climate change on the extent of zones can be clearly seen in Table 7. For example, climate change increases the extent of zones with $P_f(L, I) > 40\%$ by a factor of $1.6 - 3.2$ depending on the return interval.

Table 7: Extent of zones with $P_f(L, I) > P_{f,limit}$ over the entire area for 12-hour rainfall events of different return intervals with the proportions of moraine and fluvial deposits in the parentheses.

$P_{f,limit}$ (%)	τ = 10 yr.		τ = 50 yr.		τ = 100 yr.	
	Present	Future	Present	Future	Present	Future
10	136.98 (128.9 - 8.1)	162.33 (150 - 12.4)	195.92 (179.4 - 16.5)	213.28 (195.7 - 17.6)	211.35 (194 - 17.4)	247.2 (225.4 - 21.8)
20	73.61 (69.7 - 3.9)	97.35 (91.4 - 5.9)	132.26 (123.8 - 8.5)	141.75 (131.5 - 10.3)	140.45 (130.6 - 9.9)	161.65 (149.9 - 11.7)
30	35.3 (33.7 - 1.6)	60.84 (57.6 - 3.2)	86.47 (81.3 - 5.2)	99.54 (92.7 - 6.8)	98.59 (92.1 - 6.5)	116.08 (108.5 - 7.6)
40	5.18 (4.5 - 0.7)	16.45 (14.8 - 1.7)	24.39 (21.5 - 2.9)	43.56 (40 - 3.6)	33.59 (30.2 - 3.4)	53.13 (49.2 - 3.9)

Unit: $10^{-2} km^2$

5. Overall Discussion

This study proposed a novel implementation of probabilistic framework to quantify the overall impact of climate change on landslide susceptibility. The method combines the results from the climate and landslide models by integrating the landslide susceptibility estimates over different intensity values with varying return intervals for a given duration. By doing so, the contributions of rainfall events to the overall climate change impact were scaled with respect to their probability of occurrence. This method provided a more realistic basis to evaluate the climate change impact. Otherwise, climate change impact on landslide susceptibility would likely be overestimated by using only extreme rainfall events with long return intervals despite their low occurrence probability.

This study quantified the overall climate change impact for 6-, 12-, and 24-hour rainfall events by the proposed probabilistic framework (Section 2.3) and provided $P_f(L)$ maps for present and future climate conditions (Figure 8). The increase in $P_f(L)$ can be up to 10%, 9%, and 4% for 6-, 12-, and 24-hour rainfall events, respectively (Figure 9). For both moraine and fluvial deposits, a considerable increase in the extent of susceptible zones based on different values of $P_{f,limit}$ (Table 4) was observed. In addition to the overall climate change impact, climate change impact was also illustrated by 12-hour rainfall events of 10-, 50-, and 100-year return intervals (Figure 10). This may be particularly important for engineering structures such as infrastructures, buildings, or any other project designed based on extreme rainfall events. The study revealed that climate change increases both $P_f(L, I)$ (Table 5, Table 6) and the extent of susceptible zones (Table 7). For 12-hour rainfall events of 10-, 50-, and 100-year return intervals, the increase in $P_f(L, I)$ due to climate change can be up to 27%, 19%, and 14%, respectively. The results of this study also showed that the moraine soil type poses a higher risk than the fluvial deposits under the climate change (Table 4 and Table 7). This is due to the moraine being more located on steep slopes than fluvial deposits.

There are many sources of uncertainty in the climate modeling chain, such as biases in RCMs and the driving GCMs, assumptions about future emissions, the limited size of the model ensemble, uncertainties associated with precipitation observations, and the approximate formula used to calculate IDF curves (Eq. 1). When it comes to uncertainties associated with climate models, previous model evaluation done in connection to statistical downscaling has indicated that GCMs are able to reproduce the large-scale conditions found in nature that are important to local climate variations (Benestad, 2021).

The current study included only the high emission scenario RCP8.5, which is based on the assumptions of no climate policy, high population growth and slow technological development, resulting in continued increases of greenhouse gases throughout the 21^{st} century. The results presented here can therefore be interpreted as high-end estimates of change. Other scenarios based on assumptions of decreased emissions show smaller changes in the precipitation climate and thus would have given a smaller change in the landslide susceptibility. Similarly, the projected landslide susceptibility was provided only for the the end of the century (2071–2100). Projections of landslide susceptibility to the near future (2021-2050) were also performed. The results showed smaller increase in the probability of landslide initiation over the entire area compared to the values at the end of the century (2071–2100).

This study is promising in the way forward to quantification of the climate change impact on rainfall-induced shallow landslide susceptibility. Due to the complexities in both landslide and climate modelling chains, there exist several shortcomings which should be addressed in future studies to have more complete and comprehensive landslide susceptibility assessments. The shortcomings can be listed as follows:

- Due to the insufficient knowledge on the hydrological conditions at the instant of sliding for the historical landslides, and the lack of laboratory and field test, the hydrological parameters, K_S and D_0, were determined by conducting a parametric hydrological analysis (Appendix A), and considering the values reported in the literature. Effect of varying K_S and D_0 on the results of this study has been investigated. Except for hydraulic parameters resulting in too slow or fast infiltration, the overall findings of the current study do not change for different hydraulic parameters.
- It should be noted that this study did not account for the spatial variability of the geotechnical and hydrological model parameters, which may show strong variability through space (e.g., Lizárraga & Buscarnera, 2020). Instead, these parameters were assumed homogeneous within a single geological unit and the variability of the model parameters has been modelled with a single random variable approach using the Monte Carlo method.
- In the landslide susceptibility analyses, the complex geological and environmental processes, vegetation, and areal planning were not accounted for due to the limitations of the physical-based model and the high level of complexities involved. It should be noted that these processes, such climate change and associated natural disturbances, changes in forest management planning, may significantly affect the landslide susceptibility (Scheidl et al., 2020).
- The Euro-CORDEX ensemble is relatively small in terms of providing robust values for the future and the small sample size may lead to an unrepresentative, narrow and skewed view of the range of possible outcomes of climate change (Mezghani et al., 2019). Ideally, future regional projections should include empirical-statistical downscaling or hybrid downscaling as well as RCM results to enable including a larger ensemble of GCMs and thus provide more entrusted results (Benestad, 2021). However, empirical-statistical downscaling of precipitation and in particular the precipitation intensity is

challenging due to the large local and stochastic variations. Research is nevertheless ongoing with the aim to find good ESD-based and hybrid downscaling solutions for precipitation statistics.

- This study estimated the local effects of climate change based on dynamically downscaled data that had not been bias-corrected. To address potential issues related to biases, we opted for a delta change approach (e.g., Hay et al., 2000), where the present conditions were represented by observations and future conditions were estimated by adding the change from RCM simulations. While bias correction might have given a more physically consistent picture of the precipitation climate of the future, fewer bias corrected RCM simulations were available, and in the context of this study we considered the benefit of a larger ensemble of climate model simulations greater than the potential advantage of bias correction.
- In this study, a single climate-dependent IDf curve was developed for the entire study area as there is only one reliable weather station with long observation data. Therefore, rainfall events were modelled as constant over the entire area in the TRIGRS model. Accounting spatial variability of the precipitation may affect the landslide susceptibility (e.g. Shou & Yang, 2015) and more realistic results can be obtained.

6. Summary

The changes in the rainfall patterns are commonly known to a certain degree for different spatial and temporal scales. However, the effect of these changes on landslide susceptibility was rarely quantified explicitly. Such quantification will provide a basis for the development of mitigation strategies for landslide risk under climate change. This study presented a framework for the quantification of climate change impact on rainfall-induced landslide susceptibility. The framework consists of climate and landslide modelling chains. One of the novelties of the study comes from incorporating a simple semi-empirical formulation to estimate the approximate daily and sub-daily rainfall statistics, and utilizing these statistics in the landslide modelling chain. Additional novelties include the implementation of a probabilistic framework to integrate the two modelling chains and obtain the overall climate change impact on landslide susceptibility instead of only investigating extreme rainfall events. The proposed probabilistic framework accounts for the likelihood of extreme rainfall events for a given duration rainfall and scales the contributions of these intense rainfall events by their probability of occurrences.

The current study quantified the climate change impact on rainfall-induced shallow landslide susceptibility for a landslide-prone region located in central Norway. The overall climate change impact was quantified for varying duration rainfall events using the proposed probabilistic framework. Additionally, the impact was also quantified for extreme rainfall events of long return intervals. The results demonstrated that the landslide susceptibility over the study area increases due to climate change with higher probabilities of landslide initiation, and larger landslide-susceptible extents. The proposed probabilistic framework provided a more realistic basis for the evaluation of the climate change impact on landslide susceptibility without the bias due to extreme rainfall events with low probability of occurrence.

Acknowledgments

The authors are grateful to Dr. Graziella Devoli from the Norwegian Water Resources and Energy Directorate for her support on the interpretation of the geology and the landslide inventory. The authors acknowledge support from the R&D project KlimaDigital (2018-2022, grant number: 281059) that is funded by the Research Council of Norway and by SINTEF, Norwegian University of Science and Technology (NTNU), Norwegian Meteorological Institute (MET), Geonor, Nordic Semiconductor, Telia, Norwegian Public Roads Administration, and Norwegian Water Resources and Energy Directorate (NVE). The authors also acknowledge the support through the project KK.01.1.1.02.0027 that is financed by the Croatian Government and the European Union through the Regional Development Fund - the Competitiveness and Cohesion Operational Programme.

Declaration of Competing Interest

CRediT authorship contribution statement

Emir Ahmet Oguz: Conceptualization, Methodology, Software, Validation, Formal analysis, Investigation, Data Curation, Writing - original draft, Writing - review & editing, Visualization, Project administration

Rasmus Benestad: Methodology, Software, Validation, Formal analysis, Investigation, Data Curation, Writing - review & editing, Visualization

Kajsa M. Parding: Methodology, Software, Validation, Formal analysis, Investigation, Data Curation, Writing - review & editing, Visualization

Ivan Depina: Conceptualization, Methodology, Formal analysis, Investigation, Resources, Writing - review & editing, Supervision, Project administration, Funding acquisition

Vikas Thakur: Conceptualization, Resources, Writing - review & editing, Supervision, Funding acquisition

Declarations

Funding: The research is funded by the R&D project KlimaDigital (2018-2022, grant number: 281059).

Conflicts of interest/Competing interests: Not applicable.

Availability of data and material: Not applicable.

Code availability: Not applicable.

Authors' contributions: "CRediT authorship contribution statement" is provided.

Appendix A. Parametric hydrological analysis

Hydraulic parameters, such as conductivity, K $[ms^{-1}]$ and diffusivity, D $[m^2s^{-1}]$, have very high importance in landslide susceptibility assessment because these parameters significantly affect the transient pore pressure build up, expressed in Eq. 2, during the infiltration process. In this paper, the saturated hydraulic parameters, K_S and D_0, were used because the wet initial condition was assumed in TRIGRS model. These parameters depend on the soil texture, soil density, percentage of voids, grain size and distribution, etc., and significantly vary through space, even in the same geology unit. In the literature, a very high coefficient of variation, CoV which is the ratio of standard deviation to mean, was reported for K_S, such as $48.5 - 65.9$ % (Hu et al., 2008), 77.3% (Usowicz & Lipiec, 2021) based on the tests on a very large number of samples. Similarly, Liu and Wu (2008) reported the high variability of K_S and D_0, and stated that D_0 values reported in the literature are in the range of $(10-500)K_S$.

A parametric hydrological analysis was performed via TRIGRS model to understand the effect of hydrological parameters on the transient pore pressure response. In the parametric study, we used the K_S values in the range from $1.0 \cdot 10^{-6}$ m/s to $1.0 \cdot 10^{-4}$ m/s with the ratio of $D_0/K_S \in [10, 200]$. For illustration purpose, the results of 1.5 m thick soil with 30° inclination are shown, although different slopes with varying thicknesses have been also investigated. In TRIGRS model, the initial ground water table was assumed at the bottom of the soil layer. The rainfall was simulated as a uniform spatial event during the rainfall duration and the pore pressure profiles were obtained at the beginning and at the end of the rainfall events.

For this parametric hydrological analysis, the IDF curves for the present climate condition were obtained by examining the historical time series from the weather station, Østås i Hegra. For the future climate condition , end of the 21st century (2071-2100), the ad-hoc IDF curves were obtained by a simple approach involved multiplying μ in Eq. 1 with 1.4 to achieve a typical climate change scaling factor recommended by the Norwegian Climate Service Center (Dyrrdal & Førland, 2019). This estimate of recommended climate change scaling factor is also in accordance with a simple and crude temperature-based scaling study for μ (Benestad et al., 2016). The return values (in mm) are provided in Figure A.11a, and intensity return values (in mm/hr) are provided in Figure A.11b by dividing the return values by corresponding rainfall durations.

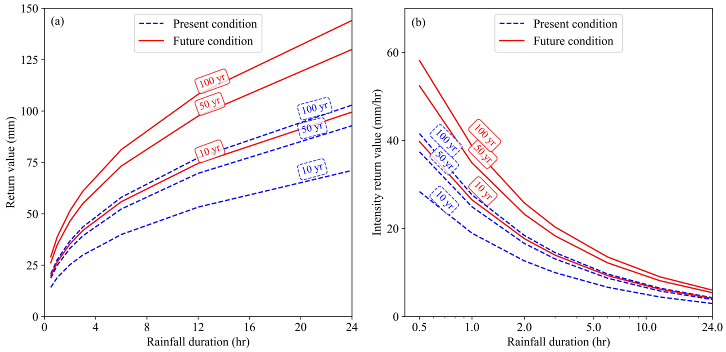

Figure A.11: IDF curves for present conditions based on observations and ad-hoc IDF curves for future climate conditions using 1.4 climate change scale factor (return intervals, τ, are stated into boxes): (a) return value, (b) intensity return value.

The analysis showed that different duration rainfall events of the same return interval, based on IDF curves, result in almost the same transient pore pressure response (Figure A.12). This is attributed to the fact that the return value in mm/hr (Figure A.11b) changes with respect to the duration. Being longer duration and corresponding lower return values compensate for each other and similar transient pore pressure responses are obtained for different duration rainfall events of same return intervals.

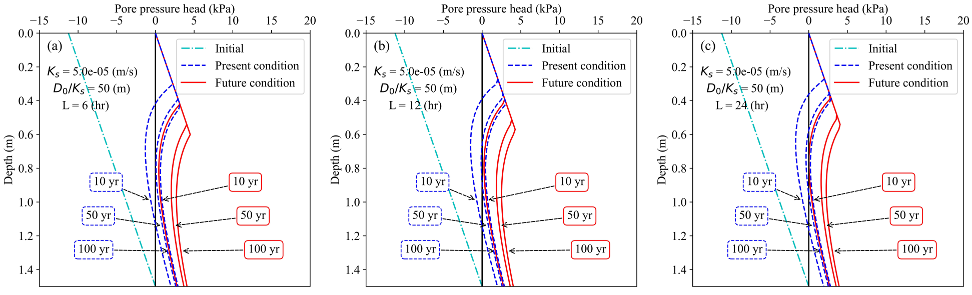

Figure A.12: Effect of duration, L, on the transient pore pressure head response where $K_S = 5.0 \cdot 10^{-5}$ m/s, and $D_0/K_S = 50$: (a) 6-hour,(b) 12-hour, (c) 24-hour.

Figure A.13 shows the effect of hydrological parameters, K_S and D_0, on the transient pore pressure response. For the illustration purpose, the results with K_S values of $1.0 \cdot 10^{-5}$,

$5.0 \cdot 10^{-5}$, and $1.0 \cdot 10^{-4}$ m/s and D_0/K_S values of 10, 50, 100 are provided for 12-hour rainfall events of 10-, 50-, and 100-year return intervals (Figure A.13). It can be seen that higher K_S does not result in faster pore pressure build up because the water infiltrates faster into the soil and drains from the bottom. Figure A.13 shows that a higher ratio of D_0/K_S results in a faster transient pore pressure response. The difference between the responses to different return intervals becomes wider when the ratio of D_0/K_S increases or K_S decreases.

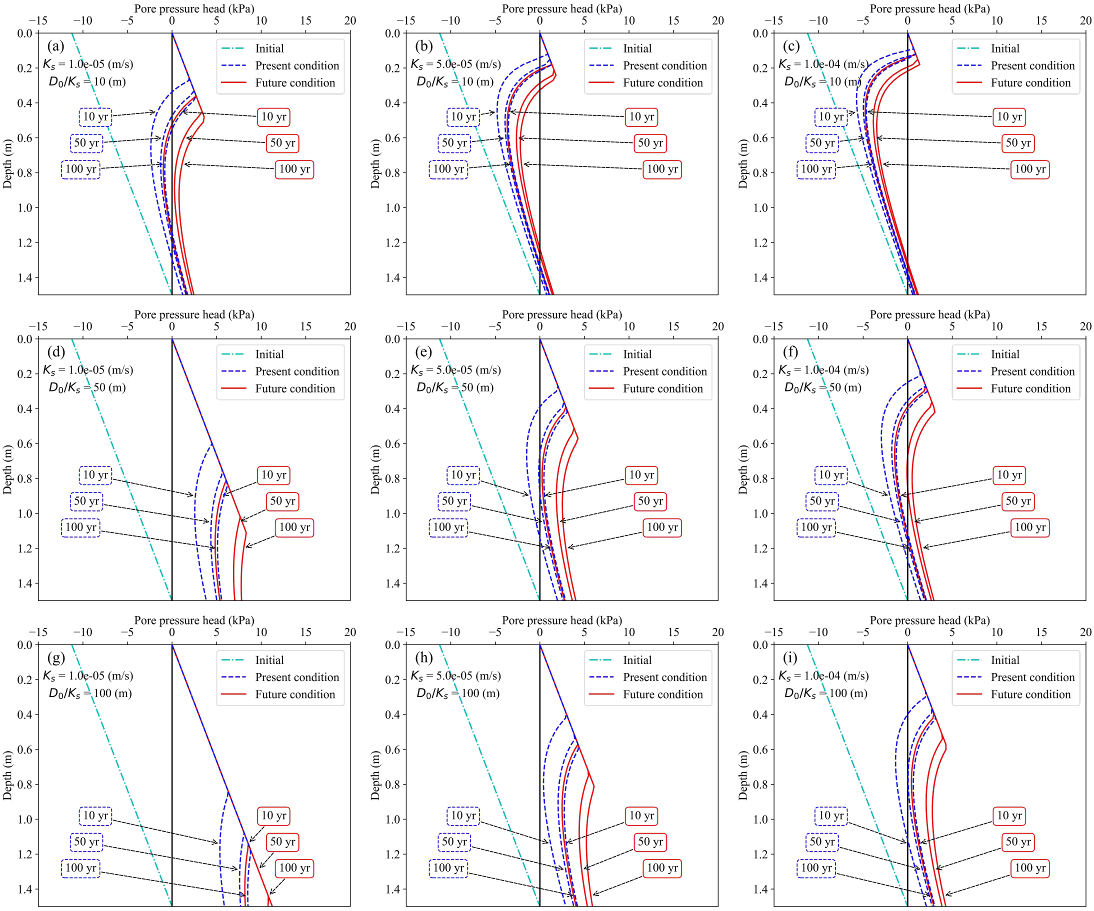

Figure A.13: Effect of hydrological parameters on the transient pore pressure head response to a 12-hour rainfall event with return intervals of 10-, 50-, 100-year: (a, d, g) $K_S = 1.0 \cdot 10^{-5}$ m/s, (b, e, h) $K_S = 5.0 \cdot 10^{-5}$ m/s, (c, f, i) $K_S = 1.0 \cdot 10^{-4}$ m/s with D_0/K_S values of (a, b, c) 10, (d, e, f) 50, (g, h, i) 100.

The analyses showed that employing very low or very high values of D_0/K_S results in no considerable change in transient pore pressure response to rainfall events at present and future climate conditions. That is, low values of D_0/K_S results in very slow transient pore pressure especially for high values of K_S, and high values of D_0/K_S cause a fully saturation condition even at low intensity values. Therefore, employing such values of D_0/K_S would result in similar transient pore pressure response and similar landslide susceptibility assessments.

References

Alvioli, M., Melillo, M., Guzzetti, F., Rossi, M., Palazzi, E., von Hardenberg, J., Brunetti, M. T., & Peruccacci, S. (2018). Implications of climate change on landslide hazard in Central Italy. *Science of the Total Environment*, *630*, 1528–1543. URL: `http://dx.doi.org/10.1016/j.scitotenv.2018.02.315`. doi:`10.1016/j.scitotenv.2018.02.315`.

Arnone, E., Dialynas, Y. G., Noto, L. V., & Bras, R. L. (2016). Accounting for soil parameter uncertainty in a physically based and distributed approach for rainfall-triggered landslides. *Hydrological Processes*, *30*, 927–944. doi:`10.1002/hyp.10609`.

Baecher, G. B., & Christian, J. T. (2005). *Reliability and statistics in geotechnical engineering*. John Wiley & Sons.

Barik, M. G., Adam, J. C., Barber, M. E., & Muhunthan, B. (2017). Improved landslide susceptibility prediction for sustainable forest management in an altered climate. *Engineering Geology*, *230*, 104–117. URL: `http://dx.doi.org/10.1016/j.enggeo.2017.09.026`. doi:`10.1016/j.enggeo.2017.09.026`.

Baum, B. R. L., Savage, W. Z., & Godt, J. W. (2002). *TRIGRS — a fortran program for transient rainfall infiltration and grid-based regional slope-stability analysis: open-file report 02-424*. Technical Report USGS.

Baum, R. L., Godt, J. W., & Savage, W. Z. (2010). Estimating the timing and location of shallow rainfall-induced landslides using a model for transient, unsaturated infiltration. *Journal of Geophysical Research: Earth Surface*, *115*. doi:`10.1029/2009JF001321`.

Baum, R. L., Savage, W. Z., & Godt, J. W. (2008). *TRIGRS — a fortran program for transient rainfall infiltration and grid-based regional slope-stability analysis, version 2.0: U.S. Geological Survey open-file report, 2008-1159*. Technical Report U.S. Geological Survey.

Beldring, S., Engeland, K., Roald, L. A., Sælthun, N. R., & Voksø, A. (2003). Estimation of parameters in a distributed precipitation-runoff model for Norway. *Hydrology and Earth System Sciences*, *7*, 304–316. doi:`10.5194/hess-7-304-2003`.

Benestad, R., Parding, K., Mezghani, A., Dobler, A., Landgren, O., Erlandsen, H., Lutz, J., & Haugen, J. (2019a). Stress Testing for Climate Impacts with "Synthetic Storms". *Eos Transactions American Geophysical Union 100*, *100*. doi:`10.1029/2019eo113311`.

Benestad, R. E. (2021). *A Norwegian Approach to Downscaling*. Technical Report Climate and Earth system modeling. URL: `https://gmd.copernicus.org/preprints/gmd-2021-176/`. doi:`10.5194/gmd-2021-176`.

Benestad, R. E., Lutz, J., Dyrrdal, A. V., Haugen, J. E., Parding, K. M., & Dobler, A. (2021). Testing a simple formula for calculating approximate intensity-duration-frequency curves. *Environmental Research Letters*, *16*. doi:`10.1088/1748-9326/abd4ab`.

Benestad, R. E., Parding, K. M., Erlandsen, H. B., & Mezghani, A. (2019b). A simple equation to study changes in rainfall statistics. *Environmental Research Letters*, *14*. doi:`10.1088/1748-9326/ab2bb2`.

Benestad, R. E., Parding, K. M., Isaksen, K., & Mezghani, A. (2016). Climate change and projections for the Barents region: What is expected to change and what will stay the same? *Environmental Research Letters*, *11*. doi:`10.1088/1748-9326/11/5/054017`.

Chiang, S. H., & Chang, K. T. (2011). The potential impact of climate change on typhoon-triggered landslides in Taiwan, 2010-2099. *Geomorphology*, *133*, 143–151. URL: `http://dx.doi.org/10.1016/j.geomorph.2010.12.028`. doi:`10.1016/j.geomorph.2010.12.028`.

Ciervo, F., Rianna, G., Mercogliano, P., & Papa, M. N. (2017). Effects of climate change on shallow landslides in a small coastal catchment in southern Italy. *Landslides*, *14*, 1043–1055. doi:`10.1007/s10346-016-0743-1`.

Ciurleo, M., Mandaglio, M. C., & Moraci, N. (2019). Landslide susceptibility assessment by TRIGRS in a frequently affected shallow instability area. *Landslides*, *16*, 175–188. doi:`10.1007/s10346-018-1072-3`.

Comegna, L., Picarelli, L., Bucchignani, E., & Mercogliano, P. (2013). Potential effects of incoming climate changes on the behaviour of slow active landslides in clay. *Landslides*, *10*, 373–391. doi:`10.1007/s10346-012-0339-3`.

Dehn, M., Bürger, G., Buma, J., & Gasparetto, P. (2000). Impact of climate change on slope stability using expanded downscaling. *Engineering Geology*, *55*, 193–204. doi:`10.1016/S0013-7952(99)00123-4`.

Depina, I., Oguz, E. A., & Thakur, V. (2020). Novel Bayesian framework for calibration of spatially distributed physical-based landslide prediction models. *Computers and Geotechnics*, *125*, 103660. URL: `https://doi.org/10.1016/j.compgeo.2020.103660`. doi:`10.1016/j.compgeo.2020.103660`.

Devoli, G., Bell, R., & Cepeda, J. (2019). *NVE report 1/2019: Susceptibility map at catchment level, to be used in landslide forecasting, Norway*. Technical Report 1 NVE Oslo, Norway. URL: `http://publikasjoner.nve.no/rapport/2019/rapport2019_01.pdf`.

Dixon, N., & Brook, E. (2007). Impact of predicted climate change on landslide reactivation: Case study of Mam Tor, UK. *Landslides*, *4*, 137–147. doi:`10.1007/s10346-006-0071-y`.

Dyrrdal, A. V., & Førland, E. J. (2019). *Klimapåslag for korttidsnedbør: Anbefalte verdier for Norge*. Technical Report 5/2019.

Erlandsen, H. B., Parding, K. M., Benestad, R., Mezghani, A., & Pontoppidan, M. (2020). A hybrid downscaling approach for future temperature and precipitation change. *Journal of Applied Meteorology and Climatology*, *59*, 1793–1807. doi:`10.1175/JAMC-D-20-0013.1`.

Eyring, V., Bony, S., Meehl, G. A., Senior, C. A., Stevens, B., Stouffer, R. J., & Taylor, K. E. (2016). Overview of the Coupled Model Intercomparison Project Phase 6 (CMIP6) experimental design and organization. *Geoscientific Model Development*, *9*, 1937–1958. doi:`10.5194/gmd-9-1937-2016`.

Fawcett, T. (2006). An introduction to ROC analysis. *Pattern Recognition Letters*, *27*, 861–874. doi:`10.1016/j.patrec.2005.10.010`.

Fenton, G. A., & Griffiths, D. V. (2008). *Risk assessment in geotechnical engineering*.

Fischer, L., Rubensdotter, L., Sletten, K., Stalsberg, K., Melchiorre, C., Horton, P., & Jaboyedoff, M. (2012). Debris flow modeling for susceptibility mapping at regional to national scale in Norway. In *Landslides and Engineered Slopes: Protecting Society through Improved Understanding - Proceedings of the 11th International and 2nd North American Symposium on Landslides and Engineered Slopes, 2012* (pp. 723–729).

Gariano, S. L., & Guzzetti, F. (2016). Landslides in a changing climate. *Earth-Science Reviews*, *162*, 227–252. URL: `http://dx.doi.org/10.1016/j.earscirev.2016.08.011`. doi:`10.1016/j.earscirev.2016.08.011`.

Haneberg, W. C. (2004). A rational probabilistic method for spatially distributed landslide hazard assessment. *Environmental and Engineering Geoscience*, *10*, 27–43. doi:`10.2113/10.1.27`.

Hanssen-Bauer, I., Førland, E. J., Haddeland, I., Hisdal, H., Lawrence, D., Mayer, S., Nesje, A., Sandven, S., Sandø, A. B., & Sorteberg, A. (2017). *Climate in Norway 2100 – a knowledge base for climate adaptation.* Technical Report 1. URL: `www.miljodirektoratet.no/M741`.

Hay, L. E., Wilby, R. L., & Leavesley, G. H. (2000). A comparison of delta change and downscaled GCM scenarios for three mountain basins in the United States. *Journal Of The American Water Resources Association*, *36*, 387–397. doi:`10.1111/j.1752-1688.2000.tb04276.x`.

Ho, K., Lacasse, S., & Picarelli, L. (2017). *Slope safety preparedness for impact of climate change*. (1st ed.). doi:`10.1201/9781315387789`.

Hu, W., Ming, A. S., Quan, J. W., Fan, J., & Reichardt, K. (2008). Spatial variability of soil hydraulic properties on a steep slope in the loess plateau of China. *Scientia Agricola*, *65*, 268–276. doi:`10.1590/S0103-90162008000300007`.

Huang, J. C., & Kao, S. J. (2006). Optimal estimator for assessing landslide model performance. *Hydrology and Earth System Sciences*, *10*, 957–965. doi:`10.5194/hess-10-957-2006`.

IPCC (2012). *Managing the Risks of Extreme Events and Disasters to Advance Climate Change Adaptation. A Special Report of Working Groups I and II of the Intergovernmental Panel on Climate Change*. Cambridge, UK, and New York, NY, USA: Cambridge University Press.

IPCC (2014). *Climate Change 2014: Synthesis Report*. Technical Report IPCC Geneva, Switzerland.

IPCC (2021). *Climate Change 2021: The Physical Science Basis. Contribution of Working Group I to the Sixth Assessment Report of the Intergovernmental Panel on Climate Change*. Technical Report 3-.

Iverson, R. M. (2000). Landslide triggering by rain infiltration. *Water Resources Research*, *36*, 1897–1910. doi:`10.1029/2000WR900090`.

Jacob, D., Petersen, J., Eggert, B., Alias, A., Christensen, O. B., Bouwer, L. M., Braun, A., Colette, A., Déqué, M., Georgievski, G., Georgopoulou, E., Gobiet, A., Menut, L., Nikulin, G., Haensler, A., Hempelmann, N., Jones, C., Keuler, K., Kovats, S., Kröner, N., Kotlarski, S., Kriegsmann, A., Martin, E., van Meijgaard, E., Moseley, C., Pfeifer, S., Preuschmann, S., Radermacher, C., Radtke, K., Rechid, D., Rounsevell, M., Samuelsson, P., Somot, S., Soussana, J. F., Teichmann, C., Valentini, R., Vautard, R., Weber, B., & Yiou, P. (2014). EURO-CORDEX: New high-resolution climate change projections for

European impact research. *Regional Environmental Change*, *14*, 563–578. doi:`10.1007/s10113-013-0499-2`.

Kartverket (). Høydedata. URL: `https://www.hoydedata.no`.

Liu, C. N., & Wu, C. C. (2008). Mapping susceptibility of rainfall-triggered shallow landslides using a probabilistic approach. *Environmental Geology*, *55*, 907–915. doi:`10.1007/s00254-007-1042-x`.

Lizárraga, J. J., & Buscarnera, G. (2020). Probabilistic modeling of shallow landslide initiation using regional scale random fields. *Landslides*, *17*, 1979–1988. doi:`10.1007/s10346-020-01438-y`.

Melchiorre, C., & Frattini, P. (2012). Modelling probability of rainfall-induced shallow landslides in a changing climate, Otta, Central Norway. *Climatic Change*, *113*, 413–436. doi:`10.1007/s10584-011-0325-0`.

Mergili, M., Marchesini, I., Rossi, M., Guzzetti, F., & Fellin, W. (2014). Spatially distributed three-dimensional slope stability modelling in a raster GIS. *Geomorphology*, *206*, 178–195. URL: `http://dx.doi.org/10.1016/j.geomorph.2013.10.008`. doi:`10.1016/j.geomorph.2013.10.008`.

MET (). What is Frost? URL: `www.frost.met.no`.

Mezghani, A., Dobler, A., Benestad, R., Haugen, J. E., Parding, K. M., Piniewski, M., & Kundzewicz, Z. W. (2019). Subsampling impact on the climate change signal over poland based on simulations from statistical and dynamical downscaling. *Journal of Applied Meteorology and Climatology*, *58*, 1061–1078. doi:`10.1175/JAMC-D-18-0179.1`.

Michel, G. P., Kobiyama, M., & Goerl, R. F. (2014). Comparative analysis of SHALSTAB and SINMAP for landslide susceptibility mapping in the Cunha River basin, southern Brazil. *Journal of Soils and Sediments*, *14*, 1266–1277. doi:`10.1007/s11368-014-0886-4`.

Montgomery, D. R., & Dietrich, W. E. (1994). A physically based model for the topographic control on shallow landsliding. *Water Resources Research*, *30*, 1153–1171. doi:`10.1029/93WR02979`.

Montrasio, L., & Valentino, R. (2008). A model for triggering mechanisms of shallow landslides. *Natural Hazards and Earth System Science*, *8*, 1149–1159. doi:`10.5194/nhess-8-1149-2008`.

Mtongori, H. I., Stordal, F., Benestad, R. E., Mourice, S. K., Justino, F., Kikuu, C., Meteorology, A., & Agricultural, P. (2015). IMPACTS OF CLIMATE AND FARMING MANAGEMENT ON MAIZE YIELD IN Among the major factors controlling agricultural productivity in Africa is climate (Sivakumar , 1988 ; Moore et al ., 2012). While total seasonal rainfall is important in crop production (Mati. *African Crop Science Journal*, *23*, 399–417.

NGU (). Datasets. URL: `https://www.ngu.no/en/topic/datasets`.

NVE (). skredregistrering. URL: `www.skredregistrering.no`.

Pack, R., Tarboton, D., Goodwin, C., & Prasad, A. (2005). SINMAP 2.0: a stability index approach to terrain stability hazard mapping. URL: `http://www.engineering.usu.edu/dtarb/sinmap.html`.

Park, D. W., Nikhil, N. V., & Lee, S. R. (2013). Landslide and debris flow susceptibility zonation using TRIGRS for the 2011 Seoul landslide event. *Natural Hazards and Earth System Science*, (pp. 2833–2849). doi:`10.5194/nhess-13-2833-2013`.

Phoon, K. K., & Kulhawy, F. H. (1999). Characterization of geotechnical variability. *Canadian Geotechnical Journal*, *36*, 612–624. doi:`10.1139/t99-038`.

Raia, S., Alvioli, M., Rossi, M., Baum, R. L., Godt, J. W., & Guzzetti, F. (2014). Improving predictive power of physically based rainfall-induced shallow landslide models: A probabilistic approach. *Geoscientific Model Development*, *7*, 495–514. doi:`10.5194/gmd-7-495-2014`.

Rianna, G., Zollo, A., Tommasi, P., Paciucci, M., Comegna, L., & Mercogliano, P. (2014). Evaluation of the Effects of Climate Changes on Landslide Activity of Orvieto Clayey Slope. *Procedia Earth and Planetary Science*, *9*, 54–63. URL: `http://dx.doi.org/10.1016/j.proeps.2014.06.017`. doi:`10.1016/j.proeps.2014.06.017`.

Rossi, G., Catani, F., Leoni, L., Segoni, S., & Tofani, V. (2013). HIRESSS: a physically based slope stability simulator for HPC applications. *Natural Hazards and Earth System Science*, *13*, 151–166. doi:`10.5194/nhess-13-151-2013`.

Salciarini, D., Brocca, L., Camici, S., Ciabatta, L., Volpe, E., Massini, R., & Tamagnini, C. (2019). Physically based approach for rainfall-induced landslide projections in a changing climate. *Proceedings of the Institution of Civil Engineers: Geotechnical Engineering*, *172*, 481–495. doi:`10.1680/jgeen.18.00216`.

Sangelantoni, L., Gioia, E., & Marincioni, F. (2018). *Impact of climate change on landslides frequency: the Esino river basin case study (Central Italy)* volume 93. Springer Netherlands. doi:`10.1007/s11069-018-3328-6`.

Scheidl, C., Heiser, M., Kamper, S., Thaler, T., Klebinder, K., Nagl, F., Lechner, V., Markart, G., Rammer, W., & Seidl, R. (2020). The influence of climate change and canopy disturbances on landslide susceptibility in headwater catchments. *Science of the Total Environment*, *742*, 140588. URL: `https://doi.org/10.1016/j.scitotenv.2020.140588`. doi:`10.1016/j.scitotenv.2020.140588`.

Shou, K. J., & Yang, C. M. (2015). Predictive analysis of landslide susceptibility under climate change conditions - A study on the Chingshui River Watershed of Taiwan. *Engineering Geology*, *192*, 46–62. URL: `http://dx.doi.org/10.1016/j.enggeo.2015.03.012`. doi:`10.1016/j.enggeo.2015.03.012`.

Simoni, S., Zanotti, F., Bertoldi, G., & Rigon, R. (2008). Modelling the probability of occurrence of shallow landslides and channelized debris flows using GEOtop-FS. *Hydrological Processes*, *22*, 532–545. doi:`10.1002/hyp.6886Modelling`.

Takayabu, I., Kanamaru, H., Dairaku, K., Benestad, R., von Storch, H., & Christensen, J. H. (2016). Reconsidering the quality and utility of downscaling. *Journal of the Meteorological Society of Japan*, *94A*, 31–45. doi:`10.2151/jmsj.2015-042`.

Taylor, K. E., Stouffer, R. J., & Meehl, G. A. (2012). An overview of CMIP5 and the experiment design. *Bulletin of the American Meteorological Society*, *93*, 485–498. doi:`10.1175/BAMS-D-11-00094.1`.

Usowicz, B., & Lipiec, J. (2021). Spatial variability of saturated hydraulic conductivity and its links with other soil properties at the regional scale. *Scientific Reports*, *11*, 1–12. URL: `https://doi.org/10.1038/s41598-021-86862-3`. doi:`10.1038/s41598-021-86862-3`.

Weidner, L., Oommen, T., Escobar-Wolf, R., Sajinkumar, K. S., & Samuel, R. A. (2018). Regional-scale back-analysis using TRIGRS: an approach to advance landslide hazard modeling and prediction in sparse data regions. *Landslides*, *15*, 2343–2356. doi:`10.1007/s10346-018-1044-7`.

Wu, W., & Sidle, R. C. (1995). A distributed slope stability model for steep forested basins. *Water Resources*, *31*, 2097–2110.

Xgeo (). Varsom Xgeo. URL: `http://www.xgeo.no/aboutXgeo.html?show=on`.

Paper III: IoT-based hydrological monitoring of water-induced landslides: a case study in central Norway

Bulletin of Engineering Geology and the Environment (2022) 81:217
https://doi.org/10.1007/s10064-022-02721-z

ORIGINAL PAPER

IoT-based hydrological monitoring of water-induced landslides: a case study in central Norway

Emir Ahmet Oguz[1] · **Ivan Depina**[2,5] · **Bård Myhre**[3] · **Graziella Devoli**[4] · **Helge Rustad**[3] · **Vikas Thakur**[1]

Received: 31 December 2021 / Accepted: 21 April 2022

Abstract

Water-induced landslides pose a great risk to the society in Norway due to their high frequency and capacity to evolve in destructive debris flows. Hydrological monitoring is a widely employed method to understand the initiation mechanism of water-induced landslides under various climate conditions. Hydrological monitoring systems can provide relevant information that can be utilized in landslide early warning systems to mitigate the risk by issuing early warnings. These monitoring systems can be significantly enhanced, and wider deployments can be achieved through the recent developments within the domain of the Internet of Things (IoT). Therefore, this study aims to demonstrate a case study on an automated hydrological monitoring system supported by the IoT-based state-of-the-art technologies employing public mobile networks. Volumetric water content (VWC) sensors, suction sensors, and piezometers were used in the hydrological monitoring system to monitor the hydrological activities. The monitoring system was deployed in a case study area in central Norway at two locations of high susceptible geological units. During monitored period, the IoT-based hydrological monitoring system provided novel and valuable insights into the hydrological response of slopes to seasonally cold climates in terms of VWC and matric suction. The effects of rainfall, snow melting, ground freezing, and thawing were captured. The current study also made an attempt to integrate the collected data into a physical-based landslide susceptibility model to obtain a more consistent and reliable hazard assessment.

Keywords Hydrological monitoring · IoT · Water-induced · Landslide · Rainfall · Snow melt

Introduction

A landslide is defined as the downslope movement of soil, rock, and organic materials under the effects of gravity. The adverse consequences of landslides such as fatalities, injuries to people, economic losses, and environmental damages are well known and documented in the literature (Froude and Petley 2018; Haque et al. 2019; Lacasse et al. 2010; Nadim et al. 2006; Petley 2012). According to the statistics of the Centre for Research on the Epidemiology of Disasters (CRED 2021), the Emergency Events Database, retrieved in November 2021, roughly 488,000 deaths happened since 2000 due to natural hazards associated with landslides, which also includes ground movement due to earthquakes. According to the database, the overall value of damages and economic losses, directly or indirectly related to landslides, was estimated to be over US$ 310 billion since 2000.

Landslides can be triggered by a wide range of factors including rainfall, snow melt, earthquakes, human activities, erosion, or a combination of different phenomena. Among different triggering factors, water is mainly involved in the majority of slope destabilizations (Michoud et al. 2013; Pecoraro et al. 2018). Water-induced landslides are one of the major hazards in Norway due to their high frequency on hillsides and capacity to turn into a high-speed destructive debris flow. They might be triggered by extreme rainfall

---

✉ Emir Ahmet Oguz
emir.a.oguz@ntnu.no

[1] Department of Civil and Environmental Engineering, Norwegian University of Science and Technology, NO-7491 Trondheim, Norway

[2] Department of Rock and Geotechnical Engineering, SINTEF, Torgarden, 4760, NO-7465 Trondheim, Norway

[3] Department of Connectivity Technologies and Platforms, SINTEF, Torgarden, 4760, NO-7465 Trondheim, Norway

[4] Norwegian Water Resources and Energy Directorate (NVE), Middelthuns Gate 29, 0368 Oslo, Norway

[5] Faculty of Civil Engineering, Architecture, and Geodesy, University of Split, Matice hrvatske 15, 21000 Split, Croatia

events, snow melt, or a combination of rainfall and snow melt. Such water-induced landslides can be initiated due to the increase in the soil water content and increasing soil weight, loss of soil suction, erosion, or artesian pressure.

The slopes in hillsides are usually unsaturated before landslide initiation (Bordoni et al. 2015). The behavior of unsaturated slopes depends highly on volumetric water content (VWC) and corresponding changes in suction (SafeLand 2012). Triggering events such as rainfall or snow melting lead to an increase in VWC and reduction in suction values, both of which are the parameters affecting unsaturated shear strength and eventually stability of the slopes. At the instant of water-induced landslide initiation, initiated slope might be either saturated with positive pore pressure due to perched water table or unsaturated with the presence of suction. Several studies performed hydrological monitoring in hillsides in order to clarify the underlying initiation mechanism of water-induced landslides (Bordoni et al. 2021, 2015; Crawford et al. 2019; Godt et al. 2009; Kim et al. 2021; Smith et al. 2014; Wei et al. 2020). Hydrological monitoring can provide important insights into the hydrological processes occurring in similar slopes (Comegna et al. 2016) such as water infiltration and corresponding changes in VWC and suction (Li et al. 2005).

In the study of Godt et al. (2009), landslide occurrence was reported in a natural slope under partially saturated conditions based on the hydrological monitoring data. The study revealed that VWC and matric suction data can be used to predict the occurrence of partially saturated shallow landslides by employing the method of infinite slope stability for unsaturated conditions (Lu and Godt 2008). Similarly in the literature, the hydrological monitored data on the VWC and suction were excessively employed in combination with the infinite slope stability method for unsaturated conditions to assess the stability condition of slopes (Bordoni et al. 2015; Kim et al. 2021; Wei et al. 2020; Yang et al. 2019). Additionally, Song et al. (2021) employed hydrological monitoring in an early warning system with the hazard levels based on the monitored parameters and corresponding stability assessment.

In this study, we examined a landslide-prone study area in central Norway where the landslide events initiate mainly due to intense rainfall events, snow melting, or a combination of them. To understand the initiation mechanism, hydrological monitoring systems were deployed at two locations with two geological units, which are susceptible to sliding. Hydrological activities were monitored with VWC sensors, suction sensors, and piezometers. In practice, such monitoring systems have been challenging due to conventional monitoring systems including costly sensors, inflexible cable-based systems, limited scalability and flexibility, and regular maintenance. However, new, small, and less expensive types of wireless sensors for monitoring geotechnical parameters started to emerge in the market, being inspired by the enabling technology of the Internet of Things (IoT). Several research studies on adopting the IoT concept in landslide monitoring (Abraham et al. 2020; Bhosale et al. 2017; Chaturvedi et al. 2018; Hou 2018) indicate that IoT can improve conventional monitoring with the provision of cost efficiency, flexibility, and ease to scale the system. Therefore, the hydrological monitoring system, in this study, was developed based on the state-of-the-art IoT technology employing public mobile networks. This provided more efficient deployment and operation of the monitoring system compared to the conventional systems. The architecture of the developed system was demonstrated by means of functional roles in typical IoT-based systems. Through deployed IoT-based hydrological monitoring system, valuable insights into the hydrological response of the slopes to seasonally cold climate conditions in Norway were obtained. The usage of collected data in landslide prediction over the study area was illustrated through an automated physical-based model, as an attempt to provide a basis for an early warning system.

On this background, the remainder of the paper is structured as follows: the "Background in IoT" section provides the background in IoT and the typical system architecture with the functional roles in an IoT ecosystem. This section will serve as a baseline for the IoT application of the current study. In the "Deployed IoT-based hydrological monitoring system" section, the deployed IoT-based hydrological monitoring system will be presented. Then, the "Case study of the IoT-based hydrological monitoring system" section will present the study area, the deployment of the system in the field, and data acquisition and interpretation of collected data. The "Data processing and early warning strategies" section will provide data processing and early warning strategies as an attempt to assess the stability condition over the study area based on collected data via a physical-based model. Finally, the "Discussion" section focuses on several discussion points, and the "Summary" section summarizes the paper.

Background in IoT

Over the last two decades, employing wireless sensors to monitor hydrological conditions has gradually moved from being an idea towards reality. As an example, Anumalla et al. (2005) pointed out the need for cost-efficient groundwater measurements, suggesting "the development of an infrastructure for acquiring, transferring and analyzing real-time data" using a modified Wi-Fi network. Some 15 years later, several companies now offer wireless groundwater sensor networks, using various wireless solutions (e.g., Trimble Water 2021; Worldsensing 2021). However, the geotechnical community is still lacking a unified and de facto standard

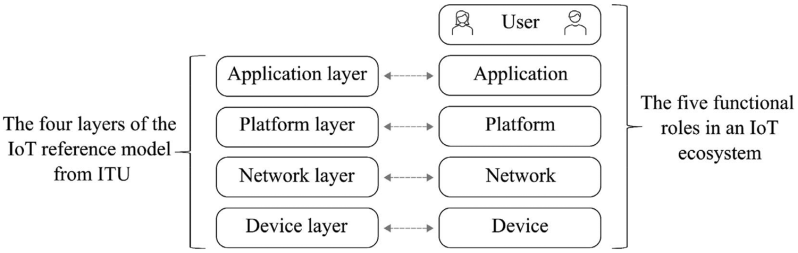

Fig. 1 The four layers of the IoT reference model as defined by ITU (to the left) and the corresponding functional roles in an IoT ecosystem (to the right) (modified after ITU 2012)

for wireless communication, not being anywhere close to the availability in personal communication and Internet access brought forth by Wi-Fi, 3G, and 4G.

For the employment of the IoT within the geotechnical engineering domain, one could benefit from some guidance on the IoT concept. One such guide can be found with the International Telecommunication Union (ITU), which issued a recommendation (ITU 2012) that aimed to provide an overview of the IoT with the main objective of highlighting this important area for future standardization. This recommendation can provide a baseline and reference for IoT applications within the geotechnical engineering domain. ITU (2012) states that the IoT can be perceived as a far-reaching idea with technological and societal implications. This is followed up by a high-level technical overview and generic requirements but without any specific details on technologies or quantifiable characteristics. ITU does however introduce an IoT reference model, consisting of four distinct layers with associated capabilities. Furthermore, ITU extends the IoT reference model with an IoT ecosystem model, adding the human user as an integral part of the IoT ecosystem.

The IoT reference model consists of four distinct layers, shown on the left part of Fig. 1, being the Device, Network, Platform, and Application layers. The Device layer consists of electronic devices that interact with physical objects and the environment, typically being sensors or actuators. These electronic devices will typically use a Network layer to communicate with a Platform layer.[1] The Network layer includes any physical or logical network providing access to a larger communication network (e.g., the Internet). The Platform layer will, on the other side, include any services related to data storage, basic data processing, and device management. This way, the Network layer addresses transportation of data, while the Platform layer addresses storage and processing of data. Finally, the Application layer performs application-specific processing, evaluation, and presentation, based on data retrieved from the Platform layer.

In the IoT ecosystem model, shown on the right side of Fig. 1, the four layers from the IoT reference model are transformed into four roles that cover the exact same functionality as the layers. These roles are conveniently called Device, Network, Platform, and Application. However, the ecosystem model also introduces a fifth role, the User,[2] who receives information from the Application role. Although the addition of the User role may seem both trivial and obvious, this extension explicitly acknowledges that no system can be regarded complete without a beneficiary. It also directs attention to the importance of addressing user needs when developing any technical system. Therefore, this study will use the IoT ecosystem model as a reference on how to understand and develop any IoT system.

Deployed IoT-based hydrological monitoring system

Figure 2 illustrates an overall concept of IoT-based hydrological monitoring and early warning system with the five functional roles in an IoT ecosystem shown in Fig. 1. In the Device layer, the sensors should be selected based on the triggering mechanism of the landslides and are responsible for sensing, actuating, controlling, and monitoring activities (Ray 2018). The monitored data is transferred to the Platform layer by the Network layer, which may involve different technologies depending on the network solutions, e.g., public mobile networks, satellite services, or unlicensed wireless technologies such as LoRa, Sigfox, and Wireless M-Bus. The Platform layer can then serve as a provider of data for hydrological monitoring and early warning systems, based on either local or cloud-based data storage and basic processing services. In the Application layer, the data from the Platform layer might be used to assess the stability conditions of a single slope or, more generally, slopes over a landslide-prone region. This can be done by relating the collected data to the stability conditions by defining threshold

---

[1] Note that ITU references the “Platform layer” as “Service support and Application support layer”.

[2] Note that ITU references the “User” role as “Application customer”.

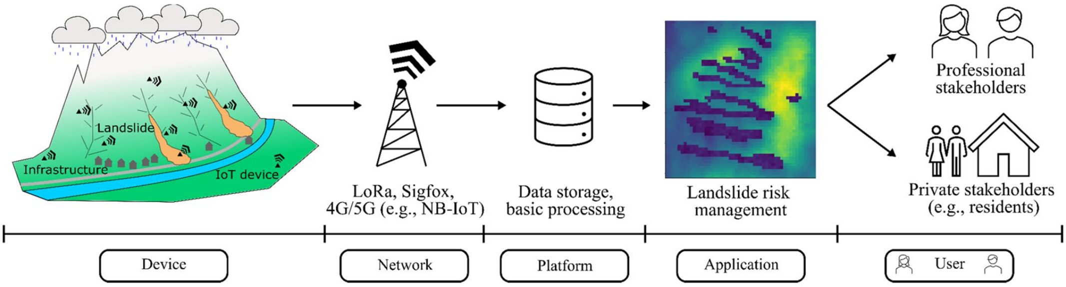

Fig. 2 The overall concept of the IoT-based hydrological monitoring of water-induced landslides and early warning systems (modified after Oguz et al. 2019)

values for different warning levels based on the monitored parameters or by utilizing physical-based models or data-driven approaches (e.g., machine learning algorithms). The Application issues warnings or transmits the landslide stability conditions to the User. The User could, for instance, be either a professional user representing authorities or infrastructure owners or residents/public that are exposed to the landslide risk in an area of relevance.

This paper focuses mainly on two of the aspects, namely how the Device role can be implemented using public mobile networks and how the collected data can be utilized in the Platform layer to understand the hydrological processes important for the stability of slopes over the study area. The other three roles, Network, Application, and User will play a less prominent part within this paper. However, they are still included to a certain detail as they are essential when it comes to establishing a fully operational IoT ecosystem.

Development of the device, network, and platform

Figure 3 illustrates the developed system architecture through the functional roles for the IoT ecosystem. Representing the Device role in Fig. 3, the IoT Devices were constructed, each consisting of two excitation units supporting one piezometer each, one Sparkfun Thing Plus Artemis microcontroller board providing interfaces to all the external sensors, one Nordic Thingy:91 Prototyping Platform communication module providing 4G connectivity through public mobile networks, and one battery pack providing power to the IoT Device. For each IoT Device, a sensor suite of up to three VWC sensors, three suction sensors, and two piezometers was supported. Each sensor was to be sampled every 15 min, with wireless transmission of the acquired measurements once every hour using the public mobile (4G) network. Furthermore, the IoT devices were required to operate on battery for 12 months without any maintenance. Regarding the selection of communication solution, the motivation for employing the public mobile network was to investigate how emerging 4G-based IoT technologies, intended for machine-type communication would work in practice, with regard to both technical integration and deployment in the field. Within the 4G/LTE[3] standard, Narrowband IoT (NB-IoT) and Long Term Evolution Machine Type Communication (LTE-M) were considered to be the most relevant technologies for long-term sensors, as both are directed at machine-type communication (Höglund et al. 2017). The difference between them lies mainly in flexibility and cost: NB-IoT is focused on low-cost and low-power applications for stationary devices (e.g., sensors), while LTE-M supports higher data rates and handover to neighboring cells at the cost of somewhat higher power consumption (Höglund et al. 2017). This may indicate that NB-IoT is a reasonable choice for geotechnical applications, supporting long-time operation in fixed positions. However, several manufacturers provide combined chipsets for NB-IoT and LTE-M (e.g., Nordic Semiconductor 2021), and within the field of professional geotechnical monitoring, it may be expected that flexibility is more important than extreme low-cost communication. Thus, the Nordic Thingy:91 Prototyping Platform, being built upon the RF9160 System-in-Package by Nordic Semiconductor supporting both LTE-M and NB-IoT, was selected as the communication module for the IoT Device.

Representing the Network role in Fig. 3, the public Mobile network provided wireless 4G coverage in the entire study area. As this service was commercially available at the time of the case study, the project's work on network coverage was limited to acquiring relevant subscriptions with relevant Norwegian national mobile operators and verifying connectivity in the study area. Due to practical issues related

---

[3] The terms 4G and LTE can for all practical purposes be used interchangeably. However, from a technical point of view, "4G" refers to a set of requirements for mobile access, while "LTE" refers to a specific technology that fulfills the "4G" requirements (Dahlman et al. 2016).

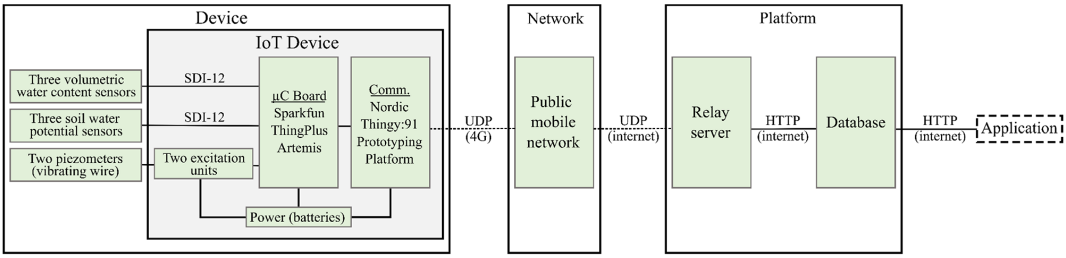

Fig. 3 System architecture and functional roles for the IoT ecosystem, including internal components of the IoT Device (Protocols: UDP: User Datagram Protocol, SDI-12: Serial Data Interface at 1200 baud, and HTTP: Hypertext Transfer Protocol)

to the selected subscriptions and national rollout plans for NB-IoT and LTE-M, the IoT Devices were configured to make use of the LTE-M part of the 4G network.

Representing the Platform role in Fig. 3, the sensor measurements were transmitted to a cloud-based Relay server, implemented on a virtual Linux server. The Relay server received UDP messages from the IoT Devices and forwarded these to a cloud-based database running on a commercial web hotel. The database served as persistent storage for sensor measurements and provided an external application programming interface (API) for downloading sensor measurements over the Internet in CSV format.

For the Application role in Fig. 3, any software that uses the data that has been made available through the database should be regarded as an application. In this paper, the Application role is being manifested by the data processing and early warning strategies with an attempt to assess the stability condition over the study area based on collected data via a physical-based model in the "Data processing and early warning strategies" section.

During the past decade, there have been several developments on IoT-based systems for landslide prediction and early warning with different architectures and varying technologies in Device and Network layers. Some of these studies, e.g., Chaturvedi et al. (2018), Khaing and Thein (2020), Pathania et al. (2020), Soegoto et al. (2021), and Sruthy et al. (2020), showed the feasibility of such IoT-based systems in data acquisition and transfer using different communication technologies. The Application roles in these studies mainly appear as landslide warning systems based on threshold levels inferred from the monitored parameters. In the current study, the physical-based modeling was employed in the Application layer and provided in the "Data processing and early warning strategies" section. In data communication, these studies employed advancements brought forth by wireless solutions, such as Wi-Fi, Bluetooth, and 2G-3G/GSM-based cellular communication. Recent developments in the domain of IoT applications provided new opportunities through a new networking concept, called Low Power Wide Area Networks (LPWANs). LPWANs address the limitations of abovementioned wireless solutions by providing cost- and power-efficient wireless data transmission over long distances. Several technologies enabling LPWAN deployments have been developed in the last few years (Mekki et al. 2019). Among them, SigFox, LoRa, LTE-M, and NB-IoT can be considered, currently, as leading technologies. In this study, the state-of-art networking solutions, NB-IoT and LTE-M, employing 4G public mobile network were utilized in the Network layer.

Sensors

The selection of sensors for the monitoring system is based on capturing the development of the main triggering conditions for the landslides in the studied area, IoT system constraints, and the implemented landslide modeling strategies. Given that the landslides are mainly triggered by the changes in hydrological conditions in response to rainfall and snow melt events, the selection of sensors is based on monitoring the development of hydrological conditions. The system consists of VWC sensors, suction sensors, and piezometers. Monitoring of surface-water and channel flow was not implemented due to the corresponding sensory solutions requiring power and data transfer exceeding the constraints of the IoT system. Although monitoring snow amounts would be of great value for the project, this was not implemented in the project due to substantial power requirements for such sensory solutions. However, the effects of snow melting and soil thawing on the development of the hydrological conditions are monitored indirectly with the VWC and suction sensors. These sensors provide temperature measurements in addition to the respective measurements of VWC and matric suction. Details on the selected sensors are provided in the following paragraphs.

VWC is measured by soil moisture sensors, TEROS 12 (METER Group 2021a). The sensor sends an electromagnetic field, a 70-MHz oscillating wave to the sensor needles that charge according to the dielectric and VWC of the surrounding soil medium. The sensor outputs a raw output voltage based on the charging time, which is proportional to the surrounding VWC. Then, the raw output voltage (mV) is converted to the VWC using a calibration equation. Although the manufacturer provides an average calibration equation for mineral soils, the custom calibration equation should be developed for the specific surrounding soil to get more accurate values, as shown in the "Laboratory tests" section.

Matric suction is measured by a soil water potential sensor, i.e., suction sensor, TEROS 21 (METER Group 2021b). The suction sensor measures the water potential in the engineered ceramic discs through the dielectric permittivity. Using the known soil water characteristics (SWCC) of the discs (i.e., the relationship between the VWC and matric suction), the matric suction is calculated. As the suction sensors are not affected by the surrounding soil type but work using the known characteristics of the ceramic discs, calibration for a specific soil type is not necessary. The suction sensor output is directly in kPa, and no conversion is needed. The measurement range is from 9 kPa to the air-dry state. However, the sensor is calibrated to provide the most accurate results in the range of 10 to 100 kPa with the accuracy being ± 10%. The predictions for drier cases rely on the linear relationship between the water potential and water content on a logarithmic scale.

Piezometers from the M-600 series (Geonor 2021) are used to measure the pore water pressure or groundwater level measurements. The piezometer is a vibrating wire sensor that measures changes in pressure based on changes in the natural frequency of a wire that is connected to a membrane that deforms with varying values of pressure on the membrane. Each piezometer is tested and calibrated in the lab by the manufacturer prior to being shipped for installation. Each of the piezometers is supplied with a calibration chart and a conversion equation to translate the frequency output of the sensor to pore pressure values.

Case study of the IoT-based hydrological monitoring system

Study area

The study area is between Hegra and Meråker located in the county of Trøndelag, central Norway (Fig. 4a). The area is a part of the catchment of the Sjørdal river and is about 200 km^2 in size. This area was chosen for the implementation of a landslide monitoring system due to being prone to shallow landslide events, with relatively steep slopes, above 20–25°, and having clear evidence of recent landslide events. Additionally, the other reasons for choosing the study area are the availability of nearby weather stations and groundwater measurements and mobile network (4G) coverage.

The bedrock in the study area is composed of Proterozoic and Cambrian metamorphic rocks deformed during the Caledonian orogenesis, covered by a thin cover of Quaternary deposits of different origins (Fig. 4b). A shallow cover of altered bedrock prevails on top of the bedrock in the western sector, formed on-site by physical or chemical decomposition of the bedrock. In the central and eastern sector, the bedrock is covered by an incoherent or thin cover of till deposits (also herein called moraine deposits), picked up, transported, and deposited by glaciers. It is usually hard-packed, poorly sorted, and can contain everything from clay to stone and block. The thickness of these deposits is mainly less than 0.5 m, but it can be much thicker locally. A humus/thin peat cover can be also observed on top of the bedrock with a thickness of 0.2–0.5 m, locally thicker. Rock exposures are frequently visible in this sector. Thick moraine deposits (with a thickness of 0.5 m to several tens of meters) and colluvial deposits left by previous landslides are not particularly representative in the study area and can be observed only locally at a few places. The bottom of the Stjørdal valley is filled with fluvial deposits, with a thickness that varies from 0.5 to more than 10 m, composed of sorted and rounded sand and gravel material. Glaciofluvial deposits are also locally represented and consist of sorted, often sloping layers of different grain sizes. Along the Sjørdal river locally, it is possible to observe marine and fjord deposits, that consist of fine-grained, marine deposits with a thickness from 0.5 m to several tens of meters.

The study area is highly susceptible to different types of landslides in soils, such as debris slides, clay/silty slides, debris avalanches, and debris flows. The area is part of the landslide domain called "Trøndelagkysten" (Devoli and Dahl 2014), where slides in clayey-silty soils are the most frequent landslide types during periods of intense rainfall or rainfall combined with intense snow melting episodes that produce high groundwater and high soil saturation. Debris slides, debris avalanches, and debris flows in moraine deposits were also observed. The high susceptibility of the study area was also confirmed by other landslide susceptibility assessments performed at the national level (Devoli et al. 2019; Fischer et al. 2012). The analysis of the Norwegian national database of mass movements (NVE n.d.), showed that 93 mass movements were registered in the study area between 1750 and 2020. Figure 5 shows the registered landslide events mainly along the main transportation lines with the regional landslide susceptibility levels. Among these registered landslide events, 36 events (35 landslides in soil and 1 slushflow) were triggered by rainfall and snowmelt.

As the majority of soil-related landslide events initiated in fluvial and moraine deposits, both types of Quaternary deposits were selected to be monitored. Following the detailed investigation in the study area, two monitoring

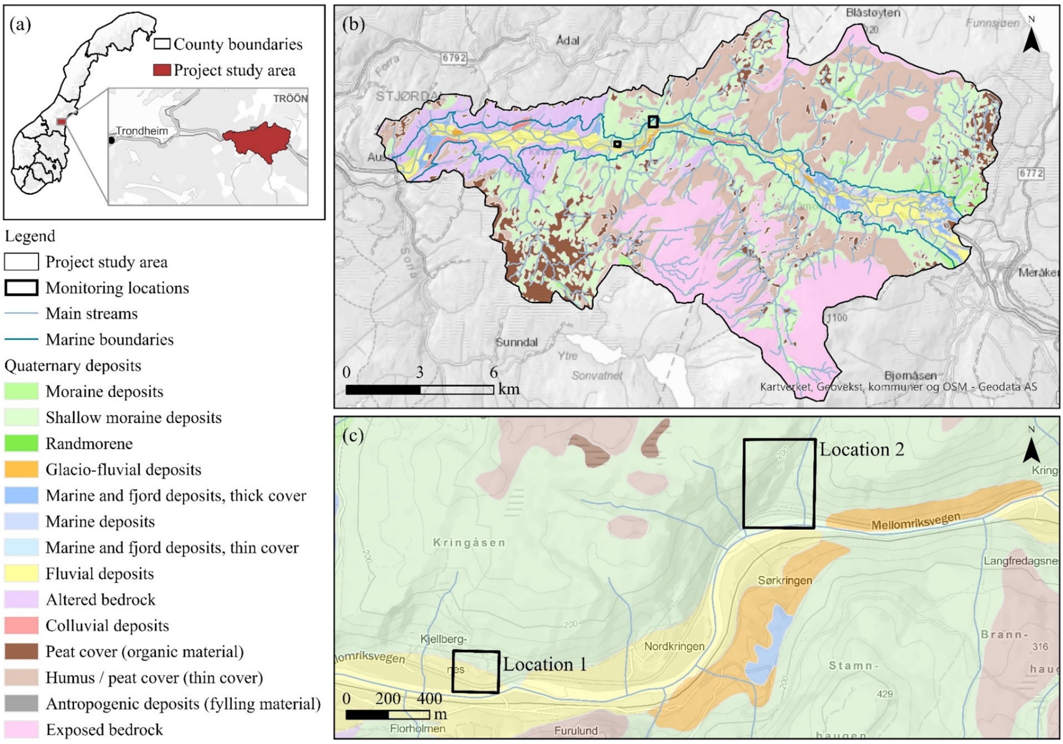

Fig. 4 **a** Study area in national and regional scale, **b** Quaternary geology over the study area, and **c** two selected monitoring locations, Location 1 and Location 2, at detailed scale

locations, which will be called "Location 1" and "Location 2" (Fig. 4c), were selected for further investigation and the installation of IoT-based hydrological monitoring systems.

Location 1, Kjelberget, is a south-facing open slope, ridge form, slightly channelized. The bedrock is covered by the thick fluvial deposit on the hillside towards the bottom of the valley, while a thin cover of moraine deposit appears on the higher parts of the hill (above 80–85 m average sea level). Location 2, Kvernbekkneset, is also a south-facing slope with a clear channelized shape and two main channels that run along this area. The bedrock is covered by moraine deposits that are locally less than 0.5 m thick.

In the national database of mass movements, three landslide events at Location 1 and one landslide event at Location 2 were recorded. Despite being poorly described, the events can be classified as flows and in the category of debris slide in Location 1 and debris flow in Location 2. The events were shallow with a small volume estimated in the range of 5–50 thousand m^3. Pictures of the deposits found in newspapers revealed that all events were characterized by high water content. The analysis of hydrometeorological conditions indicated that the landslides in both locations were triggered by intense rainfall, with values between 60 and 80 mm/24 h or by a combination of intense rainfall combined with intense snow melting (40–60 mm/24 h of water supply).

Laboratory tests

For the characterization of the geological units present at the two monitoring locations, i.e., fluvial and moraine deposits, excavation trial pits on intact slopes were constructed, and soil samples were collected for laboratory testing. In situ density measurements were performed for top soil crust with the water replacement test (ASTM D5030/D5030M-21 2021) at Location 1. Additionally, laboratory tests including methods for water content and organic content determination, sieve analysis and hydrometer tests for soil classification, pycnometer test for soil specific gravity, and large-scale direct shear tests were performed.

The measurements of wet in situ density resulted in approximately 13–15 kN/m^3 at the top 0.5 m crust at both

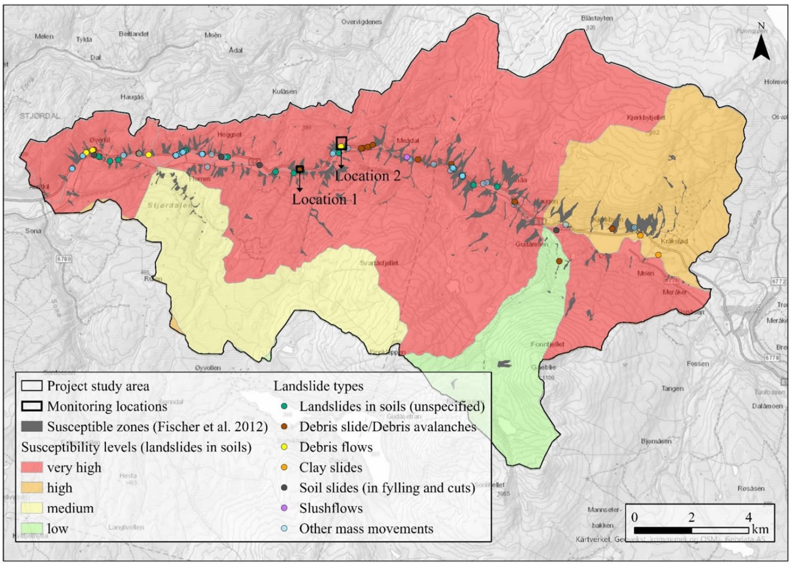

Fig. 5 Registered landslide events over the study area with regional susceptibility

locations. At Location 1, the water replacement test resulted in a wet in situ density of 18 kN/m^3 at 0.9 m depth with a gravimetric water content of 8.88%. Additionally, it was observed that the top 20–40 cm crust has much higher organic content than deeper depths at both locations.

Complete grain size distribution curves were obtained for both fluvial and moraine deposits by performing wet sieve analysis and hydrometer tests. Figure 6 shows the grain size distribution curves of both soil types. The fractions of fines, sands, and gravels are 12.9 – 46.3 – 40.8%, respectively, for fluvial deposit and 16.2 – 57.7 – 26.1% for moraine, respectively. The uniformity coefficient (c_u) and coefficient of curvature (c_c) of fluvial deposits are 40.1 and 0.4, respectively, and of moraine are 29.7 and 0.7, respectively. Both soil types were classified as silty sand according to the European Soil Classification System (ISO 14688–2:2017 2017).

For the VWC sensors, custom calibration equations were developed by recording sensory outputs on samples of fluvial and moraine deposits in a controlled lab environment with known values of VWC. The collected soil samples were saturated at different degrees of saturation level and compacted to satisfy the in situ density measurements. Figure 7 shows the calibration curves for the VWC sensors with the laboratory data and the calibration curve provided by the manufacturer. The results revealed that the raw output voltage values correspond to lower VWC values in comparison

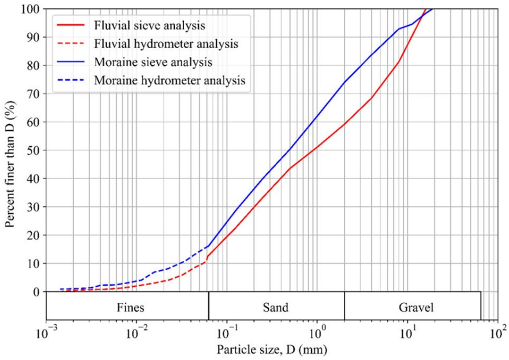

Fig. 6 Grain size distribution of moraine and fluvial deposits

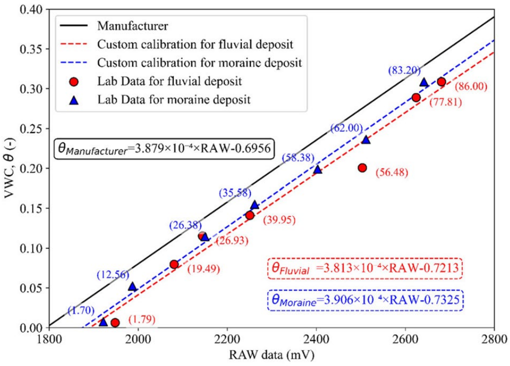

Fig. 7 Calibration chart for VWC sensor

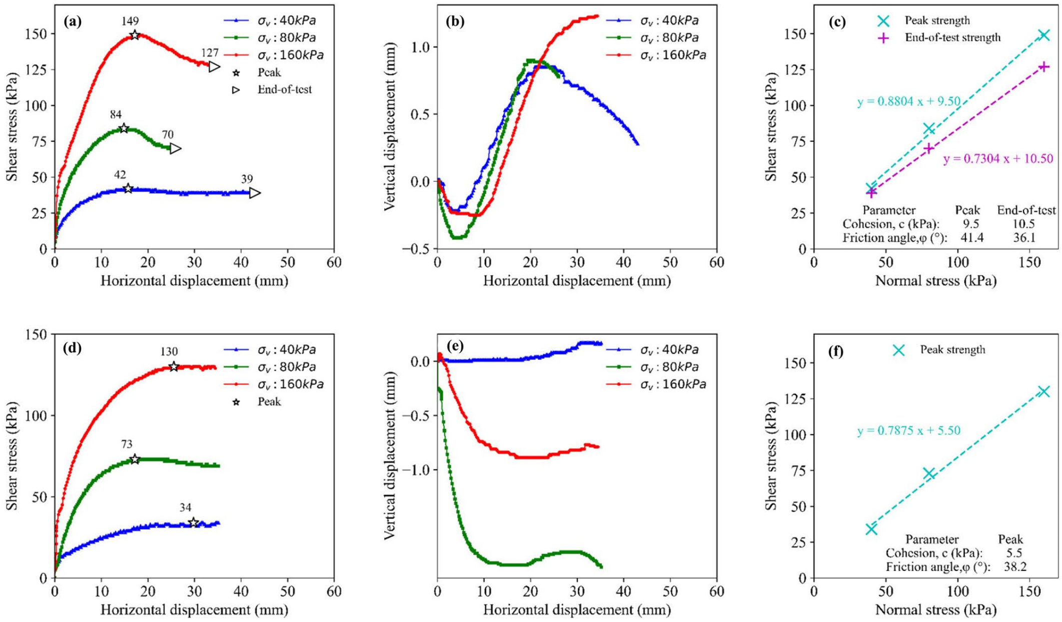

Fig. 8 Large scale direct shear test results for fluvial deposits (**a**, **b**, **c**) and moraine (**d**, **e**, **f**); shear stress data (**a**, **d**), vertical displacement data (**b**, **e**), and determination of shear strength parameters (**c**, **f**)

to the VWC values from the manufacturer's calibration equation. In Fig. 7, the values in the parentheses are the corresponding degree of saturation, Sr (%), for the soil samples used in the calibration. These custom calibration equations, developed for fluvial and moraine deposits individually, are utilized to convert the sensory reading in mV to the VWC values in m^3m^{-3}.

Large-scale (30 × 30 cm) direct shear tests (ASTM D3080/D3080M−11 2021) were performed to estimate soil strength parameters due to the high fraction of coarse particles. Soil samples were collected from the trial pits at both locations. Soil specimens for each soil type were reconstituted by compacting the samples in the shear box to their in situ density. The tests were conducted at drained conditions with a constant shear strain rate of 1 mm/min. Figure 8 shows the large-scale direct shear test result for fluvial deposits in Fig. 8a−c, and for moraine deposits in Fig. 8d−f. Figure 8a, d shows the shear stress recorded during shearing under different levels of vertical stresses. As the fluvial deposits were in a dense state, a peak and a residual strength have been observed. The vertical displacement data in Fig. 8b also complies with the behavior of a dense soil sample showing an initial contraction and then dilation until the failure. The end-of-test condition was defined as 10–15% strain along the shear plane where shear stress becomes constant and asymptotic to horizontal after the peak. Peak and end-of-test strength parameters can be seen in Fig. 8c for fluvial deposits, and only peak strength parameters are shown in Fig. 8f for moraine. The results of the large-scale direct shear tests, namely shear strength parameters, were considered in the calibration of the physical-based landslide prediction model, which can be a basis for a landslide early warning system (the "Data processing and early warning strategies" section).

Deployment of the devices in the field

The IoT-based hydrological monitoring systems were deployed at both locations with two monitoring points at each site. Due to the presence of the water channel down the hillside at both locations, the monitoring points were located on both sides of the channels at different elevations to catch possible variations in the hydrological responses along the side of the channel. The monitoring points are shown in Fig. 9b for Location 1 and in Fig. 11b for Location 2. In addition to the two monitoring points, a weather station (Fig. 9d) was installed at Location 1 to monitor the weather conditions.

The VWC and suction sensor were placed within the top 1 m of the soil as the deposits in Location 2 were observed to be locally thin, with the thickness being below 1 m. These sensors were implemented at three depths at both locations

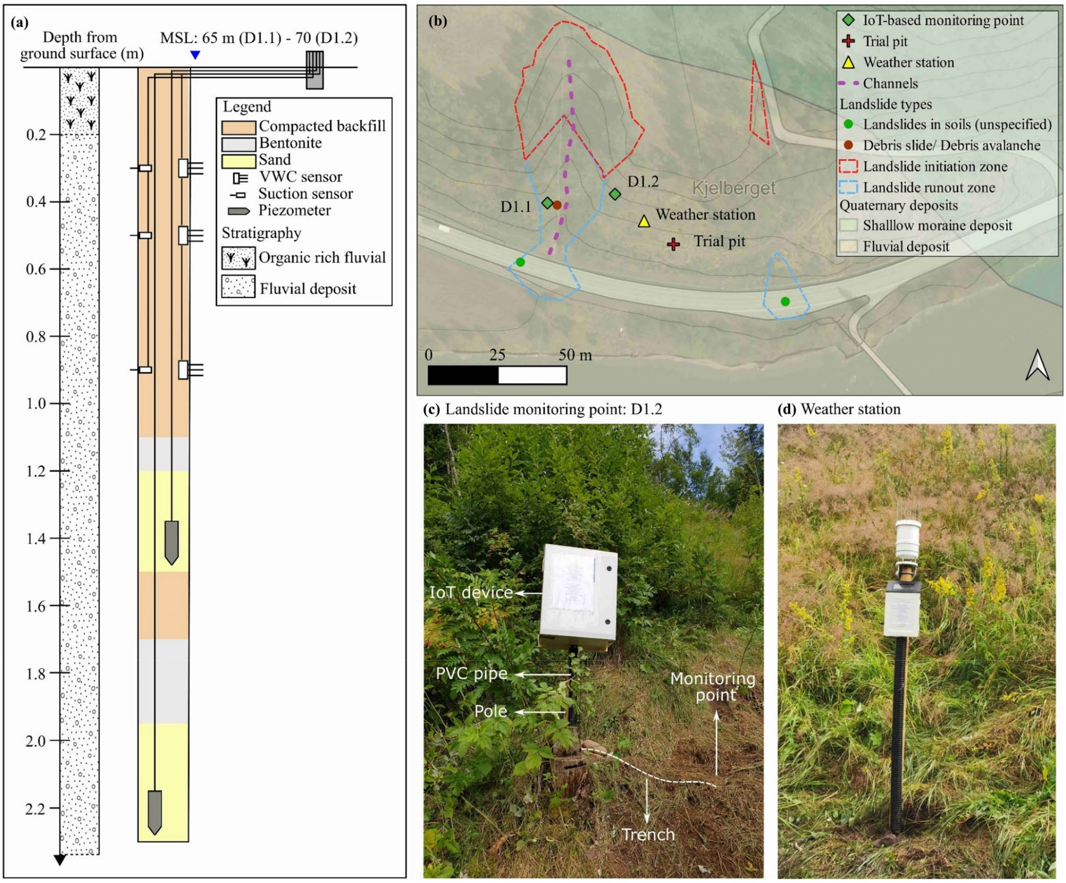

Fig. 9 Location 1: IoT-based hydrological monitoring system: **a** sensor column with soil stratigraphy, **b** aerial picture with Quaternary map, **c** monitoring point D1.2, and **d** weather station

to capture some of the nonlinearity of the infiltration process. In Location 1, the fluvial deposits were found to be much thicker, and the piezometers were placed at deeper depths to monitor potential long-term groundwater table variations and pore water pressure buildup.

In Location 1, the IoT-based hydrological monitoring setup is the full setup including two piezometers, three suction sensors, and three VWC sensors (Fig. 9a). Piezometers were placed at 1.25 m and 2.0 m depths at monitoring points D1.1 and at 1.4 m and 2.2 m depths at monitoring points D1.2 (Fig. 9b). Sand was filled as a filtering medium around the piezometers. On top of the sand fill, 10–20 cm bentonite was placed to prevent any vertical water passage. The pairs of VWC and suction sensors were installed at approximately three depths: 0.3 m, 0.5 m, and 0.9 m. VWC sensors were installed carefully to the sidewall of the excavated pit until the needles are fully inside the original undisturbed soil (Fig. 10a). For the suction sensors, a small hole was created at the sidewall, and the soil around the sensor was moisturized to obtain good contact between the sensor and the soil. Then, the moisturized soil was packed around the entire sensor discs to ensure full contact (Fig. 10b), and it was placed back to the hole on the sidewall (Fig. 10c). After the placement of a pair of sensors, the excavated pit was backfilled to preserve the in situ bulk density of the soil using the excavated soil until the next level of sensors. The IoT Device was attached to a tree or a pole at approximately 1 m above the ground surface near the monitoring point as shown in Fig. 9c. Finally, the sensor cables were connected to the IoT Device via cable trenches and a PVC pipe along the pole.

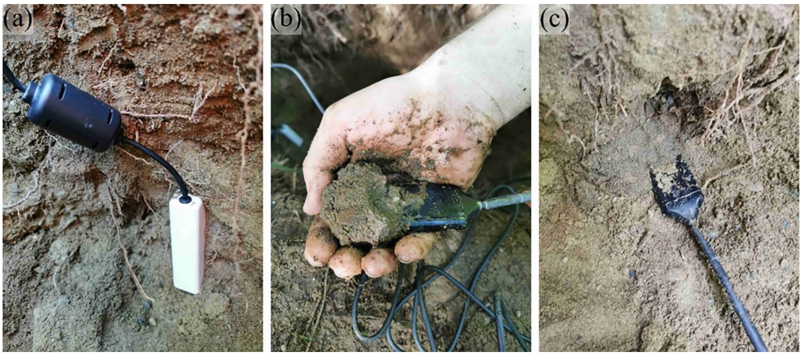

Fig. 10 **a** Placement of VWC sensor, **b** packing moisturized soil around the discs of the suction sensor, and **c** placement of the suction sensor

As shown in Fig. 11, the IoT-based hydrological monitoring setup, in Location 2, is the reduced setup including three suction sensors, and three VWC sensors at each monitoring point: D2.1 and D2.2. The abovementioned installation procedures have been followed during the installation of the VWC and suction sensors. At point D2.2 (Fig. 11b), the presence of the bedrock has been observed at approximately 1 m depth.

Data acquisition and interpretation of collected data

The IoT-based hydrological monitoring system started collecting data on VWC, matric suction, and pore water pressure in August 2020. Apart from one occurrence of hardware failure immediately after deployment, which was solved by replacing the faulty hardware, and a few instances of a short-term network outage, the system operated with no significant downtime. Additionally, it should be noted that the weather data could not be retrieved for February 2021 due to a loose cable connection. The missing weather data, such as precipitation, air temperature, and atmospheric pressure have been collected from nearby weather stations. In this section, all monitored data are presented and interpreted in the following paragraphs.

Figure 12 shows the air temperature and daily precipitation data from the weather station. In Fig. 12a, the ground temperature data retrieved from the suction sensors at D1.2 (Fig. 9b) are also provided for comparison purposes. The sensors at other monitoring points provided similar ground temperature values compared to the suction sensors at D1.2. The average air temperature was approximately 6 ℃ over the monitoring period and varied in the range from −20 ℃ to +30 ℃. The air temperature was significantly below 0 ℃ in January and February 2021 with an average of approximately −7 ℃. Then, the air temperature started to rise above 0 ℃ from March 2021. Figure 12a shows that the ground temperature was more stable on short temporal scales compared to the variations in the air temperature. It was observed that the ground temperature generally decreased with depth when the air temperature was above 0 ℃. This trend reversed in October 2020 as the air temperature started decreasing. In the cold season, from mid-October to almost April, the ground temperature increased with depth. Similar trends in ground temperature with depth were reported in the study of Bordoni et al. (2021). For the 1-year monitoring data starting from August 2020, the total

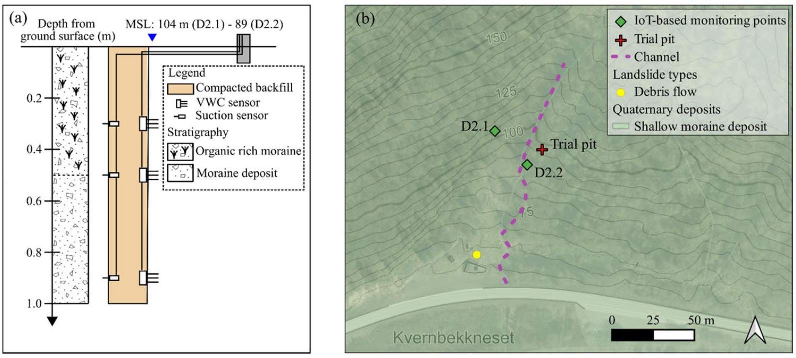

Fig. 11 Location 2: IoT-based hydrological monitoring system: **a** sensor column with soil stratigraphy (D2.2), **b** aerial picture with Quaternary map

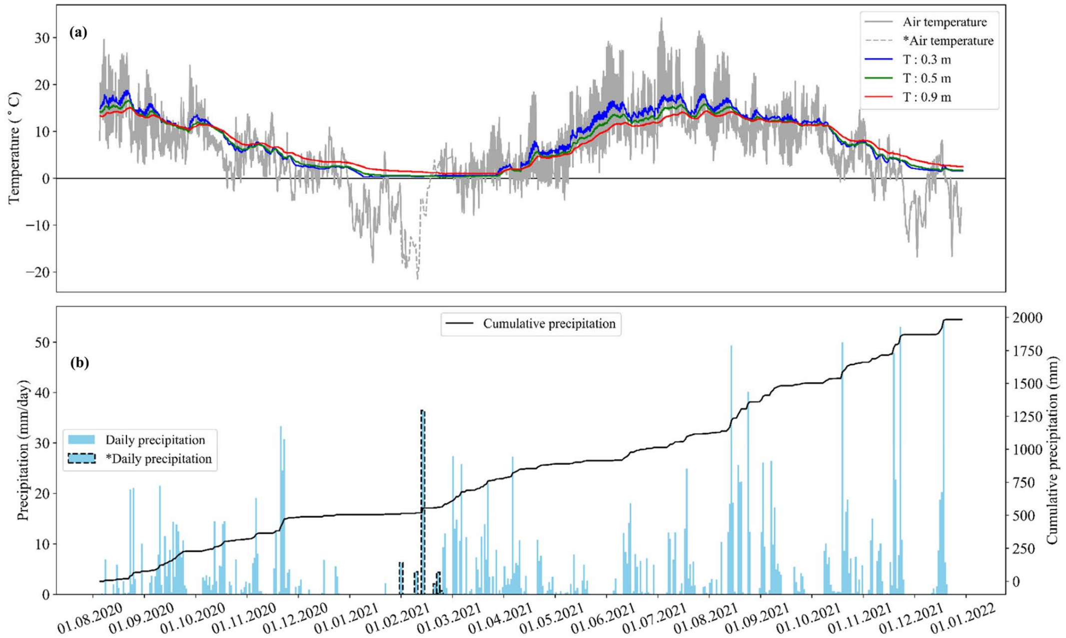

Fig. 12 Weather station data: **a** air temperature with ground temperature measurements retrieved from suction sensors at D1.2, **b** precipitation data with cumulative precipitation (*Data obtained from nearby weather stations)

cumulative rainfall is 1138 mm which is consistent with the value of 1053 mm recorded at the nearby weather station for the same monitoring period. From Fig. 12b, it can be seen that there was less rainfall from mid-November 2020 to mid-February 2021 in the winter period.

Figures 13 and 14 show the data retrieved from the VWC and suction sensors at all four monitoring points: D1.1 and D1.2 in Fig. 13 and D2.1 and D2.2 in Fig. 14. Both figures provide VWC data with the precipitation data from the weather station. The VWC sensor data were converted from sensor output in mV to the VWC by using the custom calibration equations developed for moraine and fluvial deposits (the "Laboratory tests" section). The VWC values were compared to the precipitation measurements to demonstrate the effects of rainfall on the VWC profile. It was observed that the VWC sensors responded swiftly to rainfall events. That is, VWC increased following the rainfall events and decreased in periods with less or without precipitation. In the monitored period, the VWC values ranged between 0.04 and 0.27 m^3m^{-3} at D1.1, between 0.06 and 0.35 m^3m^{-3} at D1.2, between 0.09 and 0.38 m^3m^{-3} at D2.1, and between 0.07 and 0.45 m^3m^{-3} at D2.2. Distinct periods of wetting and drying were observed at each monitoring point. High values of VWC were obtained in the periods of September to December due to intense and frequent rainfall events and mid-February to mid-April due to a combination of rainfall events and snow melt. It can be seen that the variations in the VWC data were different at different depths. Higher variations in VWC values were observed at shallow sensors, at 0.3 m depth, compared to the sensors at deeper depths with the exception of monitoring point D2.2 (Fig. 14c). At D2.2, the VWC at 0.9 m depth showed the highest variation compared to the other sensors at shallower depths. Besides, the VWC value exceeding 0.4 m^3m^{-3} was only observed at D2.2 at the deepest VWC sensor. Both high values of VWC and high variations at 0.9 m depth at D2.2 were attributed to the existence of an impermeable boundary at 1 m depth. The infiltrated water accumulated at the impermeable boundary and resulted in high VWC values. Additionally, the lateral flow might also have contributed to the VWC at the impermeable boundary. For all monitoring points, it was observed that the VWC sensors at 0.3 m depth reacted first to the rainfall events and deeper sensors started reacting with a time delay. Similar to the VWC sensors, the variations of the matric suction at three depths were different. The suction sensors at 0.3 m depth showed, in general, the highest variation in matric suction and reacted first to the rainfall events. In addition, the VWC sensors reacted faster to the rainfall events compared to the suction sensors at the same depths. In the literature, similar observations on the VWC

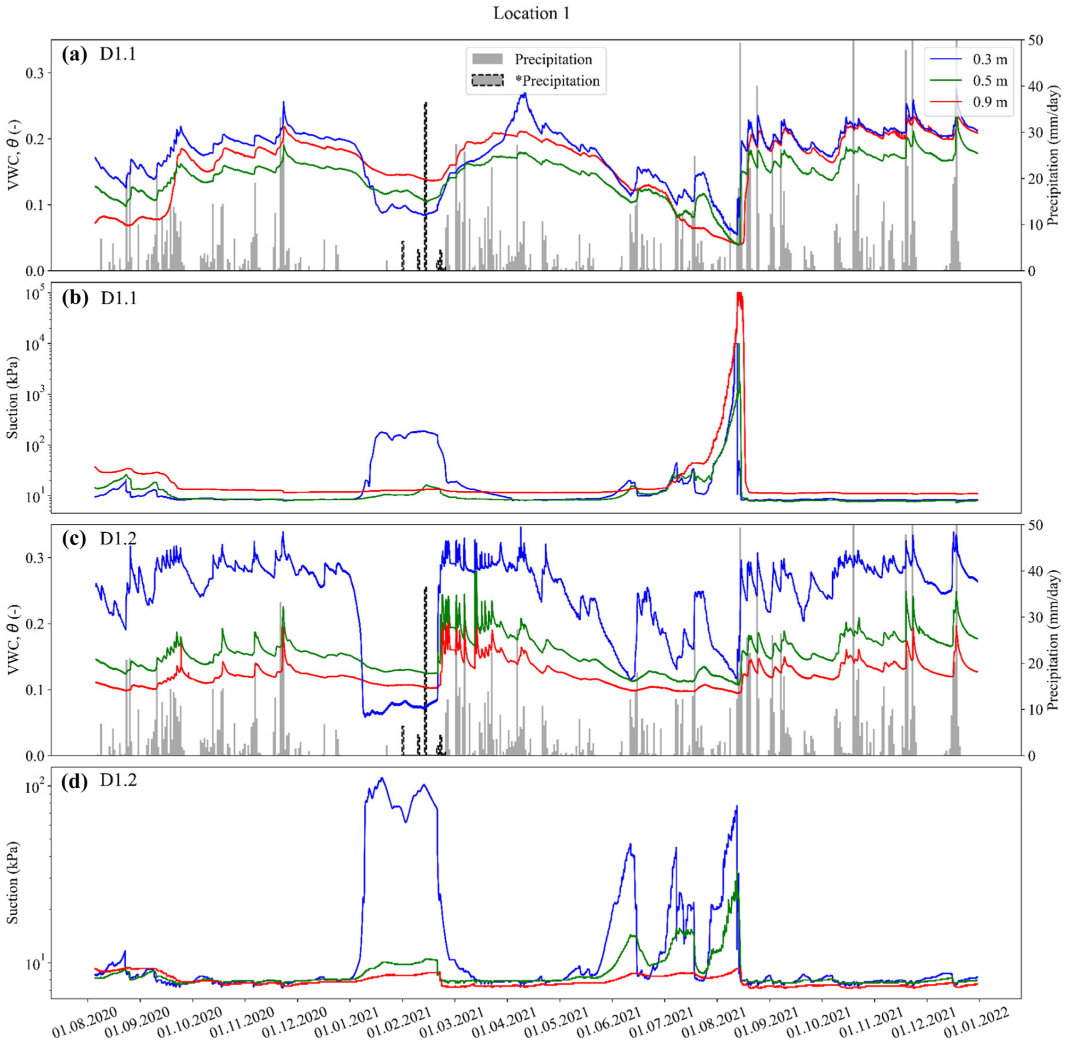

Fig. 13 VWC and suction sensor data for the monitoring points at Location 1: D1.1 **a** VWC and **b** matric suction, D1.2 **c** VWC and **d** matric suction (*Data obtained from nearby weather stations)

and suction sensor response to rainfall events, including the variations in the monitored values, changes in the response times, and variations at different depths, were reported (Comegna et al. 2016; Crawford et al. 2019; Li et al. 2005; Smith et al. 2014).

An important observation that is commonly not found in similar studies relates to the impact of the seasonally cold climate in Norway on the VWC and suction sensor readings. From both Figs. 13 and 14, it can be seen that the VWC values at 0.3 m depth dropped significantly at the beginning of January 2021 when the air temperature started decreasing below 0 ℃ (Fig. 12). In the same cold period, the matric suction values at 0.3 m depth showed a sudden increase at all monitoring points. The decrease in VWC and the increase in matric suction were attributed to the freezing of the pore water at 0.3 m depth. The frozen ground at 0.3 m depth remained frozen until mid-February 2021, when the air temperature started to increase (Fig. 12). With the increase in the air temperature, the ground started to thaw. This caused an increase in the VWC and a sharp decrease in matric suction.

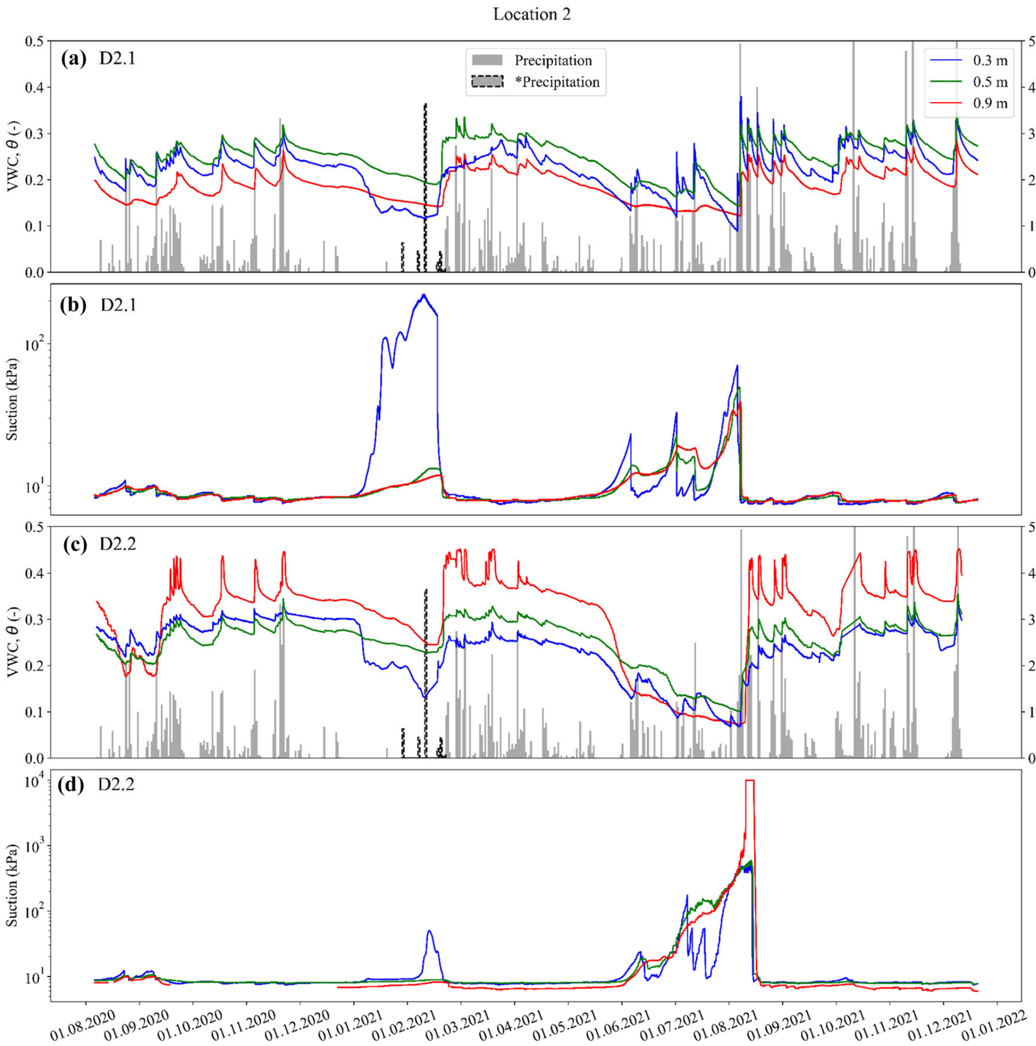

Fig. 14 VWC and suction sensor data for the monitoring points at Location 2: D2.1 **a** VWC and **b** matric suction, D2.2 **c** VWC and **d** matric suction (*Data obtained from nearby weather stations)

The matric suction values were mainly around the sensor's lower limit (9 kPa) in the periods of August to January and March to mid-May. In these periods, there were frequent rainfall events, and the VWC values were also high. Starting from mid-April 2021, a drop in VWC readings can be observed. It was attributed to the increasing air temperatures, evapotranspiration, and less frequent and less intensive rainfall events. During this dry period, the matric suction also increased considerably. The deepest suction sensors at D1.1 (Fig. 13b) and D2.2 (Fig. 14d) reached the sensor limit at the dry state beginning of August 2021. Similarly, high matric suction values and suction values exceeding the sensor limit during the dry periods were reported in the literature (Li et al. 2005; Nunes et al. 2021; Smith et al. 2014). After mid-August 2021, the air temperature started decreasing to a milder level and larger intensity and frequency rainfall events occurred. Therefore, an increase in VWC and a decrease in matric suction values were observed.

The collected data reveals the difference in the response of VWC and suction sensors in Location 1 at D1.1 and D1.2.

The data retrieved from the sensors at D1.2 (Fig. 13c, d) show that the sensors responded even to small size precipitation events and showed higher variability at each depth. Compared to the data collected at D1.1, the VWC data at D1.2 have higher values exceeding 0.3 m^3m^{-3} at the shallowest depth. These local differences in the collected data at Location 1 were attributed to the difference in the vegetation cover. While the monitoring point D1.2 has less dense vegetation cover in the form of grass (Fig. 9c), the location of D1.1 is more densely vegetated with tall trees, which prevents small precipitation amounts in easily reaching the ground. At Location 2, the main difference in the collected data, at D2.1 and D2.2, arises from the abovementioned presence of the impermeable boundary at D2.2.

The piezometer sensor readings at monitoring points D1.1 and D1.2 were converted to the pore water pressure in kPa. It was observed that the piezometer sensors have only responded to the atmospheric pressure and were not affected by the precipitation or air temperature (Fig. 12). In general, it was concluded that the converted values were not representing the pore pressure conditions at the study area and were highly under the effect of atmospheric pressure. This is likely due to very low or no groundwater levels at the positions where the piezometers were installed.

Data processing and early warning strategies

The collected data can be used in combination with data-driven or physical-based landslide prediction models to assess the landslide hazards in the study area. Assessment of landslide hazard is essential in implementing landslide risk management strategies based on monitoring and early warning solutions (Dai et al. 2002). This study features an implementation of the physical-based landside prediction model, TRIGRS (Baum et al. 2008), to evaluate potentially unstable areas in the study area. TRIGRS is a state-of-the-art physical-based model that couples hydrological infiltration and surface runoff models with the infinite slope stability model to evaluate landslide susceptibility to storm events on local to regional levels. TRIGRS features several geotechnical and hydrological model parameters (e.g., soil strength parameters, diffusivity) that were calibrated based on the conducted laboratory and field tests and the inventory of historical landslide events in the area that were presented in earlier sections.

Landslide susceptibility assessment of the study area with TRIGRS is automated to provide predictions of potentially unstable areas for a period of 48 h based on the precipitation predictions for the study area and the sensory readings. The precipitation predictions are downloaded automatically for the study area from the weather services provided by the Norwegian Meteorological Institute (Yr 2021). The sensory readings are used to update the initial groundwater conditions for the TRIGRS model. The initial groundwater conditions are adjusted to correspond to the average VWC values measured by the sensors in the moraine and fluvial deposit regions, respectively. The suction values are used indirectly in the updating of initial groundwater conditions by calibrating Gardner's SWCC equation in the unsaturated formulation of the TRIGRS model (Baum et al. 2008). The focus in the updating of initial groundwater conditions is on VWC sensory readings because they provide higher resolution on the part of the SWCC with low suction values. This is of high importance for wet periods of the year when most of the landslide events occur with the soil having relatively high saturation levels.

Figure 15 presents an example of the landslide susceptibility assessment of the study area with the factor of safety values for $t=0$ h, 24 h, and 48 h for the precipitation prediction shown in Fig. 15d. A factor of safety value below one indicates a landslide susceptible area, while higher values indicate increasing levels of stability. Note that the colors in the legend are only for illustration purposes to differentiate different levels of the factor of safety values and do not represent hazard or warning levels.

As seen in Fig. 15a, the slopes in the study area are stable with the majority of the factor of safety values being above 2 and the remaining between 1 and 2. Following the infiltration of the precipitation within the first 24 h, an overall decrease in the values of factor of safety can be observed with some areas having a factor of safety below one, as shown in Fig. 15b. In the following 24 h, the values of the factor of safety somewhat increase due to lower amounts of rainfall with no potentially unstable areas. These results illustrate the potential of IoT-based hydrological monitoring systems to provide relevant information that can be used in various data-driven or physical-based models to estimate landslide hazards. The system implemented in this study will be tested and developed further to contribute to the implementation of an early warning system for a regional or catchment scale and more advanced model updating strategies to integrate sensory measurements into landslide modeling.

Discussion

In the implementation of a hydrological monitoring system, it is important to have prior knowledge of the landslide events and the local geological setting of the study area. Studying landslide inventory is essential to understand the most frequent type of landslides with the corresponding initiation mechanism and triggering conditions. Additionally, landslide inventories provide a basis to interpret the frequency of sliding, expected dimensions,

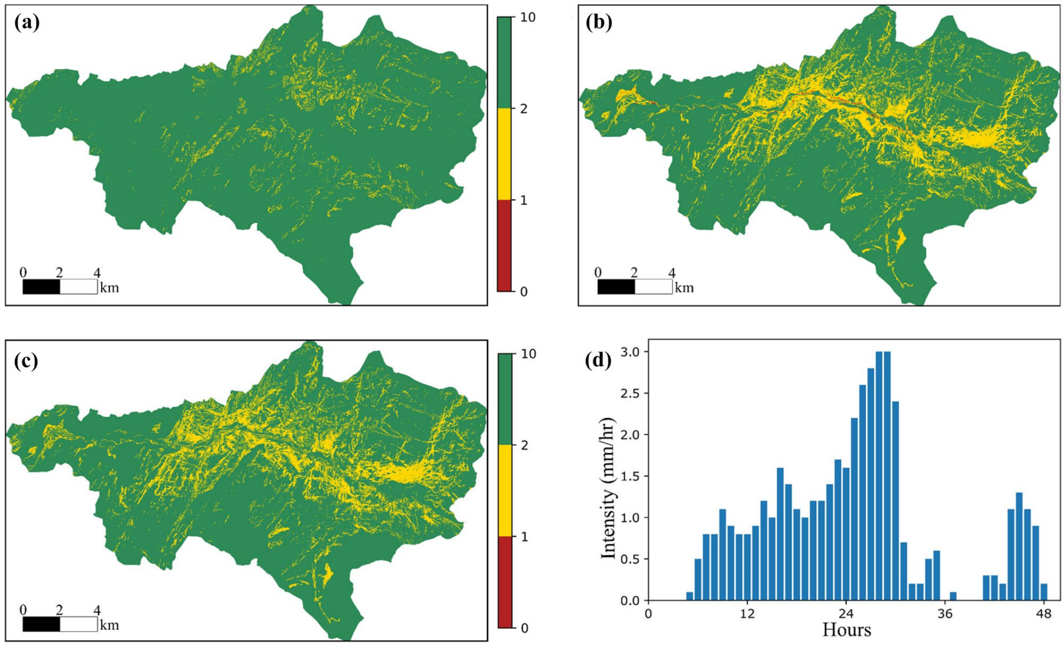

Fig. 15 Landslide susceptibility assessment of the study area with the factor of safety values for **a** $t=0$ h, **b** $t=24$ h, **c** $t=48$ h, and **d** precipitation prediction within the considered 48 h period

and the characteristics of initiation zones. Collecting and interpreting the geological information helps to identify the landslide-prone extent and to estimate the characteristics such as soil thickness and layering, geotechnical and hydrological properties, and groundwater level and flow. A comprehensive investigation of the landslide inventory and the geology is essential in determining the optimal locations to install the monitoring system and monitoring the relevant triggering conditions. While analyzing various landslide inventories, such as Norwegian database, it is important to assess the quality of the registered landslide events in the study area. Additionally, completeness of a landslide inventory is important to decide on the extent of landslide susceptible zones and locations of monitoring points. Remote sensing methods with automated advanced image processing techniques (e.g., Lu et al. 2019) have proved to be useful in developing complete landslide inventories. In a landslide inventory, errors related to the landslide location, type, and time of occurrence should be detected and corrected through quality control. Although this step is sometimes found to be tedious due to the difficulties in collecting additional information, it enhances the decision-making in designing and implementing a landslide monitoring system with improved and more reliable information.

The collected data on VWC and suction provided valuable insights into the hydrological response of the slopes to the seasonally cold climate in Norway. With the current sensory setup, the onset of ground freezing, and thawing were detected with the temperature sensors, while the effects of snow melting on hydrological conditions were measured with the VWC and suction sensors. One of the main findings through the monitoring system is the impact of ground freezing and thawing. At all monitoring points, the VWC values at the shallowest depth of 0.3 m dropped sharply due to the freezing of the soil crust layer, and the matric suction values increased simultaneously. Then, opposite changes were observed due to the thawing following the increase in the air temperature. The VWC data revealed that the intense and frequent rainfall events and combination of rainfall and snow melting resulted in high values of VWC in the ground. The suction sensors showed very low matric suction values over the large part of the year showing that the ground mainly had a high degree of saturation. However, very high matric suction values were also observed in the case of ground freezing and the summer period with no substantial rainfall events.

The VWC sensors were calibrated for the soil types at the locations of deployment as the readings are affected by the surrounding soil type. The calibration is highly important to understand the response; otherwise, inaccurate VWC data might be obtained. The overall performance of the VWC and suction sensors in responding to the rainfall events and snow melting was fulfilling. One shortcoming of the sensory setup was regarded as suction sensors not covering the suction range below 9 kPa. This would be important to reveal the soil–water characteristics at highly saturated conditions. Additionally, piezometer readings were mainly affected by the fluctuations in atmospheric pressure, and no data representing the pore pressure conditions could be obtained. This was attributed to installing piezometer sensors in unsaturated zones where there was no groundwater during the monitored period.

The collected data on VWC and matric suction provided valuable information that can be utilized to reduce landslide risks in the study area through the deployment of an early warning system. Early warning systems are often employed as a cost-efficient landslide risk management measure in comparison to alternatives such as costly engineering solutions and restrictive areal planning measures (Calvello 2017; Dai et al. 2002). Monitoring the hydrological response of sloped terrain can be used in combination with physical-based or data-driven landslide models to estimate hazard levels in the area (e.g., Song et al. 2021). The estimated hazard levels can provide a basis for issuing timely warnings, for example, to evacuate people or close roads or railways to reduce the consequences. Integration of sensory data in landslide models is important to extrapolate the information on hydrological conditions from several monitoring locations to the study area spanning several hundreds of square kilometers. Such integration will be crucial to understand in situ conditions for an accurate prediction of landslide hazards (Abraham et al. 2020). Long-term collection of sensory data is important for developing reliable physical-based and data-driven landslide models. Physical-based landslide models have the advantage of being based on physical laws that can often provide accurate landslide predictions given the known values of various model parameters. However, these parameters are often uncertain due to the costly and time-consuming field and laboratory tests required to estimate them. Long-term data on hydrological conditions can be used to reduce uncertainties in the model parameters through the calibration of physical-based models. Similarly, long-term data can be used to improve the reliability of data-driven models by expanding the training dataset with more extreme events (e.g., rainfall with a 10-year return period).

The implemented IoT-based hydrological monitoring system has some limitations. These are reflected mainly in the limited numbers of sensors, sensory locations, and sensor types. Additional sensory locations across the study area with more sensors per location would contribute to obtaining better insight into the variations of various triggering parameters across the relatively large study area. Similarly, monitoring additional important parameters such as slope deformations and snow amounts would be of great importance for detecting the onset of slope failure and predicting the slope stability conditions during soil thawing and snow melting events. As indicated earlier, these events present some of the most critical triggering conditions for landslides in the study area.

Typical cost components for wireless communication are device costs, infrastructure costs, subscription costs, deployment costs, and maintenance costs. The connectivity expenses of an IoT system will thus vary depending on the selected communication technology and on the possibility of employing existing communication infrastructures. In this study, a 4G-based communication solution based on low power wide area networks proved to be cost-efficient with no infrastructure costs and low costs for devices, subscriptions, deployment, and maintenance. Regarding deployment and operation of the 4G-based IoT Devices, this proved both effortless and reliable. During the system operation, some of the IoT Devices experienced minor periods of network outage, but nothing that reduced the quality of the data acquisition. If the IoT Devices were a part of an operational early warning system, such outages would however be more critical, particularly if they happen during periods of increased landslide risk. A major task for further development and implementation hence is to provide robust and resilient elements throughout the whole system. Thus, an IoT ecosystem that addresses safety issues may require a more formal collaboration with the mobile network operators, to ensure reliable operation. Although the system performance after 1 year seems promising, monitoring systems are often designed and developed for long-term monitoring over several years or decades. Similarly, the performance of the implemented system will be monitored in the years to come. Additionally, the authors expect that the continuous evolution and rapid development within IoT technology will allow for further optimizations of IoT-based hydrological monitoring systems in terms of efficiency and reliability.

Regarding the development of the IoT ecosystem, selecting a suitable communication solution will be a fundamental task that lays the foundation for several other activities throughout the lifespan of the system. As this study aimed at employing the public mobile network, its focus was exclusively on 4G-based solutions. Still, there is a need to make a decision on whether to support NB-IoT, LTE-M, or both. One would also need to ensure that the relevant mobile communication services are deployed in the field of interest and that the mobile network operators provide suitable subscriptions. If considering international deployments, one may also want to consider subscriptions with roaming agreements, thus lowering the cost and effort for entering a global market. While these questions, at first sight, may seem quite intelligible, they may however be affected by both the technological and commercial development in the mobile network sector. As the global IoT market is expected to grow more than 20% annually over the next 5–10 years (Gartner 2019), one should be aware of the risk that network operators, and technology providers may focus on short-term benefits and strategic positioning, instead of long-term customer benefit. Therefore, doing elaborate considerations on the long-term requirements of an IoT ecosystem may be beneficial, to ensure settling for a communication solution that is as sustainable and future-proof as possible.

Summary

This study provided an overview of a case study on IoT-based hydrological monitoring of water-induced landslides in central Norway and highlighted several important findings on the implementation of IoT-based monitoring systems. The system utilized the state-of-the-art IoT technology that employs 4G public mobile networks. This provided an effortless monitoring operation with automated real-time data collection. The monitoring locations were decided through a detailed investigation of the study area in terms of geological setting and landslide inventory. The collected data on hydrological activities in terms of VWC and matric suction provided novel and valuable insights into the hydrological responses of slopes in seasonally cold climates. The effects of rainfall, snow melting, ground freezing, and ground thawing on the monitored parameters were observed. Very high values of volumetric water content were observed during the periods of snow melting or rainfall. The collected data and gained knowledge on the hydrological response of the slopes can be of high value to future efforts in reducing landslide risks through early warning system and supporting digital transformation in managing geohazards risks with IoT technologies. Besides, the current study provided an example of how the collected data could be used to obtain better hazard assessments for a regional scale early warning system.

Acknowledgements The authors acknowledge support from the R&D project KlimaDigital (2018–2022, grant number: 281059) that is funded by the Research Council of Norway and several public and private partners. The authors also acknowledge the support through project KK.01.1.1.02.0027 that is financed by the Croatian Government and the European Union through the Regional Development Fund — the Competitiveness and Cohesion Operational Programme.

Author contribution Emir Ahmet Oguz: Conceptualization; methodology; software; validation; formal analysis; investigation; resources; data curation; writing, original draft; writing, review and editing; visualization. Ivan Depina: Conceptualization; methodology; software; validation; formal analysis; investigation; resources; data curation; writing, review and editing; supervision; project administration; funding acquisition. Bård Myhre: Software, validation; writing, original draft; writing, review and editing; visualization. Graziella Devoli: Investigation, writing, review and editing; visualization. Helge Rustad: Software, validation, investigation, writing, review and editing. Vikas Thakur: Conceptualization; resources; writing, review and editing; supervision; funding acquisition.

Funding Open access funding provided by NTNU Norwegian University of Science and Technology (incl St. Olavs Hospital - Trondheim University Hospital). The research is funded by the R&D project KlimaDigital (2018–2022, grant number: 281059).

Declarations

Conflict of interest The authors declare no competing interests.

References

Abraham MT, Satyam N, Pradhan B, Alamri AM (2020) Iot-based geotechnical monitoring of unstable slopes for landslide early warning in the Darjeeling Himalayas. Sensors (switzerland). https://doi.org/10.3390/s20092611

Anumalla S, Ramamurthy B, Gosselin DC, Burbach M (2005) Ground water monitoring using smart sensors. 2005 IEEE Int Conf Electro Inf Technol. https://doi.org/10.1109/eit.2005.1626962

ASTM D3080/D3080M−11 (2021) Standard test method for direct shear test of soils under consolidated drained conditions. 9. https://doi.org/10.1520/D3080_D3080M-11

ASTM D5030/D5030M-21 (2021) Standard test methods for density of in-place soil and rock materials by the water replacement method in a test pit. https://doi.org/10.1520/D5030_D5030M-21

Baum BRL, Savage WZ, Godt JW (2008) TRIGRS—a Fortran program for transient rainfall infiltration and grid-based regional slope-stability analysis, version 2.0

Bhosale A, Nimbore P, Shitole S, Govindwar O (2017) Landslide monitoring system using IoT. IOP Conf Ser Mater Sci Eng 263:999–1002. https://doi.org/10.1088/1757-899X/263/4/042027

Bordoni M, Bittelli M, Valentino R, Vivaldi V, Meisina C (2021) Observations on soil-atmosphere interactions after long-term monitoring at two sample sites subjected to shallow landslides. Bull Eng Geol Environ 80:7467–7491. https://doi.org/10.1007/s10064-021-02334-y

Bordoni M, Meisina C, Valentino R, Lu N, Bittelli M, Chersich S (2015) Hydrological factors affecting rainfall-induced shallow landslides: from the field monitoring to a simplified slope stability analysis. Eng Geol 193:19–37. https://doi.org/10.1016/j.enggeo.2015.04.006

Calvello M (2017) Early warning strategies to cope with landslide risk. Riv Ital Di Geotec 51:63–91. https://doi.org/10.19199/2017.2.0557-1405.063

Chaturvedi P, Thakur KK, Mali N, Kala VU, Kumar S, Yadav S et al (2018) A low-cost iot framework for landslide prediction and risk communication. Internet Things A to Z p 593–610. https://doi.org/10.1002/9781119456735.ch21

Comegna L, Damiano E, Greco R, Guida A, Olivares L, Picarelli L (2016) Field hydrological monitoring of a sloping shallow pyroclastic deposit. Can Geotech J 53:1125–1137. https://doi.org/10.1139/cgj-2015-0344

Crawford MM, Bryson LS, Woolery EW, Wang Z (2019) Long-term landslide monitoring using soil-water relationships and electrical data to estimate suction stress. Eng Geol 251:146–157. https://doi.org/10.1016/j.enggeo.2019.02.015

CRED (2021) Centre for Research on the Epidemiology of Disasters. https://www.cred.be/. Accessed 31 Dec 2021

Dahlman E, Parkvall S, Skold J (2016) 4G, LTE-advanced pro and the road to 5G. Academic Press. https://doi.org/10.1016/C2015-0-01834-2

Dai FC, Lee CF, Ngai YY (2002) Landslide risk assessment and management: an overview. Eng Geol 64:65–87. https://doi.org/10.1016/S0013-7952(01)00093-X

Devoli G, Bell R, Cepeda J (2019) NVE report 1/2019: Susceptibility map at catchment level, to be used in landslide forecasting, Norway

Devoli G, Dahl M-P (2014) NVE report 37/2014: Preliminary regionalization and susceptibility analysis for landslide early warning purposes in Norway. Oslo, Norway

Fischer L, Rubensdotter L, Sletten K, Stalsberg K, Melchiorre C, Horton P, and Jaboyedoff M (2012) Debris flow modeling for susceptibility mapping at regional to national scale in Norway. In Proceedings of the 11th International and 2nd North American Symposium on Landslides (pp. 3-8).

Froude MJ, Petley DN (2018) Global fatal landslide occurrence from 2004 to 2016. Nat Hazards Earth Syst Sci 18:2161–2181. https://doi.org/10.5194/nhess-18-2161-2018

Gartner (2019) Press release: Gartner Says 5.8 Billion enterprise and automotive IoT endpoints will be in use in 2020. https://www.gartner.com/en/newsroom/press-releases/2019-08-29-gartner-says-5-8-billion-enterprise-and-automotive-io. Accessed 11 Aug 2021

Geonor (2021) Geonor M-600 series high performance piezometer. https://www.geonor.no/produkter/poretrykkmalere. Accessed 31 Dec 2021

Godt JW, Baum RL, Lu N (2009) Landsliding in partially saturated materials. Geophys Res Lett 36:1–5. https://doi.org/10.1029/2008GL035996

Haque U, da Silva PF, Devoli G, Pilz J, Zhao B, Khaloua A et al (2019) The human cost of global warming: Deadly landslides and their triggers (1995–2014). Sci Total Environ 682:673–684. https://doi.org/10.1016/j.scitotenv.2019.03.415

Höglund A, Lin X, Liberg O, Behravan A, Yavuz EA, Van Der Zee M et al (2017) Overview of 3GPP release 14 enhanced NB-IoT. IEEE Netw 31:16–22. https://doi.org/10.1109/MNET.2017.1700082

Hou X (2018) Geotechnical engineering slope monitoring based on internet of things. Int J Online Biomed Eng 14:165–176. https://doi.org/10.3991/ijoe.v14i06.8706

ISO 14688–2:2017 (2017) Geotechnical investigation and testing — identification and classification of soil — Part 2: Principles for a classification

ITU (2012) Overview of the Internet of things (recommendation ITU-T Y.2060)

Khaing CC, Thein TLL (2020) Prediction of rainfall based on deep learning and internet of things to prevent landslide. 2020 IEEE 9th Glob Conf Consum Electron GCCE: 190–1. https://doi.org/10.1109/GCCE50665.2020.9292057

Kim K, Jeong S, Song Y, Kim M, Park J (2021) Four-year monitoring study of shallow landslide hazards based on hydrological measurements in a weathered granite soil slope in South Korea

Lacasse S, Nadim F, Kalsnes B (2010) Living with landslide risk. Geotech Eng J SEAGS AGSSEA 41

Li AG, Yue ZQ, Tham LG, Lee CF, Law KT (2005) Field-monitored variations of soil moisture and matric suction in a saprolite slope. Can Geotech J 42:13–26. https://doi.org/10.1139/t04-069

Lu N, Godt J (2008) Infinite slope stability under steady unsaturated seepage conditions. Water Resources Research 44:1–13. https://doi.org/10.1029/2008WR006976

Lu P, Qin Y, Li Z, Mondini AC, Casagli N (2019) Landslide mapping from multi-sensor data through improved change detection-based Markov random field. Remote Sens Environ 231:111235. https://doi.org/10.1016/j.rse.2019.111235

Mekki K, Bajic E, Chaxel F, Meyer F (2019) A comparative study of LPWAN technologies for large-scale IoT deployment. ICT Express 5:1–7. https://doi.org/10.1016/j.icte.2017.12.005

METER Group (2021a) Teros 12 Manual. https://www.metergroup.com/environment/products/teros-12/.Accessed 31 Dec 2021

METER Group (2021b) Teros 21 Manual. https://www.metergroup.com/environment/products/teros-21/.Accessed 31 Dec 2021

Michoud C, Bazin S, Blikra LH, Derron MH, Jaboyedoff M (2013) Experiences from site-specific landslide early warning systems. Nat Hazards Earth Syst Sci 13:2659–2673. https://doi.org/10.5194/nhess-13-2659-2013

Nadim F, Kjekstad O, Peduzzi P, Herold C, Jaedicke C (2006) Global landslide and avalanche hotspots. Landslides 3:159–173. https://doi.org/10.1007/s10346-006-0036-1

Nordic Semiconductor (2021). nRF9160. https://www.nordicsemi.com/Products/nRF9160. Accessed 29 Jul 2021

Nunes GB, de Oliveira OM, Massocco NS, dos Reis Higashi RA (2021) Study of the influence of suction profile seasonal variations in the global sliding safety factor of a granite residual soil slope. Bull Eng Geol Environ 80:7253–7267. https://doi.org/10.1007/s10064-021-02367-3

Oguz EA, Robinson K, Depina I, Thakur V (2019) IoT-based strategies for risk management of rainfall-induced landslides: a review. 7th Int Symp Geotech Saf Risk (ISGSR 2019) p 733–8. https://doi.org/10.3850/978-981-11-2725-0-is13-2-cd

Pathania A, Kumar P, Sihag P, Chaturvedi P, Singh R, Uday K et al (2020) A low cost, sub-surface IoT framework for landslide monitoring, warning, and prediction. 2020 Int Conf Adv Comput Commun Embed Secur Syst

Pecoraro G, Calvello M, Piciullo L (2018) Monitoring strategies for local landslide early warning systems. Landslides. https://doi.org/10.1007/s10346-018-1068-z

Petley D (2012) Global patterns of loss of life from landslides. Geology 40:927–930. https://doi.org/10.1130/G33217.1

Ray PP (2018) A survey on internet of things architectures. J King Saud Univ Comput Inf Sci 30:291–319. https://doi.org/10.1016/j.jksuci.2016.10.003

SafeLand (2012) Living with landslide risk in Europe: assessment, effects of global change, and risk management strategies. Deliverable 4.6: Report on evaluation of mass movement indicators

Smith JB, Godt JW, Baum RL, Coe JA, Burns WJ, Lu N et al (2014) Hydrologic monitoring of a landslide-prone hillslope in the Elliott state forest , Southern Coast Range, Oregon, 2009 – 2012. https://doi.org/10.3133/ofr20131283

Soegoto ES, Fauzi FA, Luckyardi S (2021) Internet of things for flood and landslide early warning. J Phys Conf Ser. https://doi.org/10.1088/1742-6596/1764/1/012190

Song YS, Chae BG, Kim KS, Park JY, Oh HJ, Jeong SW (2021) A landslide monitoring system for natural terrain in korea: development and application in hazard evaluations. Sensors 21:1–22. https://doi.org/10.3390/s21093040

Sruthy MR, Anjana R, Archana R, Dhanya V, Hridya AH (2020) IoT based landslide detection and monitoring system. Int J Res Eng Sci Manag: 596–9

The Norwegian Water Resources and Energy Directorate - NVE. skredregistrering n.d. www.skredregistrering.no. Accessed 14 Sep 2021

Trimble Water (2021) Wireless Aquifer Level Monitoring. https://www.trimblewater.com/wireless-aquifer-level-monitoring. Accessed 28 Jul 2021

Wei X, Fan W, Cao Y, Chai X, Bordoni M, Meisina C et al (2020) Integrated experiments on field monitoring and hydro-mechanical modeling for determination of a triggering threshold of rainfall-induced shallow landslides. A case study in Ren River catchment, China. Bull Eng Geol Environ 79:513–532. https://doi.org/10.1007/s10064-019-01570-7

Worldsensing (2021) Remote wireless tunnel monitoring of ground water and pore pressure. https://www.worldsensing.com/success-story/groundwater-monitoring-fornebu-metro-oslo-norway-2/. Accessed 28 Jul 2021

Yang Z, Cai H, Shao W, Huang D, Uchimura T, Lei X et al (2019) Clarifying the hydrological mechanisms and thresholds for rainfall-induced landslide: in situ monitoring of big data to unsaturated slope stability analysis. Bull Eng Geol Environ 78:2139–2150. https://doi.org/10.1007/s10064-018-1295-5

Yr (2021) Free weather data service from Yr. https://hjelp.yr.no/hc/en-us/articles/360001940793-Free-weather-data-service-from-Yr. Accessed 22 Aug 2021

ISBN 978-82-326-6230-2 (printed ver.)
ISBN 978-82-326-6459-7 (electronic ver.)
ISSN 1503-8181 (printed ver.)
ISSN 2703-8084 (online ver.)

NTNU
Norwegian University of
Science and Technology